Doctoral Dissertation
Doctoral Program in Metrology (31st cycle)

A novel setup for trapping and cooling Barium ions for atom-ion experiments

Elia Perego

* * * * * *

Supervisors
Prof. M. Inguscio, Supervisor
Dott. C. Sias, Co-supervisor

Politecnico di Torino
April 29, 2019

This thesis is licensed under a Creative Commons License, Attribution - Noncommercial-NoDerivative Works 4.0 International: see www.creativecommons.org. The text may be reproduced for non-commercial purposes, provided that credit is given to the original author.

I hereby declare that, the contents and organization of this dissertation constitute my own original work and does not compromise in any way the rights of third parties, including those relating to the security of personal data.

. . . . . .

Elia Perego

Turin, April 29, 2019

Summary

Ultracold atoms and trapped ions are among the most studied physical systems in experimental quantum physics. On the one hand, ultracold neutral atoms form coherent ensembles of a great number of particles whose interactions, dimensionality and motion can be precisely controlled by well established techniques. On the other hand, trapped ions constitute smaller samples that can be efficiently confined for long periods of time. Due to Coulomb repulsion, trapped ions crystallize in spatially well separated structures, hence granting the possibility of detecting and addressing a single ion more easily with respect to neutral atoms.

Atom-ion quantum mixtures are promising candidates for investigating several open problems in experimental quantum physics and condensed matter physics from a different standpoint. In addition to the features of each individual quantum system, this hybrid system gives rise to atom-ion interactions, which are more long-ranged than atom-atom ones. Atom-ion interactions can represent an extremely useful tool in order to simulate condensed matter problems, to explore new hardware for quantum technologies, to investigate fundamental chemical reactions, and to advance metrology standards. Elastic collisions between ions and atoms can be exploited to sympathetically cool the ions and try to reach the so-far elusive s-wave scattering regime, in which atom-ion collisions can lead to a quantum coherent evolution of the composite system.

Creating an atom-ion quantum mixture represents an experimental challenge, since two complex setups must be integrated in the same apparatus. Moreover, the ultracold atom-ion mixtures realized so far were not brought to the s-wave scattering regime because of the so-called "micromotion", a driven motion affecting the dynamics of the ions trapped in Paul traps. From the experimental point of view, the main levers upon which to act in order to reach the s-wave scattering regime are basically two. The choice of the atomic species and the trapping strategy for confining the ions. For what regards the pair of atomic species, these must be carefully chosen on the basis of their mass ratio and the characteristics of their mutual interaction. We opted for fermionic Lithium for the atoms and Barium for the ions, since in their ground states they are chemically stable for charge-exchange reactions. For what concerns the ions' trapping strategy, the micromotion could be eliminated by using traps not based on radiofrequencies. We explored a possible

alternative based on optical trapping techniques and static electric fields.

In this thesis, I describe the design and the assembly of an experimental apparatus for trapping ions, projected for being integrated with a setup for trapping and cooling atoms, in order to realize hybrid quantum systems that can reach the s-wave scattering regime. The main elements of the apparatus that are reported in the thesis are: the ions' trap design, simulation and realization; the design of novel lasers and their related optical circuits; the realization of a new control software inspired by the requirements for managing an experiment with hybrid quantum mixtures.

Contents

List of Tables VII

List of Figures VIII

1 Introduction 1

2 Atom-ion physics 5
- 2.1 Atom-ion interaction . . . 5
- 2.2 Ion trapping . . . 9
  - 2.2.1 The Paul trap . . . 9
  - 2.2.2 Micromotion . . . 12
- 2.3 Atom trapping . . . 14
- 2.4 Atom-ion collisions in Paul traps . . . 17
  - 2.4.1 Elastic processes . . . 17
  - 2.4.2 Inelastic processes . . . 20
  - 2.4.3 Applications of atom-ion physics . . . 22
- 2.5 Ten years of cold atom-ion mixtures: towards the quantum regime . 25

3 A novel atom-ion machine 29
- 3.1 Ba^+ – Li physics . . . 29
  - 3.1.1 Ba^+ – Li interactions . . . 32
- 3.2 Trapped ion physics: Ba^+ . . . 32
  - 3.2.1 The electro-optical trap . . . 33
  - 3.2.2 Two-dimensional ion crystals . . . 43
  - 3.2.3 Ion loading in an electro-optical trap . . . 45
- 3.3 Ultracold atoms physics: Li . . . 50

4 Ion experimental setup 53
- 4.1 Ion trap design . . . 53
  - 4.1.1 The electro-optical trap . . . 54
  - 4.1.2 The Paul trap . . . 58
  - 4.1.3 Neutral Barium ovens . . . 61
  - 4.1.4 Technical notes on the trap components . . . 63

4.2 Simulations on the trapping system 67
4.2.1 Electric simulations 68
4.2.2 Thermal simulations 73
4.3 Other elements of the experimental setup 76
4.3.1 Imaging objective 76
4.3.2 Radiofrequency drive 76
4.3.3 The atom section of the setup 77

5 Ion laser system 79
5.1 External cavity diode lasers 80
5.2 The design of the external cavity diode laser mountings 84
5.2.1 A "traditional" Littrow design 84
5.2.2 A modified Littrow design 87
5.3 Laser production and setup 95
5.3.1 The trapping laser 96
5.3.2 The deshelving laser 106
5.3.3 Achieved laser powers 107
5.4 Locking strategy 107

6 A novel control software 111
6.1 Control software overview 112
6.2 The application architecture 113
6.2.1 The structure of the experimental sequences 115
6.2.2 Model structure 117
6.2.3 Views and controllers in sequences construction 123
6.3 Control instrumentation 126
6.3.1 The hardware part of the complete control system 127
6.3.2 Communication with a custom serial device 129

7 Conclusions and outlooks 133

A Atom-field interaction: the radiative force 135
A.1 Dipolar force 137
A.2 Radiation pressure 139

B Second harmonic generation theory 141

Bibliography 149

List of Tables

2.1 Length and energy scales of atom-ion interaction potential 8
3.1 Interaction energy scales in the laboratory and center of mass frames for different atom-ion pairs 30
3.2 Stable Barium isotopes 31
3.3 Magic wavelengths and atomic polarizability for the cooling transition energy levels 35
3.4 Budget of the electro-optical trap parameters $\Omega^2_{\phi,i}$ and $\Omega^2_{P,i}$ 41
5.1 List of the commercial components used in our ECDLs. 89
5.2 Laser diodes for Ba^+ wavelengths 95
5.3 List of the wavelengths needed to produce and manipulate Ba^+ ions 107

List of Figures

2.1 Effective interaction potential between ^{6}Li and ^{138}Ba^{+} 7
2.2 Linear Paul trap stability diagram 12
2.3 Scheme of a magneto-optical trap 16
2.4 Logarithmic energy probability distributions of ions immersed in ultracold buffer gases for three different mass ratios 20
2.5 Charge exchange and molecule formation processes 21
3.1 Barium ion Grotrian scheme 30
3.2 Lithium Grotrian scheme 31
3.3 Atomic polarizability of the cooling transition energy levels. 35
3.4 Two crossed focused gaussian beams 37
3.5 Intensity profiles of the interference between two focused gaussian beams 39
3.6 Sketch of the electro-optical trap 40
3.7 Electro-optical trap stability diagram 43
3.8 Montecarlo simulations of Coulomb crystals with different numbers of ions 44
3.9 Toy-model of the Paul trap integrated into the electro-optical trap structure 47
3.10 Overview of the Paul and electro-optical traps 48
4.1 CAD assembly of the electro-optical trap 55
4.2 Different views of the bow-tie cavity mirror mount 56
4.3 CAD assembly of the mirror mount on the metallic base 57
4.4 CAD representations of the four blade electrodes arrangement . . . 58
4.5 CAD assembly of the endcap electrodes 59
4.6 CAD representation of the ceramic lateral supports 60
4.7 CAD section of the ovens system for neutral Barium 62
4.8 Measurements on the oven chimney tubes 64
4.9 Measurements of the electrodes distances 65
4.10 CAD representation of the external side of the ions' vacuum chamber lower flange 66
4.11 Picture of the electrical connection of the oven chimney tubes . . . 67
4.12 Mesh representation of the the electrodes 68

4.13 Paul trap stability diagram having a coupling angle of 45° 70
4.14 Stability diagram of a Paul trap having a coupling angle of 35° . . . 71
4.16 CAD assembly of ions' vacuum chamber lower flange 74
4.18 CAD assembly of the atom-ion experimental apparatus 77
5.1 Wavelengths needed to manipulate Ba^+ ions 79
5.2 Spectra involved in the mode competition that determines the ECDL output frequency 81
5.3 Examples of ECDL configurations 82
5.4 CAD assembly of our Littrow ECDL 85
5.5 Exploded view of our Littrow ECDL. 86
5.6 ECDL base mounting 87
5.7 Exploded view of the modified Littrow ECDL 88
5.8 A section view of the second ECDL version diode mounting 89
5.9 Frequency tuning of the short and long modified Littrow ECDLs as a function of the temperature 91
5.10 Frequency tuning of the short and long ECDL mountings as a function of the laser diode current. 92
5.11 Frequency tuning of the short and long ECDL mountings as a function of the piezo voltage 93
5.12 Heterodyne beat spectra of the short and long ECDL mountings with an ordinary Littrow ECDL 94
5.13 General scheme of a laser optical circuit 96
5.14 Sketch of the 451.7 nm optical circuit 97
5.15 CAD assembly of the "long" Littrow ECDL mounting. 99
5.16 CAD assembly of the tapered amplifier mounting 100
5.17 Exploded view of the tapered amplifier mounting 101
5.18 Second harmonic power evolution as a function of the intensity reflection coefficient of the input coupler 103
5.19 Second harmonic power evolution as a function of the normalized waist position 104
5.20 Second harmonic power evolution as a function of the focusing parameter 104
5.21 Section view of the SHG enhancement cavity CAD assembly 105
5.22 Scheme of the deshelving laser production 106
5.23 Locking optical scheme 108
5.24 Optical scheme for the locking setup of the lasers 109
6.1 Sketch of the experimental sequence composition in our software . . 116
6.2 Software model structure and its classes inheritance diagram 120
6.3 Screenshot of an empty sequence file in the control application . . . 124
6.4 Screenshot of the application during the creation of a waveform . . 124
6.5 Screenshot of the application during the creation of a sequence starting from a previously defined one 126

6.6 Example of the tree structure of the electronic hardware 128
6.7 Picture of the double-purpose electronic board 130
B.1 Set of $H(\sigma, \xi)$ functions plotted for different mismatching parameters σ 146
B.2 Plot of the function $H(\sigma, \xi)$ with the optimized focusing parameter 146

Chapter 1

Introduction

Over the last several decades, quantum physics has undergone an extraordinary evolution thanks to the possibility of isolating single quantum systems in the laboratory. In particular, atomic systems can be confined by applying external fields (optical, electric, magnetic) and can be cooled with laser fields, which can also be used to precisely control the internal state of the particles.

Within atomic physics, research on trapped atomic and molecular ions has attracted a lot of interest over the past decades. The interplay of Coulomb repulsion and the external confinement potential leads, at sufficient low temperatures, to the formation of Coulomb crystals of ions [1], in which the individual particles can be observed with standard optical techniques. The internal and external degrees of freedom of trapped ions can be manipulated by applying laser fields: ions can be prepared in selected internal state with a coherence time of tens of seconds [2], and their motion can be cooled through laser cooling and resolved side-band cooling, ideally down to the absolute ground state [3]. These features make of Coulomb crystals one of the best physical systems for advancing different research fields, e.g. quantum technologies [4], precision spectroscopy and metrology [5], low-temperature molecular physics [6].

Another prominent quantum system developed in experimental atomic physics is represented by ultracold gases of neutral atoms, in which the quantum nature of matter becomes particularly relevant at low temperatures [7]. Atomic gases can be produced in different sizes, from billions of atoms in a magneto-optical trap to single particles in optical potentials [8], and in different dimensions, from one-dimensional strings to three-dimensional samples. The interactions between atoms – which at low temperature can be described in terms of a single parameter, i.e. the scattering length – are typically short-ranged (van der Waals interactions) [9], but their magnitudo and attractive or repulsive nature can be manipulated through magnetic Feshbach resonances [10]. Nowadays, ultracold quantum bosonic and fermionic gases are commonly prepared in the laboratory, providing a platform for many applications, e.g. for studying condensed-matter and solid-state physics [11,

12], exploring many-body quantum physics [9], advancing quantum computation, metrology and sensing [13, 14, 15].

In recent years, a lot of interest has risen on the possibility of merging together ultracold atoms and trapped ions in the same experimental setup in order to form composite, hybrid atom-ion quantum systems [16]. These systems inherit most of the advantages of their constituents, i.e. the possibility of singly addressing and precisely controlling space localized trapped ions, and creating large ensembles of coherent matter with quantum gases. In addition to these features, atom-ion systems can exploit a new "tool" in the experimental toolbox: atom-ion interactions. These interactions are much longer-ranged than atom-atom interactions, and their magnitudo can in principle be tuned via Feshbach resonances [17]. Systems of ultracold atoms and trapped ions complement each other and represent an extremely versatile and powerful experimental platform, in which atoms and ions simultaneously play the role of probe and system [18]. For example, a single ion immersed in an ultracold bath of neutral atoms can be conceived as a localized impurity in a many-body system. In this scenario, the ion can be exploited as a probe for measuring local properties of the atomic gas, like its densities or correlations [19]. Analogously, the atomic cloud at low temperatures acts as an ultracold buffer gas that continuously cools the ions through elastic collisions, realizing a coolant that is transparent at the wavelengths used to manipulate the internal states of the ions [20]. A system of sympathetically cooled ions represents a promising starting point for carrying out efficient protocols of quantum computation without stopping the operations for cooling the trapped ions hardware. Moreover, ions increase the local density of the neutral atoms cloud, thus acting as reaction centers for chemical processes, e.g. charge-exchange and molecule formation, and offering the possibility of studying in a controlled way chemical reactions at low temperature [21, 22].

In most experiments, the collisional energy is set by the driven component of the ions' dynamics in radiofrequency traps (micromotion), since collisions with cold atoms cause a coupling of energy from the driving field to the ions secular motion [23]. A relatively large collisional energy represents a limitation for experiments aiming at exploiting the quantum nature of atom-ion interactions, which arise mainly when atom-ion interactions can be characterized by s-wave phase shift, i.e. the scattering length. In this so-called s-wave scattering regime, the collisions could be controlled via Feshbach resonances and atom-ion interactions could lead to a coherent evolution of the two quantum systems [18]. However, this regime has never been reached so far.

The work reported in this thesis is devoted to the construction of a novel experimental setup for trapping and cooling ions, which is intended to be part of a wider apparatus for exploring cold atom-ion quantum systems in s-wave scattering regime. We considered a mixture of Li and Ba^+, in which we can be able to reduce and even suppress chemical interactions, like charge-exchange processes or three-body recombinations. In the ion experimental setup, we conceived a novel

ion trapping scheme in order to remove the limitations set by micromotion. Several technical problems had to be considered and solved, since the ion's experimental setup must be matched with the equally complex setup for producing, cooling and trapping atomic quantum gases. Moreover, another difficulty was the local lack of know-how concerning ion trapping: in fact, this is the first experiment of this kind in Italy.

The work of this thesis is devoted to find physical and technical solutions to several questions: can we design an ion trap in which atom-ion collisions can enter the s-wave regime? Can we build a laser system that is cheap and reliable for manipulating the ions and the atoms? Can we realize an experimental control system that can help us operate in the most efficient way an atom-ion experiment?

The thesis is organized as follows:

Chapter 2 Atom-ion physics This chapter introduces the basic principles of atom and ion trapping, and the physics of collisions. These fundamental concepts are used to set the limits over which atom-ion collisions enter the s-wave regime, and to show why this regime cannot be reached in current atom-ion experiments. An alternative experimental approach to ion trapping that may solve this limitation is then proposed.

Chapter 3 A novel atom-ion machine Our strategy for reaching the quantum regime involves a new trapping scheme for the ions based on static electric and optical fields, and the proper choice of the atomic species, i.e. Barium for the ions and Lithium for the atoms. This chapter provides the reasons why this pair of atomic species is particularly suited for creating ultracold atom-ion quantum mixtures. In addition, the details regarding the design of the ion trap and the ion loading are reported.

Chapter 4 Ion experimental setup This chapter shows all the technical aspects of the ion "side" of the experimental apparatus. First, the realization of the electrodes of the ion trap is described. Then, the results of electrical, mechanical, and thermal simulations of these components are reported. The chapter concludes with an overview of the other experimental elements of the setup that were not developed within the work of this thesis, i.e. the imaging system, the radiofrequency drive for feeding the electrodes of the linear Paul trap, and the atom "side" of the apparatus.

Chapter 5 Ions laser system This chapter is entirely devoted to the description of the laser systems needed to produce and manipulate Barium ions. The first part of the chapter describes first the fundamental principles of extended cavity diode

lasers (ECDLs), and then two different designs for ECDLs that we realized in the laboratory. The second part of the chapter describes two examples of optical circuits and the locking strategy for producing the laser light for cooling and manipulating the Ba^+ ions. Finally, some considerations about the locking strategy are exposed.

Chapter 6 A novel control software A new control apparatus was designed for this experiment and, more in general, for managing experiments with quantum hybrid systems. This chapter focuses in particular on the software part of the control system. An overview of the application architecture is given, with some code extracts and the details about the construction of the experimental sequences. Finally, as an example about the possibility of integrating the control of custom-made electronic devices, the strategy for managing an electronic board provided with a microcontroller is discussed.

Chapter 7 Conclusions and outlooks The last chapter summarizes the work described in the thesis, and provides a discussion on the physics that we aim at exploring with the new experimental apparatus.

Chapter 2

Atom-ion physics

In this chapter, we will give an overview of the most important characteristics of atom-ion interaction and its applications. First, the physics of atom-ion interactions is described in Sec. 2.1. Then, the following two sections are devoted to illustrate the common strategies for trapping ions and atoms: in Sec. 2.2 Paul traps are explained in details, while Sec. 2.3 proposes an overview of the most common techniques for trapping and cooling atoms. Sec. 2.4 reports on the elastic and inelastic scattering processes in atom-ion mixture where the ions are confined in Paul traps. In addition, the section presents a series of applications that exploit these interactions for advancing different fields of physics and quantum technology. In the last Sec. 2.5, a brief review about the experiments with cold atom-ion mixtures reports on the efforts to lower the system temperature in order to reach the s-wave scattering regime.

2.1 Atom-ion interaction

When an ion approaches an atom, its electric field induces an electric dipole moment on the atom that can be expressed in terms of atomic static polarizability α_0 as [18]

$$\vec{p}(\vec{r}) = \alpha_0 \vec{E}(\vec{r}) \quad \text{with} \quad \vec{E}(\vec{r}) = \frac{1}{4\pi\varepsilon_0} \frac{Z|e_0|}{r^3} \vec{r}$$

where $\vec{r}$ is the inter-nuclear distance and $Z|e_0|$ ($Z \in \mathbb{Z}$) is the ion charge.

The interaction of such induced dipole with the ion's charge leads to an attractive interaction potential of the form

$$V(r) = -\frac{1}{2} \frac{C_4}{r^4} \tag{2.1}$$

where $C_4 = \alpha_0 Z^2 e_0^2/(4\pi\varepsilon_0)^2$.

The potential of Eq. 2.1 is typically the dominant term in the asympthotic behaviour of atom-ion interaction, which is described at short range by a repulsive hard-core term.

In the classical picture of the atom-ion scattering problem, a generic collision in the center-of-mass (COM) frame has energy $E_{\text{coll}} = \frac{1}{2}\mu v^2$ and angular momentum $L = \mu v b$, where v is the relative velocity, b is the impact parameter, and $\mu = m_{\text{ion}} m_{\text{atom}}/(m_{\text{ion}} + m_{\text{atom}})$ is the reduced mass. The possible trajectories after a collision are divided into two different sets on the basis of b being smaller or bigger than the critical impact parameter defined as $b_c = (2C_4/E_{\text{coll}})$ [24]. If $b > b_c$, the collisions are called "forward collisions" since the free-particle trajectories are just slightly modified. Contrarily, if $b < b_c$, the trajectories are strongly modified and the particles are isotropically scattered by the hard-core repulsive potential. This type of collisions is named "Langevin collision" after the seminal paper of Langevin in which the scattering from an r^{-4} potential was firstly studied [25]. The associated Langevin cross section

$$\sigma_L = \pi b_c^2 = \pi \sqrt{\frac{2C_4}{E_{\text{coll}}}}$$

scales with $E_{\text{coll}}^{-1/2}$. This implies that, when an ion is immersed in a gas of neutral particles, the collisional rate constant $K_L = \sigma_L v$ is independent of the energy E_{coll}, a special feature due to the interaction potential r^{-4} scaling.

In the semi-classical approach, the interaction is still described by Eq. 2.1, but the scattering particles are quantum-mechanically treated. Since the interaction potential is spherically symmetric, the solution of the Schrödinger equation in the COM coordinates can be expanded in the spherical harmonics basis as

$$\Psi(r,\theta,\phi) = \sum_{l=0}^{\infty} \sum_{m=-l}^{l} Y_l^m(\theta,\phi) \frac{u_{l,m}(r)}{r}$$

The resulting one-dimensional Schrödinger equation is then

$$\left(-\frac{\hbar^2}{2\mu}\frac{\partial^2}{\partial r^2} + \frac{\hbar^2}{2\mu}\frac{l(l+1)}{r^2} - \frac{1}{2}\frac{C_4}{r^4}\right) u_{l,m}(r) = E\, u_{l,m}(r) \tag{2.2}$$

where μ is the reduced mass and $u_{l,m}(r)$ is the radial part of the solution $\Psi(r,\theta,\phi)$ to the Schrödinger equation.

As Eq. 2.2 shows, two terms contribute to the effective potential: the original interaction potential $V(r)$ and the so-called centrifugal term. The latter is responsible for the presence of a potential barrier in collisions characterized by a non-zero angular momentum. For example, the effective potential describing the interaction between ^{6}Li and ^{138}Ba$^+$ for different values of l is plotted in Fig. 2.1.

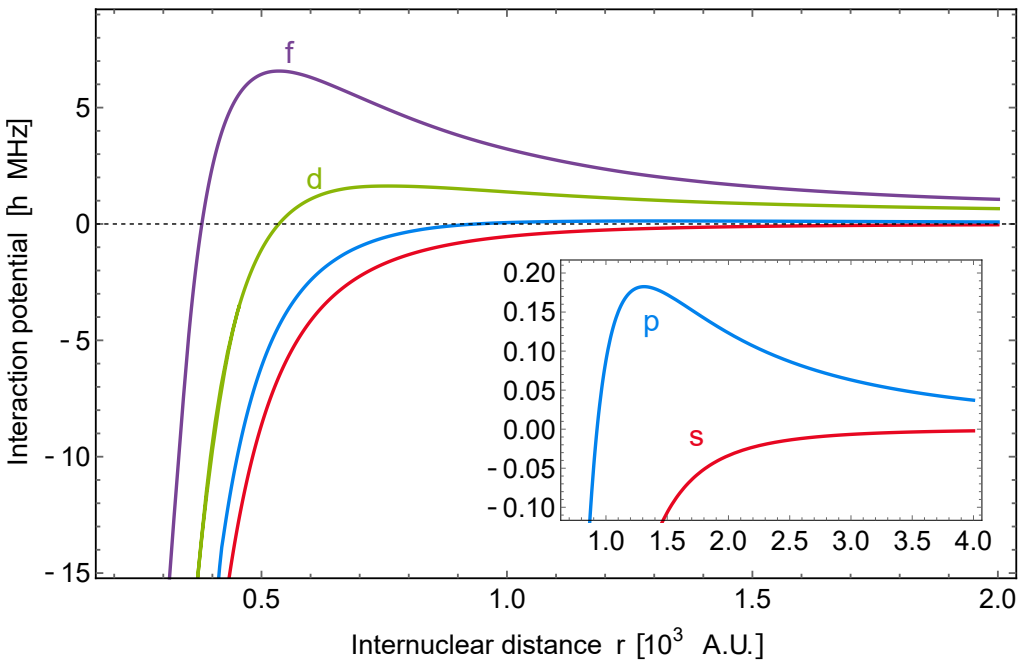

Figure 2.1: Effective interaction potential between ^{6}Li and ^{138}Ba$^+$ for different values of angular momentum quantum number l.

The centrifugal barrier position and height are given by

$$R_B(l) = \sqrt{\frac{2}{l(l+1)}}\, R^* \qquad E_B(l) = \frac{1}{4}\, l^2(l+1)^2\, E^*,$$

where R^* and E^* are the characteristic length and energy scales of the potential

$$R^* = \sqrt{\frac{C_4\mu}{\hbar^2}} \qquad E^* = \frac{\hbar^2}{2\mu R^{*2}}$$

For a given l, if the collisional energy is smaller than $E_B(l)$ and resonant tunneling processes are not considered, the probability that the two particles approach at short distances ($r < R_B(l)$) is negligible. In Tab. 2.1, the characteristic length and energies for some atom-ion pairs are reported. In particular, the data in the last column show that E^* – which also corresponds to the barrier height of the p-wave ($l = 1$) wave function – is very small, thus making it challenging to reach the so-called s-wave scattering regime, in which particles collisions can approach short distances only if $l = 0$.

Following the decomposition of the wavefunction in spherical harmonics, in the semi-classical approach the cross section is expressed as the sum of all the contributions evaluated by solving the Schrödinger equation for each l-dependent

Ion	Atom	α_0 [A.U.]	R* [A.U.]	E* [h kHz]	E* [k_B μK]
$^{174}Yb^+$	^{6}Li	164.1	1317	179.4	8.61
$^{87}Rb^+$	^{87}Rb	319.9	5036	1.636	0.08
$^{174}Yb^+$	^{87}Rb	319.9	5816	0.920	0.04
$^{138}Ba^+$	^{6}Li	164.1	1311	182.5	8.76
$^{138}Ba^+$	^{7}Li	164.1	1412	136.0	6.53
$^{138}Ba^+$	^{23}Na	162.7	2418	15.66	0.75
$^{138}Ba^+$	^{40}Ca	169	3091	6.092	0.29
$^{138}Ba^+$	^{40}K	293.6	4074	3.507	0.17
$^{138}Ba^+$	^{87}Rb	319.9	5578	1.087	0.05

Table 2.1: Length and energy scales of the interaction potential between different atom-ion pairs. In the second section, the ion is always $^{138}Ba^+$. The static atomic polarizabilities are taken from [26, 27].

potential[1]

$$\sigma_q = \frac{4\pi}{k^2}\sum_{l=0}^{\infty}(2l+1)\sin^2(\delta_l) \tag{2.3}$$

where the momentum of the colliding particles in the COM frame is $\hbar k = (2\mu E_{\text{coll}})^{1/2}$ and δ_l is the phase shift of the l-th partial wave.

Driving a parallelism with the classic case, Langevin cross section corresponds to the sum of all the terms in Eq. 2.3 for which the centrifugal barrier is smaller than the collisional energy, i.e. for the angular momentum quantum number l smaller than $L = (1/\hbar)(2\mu)^{1/2}(2C_4E_{\text{coll}})^{1/4}$. In such regime, the particles have enough energy to pass over the centrifugal barrier and directly scatter on the repulsive potential. Otherwise, if $l > L$, the particles collide from the centrifugal barrier. In the case of Langevin collisions, the hard-wall potential must be exactly known in order to evaluate the several phase shift contributions δ_l, which however can be considered in first approximation equally distributed between 0 and 2π, so that $\sin{\delta_l}^2 \simeq 1/2$ in Eq. 2.3. Instead, if $l > L$ the following approximation can be assumed [18]

$$\delta_{l>L} \simeq -\frac{\pi\mu^2 C_4}{4\hbar^4}\frac{E_{\text{coll}}}{l^3}$$

and, consequently, the summation term in Eq. 2.3 becomes $(2l+1)\sin^2(\delta_l) \simeq 2\delta_l^2$.

[1]Here only the elastic cross section is considered, therefore energy transfers from/to electronic energy states are suppressed.

The total elastic cross section can be obtained by summing up all the scattering contribution

$$\sigma_q(E_{\text{coll}}) = \pi \left(\frac{\mu\, C_4^2}{\hbar^2}\right)^{1/3} \left(1 + \frac{\pi^2}{16}\right) E_{\text{coll}}^{-1/3} \tag{2.4}$$

In this case, the collisional rate constant is energy dependent and it scales with $E_{\text{coll}}^{1/6}$, differently from the purely classic Langevin treatment. The expression 2.4 of the cross section in semi-classical approximation gives results in good agreement with the exact ones for high values of the collisional energy E_{coll}. Instead, for low energies, exact quantum mechanical calculations show a deviation from the semi-classical behavior. In fact, in such situations, the few partial waves contributing to the total cross section are strongly dependent on the hard-wall potential, thus invalidating the approximation on the phase shift used to obtain $\sigma_q(E_{\text{coll}})$ [28].

2.2 Ion trapping

Earnshaw theorem states that it is not possible to maintain in stationary equilibrium a collection of charged particles by using an arrangement of purely static electric fields. Thereby, a starting point is the saddle-like potential, which is at most trapping along two orthogonal directions and anti-trapping in the remaining one. Typically, there are two main methods for creating a three-dimensional confinement of charged particles: the Penning trap [29] and the Paul trap [30]. The first is based on the action of a static electric quadrupole potential and a static homogeneous magnetic field. The working principle is that a particle moving away from the quadrupole center experiences a velocity-dependent Lorentz force that deviates its motion. Hence, in a Penning trap the particles remain confined while undergoing closed cyclotron trajectories. This mechanism can represent a problem for hybrid systems, since atom-ion collisions change the motional state of the ion and therefore the Lorentz force acting on it, leading to possible ion losses and limiting the feasibility of sympathetic cooling to low temperatures [31]. Therefore, Paul traps are typically used for confining ions in atom-ion mixtures, since the trapping potential relies on the presence of a real restoring force acting on the ions.

In this section, we provide a theoretical description of Paul traps and of the dynamics of particles there trapped.

2.2.1 The Paul trap

In a Paul trap, also known as RF trap, radiofrequency fields are used to confine charged particles. In the most general arrangement, the confinement is achieved by the interplay of the pseudo-harmonic time-averaged potential created by the

quadrupole RF field and a static electric quadrupole potential. The generic expression of the electric potential near the trap center is given by

$$\begin{aligned}\Phi_{tot}(x,y,z,t) &= \Phi_{RF}(x,y,z,t) + \Phi_{DC}(x,y,z) \\ &= (\alpha x^2 + \beta y^2 + \gamma z^2)\cos(\omega_{RF}t) + (\alpha' x^2 + \beta' y^2 + \gamma' z^2)\end{aligned}$$

where ω_{RF} is the RF frequency and the sets of real coefficients (α, β, γ) and $(\alpha', \beta', \gamma')$ individually satisfy the Laplace equations $\nabla^2\Phi_{RF} = 0$ and $\nabla^2\Phi_{DC} = 0$. To fix the remaining degrees of freedom, other constraints that depend on the electrical potential fed to trap electrodes and their mutual disposition can be imposed. For example, the case of a linear Paul trap with parallel RF electrodes aligned along the z axis and a pair of DC electrodes placed along the axial direction (z axis) is described by the two sets of coefficients $(\alpha, \beta, \gamma) = (1, -1, 0)$ and $(\alpha', \beta', \gamma') = (-1, -1, 2)$. It has to be noticed that the omission of the z-component in the RF field expression ($\gamma = 0$) is valid only under the approximation of infinitely long electrodes. In real linear Paul traps, there will be a small $U_{RF}(z)$ term, considered negligible for the moment.

The overall potential with the coefficient sets of linear Paul traps is

$$\Phi_{tot}(x,y,z,t) = \frac{\phi_{RF}}{2}\frac{\kappa_{RF}}{R_{RF}^2}(x^2 - y^2)\cos(\omega_{RF}t) + \frac{\phi_{DC}}{2}\frac{\kappa_{DC}}{R_{DC}^2}(2z^2 - x^2 - y^2) \quad (2.5)$$

where ϕ_{RF} is the peak-to-peak RF amplitude and ϕ_{DC} is the potential applied on the DC electrodes, R_{RF} and R_{DC} are respectively the distances of the RF and DC electrodes from the trap center, and κ_{RF} and κ_{DC} are geometrical factors smaller than unity that take into account electrodes' shapes and shielding effects.

The force acting on a particle having charge $Z|e_0|$ ($Z \in \mathbb{Z}$) can be evaluated as $\vec{F}(x,y,z,t) = -\nabla U(x,y,z,t) = -Z|e_0|\nabla\Phi(x,y,z,t)$; therefore, the motion equation for an ion[2] with mass m_{ion} can be written in form of a Mathieu equation as

$$\ddot{\vec{x}} + (\vec{a} + 2\vec{q}\cos(2\tau))\,x = 0 \quad (2.6)$$

where $2\tau = \omega_{RF}t$ and the dimensionless Mathieu parameters $\vec{a}$ and $\vec{q}$ are defined as

$$\begin{aligned}\vec{q} &= q\begin{pmatrix}1, & -1, & 0\end{pmatrix} = \frac{2e_0\,\phi_{RF}}{m_{\text{ion}}\,\omega_{RF}^2}\frac{\kappa_{RF}}{R_{RF}^2}\begin{pmatrix}1, & -1, & 0\end{pmatrix} \\ \vec{a} &= a\begin{pmatrix}-1, & -1, & 2\end{pmatrix} = \frac{4e_0\,\phi_{DC}}{m_{\text{ion}}\,\omega_{RF}^2}\frac{\kappa_{DC}}{R_{DC}^2}\begin{pmatrix}-1, & -1, & 2\end{pmatrix}\end{aligned} \quad (2.7)$$

[2]From now on, the case of a positive ion with charge $+|e_0|$ is considered, so $Z|e_0| \to e_0$.

In general, Mathieu equations are differential equations with periodic coefficients, whose stable solution along the i-th coordinate has the following form [32]

$$x_i(t) \;=\; A\, e^{i\beta_i t} \sum_{n=-\infty}^{\infty} C_{2n}\, e^{2int} \;+\; B\, e^{-i\beta_i t} \sum_{n=-\infty}^{\infty} C_{2n}\, e^{-2int} \tag{2.8}$$

where A and B are arbitrary constants, C_{2n} are recursive coefficients depending only on a_i and q_i, and β_i is the so-called characteristic exponent.

In adiabatic approximation ($|a_i| \ll |q_i|$ and $|q_i| \ll 0.4$) [29], the solution 2.8 to the motion equation Eq. 2.6 reduces to

$$x_i(t) \;\simeq\; x_{1,i} \cos(\omega_i t + \varphi_i) \left(1 + \frac{q_i}{2} \cos(\omega_{RF} t)\right). \tag{2.9}$$

The first term of Eq. 2.9 refers to the so-called "secular motion", which is characterized by amplitude $x_{1,i}$ and phase φ_i, both depending on the initial conditions, and by the frequency

$$\omega_i \;=\; \frac{\omega_{RF}}{2}\, \beta_i \;\simeq\; \frac{\omega_{RF}}{2} \sqrt{a_i + q_i^2/2} \ll \omega_{RF}$$

The second term of Eq. 2.9, known as "micromotion", is instead driven by the applied RF field, and its amplitude is equal to the secular motion amplitude reduced by a factor $q_i/2$. In the next Sec. 2.2.2, the effects of the micromotion on the trapped ions' dynamics are discussed.

Stability diagram From the general expression Eq. 2.8 of the solution to the motion equation, the stability conditions can be inferred: the characteristic exponent β_i must be real for each axis $i = x, y, z$ [33]. For the trap geometry described by the vectors in Eq. 2.7 (i.e. linear Paul trap with axial DC electrodes), the stability diagram is reported in Fig. 2.2. In such case, the radial – i.e. along x and y axes – stability conditions are degenerate, while the axial confinement is granted only if a_z is positive. In principle, the confinement is possible for any value of ϕ_{RF}, even if the stability region becomes sharper when q is increased [34].

Finite dimensions of the electrodes, misalignments and machining defects may change the potential of a real Paul trap from the ideal case. Moreover, the previous analysis is valid only for a single trapped particle: in presence of more than one confined ion, spatial-distributed charges must be taken into account as an additional deviation from the ideal representation. In this scenario, a coupling between secular motion and micromotion may occur since contributions of orders higher than the quadrupole term in the electric potential expansion are not anymore negligible [35]. As a result, with certain values of the a and q parameters for which a charged particle would be trapped in an ideal trap, the particle motion turns out to be unstable. These conditions, which dig instabilities "canyons" in the ideal quadrupole stability

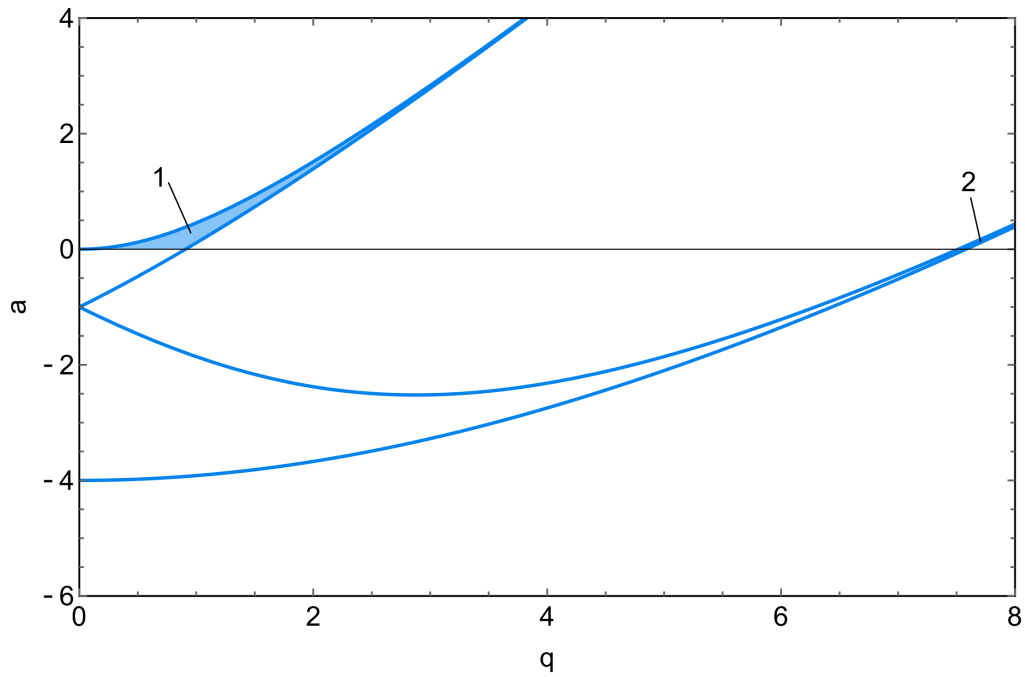

Figure 2.2: Linear Paul trap stability diagram. The blue areas are the primary (1) and secondary (2) stability zones, where all the stability conditions for the three axes are satisfied. Contrarily to the mass filter case, in which the DC potential has a saddle shape in the plane orthogonal to the RF electrodes (x-y plane) [30], in the described linear Paul trap the DC potential is either attractive or repulsive (depending on ϕ_{DC}) along both the x and y axes. Therefore, the stability conditions are degenerate for those axes, giving rise to the stability regions delimited by the blue lines [34].

region, can be expressed in terms of the characteristic exponents β_r $(r = x, y)$ and β_z [36]

$$n_r\beta_r + n_z\beta_z \;=\; 2k$$

with $n_r, n_z, k \in \mathbb{Z}$, and $n_r + n_z = N$, where N is the instability order.

2.2.2 Micromotion

The solution 2.9 to the motion equation, developed with a classical approach, shows that the micromotion amplitude depends on the amplitude of the secular motion, thus suggesting that by cooling the ion the micromotion can be reduced down to zero. Instead, a quantum mechanics treatment reveals that the dispersion of the ion wave-packet leads to a minimum amplitude of micromotion $x_{mm,i} = \sqrt{\hbar/(2m\omega_i)}q_i/2$, which is independent of the secular motion [3]. Therefore,

the energy associated with this motion sets a limit on the lowest temperature reachable by the ion in a Paul trap to $T_{\min} = m\omega_{RF}^2 x_{mm}^2/(4k_B) \simeq \hbar\omega_{RF}/(4k_B)$, where in the last step $a \to 0$ has been assumed. The conclusion is that micromotion is a direct consequence of the technique employed to confine the ions, and can not be avoided neither by applying cooling techniques, since it is driven motion.

Excess micromotion In the practical realization of a Paul trap, micromotion can be increased by the action of several mechanisms, the contributions of which are generally called "excess micromotion". Typically, the main contributions arise from stray electric fields due to the the presence of other trapped ions or charge patches on the electrode surfaces, imperfections in the trap realization (misalignments, machining flaws, length difference in the RF wires, etc.), and the effect of the finite length of the electrodes contribute to the micromotion, as well as any deviation of the phase relation between the radiofrequency signals from the ideal in-phase condition (for opposite electrodes). Once the ion is pushed for any reason out of the RF node, it is subject to a micromotion with larger amplitude with respect to the case where it is not displaced.

If the presence of additional DC fields E_{DC} and phase mismatches are taken into account, then the classical solution Eq. 2.9 in adiabatic approximation becomes [37]

$$x_i(t) \simeq \Big(x_{0,i} + x_{1,i}\cos(\omega_i t + \varphi_i)\Big)\left(1 + \frac{q_i}{2}\cos(\omega_{RF} t)\right) - q_i \frac{R_{RF}\kappa_{RF}}{4}\varphi_{RF}\sin(\omega_{RF} t) \tag{2.10}$$

where φ_{RF} is the phase difference between the potential applied to opposite RF electrodes (considered small), and

$$x_{0,i} \simeq \frac{e_0\, E_{DC,i}}{m\omega_i^2}$$

is the ion's average position.

From Eq. 2.10, it can be deduced that the excess micromotion is non-zero for any position (unless $\varphi_{RF} = 0$), and that its amplitude due to DC stray fields is $x_{0,i}q_i/2$ [38]. Thereby, the ion mean energy due to the micromotion is

$$E_{mm,e} \simeq \frac{m_{\text{ion}}}{16}\left(q_i\omega_{RF}x_{1,i}\right)^2 + \frac{m_{\text{ion}}}{16}\left(q_i\omega_{RF}x_{0,i}\right)^2 + \frac{m_{\text{ion}}}{64}\left(q_i\kappa_{RF}R_{RF}\varphi_{RF}\omega_{RF}\right)^2 \tag{2.11}$$

where the last two terms take into account the excess micromotion.

For detecting the excess micromotion several techniques can be adopted, for instance based on monitoring the average position of the ions when DC stray electric fields are fed on purpose to the electrodes [38], or observing the spectral composition

of the ion transitions [37], a technique that has the advantage of making it possible to distinguish the micromotion contributions on each orthogonal direction. Other detecting method is based on the parametric excitation of the ions induced by providing to the RF electrodes an oscillating field having a frequency closed to the secular frequency of the ions' motion [39]. In hybrid systems of atoms and ions, the excess micromotion can also be deduced by monitoring the losses from the atomic cloud due to collisions with the ions [40, 20].

Following its detection, excess micromotion can be compensated by applying additional potentials to the ions. The compensation of stray fields is typically realized by applying DC voltages to the existing or to dedicated electrodes, while the compensation of RF stray fields (e.g. due to mechanical imperfections of the electrodes) can be performed by using additional RF signals.

2.3 Atom trapping

Cold atoms are typically produced by performing laser cooling on a hot gas originating in most of the cases either from an oven or from dispensers. These samples of hot neutral atoms can be confined by using trapping schemes based on optical and/or magnetic fields. The typical cooling stages that bring from a sample of hot atom to a quantum degenerate gas are briefly reviewed in the following paragraphs.

Zeeman slower Hot atoms are first slowed down by exploiting the radiation pressure which arises from the interaction between the atoms and a laser with angular frequency near an atomic resonance (see Appendix A). If we consider a one dimensional problem of atoms traveling in one direction and a counter-propagating laser beam, the radiation pressure will depend on the velocity-dependent Doppler shift of the atoms [41]. As a consequence, the laser frequency has to be continuously tuned in order to match the atomic resonance that changes with the atom velocity, and maximize the decelaration imposed by the radiation pressure. In a more practical and common arrangement, the atom's energy levels themselves can be shifted by the Zeeman effect by applying an external magnetic field [42]. This technique is used in a so-called Zeeman slower, a tube connected to the oven that is wrapped in coils for creating an inhomogeneous magnetic field properly tailored for compensating the varying Doppler shift [43]. The ideal shape of the magnetic field can be found by choosing the maximum decelerating force on the atoms and imposing the effective detuning to be equal to zero

$$\delta_{\text{eff}}(\vec{v}\,) \;=\; \omega_L - \omega_{\text{atom}} - \vec{k}_L \cdot \vec{v} - \frac{\mu_B B}{\hbar} \;=\; 0$$

where ω_{atom} is the frequency of the unperturbed cooling transition, ω_L and k_L

are respectively the laser frequency and wave-vector, v is the atom velocity and μ_B is the Bohr magneton[3]. Therefore, the magnetic field B should be modeled as

$$B = \frac{\hbar}{\mu_B}\left(\delta + k\sqrt{{v_i}^2 - 2az}\right) = \frac{\hbar}{\mu_B}\left(\delta + \left(k^2{v_i}^2 - \frac{2\hbar k^2\Gamma z}{m_{\text{atom}}}\frac{\Omega^2/2}{\delta^2 + \Omega^2/2 + \Gamma^2/4}\right)^{\frac{1}{2}}\right)$$

where in the last passage the acceleration a has been estimated as half the maximum value obtained from $\vec{F}_{\text{rad}} = m_{\text{atom}}\,\vec{a}$ of Eq. A.12.

Magneto-optical traps One of the most common traps for collecting large clouds of atoms is the magneto-optical trap (MOT) [44], in which a magnetic quadrupole and three pairs of counter-propagating, near-resonant laser beams are used to both confine and cool a quite dilute cloud (typical density $\approx 10^9\,\text{cm}^{-3}$) composed by up to several billion of atoms. Specifically,(see Fig. 2.3), the MOT consists of six red-detuned counter propagating laser beams with opposite circular polarization and a magnetic field gradient (realized with coils in anti-Helmotz configuration). Including the Zeeman splitting of the excited state hyperfine structure ΔE_{HF} operated by the external magnetic field $B(z) = B_z\,z$, the force acting in the MOT on an atom moving with velocity $\vec{v}$ is [45]

$$\vec{F}_{MOT} = \hbar|\vec{k}|^2\,\frac{I}{I_{sat}}\frac{8\delta/\Gamma}{(1\,+\,(2\delta/\Gamma)^2)^2}\left(\vec{v} + \frac{\Delta E_{HF}}{\hbar}\right) = \eta\vec{v} + K\vec{r} \tag{2.12}$$

where the limits $kv \ll \delta$ and $\Delta E/\hbar \ll \delta$ have been assumed.

The opposite circular polarization of the laser beams and the space-dependent hyperfine energy splitting caused by the magnetic field gradient ensure that the atoms enter in resonance only with the counter propagating photons. Therefore, in case of red detuning, the force acting on the atoms in a MOT has both the viscous component of the optical molasses and a restoring component which confines the atoms in the low magnetic field region ($\eta, K < 0$).

The spatial dimension of the MOT can be evaluated with the capture range, which is defined as the maximum distance from the MOT center that an atom can have to be trapped. In other words, the capture range r_c is the distance where an atom at rest is in resonance with a MOT beam. Thus, from the relation $\Delta E_{HF} = \hbar|\delta|$, the capture range is

$$r_c = \frac{\hbar|\delta|}{\mu_B g_F m_F B_z}\,. \tag{2.13}$$

[3]The applied magnetic field is supposed to be high enough to bring the atom in the regime of strong coupling (Paschen-Back) and write the hyperfine energy splitting as $\Delta E_{HF} = \mu_B B$.

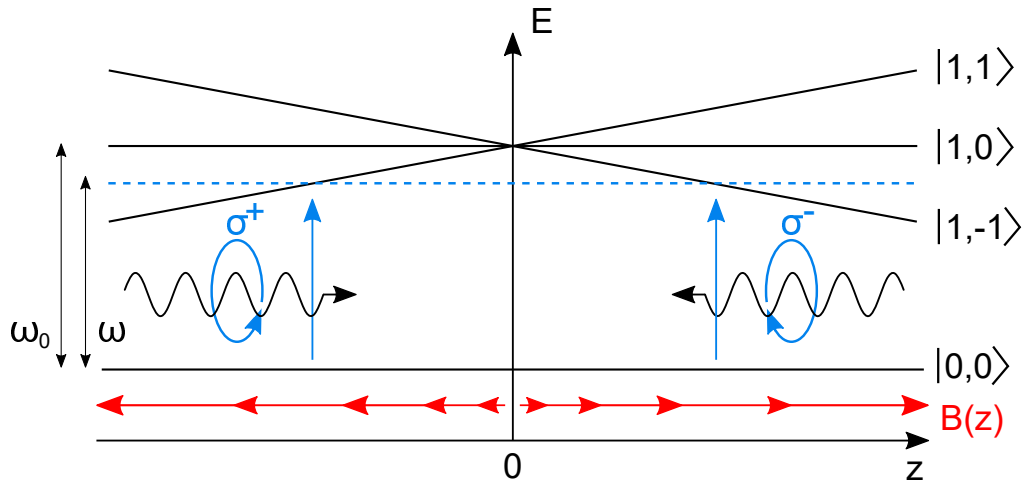

Figure 2.3: Scheme of a magneto-optical trap. The circular polarization of the beams ensures that the atoms interact only with the counter-propagating beam, simulating the action of a restoring force towards the MOT center (where the magnetic field vanishes).

where g_F is the Landé g-factor and m_F is the hyperfine magnetic quantum number.

From Eq. 2.13 the dependence of the MOT dimension on the magnetic field gradient can be inferred. Typical values for B_z are on the order of tens of Gauss/cm, for detunings of 2-3 Γ [45].

The temperature scale of atoms trapped in a MOT is set by the Doppler temperature of the cooling transition

$$k_B T_D = \hbar \frac{\Gamma}{2}. \tag{2.14}$$

Typically, for alkali metals, the Doppler temperature is on the order of hundreds of μK. It is clear from Eq. 2.14 that MOTs operating on narrower transitions are colder, thus one might be tempted to choose a very narrow transition. Nevertheless, the drawback of this approach is that the excited level of the narrow transition has a lifetime longer than the timescales of heating and loss mechanisms (e.g. collisions from background gas).

Dipolar and magnetic traps In order to achieve lower temperatures and higher densities, atoms must be transferred from a MOT to either an optical dipolar trap or to a magnetic trap. In these traps, the atom's internal state is usually well controlled by performing optical pumping, and the density increases by a few orders of magnitude with respect to the MOT. Therefore, interactions provide a non-negligible contribution to both the dynamics and the thermodynamics of the

atoms. In fact, collisions can be exploited to perform evaporative cooling, a process in which the atoms lying on the tail of the Maxwellian distribution of the clouds kinetic energy are expelled from the trap, while the remaining atoms thermalize to a lower temperature through collisions. In dipolar and magnetic traps atoms can be cooled down to hundreds of nK or even lower temperatures, at which the gases become quantum degenerate [46]. The behavior of these quantum gases depends strongly on the statistical nature of the particles, i.e. if the particles are fermions or bosons. In both cases, the quantum gas can show quantum coherence which can last up to seconds. The typical number of particles in a quantum gas can reach a few million atoms, and the density can be as large as a few $10^{14}\,\mathrm{cm}^{-3}$.

2.4 Atom-ion collisions in Paul traps

In order to study atom-ion physics, one has to realize a hybrid apparatus in which a trap for ions and a trap for neutral atoms are in the same physical location. While there are several options for trapping atoms, ion trapping in atom-ion experiments is typically achieved only by using Paul traps. However, the dynamics of an ion in a Paul trap is strongly modified by the presence of an ultracold buffer gas. In this section we describe this dynamics, and the fundamental problems that have prevented so far atom-ion experiments from reaching the s-wave regime.

2.4.1 Elastic processes

The typical frequencies of atom traps and Paul traps differ by orders of magnitude. While Paul traps frequencies have usually order of magnitude 100 kHz - 20 MHz, atom traps reach at most frequencies of order of magnitude 1 kHz. Moreover, the temperature of atomic clouds (expressed in frequency) is typically lower than 10 MHz, and can be as low as a few kHz for a quantum gas. Therefore, a first effect that one may expect in atom-ion systems is the sympathethic cooling of the ions by elastic collisions with ultracold atoms. This perspective has risen a lot of interest in the atomic physics community, since an efficient sympathetic cooling could be useful for several applications, like ion-based quantum computers [4] and quantum simulators [47].

In the last few years, atom-ion sympathetic cooling was realized in experiments with one or more ions confined in a RF trap and immersed into a cold cloud of atoms, which were trapped either in magnetic, optical or magneto-optical traps. Associated with sympathethic cooling, a depletion and a rise in temperature of the atomic gas has been observed [40].

Although there is in principle no limit to the temperature reachable with the sympathetic cooling technique, up to now no experimental group was able to report

sympathetic cooling down to temperatures at which atom-ion collisions are in the s-wave regime [16]. As a consequence, in all the experiments realized so far atom-ion collisions are basically classical, since they are described by a scattering cross-section to which many partial waves contribute (see Eq. 2.3). As a result, the atom-ion evolution is not coherent, and phenomena like Feshbach resonances have not yet been observed. A Feshbach resonance is an effect of coupling of a two-particle scattering state of a molecular potential to a bound state of a second molecular potential; by changing a magnetic field one can tune the coupling and thus the interactions between the colliding particles. Considering the importance in realizing coherent quantum mixtures in which the mixtures' properties (like collisions) can be controlled, achieving a low energy in atom-ion systems represents a great experimental challenge and a valid motivation to improve the sympathetic cooling efficiency.

The main mechanism that prevents atom-ion mixtures from reaching ultralow temperatures is a heating effect due to the presence of micromotion in the ion dynamics. The instantaneous velocity of an ion in a Paul trap has two contributions: the component of velocity of the secular motion $\vec{v}_{\text{sec}}$ and the one of the micromotion $\vec{v}_{\text{mm}}$, i.e.

$$\vec{v}_{\text{ion}} = \vec{v}_{\text{sec}} + \vec{v}_{\text{mm}} \tag{2.15}$$

If we consider a scattering event with an atom at rest in the laboratory frame, energy and momentum conservation set the velocity of the ion after the collision [48]

$$\vec{v}_{\text{ion, f}} = (1-\beta)\,\vec{v}_{\text{ion, i}} + \beta R\,\vec{v}_{\text{ion, i}} \tag{2.16}$$

where $\vec{v}_{\text{ion, i}}$ and $\vec{v}_{\text{ion, f}}$ are respectively the initial and final ion velocity given by Eq. 2.15, β is a parameter equal to μ/m_{ion}, and R is a rotation matrix that considers the rotation of the initial vector of an angle θ, ϕ with respect to $\vec{v}_{\text{ion, i}}$. If we now reformulate Eq. 2.16 by expressing the velocities in the form of Eq. 2.15, we obtain

$$\vec{v}_{\text{sec, f}} = (1-\beta)\,\vec{v}_{\text{sec, i}} + \beta R\,\vec{v}_{\text{sec, i}} + \beta(R-\mathbb{I})\vec{v}_{\text{mm}} \tag{2.17}$$

The last term of Eq. 2.17 shows the coupling of the micromotion into the secular motion of the ion after the collision. Interestingly, this contribution could reduce or increase the secular velocity, i.e. leading to cooling or heating, depending on the direction and amplitude of $\vec{v}_{\text{mm}}$ at the moment of the impact. However, on average, this coupling leads to a net heating of the colliding particles. The energy scale of the atom-ion collisions is then given by the average kinetic energy of the micromotion due to the ion motion (first term of Eq. 2.11) [49], i.e.

$$E_{mm,e} = \sum_i \frac{m_{\text{ion}}}{16}(q_i\omega_{RF}x_{1,i})^2,$$

which, alternatively, can be expressed as [48]

$$E_{mm,e} = \sum_i \frac{1}{2} m_{\text{ion}} (v^i_{mm,e})^2 \quad \text{with} \quad v^i_{mm,e} = \frac{e_0 \phi_{RF}}{m_{\text{ion}} \omega^2_{RF}} \frac{\kappa_{RF}}{R^2_{RF}} x_{1,i} \cos(\omega_{RF} t) \tag{2.18}$$

This energy can in principle be reduced by compensating the micromotion down to tens of μK with standard micromotion compensation techniques [49]. However, micromotion compensation is not sufficient. In fact, atom-ion collisions happen in the center of mass of the colliding particles. As a result, even if the ion is initially very carefully placed at the center of the RF quadrupole, an approaching atom will cause the displacement of the ion out of its initial position due to the atom-ion attractive r^{-4} interaction potential, and the atom-ion collision will be affected by an unavoidable micromotion component [50, 51]. This effect, which was directly observed by detecting the collisional heating of an ion initially placed in the absolute ground state of its trapping potential [52], can be minimized only by increasing the mass ratio between the ions and the atoms, so the best candidates for reaching the s-wave regime are mixtures with a strong mass imbalance, as Yb^+-Li [50] and Ba^+-Li [53].

Numerical simulations of atom-ion systems in compensated Paul traps lead to the ultimate temperature limit [50]

$$T_{\text{limit}} = \frac{1}{k_B} \sum_i \left(\frac{\mu^5}{m^3_{\text{ion}}} \omega^2_{RF} \omega^2_i C_4 \right)^{1/3} \tag{2.19}$$

where the assumption of shallow axial trapping has been made ($a \to 0$), μ is the reduced mass and the potential coefficient C_4 depends on the atomic polarizability (Eq. 2.1). Thereby, as anticipated, the atomic species must be chosen so that $m_{\text{atom}}/m_{\text{ion}} \ll 1$, i.e. heavy ions in gases of light atoms. In this sense, the most promising couple is represented by ^{174}Yb ions immersed in a gas of fermionic ^{6}Li ($T_{\text{limit}} = 0.19\,\mu$K, with $q = 0.3$ and $\hbar\omega/k_B = 2.4\,\mu$K).

Another remarkable consequence of the presence of micromotion is that the energy distribution of interacting atom-ion mixtures is not maxwellian, but rather a power-law distribution (see Fig. 2.4). Interestingly, this is the same distribution of several complex systems in nature, like the distribution of the earthquakes [54], and in human-related behaviors, like insurgent and terrorist activities [55]. Such distribution is characterized by longer tails with respect to the maxwellian ones, which reach much higher temperature than that of the buffer gas [56]. Along with the trapping parameters, the mass ratio $m_{\text{atom}}/m_{\text{ion}}$ well parametrizes the deviation of the power-law from the thermal distribution, with the feature that the smaller the atom-ion mass ratio is, the more the power-law closely fits the Maxwell distribution [57]. As a result, only atom-ion pairs for which $m_{\text{ion}} \gtrsim m_{\text{atom}}$ can be used reliably without strongly affecting the ion trap lifetime.

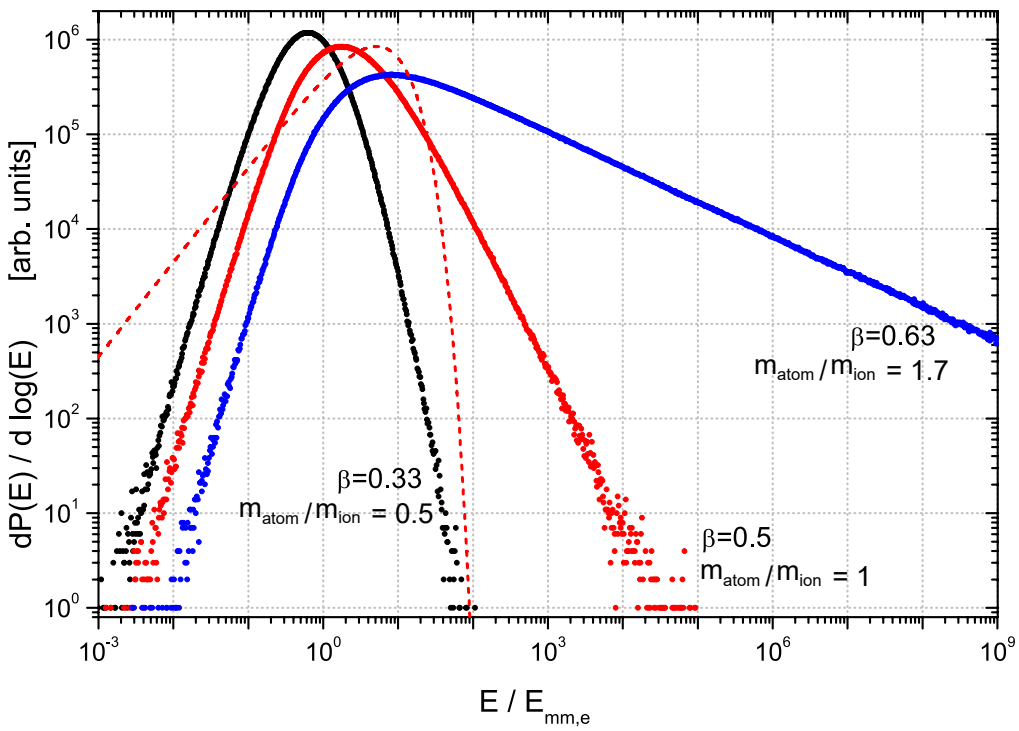

Figure 2.4: Logarithmic energy probability distributions $dP(E)/d(\log(E))$ of ions immersed in ultracold buffer gases for three different mass ratios as a function of the energy scale $E_{mm,e}$ set by the average excess micromotion energy (see Eq. 2.18). The parameter β is defined as in Eq. 2.16. The red dashed line corresponds to a thermal energy distribution with $5\,E_{mm,e}$. Figure adapted from Ref. [48].

2.4.2 Inelastic processes

After inelastic collisions, the atom or the ion (or even both) undergo to either a change of the internal state or a chemical reaction. Energy conservation imposes that the energy difference between the initial and the resulting atom-ion systems must be released[4] either by the emission of a photon (radiative processes) or by an increase of kinetic energy (non-radiative processes). The particles must approach each other to short distance to collide, therefore inelastic interactions usually occur at a rate proportional to the Langevin one. Depending on the outcomes, different inelastic processes can be identified.

[4]Since we are interested in atom-ion collision in low temperature regimes, only exothermic processes will be taken into account.

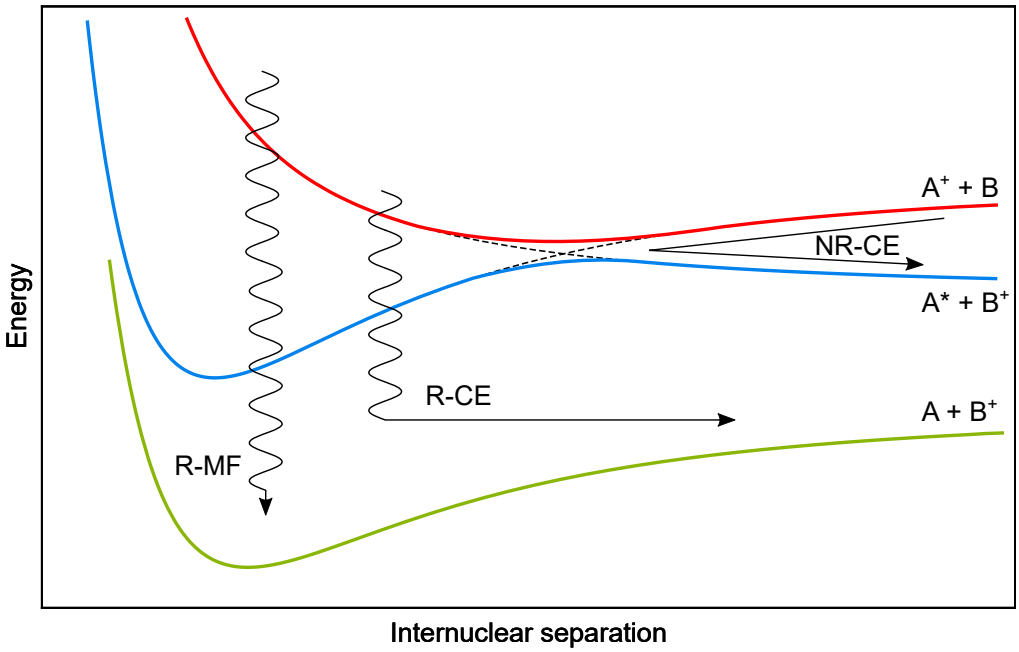

Figure 2.5: Charge exchange and molecule formation processes in atom-ion collisions. (NR-CE) Non-radiative charge exchange. (R-CE) Radiative charge exchange. (NR-CE) Radiative molecule formation.

Charge exchange $\mathbf{A^+ + B \Rightarrow A + B^+}$

In a charge exchange process, the atom B gets ionized, while the ion A^+ gains the electron in excess becoming neutral and thus insensitive to electric-based trapping. As illustrated in Fig. 2.5, charge transfer can occur in atom-ion collisions both in radiative (R-CE) and non-radiative (NR-CE) processes, characterized with different probabilities that depend on the electronic state of the colliding particles. In principle, the newly formed ion B^+ can be trapped after its creation, and typically this is the case of radiative charge exchange. In experiments where several ions are trapped, R-CE processes can be revealed when an ion suddenly becomes "dark" [58], since in general the ion B^+ will be insensitive to the lasers used to cool the ion A^+. Instead, if the charge exchange is non-radiative, then the newly formed ion B^+ might have enough kinetic energy for evading the trap. From an experimental point of view, such process is revealed by the ion loss from the crystal [22].

Charged molecule formation $\mathbf{A^+ + B \Rightarrow (AB)^+}$

Another chemical reaction that may occur after an inelastic collision is molecule formation. Typically, the products of these association processes are stabilized either through spontaneous emission of a photon (R-MF in Fig. 2.5) or through a

collision with another neutral atom (if the atomic cloud is sufficiently dense) [22].

Molecule formation and, more generally, all the inelastic collisions are short-range processes, because only scattering events from the hard-core potential barrier, thus at small interatomic distances, may have outcome channels as bound states.

Three body recombination $\mathbf{A^+ + B + B \Rightarrow A^+ + B_2}$

Three body recombination is a mechanism in which the creation of a neutral molecule starting from an atom-atom pair is assisted by the presence of an ion that absorbs a portion of the momentum, thus ensuring momentum conservation [59, 60]. Therefore, this is a non-radiative process, in which the binding energy of the molecule is transformed into kinetic energy of the colliding particles. Since the atom-ion interacting potential is long-ranged and attractive, at low temperature there is a relevant probability for two atoms to interact simultaneously with the same ion (unless prevented by other mechanisms like the Pauli exclusion principle), even at low atomic densities: in fact, the ionic electric field has the effect of locally increasing the atomic density.

Quenching collisions $\mathbf{A^+ + B^* \ / \ (A^+)^* + B \Rightarrow A^+ + B}$

Quenching collisions occur when, after an inelastic collision, the atom-ion pair undergo to relaxations of their internal states, or even to disexcitations. These effects may reduce the lifetime of the ions' excited states, which must be well known for performing techniques as ion storage and realizing frequencies standards [61, 62].

A particular type of quenching collisions are spin exchange or relaxation processes. These mechanisms can cause a loss of coherence in the system and, in case of non-radiative process, an increase of the kinetic energy of the particle, with the possibility of particle losses. Nevertheless, it can be exploited to sympathetically cool internal excitations in addition to the external motion, for instance in a molecular ion [63]. In general, the problem of controlling quenching processes is particularly relevant, e.g. if a qubit is encoded in an ion's internal state, since quenching reduces the coherence of the qubit [64].

2.4.3 Applications of atom-ion physics

In this section, some of the most interesting applications for experiments with ultracold atom-ion quantum mixtures are listed. These applications range from quantum computation to quantum simulation, from controlled quantum chemistry to metrology and precision spectroscopy related studies.

Quantum computation One among the most natural applications of atom-ion systems is the implementation of quantum gates, suggested by the long-range

interaction potential between atoms and ions. In a recent proposal [65], state-dependent interactions are used as a tool to control the state of a qubit encoded in the internal state of an atom. In this applications, the fidelity of the quantum gates and the coherence of the quantum memory may be compromised by the micromotion due to the RF quadrupole of Paul traps that drives the ions' motion. A solution to circumvent this problem may be to keep atoms and ions far enough to suppress the couplings. Even in this condition, gate implementation should be possible if the interactions are sufficiently strong. For this reason, the case of atoms in Rydberg states was proposed in order to increase the strength of atom-ion interactions and entangle the atoms with internal or motional states of the ion with high fidelity, even in presence of state imperfections [66]. Alternatively, technical limitations such as micromotion can be avoided by changing the trapping scheme of the ions and, for instance, adopting optical trapping techniques [67].

Quantum simulation Quantum simulation aims at emulating condensed matter models with physical systems on which experimentalists can exert a high level of control on the systems' parameters [68]. Both trapped ions and cold atoms have successfully been employed as quantum simulators. On the one hand, cold atoms can be arranged in spatially periodic structures when confined in optical lattices and can be prepared in ensembles of many thousands of particles (either bosons or fermions), which can be simultaneously manipulated [69]. Nevertheless, addressing the single particles and realizing long-range interactions are challenging tasks, since the interactions are typically short-ranged and the lattice constants have sub-micron dimensions. On the other hand, trapped ions are an ideal system for manipulating and accurately detecting the internal states of single particles [47]. In addition, since ions are made to interact with each other by pulses of laser or microwave radiation, they can even be employed to simulate hamiltonians characterized by long-range interactions. However, scalability represents an issue: in RF traps cold crystals of trapped ions can be realized only with ions trapped along the axis of a linear Paul trap, which then suffer a reduced micromotion. Therefore, the number of ions that form a quantum simulator can be increased only by creating extremely long linear crystals [70].

Thereby, in atom-ion systems, the presence of a new type of long-range interaction makes it possible to conceive new methods for emulating condensed matter models. In a recent proposal, it was suggested to use a one-dimensional crystal of trapped ions to create a quasi-periodic potential for ultracold atoms and induce a band structure [71]. The advantage of this approach relies in the fact that the atomic degrees of freedom couple to phonons of the ion lattice, thus emulating a natural thermally excited solid-state system. This feature, which naturally arises in atom-ion systems, is instead totally absent in other systems used as solid state physics simulators, as e.g. ultracold atoms trapped in optical lattices.

Moreover, atom-ion mixtures were proposed as candidates for simulating bosonic

Josephson junctions [72], in which a single ion is exploited to control the dynamics of a degenerate quantum gas of bosons confined in a double well potential. Finally, this model can be scaled by using an atomic gas in an optical lattice, a system in which the atomic interactions can be controlled with a chain of trapped ions [73].

Quantum chemistry and astro-chemistry In addition to the many applications in the field of condensed-matter physics, quantum simulators based on atom-ion hybrid systems can be employed to investigate fundamental chemical reactions at the single particle level, thus entering the realm of controlled quantum chemistry. By manipulating both atom and ion quantum states, atom-ion inelastic collisions – including charge exchange and three-body recombination processes – can be tuned, thus ensuring the possibility of studying controlled chemical reactions in terms of reaction rates, branching ratios, and product kinematics [21, 74]. Chemical reactions in atom-ion systems can provide a high-flux source for slow molecular beams, which find applications in high-precision spectroscopy, scattering experiments, and studies of collective dynamics of strongly interacting systems at low temperatures [75, 76]. Moreover, the possibility of producing cold ionic molecules with controllable process leads to several applications in the astro-chemistry research field [77], e.g. the investigation of the processes occurring in interstellar clouds [78], where molecules are created under dilute (density from $10^4\,\mathrm{cm}^{-3}$ to $10^6\,\mathrm{cm}^{-3}$ in "dense" clouds) and cold (average temperature $< 100\,\mathrm{K}$, even $\approx 10\,\mathrm{K}$ is some clouds) conditions [79].

Metrology Trapped ions and cold atoms represent, taken singularly, the best hardware for realizing an optical clock based on precision spectroscopy in the visible region of the electromagnetic spectrum. Although the spectroscopic methods are basically the same, there a few differences in the operation of atom-based and ion-based optical clocks. In ion-based optical clocks, a small crystal of ions (typically one) is confined and cooled in a Paul trap, before being spectroscopically interrogated [80]; the particles are usually recycled, and a second interrogation can be performed shortly after the previous one [81]. In atom-based clocks, a large sample of cold atoms ($> 10^4$) is typically first accumulated in a magneto-optical trap and then loaded in a one dimensional optical lattice for quantizing the motion in one spatial direction [82]. Then, the atoms are interrogated all at the same time. At the end of the interrogation the cloud falls by gravity and a new cloud has to be created. Given the differences in the operation of the two clocks, the two uncertainty budgets have specific contributions. In atom-based clocks, the drawback of interrogating many particles in one run is the presence of interaction-induced frequency shifts. In ion-based clocks, the presence of Coulomb repulsion ensures that no interaction-shift is present. Nevertheless, the longer-ranged r^{-4} interaction potential with neutral particles makes the ions more sensitive to collisions with particles of the background gas. Additionally, ion-based clocks suffer from a

micromotion shift, which is the largest contribution to the overall uncertainty in state-of-the-art ion-based clocks.

Atom-ion systems can provide a novel platform to study some of the open problems, with the goal of improving the performances of optical clocks. First, understanding atom-ion interactions at both quantum and classical level can considerably improve the estimate of the frequency shift due to collisions with background particles in ion-based clocks. This estimate is at the moment based only on theoretical calculations within a semiclassical approximation [83, 84], but a measurement of the background collisional shift has been so far realized only in atom-based clocks [5]. Second, atom-ion collisions in the presence of micromotion cause atoms losses. Interestingly, these losses can be used as a probe for measuring the ions micromotion [85]. In fact, this alternative method is currently the most accurate in detecting and estimating the excess micromotion, and could be used in ion-based clocks to better estimate the micromotion-induced second-order Doppler shift. Finally, different methods for trapping ions, like optical trapping, have been recently tested [67]. A possible method to ensure cooling in these micromotion-free traps can rely on collisions with a cold buffer gas; this hardware can represent an alternative platform for realizing ion-based optical clocks.

2.5 Ten years of cold atom-ion mixtures: towards the quantum regime

The first theoretical proposals about combining ultracold atomic gases and cold trapped ions in the same quantum system date back to the first years of 2000s. Elastic and inelastic atom-ion collisions (e.g. Ref. [86], 2000) and the behavior of trapped ions in a BEC (e.g. Ref. [87], 2002) were initially studied from a theoretically point of view. A few years later, the first experiment showing cold atom-ion collisions was published [88] (2009).

In this experimental realization, RF-trapped ions are characterized by relatively high temperatures with respect to the typical temperatures of the neutral in the MOT (hundreds of μK), due to the presence of the micromotion. In such conditions, atom-ion scattering can be observed in the energy range $1 - 10^{-3}$ K (cold regime), where several partial waves contribute to the collision.

While this energy scale is large with respect to the typical centrifugal barrier heights, it is low with respect to the molecular energy levels' scale. Therefore, trapped ions in a MOT of neutrals find an immediate application in cold quantum chemistry and astro-chemistry (refer to Sec. 2.4.3), since chemical associative reactions can be studied in a controlled fashion [22, 89]. Other investigated chemical reactions are charge-exchange collisions, both in homonuclear atom-ion pairs (e.g. Na^+/Na [90], Yb^+/Yb [88], Rb^+/Rb [91, 59]) and heteronuclear pairs (e.g. Ca^+/Na [92], Yb^+/Rb [21, 40], Ba^+/Rb [93]), three-body recombination (e.g. Rb^+/Rb_2

[94]), and photodissociation (e.g. Rb_2^+ [95]). Additionally, sympathetic cooling was shown to be effective to reduce the vibrational energy of cold molecules [63], and the extension of this cooling technique to multipole RF traps was also proposed [96].

Decreasing the temperature of the system is crucial in order to observe atom-ion collisions with contributions from a lower number of partial waves; moreover, atom-ion systems at low temperatures are suitable platforms also for exploring spin dynamics and decoherence [97]. Phenomenons as spin-exchange [98] and spin-relaxation [64, 99] are studied with a view to understanding from which kind of coupling between states they originate and which states are more protected against the coherence loss.

The first attempts to reach a colder regime were focused on lowering the atoms' temperature by substituting the MOT with a Bose-Einstein Condensate (BEC) [20, 58], which is characterized by temperatures lower than $1\,\mu$K [100]. Nevertheless, it turned out that the ions do not thermalize via elastic scattering at the atoms' temperature as one might expect because of the micromotion, and that the energetic collisions with the ion cause continuous atoms' losses from the BEC.

Another possible strategy to reach a colder regime is to start with an ultracold ion. In Ref. [52], a single $^{88}Sr^+$ ion is first optically cooled to the motional ground state and then immersed in an ultracold buffer gas of ^{87}Rb. However, an increase of ion temperature was observed since the effects of micromotion are enhanced by the $Sr^+/Rb \approx 1$ mass ratio. Nevertheless, this condition made it possible to experimentally detect for the first time the ions' power-law energy distribution (see Sec. 2.4.1).

Other strategies have been suggested to lower the temperature of atom-ion mixtures. A possible solution to reach the quantum regime with RF-trapped ions immersed in an ultracold cloud of atoms is to properly choose the atomic species on the basis of their mass ratio, thus limiting the energy transfer from the RF trapping field to the atom-ion system due to the presence of micromotion, and lowering the experimentally attainable temperature [101].

Alternatively, a drastic solution for circumventing this obstacle is to change the ion confinement technique. For instance, ions can be trapped in optical dipole traps [67, 102]. This strategy is quite challenging since the typical magnitude of the optical forces exerted on an ion are typically smaller than the forces arising from electric stray fields. However, purely optical trapping of a single $^{138}Ba^+$ ion has been realized for up to 3 s with a complex trapping scheme based on two lasers having different frequencies [103]. Optical trapping of single ions in absence of any electric field has been obtained even by employing one-dimensional optical lattices formed by two counter-propagating beams [104]. Very recently, small crystals of up to six Ba^+ ions were trapped in a single-beam dipolar trap [105]. Hence, ion optical trapping represents an encouraging solution to overcome the temperature limitations existing in radiofrequency traps, but it still has to prove long lifetimes

of the confined particles, and reduced heating and decoherence rates in order to ensure the possibility of controlling the ions down to the quantum level [106].

Finally, a different approach is to start from a cold two-body wavepacket: Ref. [107] proposes to initiate the atom-ion collision from an ultracold Rydberg molecule without involving any ion trapping. In this proposal, the photoionization of the Rydberg molecule triggers a scattering event between the components of the Rydberg molecule ionic core in presence of the r^{-4} interaction potential. By measuring the evolution of the two-body wavefunction, it is possible to measure the scattering length.

Chapter 3

A novel atom-ion machine

The aim of our experiment is to realize an hybrid system of trapped atoms and ions that can be cooled enough to enter the quantum regime. As highlighted in the previous chapter, the two main levers upon which to act in order to achieve our purpose are the choice of the atomic species and the ion trapping strategy. For what concerns the elements, we opted for $^{138}Ba^+$ and ^6Li. The reasons sustaining this choice are discussed in Sec. 3.1. For what regards the ion trap, we decided to implement, in addition to a Paul trap, an "Electro-Optical" (EO) trap, i.e. an ion confining scheme formed by a static electric quadrupole and an optical field, in which there is intrinsically no micromotion. Details on the EO trap and ion loading are exposed in Sec. 3.2. Finally, the last section 3.3 proposes a quick overview on the production strategy of quantum gases of fermionic Lithium.

3.1 Ba^+ – Li physics

In choosing a pair of atomic species for an atom-ion experiment, a crucial parameter is the height of the p-wave centrifugal barrier in the interaction potential, since this sets the collisional energy scale for which the atom-ion pair can enter the s-wave regime. The values of the p-wave centrifugal barrier reported in Tab. 2.1 for different atom-ion pairs are evaluated in the center-of-mass frame. However, the kinetic energy of the particles is usually measured in the laboratory frame. Therefore, it is useful to relate the kinetic energy in the laboratory frame, i.e. K_{lab}, to the collision energy in the COM frame K_{coll}; assuming that the ion has a much larger kinetic energy than the atom, this relation reads [101]

$$K_{\text{lab}} \simeq \frac{3}{2}\frac{\mu}{m_{\text{ion}}}K_{\text{coll}}. \tag{3.1}$$

Tab. 3.1 lists the temperatures corresponding to the kinetic energies K_{lab} in the laboratory frame related to the height of the p-wave barrier in the COM frame for a number of atom-ion pairs. Given the ratio μ/m_{ion} in Eq. 3.1, atom-ion pairs

Ion	Atom	E* [$k_B\,\mu$K]	$K_{\rm lab}$ [$k_B\,\mu$K]
^{174}Yb$^+$	^{6}Li	8.61	172.3
^{87}Rb$^+$	^{87}Rb	0.08	0.105
^{174}Yb$^+$	^{87}Rb	0.04	0.088
^{138}Ba$^+$	^{6}Li	8.76	140.2
^{138}Ba$^+$	^{7}Li	6.53	90.15
^{138}Ba$^+$	^{23}Na	0.75	3.508
^{138}Ba$^+$	^{40}Ca	0.29	0.868
^{138}Ba$^+$	^{40}K	0.17	0.499
^{138}Ba$^+$	^{87}Rb	0.05	0.090

Table 3.1: Interaction energy scales in the laboratory and center of mass frames for the atom-ion pairs considered in Tab. 2.1.

with the large mass imbalance, like Yb$^+$-Li and Ba$^+$-Li, are the best candidates for reaching the s-wave regime.

Barium ions Neutral Barium is an alkaline earth metal with atomic number 56. It has high chemical reactivity, so it can not be found in nature as a free element and, when exposed to air, it quickly reacts with the molecular oxygen to form Barium oxide. Its stable isotopes are reported in Tab. 3.2.

The ion ^{138}Ba$^+$ has been successfully trapped by many groups, in fact it has been one of the first isolated and detected ions [110]. First, ^{138}Ba$^+$ has the electronic configuration of the xenon with an additional electron in the $6^2S_{1/2}$ state, which

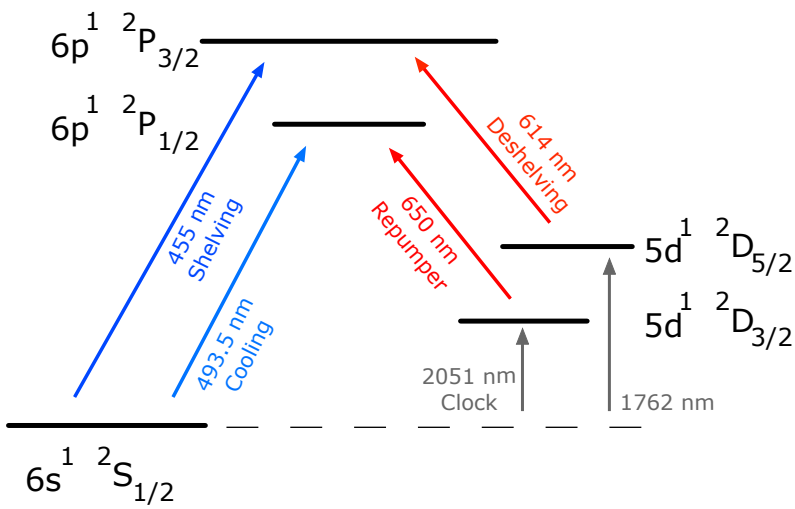

Figure 3.1: ^{138}Ba$^+$ ion Grotrian scheme [108].

Isotope	^{130}Ba	^{132}Ba	^{134}Ba	^{135}Ba	^{136}Ba	^{137}Ba	^{138}Ba
Nuclear spin I [$\hbar$]	0	0	0	3/2	0	3/2	0
Abundance [%]	0.1	0.1	2.4	6.6	7.3	11.3	71.7

Table 3.2: Stable Barium isotopes along with their nuclear spin and abundance [109].

makes its level scheme similar to the alkaline ones. Moreover, since its nuclear spin is null, it does not exhibit any hyperfine structure. As can be seen from the Ba^+ Grotrian scheme reported in Fig. 3.1, the wavelengths for addressing its lower transitions are all in the visible range.

Lithium atoms The fermionic isotope of Lithium, ^{6}Li, was chosen as the atomic element in the atom-ion mixture. It has a non-null nuclear angular momentum ($I = 1$) that gives rise to a rich hyperfine structure. The energy level diagram is sketched in Fig. 3.2. The dipole transitions from the ground state $^2S_{1/2}$ to the excited states $^2P_{1/2}$ and $^2P_{3/2}$, which are traditionally dubbed as D1 and D2, respectively, are very close (frequency difference of approximately 10 GHz).

^{6}Li is an excellent isotope for producing quantum degenerate gases, since it has

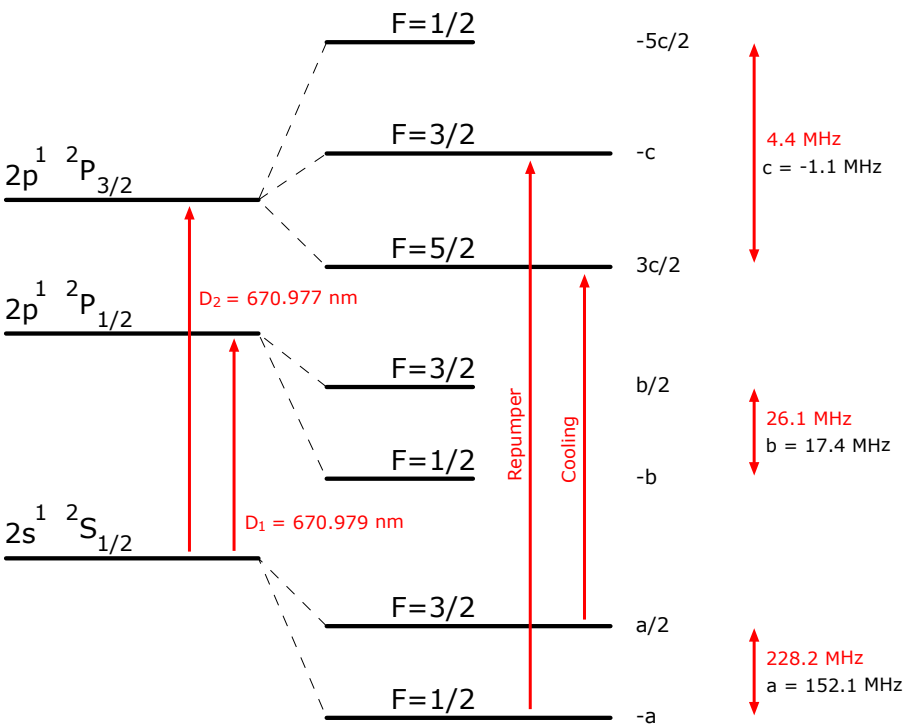

Figure 3.2: Grotrian scheme of the ^{6}Li hyperfine structure [111].

accessible transitions in the visible range and it is one of the two stable fermionic atom among the alkali metals, along with ^{40}K. One of the great advantages in using ^{6}Li lies in the presence of a broad Feshbach resonance located between the hyperfine levels of the ground state. This property makes ^{6}Li one of the best systems for observing fundamental phenomenons in strongly correlated fermions, like the BEC-BCS crossover and the growth of magnetic phases [112, 113].

3.1.1 Ba^+ – Li interactions

In general, the possibility of controlling inelastic processes in atom-ion collisions would be very useful, e.g. for suppressing the collisions that are not subject of a specific investigation, and isolating the phenomenon of interest. For this reason, the proper choice of the atomic species is a powerful tool to gain some controllability on the system. For instance, charge exchange reactions are an important mechanisms, but they are often undesired in atom-ion experiments because they may cause either particle losses or the trapping of ions that have optical transitions in the deep UV. The pair Ba^+ and Li in the ground state has the lowest energy molecular curve; therefore, charge-exchanges due to ground state inelastic collisions are prohibited because of energy conservation principle. However, the choice of working with Ba^+ and Li does not preclude the observation of charge exchange processes in general, since they could be activated by exciting the either the atoms or the ions to an excited electronic level.

Other chemical processes as three body recombinations are suppressed when Barium ions interact with a spin-polarized gas of fermionic Lithium at ultracold temperatures, because of Pauli exclusion principle. In fact, the spatial wavefunction of two Lithium atoms in the triplet state must be antisymmetric since their spin wavefunction is symmetric. Therefore, the scattering amplitude vanishes for the partial waves with even angular momentum quantum numbers, e.g. the s-wave contributions. Since scattering processes at ultracold temperatures occur mostly in s-wave, three body recombinations are suppressed.

Finally, Barium ion is an interesting reactant for exploring and controlling chemical reactions because it has two accessible ^{2}D metastable energy states, that can be used to study atom-ion interactions out of the ground state. These collisions have proved to be extremely interesting for other pairs of atoms and ions, e.g. in the $RbCa^+$ molecule formation [22].

3.2 Trapped ion physics: Ba^+

Ions confined in Paul traps inevitably suffer from the radiofrequency induced micromotion. A possible method to eliminate the problem is to substitute the Paul trap with an electro-optical trap. Our design of an EO trap has undergone

an evolution from the general idea of a purely optical confinement to its final implementation. This transformation is resumed step-by-step in the next Sec. 3.2.1. Section 3.2.2 reports some details about two-dimensional Coulomb crystals in an EO trap, which are investigated by using Montecarlo simulations. In section 3.2.3, finally, the strategy chosen for loading the ions into the the EO is exposed.

3.2.1 The electro-optical trap

Our electro-optical trap is formed by a one-dimensional optical lattice overlapped with a static electric quadrupole. The optical lattice is realized by an optical cavity in order to raise the trapping potential depth. The trapping laser is blue detuned with respect to the transition D1 of Ba^+ for reducing the off-resonant scattering from the trap. Moreover, the laser causes the same light shift to the levels $6\,^2S_{1/2}$ and $6\,^2P_{1/2}$ of the D1 transition, so that laser cooling can be still employed when the ions are optically trapped. In such scenario, the ions are confined only in one direction, in correspondence of the minima of the laser interference pattern. The confinement along the other two directions is provided by a static electric quadrupole realized with a pair of electrodes supplied with a negative voltage.

In the literature, the use of a periodic optical potential was also investigated in the presence of RF trapping [114, 115], and often this periodic potential is created by the presence of an optical cavity [116, 117], which makes it possible to increase the optical potential depth and make it compete with the electric potential [118]. The mechanism of trapping ions only with an optical dipolar trap was investigated so far mainly by the Schaetz group [67], who, however, observed a limited ions' lifetime due to intrinsic recoil heating by the dipolar trap beam [119]. The same group also experimented a purely optical 3D trapping scheme based on a red-detuned 1D optical lattice [104]. However, even in this case, recoil heating and dipole force fluctuation heating were detected. In addition, if the ions are loaded from the Paul trap directly into the lattice potential, RF-induced heating is individuated as the dominant heating mechanism.

This section is devoted to explain the conceiving of our model of electro-optical trap and its details, starting from the simple confinement achieved by a dipolar trap, the choice of the proper wavelength for the trapping laser, until reaching the actual configuration of the EO trap.

Far-off resonant optical trap The simplest way to realize an optical three-dimensional confinement of particles is a dipole trap [120] made with a single red-detuned gaussian laser beam, whose spatial intensity distribution is described by [121]

$$I(x,y,z) \;=\; I_0 \exp\left(-2\,\frac{x^2+y^2}{w(z)^2}\right)$$

where $I_0 = 2\,P/\pi w(z)^2$ is the peak intensity and P is the laser power. The beam radius $w(z)$, defined as the distance from the beam axis over which the intensity decreases by a factor $1/e^2$, depends on the axial coordinate z as

$$w(z) \;=\; w_0 \left(1+\left(\frac{z}{z_R}\right)^2\right)^{1/2} \tag{3.2}$$

where w_0 is the minimum radius, called "beam waist", and $z_R = \pi w_0^2/\lambda$ is the Rayleigh range.

The optical potential energy can be derived from the intensity distribution of the beam (see Appendix A). If the thermal energy of the atomic ensemble is smaller than the potential energy, the optical potential can be approximated by a harmonic oscillator potential

$$U(x,y,z) \;=\; -U_0 \left(1-2\frac{x^2}{w_0^2}-2\frac{y^2}{w_0^2}-2\frac{z^2}{z_R^2}\right) \tag{3.3}$$

where the potential depth is $U_0 = \alpha I_0$ and α is the static atomic polarizability.

As Eq. 3.3 shows, the potential in the axial direction is much shallower than in the other two directions since the Rayleigh range is larger than the beam waist by a factor $\pi w_0/\lambda$. In case of charged particles, this disadvantage can be compensated by adding a static electric field providing a further confinement along the axial direction, though it would add an anti-trapping potential on at least one of the radial directions [122].

In general, the electrostatic repulsion between ions sets the energy scale for the dipolar potential, which, therefore, must be as deep as possible. It is also fundamental to limit any heating mechanism, e.g. arising from the ion loading techniques, or caused by off-resonant scattering from the trap beam [119]. For these reasons, the wavelength of the trapping laser must be carefully chosen on the basis of its maximum available power and the Ba^+ polarizability $\alpha(\lambda)$. Moreover, as explained in the following paragraph, the trapping laser should ensure the possibility of performing laser cooling during the ion loading and trapping, and suppress off-resonant scattering heating.

The magic wavelength

If the trapping wavelength causes the same light shift on the levels $6\,^2S_{1/2}$ and $6\,^2P_{1/2}$ of Ba^+, the resonance with the cooling laser is maintained, thus ensuring the possibility of cooling and detecting the ions during the trap loading process and when they are confined into the EO trap. Wavelengths realizing this condition are

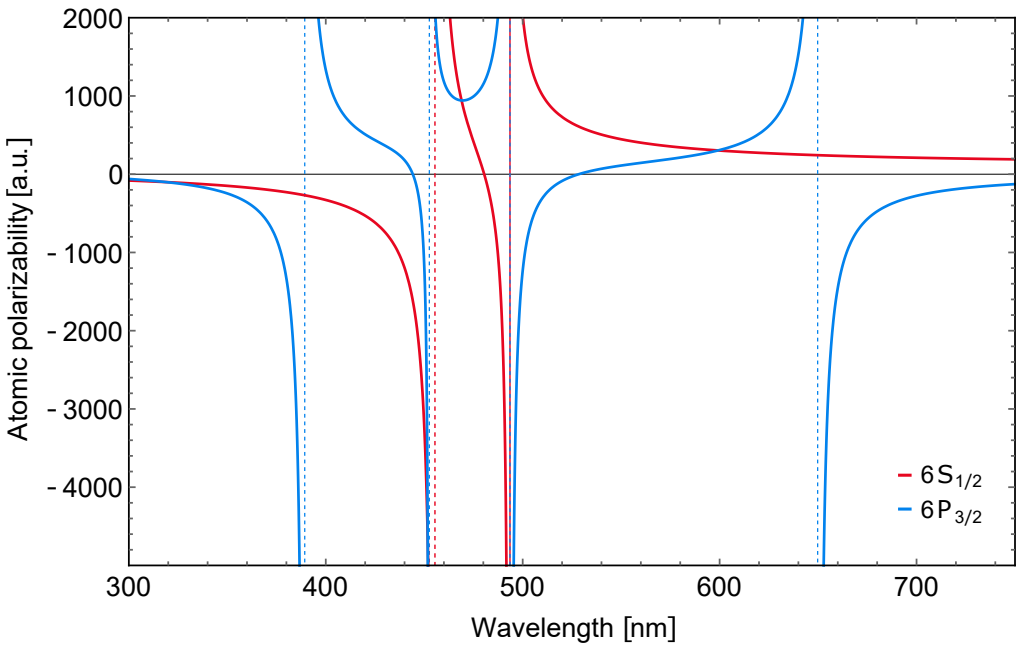

Figure 3.3: Atomic polarizability for the electric field expressed in atomic units for the energy levels of the cooling transition.

said "magic" for the given transition and can be evaluated by matching the light shifts of the two states. The atomic polarizability expressed in Eq. A.11 (for the electric field) is plotted for both the energy levels in Fig. 3.3 [123], whereas some of the magic wavelengths calculated are resumed in Tab. 3.3.

λ_{magic}	318.982 nm	451.762 nm	468.952 nm	559.144 nm
$\alpha(\lambda_{\text{magic}})$	-101 a.u.	-4460 a.u.	943 a.u.	304 a.u.

Table 3.3: Magic wavelengths and atomic polarizability for the cooling transition energy levels.

We chose 451.7 nm as magic λ because it falls in the visible range and because the related atomic polarizability is the highest, thus leading to a deep dipole trap. Moreover, it is blue-detuned with respect to the transition D1, causing a low off-resonant scattering rate, as evaluated in the following paragraph. For trapping particles with a blue-detuned beam, we consider a trapping scheme different from a far-off resonant trap, i.e. a one-dimensional optical lattice.

Optical lattices When combining two laser beams, a one-dimensional periodical intensity pattern is produced due to the beam interference. Since the chosen wavelength is blue-detuned, the ions will be trapped in the minima of this structure.

Along the other two directions the potential still remains anti-trapping. A possible strategy to obtain a three-dimensional confinement consist to add a static electric quadrupole potential that is attractive along the directions orthogonal with respect to the interference pattern. The drawback is that the anti-trapping direction of the electric potential would work against the optical lattice potential, thus lowering the trap depth. In such resulting potential, the ions will be trapped along the optical lattice minima, forming equally-spaced structures resembling to disks.

From the experimental point of view, the simplest way to realize such a 1D optical potential is to retro-reflect a laser beam with a mirror. This technique has the advantage to ensure an experimental setup relatively simple. Moreover, thanks to the interference, the potential depth would gain a factor 4. The distance between the minima is fixed by the wavelength and is equal to $\lambda/2 \simeq 226\,\mathrm{nm}$, a value too small for ensuring the ions' loading only in one minimum of the potential. In addition, an orthogonal imaging of the disks would be physically hindered by the presence of either the mirror or the laser source. In order to increase the lattice constant, the interference pattern can be created by two laser beams crossing at an angle smaller that π: in fact, with such arrangement the lattice constant d is determined not only by the laser wavelength, but also by the crossing angle $2\theta_c$ between the beams, according to the formula

$$d = \frac{\lambda/2}{\sin(\theta_c)}.$$

Moreover, the imaging inconvenient would be addressed too.

This optical lattice can be realized by a resonator in order to exploit the cavity amplification and increase the lattice depth. Specifically, it can be produced by the interference between the two crossed arms of a bow-tie cavity.

Interference pattern from two crossed focused gaussian beams

The generic expression of the electric field of an elliptic gaussian beam with different waists w_{0x} and w_{0y} in the origin of the reference frame, traveling along the z direction, can be written as

$$\vec{E}(x,y,z) = \vec{\varepsilon}\, E_0 \sqrt{\frac{w_{0x} w_{0y}}{w_x(z) w_y(z)}}\, e^{-x^2/w_x(z)^2}\, e^{-y^2/w_y(z)^2}\, e^{-ikz}\, e^{-i(x^2+y^2)/R(z)^2}\, e^{i\zeta(z)}\, e^{i\phi_g}$$

where $\vec{\varepsilon}$ is the unitary polarization vector, E_0 is the field amplitude, $w_x(z)$ and $w_y(z)$ are the beam radii (Eq. 3.2), $k = 2\pi/\lambda$ is the wave vector, $R(z)$ is the radius of curvature

$$R(z) = z\left(1 + \frac{z_R^2}{z^2}\right)$$

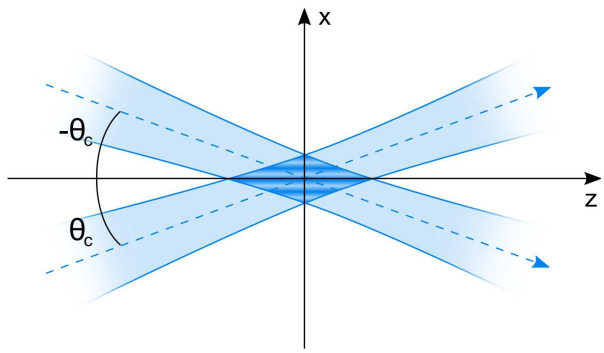

Figure 3.4: Sketch of two focused gaussian beams that cross at angle $2\theta_c$ and give rise to an interference pattern along the x axis.

$\zeta(z)$ is the Gouy phase

$$\zeta(z) \;=\; \arctan(z/z_R)$$

and ϕ_g is a generic phase.

In paraxial approximation ($z \ll z_R$, $x \ll w_{0x}$ and $y \ll w_{0y}$), the electric field becomes

$$\vec{E}(x,y,z) \;=\; \vec{\varepsilon}\, E_0 \left(1 - \frac{z}{2\, z_R}\right) e^{-x^2/w_{0x}^2}\, e^{-y^2/w_{0y}^2}\, e^{-ikz}\, e^{i\, z/z_R}\, e^{i\phi_g}$$

If the beam is rotated by an angle θ_c around the y axis, it remains in the x-z plane but it travels at the angle θ_c with the z axis (see Fig. 3.4). The coordinates of the new beam x', y', z' can be expressed in terms of the initial frame ones x, y, z by applying the rotation matrix

$$\begin{pmatrix} x' \\ y' \\ z' \end{pmatrix} = \begin{pmatrix} \cos(\theta_c) & 0 & \sin(\theta_c) \\ 0 & 1 & 0 \\ -\sin(\theta_c) & 0 & \cos(\theta_c) \end{pmatrix} \begin{pmatrix} x \\ y \\ z \end{pmatrix}$$

The electric field of the rotated beam is then given by

$$\begin{aligned} \vec{E}(x,y,z;\theta_c) \;=\; \vec{\varepsilon}\, E_0 \left(1 - \frac{\cos(\theta_c)z - \sin(\theta_c)x}{2\, z_R}\right) \exp\left(\frac{-(\cos(\theta_c)x + \sin(\theta_c)z)^2}{w_{0x}^2}\right) \exp\left(\frac{-y^2}{w_{0y}^2}\right) \\ \exp\left(-ik(\cos(\theta_c)z - \sin(\theta_c)x)\right) \exp\left(\frac{i\,(\cos(\theta_c)z - \sin(\theta_c)x)}{z_R}\right) e^{i\phi_g} \end{aligned}$$

Analogously, the second tilted beam can be described by the same formula, but applying the inversion $\theta_c \to -\theta_c$.

The intensity distribution of the sum of such rotated beams, derived with the assumptions of identical fields amplitudes $E_{0,\theta_c} = E_{0,-\theta_c}$ and same polarization $\vec{\varepsilon}_{\theta_c} = \vec{\varepsilon}_{-\theta_c}$, is

$$\begin{aligned} I(x,y,z) &= \frac{1}{2}c\varepsilon_0\left|\vec{E}(x,y,z;\theta_c) + \vec{E}(x,y,z;-\theta_c)\right|^2 \\ &= I_0 \exp\left(\frac{-y^2}{w_{0y}^2}\right)\exp\left(-2\,\frac{\cos(\theta_c)^2x^2 + \sin(\theta_c)^2z^2}{w_{0x}^2}\right) \\ &\left[\left(2\cosh\left(\frac{2}{w_{0x}^2}\sin(2\theta_c)xy\right) + 2\cos\left(2\sin(\theta_c)\left(k - \frac{1}{z_R}\right)x - 2\phi_g\right)\right)\right. \\ &\left.\left(1 - \frac{\cos(\theta_c)^2z^2 + \sin(\theta_c)^2x^2}{z_R^2}\right) - \frac{\sin(2\theta_c)xz}{2z_R^2}\,\sinh\left(\frac{2}{w_{0x}^2}\sin(2\theta_c)xy\right)\right] \end{aligned} \tag{3.4}$$

where I_0 expressed in terms of the laser beam power P is

$$I_0 = \frac{2P}{\pi w_{0x} w_{0y}}$$

In Eq. 3.4, the term

$$\cos\left(2\sin(\theta_c)\left(k - \frac{1}{z_R}\right)x - 2\phi_g\right) \approx \cos\left(\frac{2\pi}{d}x - 2\phi_g\right)^2 \tag{3.5}$$

can be recognized as the interference term, where

$$d = \frac{2\pi}{\sin(\theta_c)}\left(k - \frac{1}{z_R}\right)^{-1}$$

The resulting intensity profile is plotted in Fig. 3.5. Eq. 3.5 shows that the interference pattern appears along the x direction and that it assumes its maximum value for $x = nd/2 + 2\phi_g$, where n is an integer number and $d/2$ is the spacing between two consecutive maxima. The lattice constant depends on the semi-angle between the two beams, therefore the spacing can be increased by tuning the crossing angle formed by the two laser beams.

Since in our case the ions will be confined in the lattice minima, the intensity profile in Eq. 3.4 can be simplified by expanding all its terms around one of its minima. To this aim, the translation term of the interference pattern $2\phi_g$ can be used to shift a minimum to the $x = 0$ position. Keeping only the terms up to the second order, the intensity profiles becomes

$$I(x,y,z) = 4\,I_0\left[\left(\left(\frac{2\pi}{d}\right)^2 - \frac{1}{\tilde{w}_x{}^2}\right)x^2 - \frac{1}{w_{0y}^2}y^2 - \frac{1}{\tilde{w}_z{}^2}z^2\right] \tag{3.6}$$

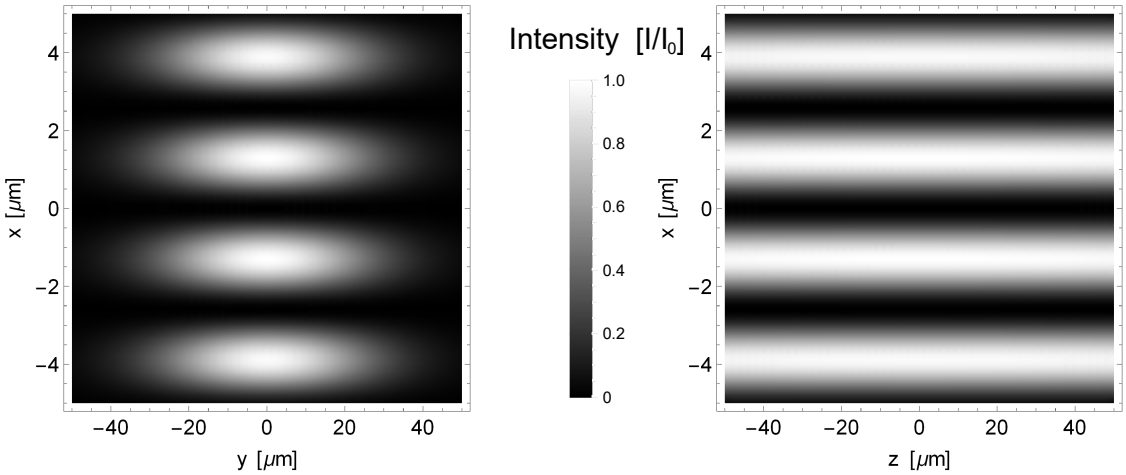

Figure 3.5: Intensity profiles of the interference between two focused gaussian beams forming a crossing angle $2\theta = 10°$. The translation phase is assumed to be $\phi = \pi/4$ so that the minimum of the intensity is shifted to the position $x = 0$.

where

$$\tilde{w_x} = \left(\frac{\cos(\theta_c)^2}{w_{0x}^2} + \frac{\sin(\theta_c)^2}{2z_R^2}\right)^{-1/2} \quad \text{and} \quad \tilde{w_z} = \left(\frac{\sin(\theta_c)^2}{w_{0x}^2} + \frac{\cos(\theta_c)^2}{2z_R^2}\right)^{-1/2}$$

are the rotated beam radii along the x and z directions.

This approximated form of the potential can be used to make an estimation of the off-resonant photon scattering rate, which can be evaluated as [120]

$$\Gamma_{\text{sc}}(\vec{r}) = \frac{3\pi c^2}{2\hbar\omega_0^3}\left(\frac{\Gamma}{\delta}\right)^2 I(\vec{r}) \tag{3.7}$$

where $\delta = \omega - \omega_0$ is the detuning, ω_0 is the atomic resonant frequency, ω is the laser frequency under consideration, and Γ is the damping rate defined as

$$\Gamma = \frac{\omega_0^3}{3\pi\varepsilon_0\hbar c^3}|\langle e|\mu|g\rangle|^2$$

The factor $I(\vec{r})$ in Eq. 3.7 can be evaluated as the the mean intensity $\bar{I}$ along the characteristic dimension of the one-dimensional wave-packet in the ground state of the potential (considered harmonic), i.e. as

$$\bar{I} = \frac{4I_0}{3}\left(\left(\frac{2\pi}{d}\right)^2 - \frac{1}{\tilde{w_x}^2}\right)\frac{\hbar}{m\omega}$$

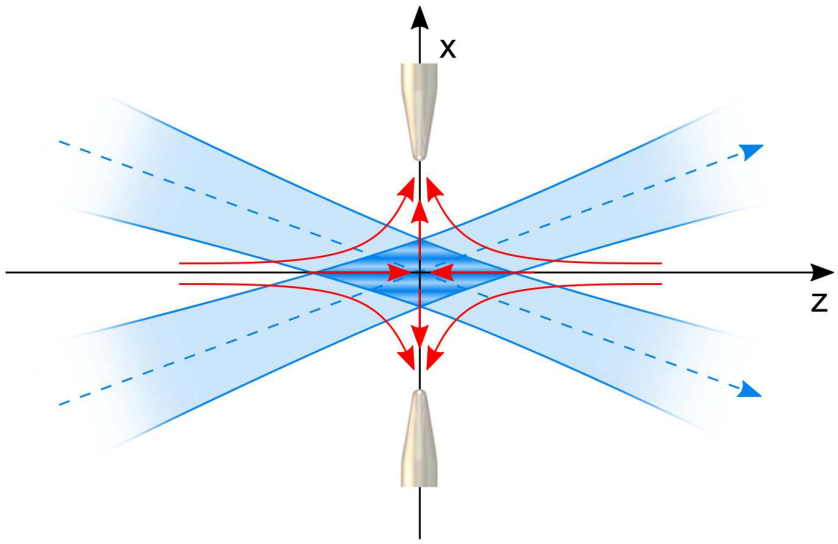

Figure 3.6: Sketch of the electro-optical trap, in which a static electric quadrupole potential (red arrows) is used for trapping ions along two orthogonal directions (here, y and z axes), while the confinement along the antitrapping direction (x axis) is provided by the interference pattern of two crossed gaussian laser beams (drawn in blue). For positive ions, the electrodes generating the quadrupole potential must be negatively charged.

For example, if a laser power of 200 mW is injected in the bow-tie cavity having a finesse of approximately 2000, the off-resonant scattering rate for the transition D1 is about 14 mHz.

The electro-optical trap The full potential created in the electro-optical trap will be the combination of a static electric quadrupole potential and the optical one (see Fig. 3.6). From Eqs. 2.5, 3.6, and A.11, the potential approximated in the local minimum of the intensity pattern can be written as[1]

[1]The subscript "DC" is omitted for the sake of readability.

Direction	ω_{el}^2 $[(2\pi\cdot\text{kHz})^2/\text{V}]$	ω_{opt}^2 $[(2\pi\cdot\text{kHz})^2/\text{W}]$
x	10^4	$3\cdot 10^4$
y	$-0.5\cdot 10^4$	-12.8
z	$-0.5\cdot 10^4$	-0.1

Table 3.4: Budget of the parameters $\Omega_{\phi,i}^2$ and $\Omega_{P,i}^2$ for our electro-optical trap. A negative contribution stands for an antitrapping term.

$$\begin{aligned}\Phi_{eo}(x,y,z) &= \Phi_{opt}(x,y,z)+\Phi_{el}(x,y,z)\\ &= -\alpha\, I(x,y,z) + \frac{\kappa e_0\phi}{2R^2}\left(2x^2-y^2-z^2\right)\\ &= \left(\frac{8\,\alpha P}{\pi\, w_{0x}\, w_{0y}}\left(\frac{1}{\tilde{w}_x{}^2}-\frac{4\pi^2}{d^2}\right)+\frac{\kappa e_0\phi}{R^2}\right)x^2+\\ &+\left(\frac{8\,\alpha P}{\pi\, w_{0x}\, w_{0y}}\frac{1}{w_{0y}^2}-\frac{\kappa e_0\phi}{2R^2}\right)y^2+\left(\frac{8\,\alpha P}{\pi\, w_{0x}\, w_{0y}}\frac{1}{\tilde{w}_z{}^2}-\frac{\kappa e_0\phi}{2R^2}\right)z^2.\end{aligned} \tag{3.8}$$

In analogy with the anisotropic three-dimensional harmonic oscillator, the following trapping frequencies can be extracted from Eq. 3.8

$$\begin{aligned}\omega_{eo,\,x}^2 &= \frac{16\,\alpha P}{\pi\, m_{\text{ion}}\, w_{0x}\, w_{0y}}\left(\frac{1}{\tilde{w}_x{}^2}-\frac{4\pi^2}{d^2}\right)+\frac{2\kappa|e|\phi}{m_{\text{ion}}\,R^2}\\ \omega_{eo,\,y}^2 &= \frac{16\,\alpha P}{\pi\, m_{\text{ion}}\, w_{0x}\, w_{0y}}\frac{1}{w_{0y}^2}-\frac{\kappa|e|\phi}{m_{\text{ion}}\,R^2}\\ \omega_{eo,\,z}^2 &= \frac{16\,\alpha P}{\pi\, m_{\text{ion}}\, w_{0x}\, w_{0y}}\frac{1}{\tilde{w}_z{}^2}-\frac{\kappa|e|\phi}{m_{\text{ion}}\,R^2}\end{aligned} \tag{3.9}$$

Once the trapping wavelength, the crossing angle between the two cavity arms, and the electrode geometry are fixed, the electro-optical potential depends only on the laser power P and on the applied potential ϕ. In our case, the beam waists are $w_{0x} = w_{0y} = 40\,\mu$m and the crossing angle $2\theta_c = 10°$. The angle is sufficient to realize a lattice constant of about $2.6\,\mu$m, and to limit any astigmatism issue for the laser beam in the bow-tie cavity.

For these cavity parameters, the single electric and optical contributions to the trapping frequencies were evaluated as $\omega_{opt,i}$ and $\omega_{el,i}$ $(i = x, y, z)$. In order to compare the magnitudo of these contributions, the trapping frequencies are reformulated in terms of $\Omega_{\phi,i}^2$ and $\Omega_{P,i}^2$, defined as

$$\omega_{el,i}^2 = \Omega_{\phi,i}^2\cdot\phi \quad\text{and}\quad \omega_{opt,i}^2 = \Omega_{V,i}^2\cdot V$$

and resumed in Tab. 3.4. It is evident that the contributions coming from the optical potential for the y and z directions are negligible with respect to the electrical ones. Moreover, in order to obtain an overall trapping potential in the radial directions, the applied static potential must be negative. However, the degeneracy in the radial trapping frequencies is weakly lifted by the presence of the optical potential. For instance, if $P = 0\,\mathrm{W}$, a confinement of 100 kHz along the y and z axes is realized with a voltage of approximately $-1.98\,\mathrm{V}$ applied on the cone electrodes. When the laser power is switched on, the voltage must be increased in order to obtain the same confinement of 100 kHz along the y direction (e.g., -2.14 V for $P = 60\,\mathrm{W}$). Consequently, the confinement along the z direction increases, since the confinement along the z direction is less dependent on the optical potential (e.g., $\omega_{eo,z} \simeq 2\pi \cdot 104\,\mathrm{kHz}$ for -2.14 V and $P = 60\,\mathrm{W}$).

Electro-optical trap stability diagram The "stability diagram" of the electro-optical trap can be deduced from Eqs. 3.9. The potential acting on the ions provides a stable confinement in all three directions if the frequencies associated to the harmonic potentials are all non-negative. The stability plot evaluated for our trap parameters is presented in Fig. 3.7. We note that the electrode potentials must be negative for ensuring an attractive potential along the y and z axes. Moreover, the laser must have enough power to prevail over the anti-trapping electric potential along the x axis. For negative electric potentials, the frequencies along the y and z axes are basically equal, and the parameters $\{P_{\mathrm{iso}}, \phi_{\mathrm{iso}}\}$ corresponding to an isotropic confinement lie on the curve defined by the equation $\omega_{eo,\,x} = \omega_{eo,\,y}$. These values are plotted in red on the stability diagram in Fig. 3.7. Therefore, for a given laser power P, the shape of the electro-optical potential can be tuned by changing the electric potential V_{el} on the electrodes in the range $[0, V_{\mathrm{trap}}]$, where V_{trap} is the largest value for which the particles are still trapped along the interference direction (x axis). The possible scenarios are thus

$0 > V_{el} > V_{\mathbf{iso}}$ The ions can be trapped in a single minima of the optical lattice, thus forming a disk-shaped crystal (or cloud).

$V_{el} = V_{\mathbf{iso}}$ The three trapping frequencies are equal, so the potential is isotropic.

$V_{\mathbf{iso}} > V_{el} > V_{\mathbf{trap}}$ The confinement along the interference direction is weaker than the other two. Considering the typical depth of the optical potentials and the Coulomb repulsion, we may expect that under this condition the ions will lie in different minima of the optical lattice.

We are particularly interested in working with $V_{el} \ll V_{\mathrm{iso}}$, since in that kind of potential the ions are confined in a two-dimensional space and should crystallize in 2D structures.

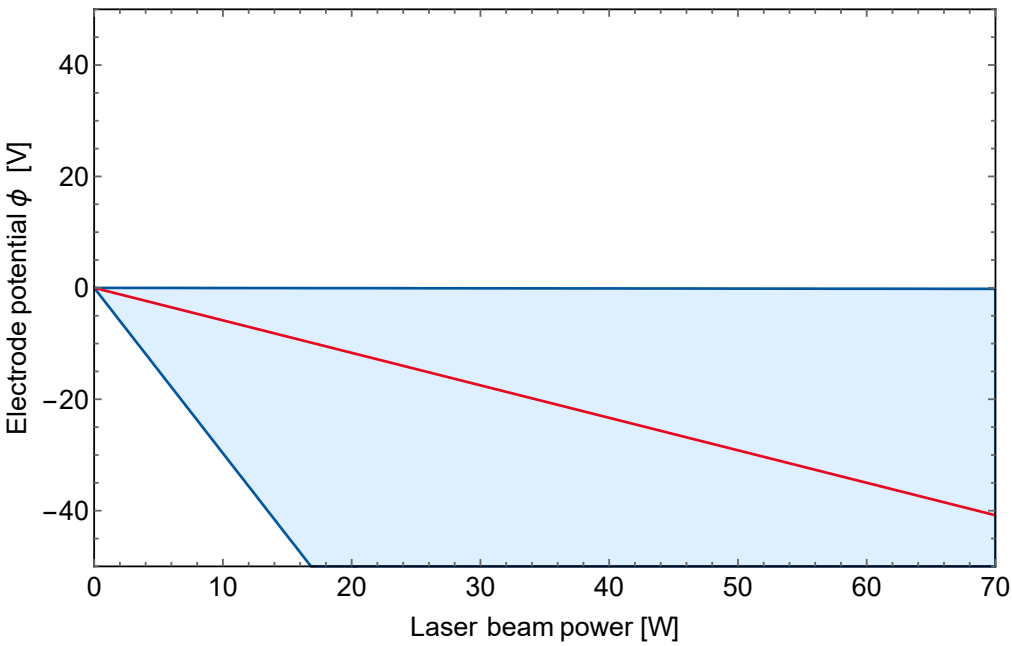

Figure 3.7: Electro-optical trap stability diagram. The shaded region shows all the pairs $\{P, \phi\}$ for which the trapping frequencies in the three directions are simultaneously positive, thus indicating a stable trapping potential. The wavelength, the beam waists, and the crossing angle are $\lambda = 451.7\,\text{nm}$, $w_{0x} = w_{0y} = 40\,\mu\text{m}$, and $2\theta_c = 10°$, respectively. The red line indicates the pairs of parameters $\{P_{\text{iso}}, \phi_{\text{iso}}\}$ for which the confinement is equal in each direction. The region above this line corresponds to a disk-like shape potential.

3.2.2 Two-dimensional ion crystals

A sample of cold ions confined in a two-dimensional space may undergo a spatial-ordered self-arrangement, thus forming a so-called Coulomb crystal [124]. The interest in similar objects is e.g. due to the fact that they are assumed to be involved in the structure of exotic astrophysics bodies, as white dwarfs and neutron stars [125]. Among the reasons of interest [1], another is that they represent a magnified reproduction of solid crystalline lattices, thus lending themselves as platform for simulating condensed-matter physics systems. In particular, this application becomes even more interesting if the ion crystal is immersed in a cloud of ultracold fermionic atoms mimicking the electron gas of a natural solid-state system [71]. In addition, this hybrid system is an ideal starting point for studying different types of inelastic interactions within the same experimental run. Finally, it could also be used to investigate non-trivial dynamics, e.g. the motion of a rotating crystal in a superfluid and/or in a strongly correlated gas [126, 127].

In order to achieve this general experimental platform, we need to estimate the size of the 2D Coulomb crystals, since this sets a constraint on the size of the

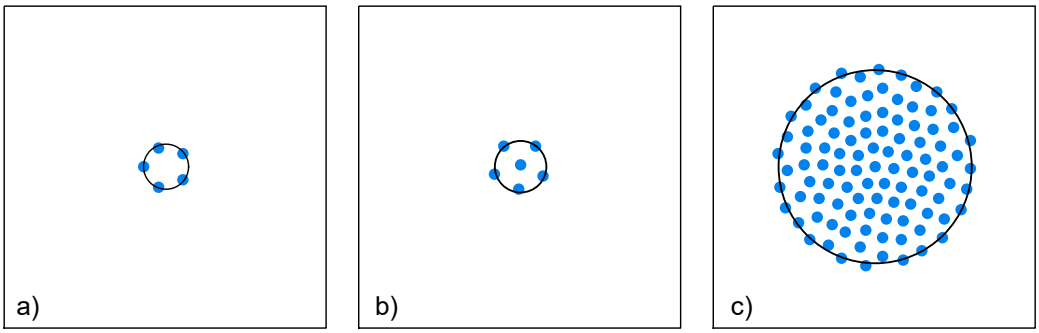

Figure 3.8: Montecarlo simulations of Coulomb crystals with different numbers of ions: a) 5 ions, b) 6 ions and c) 100 ions. The trap frequency is $2\pi \cdot 1\,\mathrm{MHz}$. The crystals are enclosed by circumferences having radii a) $3.7\,\mu$m b) $4\,\mu$m and c) $15\,\mu$m. The box side is $50\,\mu$m long.

atomic cloud. In fact, once the overlap of the atomic gas with the trapped ions is accomplished, we are interested in immersing the whole ion crystal in the ultracold atomic bath, so that all the ions can interact with the atoms.

We performed Montecarlo simulations to predict the mean distance between the particles and the overall dimensions of the crystal. During the simulation, the potential composed by the static electric quadrupole and the anti-trapping contribution of the optical lattice was assumed to be harmonic along the radial directions, with a frequency much lower than the axial one, since the problem was considered only in two dimensions. In each step of the simulation, an ion is selected randomly and then its energy is calculated in each point of a finite 2D discrete grid centered in the ion position. Both the mutual repulsion with all the other ions and the interaction with the trapping potential are taken into account in the energy evaluation. Finally, the loop is completed by placing the ion in the position of minimum total energy. The loop is iterated and the positions of the ions are progressively adjusted until convergence is reached, i.e. until the optimization procedure ran on each ion does not reduce anymore the total energy.

The shape of the crystal has a strong dependence on the number of ions. For instance, in the case of 5 particles in a radial harmonic potential of frequency $\omega_r = 2\pi \cdot 1\,\mathrm{MHz}$, the ions form a pentagon (see Fig. 3.8.a). Their mean distance is about $3.9\,\mu$m, while the crystal can be inscribed in a circumference of radius $3.7\,\mu$m. Interestingly, when the sixth ion is added to the simulation, the crystal reaches its minimum energy configuration when five ions are equally disposed in pentagon and the sixth ion is placed in the center (see Fig. 3.8.b). The crystal structure becomes even richer for a large number of particles: e.g. Fig. 3.8.c shows the shape of a crystal formed by 100 ions.

The Lithium atoms are also trapped in the minima of the lattice potential, and

the frequency of the trapping lattice is a factor ≈ 1.75 smaller than the corresponding frequency for the Barium ions. Considering the tight confinement along the lattice direction, the gas of ^{6}Li atoms can be considered as a two dimensional gas. The size of a confined gas at zero temperature can be estimated by calculating the Fermi radius [128]

$$r_{F,2D} = (8\,N)^{1/4} \left(\frac{\hbar}{m_{\text{atom}}\,\omega_r} \right)^{1/2}$$

where N is the number of atoms, m_{atom} is the atomic mass, and ω_r is the radial trapping frequency. In order to obtain a gas distribution with a Fermi radius exactly equal to the diameter of a Coulomb crystal with $N = 100$ ions, the trapping potential must have a frequency of $\omega_r = 2\pi \cdot 6.7\,\text{kHz}$. Providing such radial confinement to a 2D atomic cloud of $N = 10^5$ spin-polarized particles, the corresponding Fermi temperature is $\hbar\omega_r\sqrt{2N}/k_B \simeq 2\,\text{mK}$ [128], which is much higher than the temperature associated with the quantized states of potential well, $\hbar\omega_r/k_B = 4.8\,\mu\text{K}$.

3.2.3 Ion loading in an electro-optical trap

In most ion trapping experiments, ions are produced by ionizing a hot vapor of atoms created in a small oven. This process relies on the depth of RF traps, which easily reaches 1000 K, so that a hot ion can be stored in the trap and then laser cooled. In an electro-optical trap, however, the depth is limited mainly by the optical component of the potential, the depth of which is typically well below 1 K. For this reason, a different strategy for loading ions in an electro-optical trap must be devised. The principal solutions are

- The atoms are trapped and cooled in a magneto-optical trap, then the EO trap is switched on, and cold ions are produced via a photoionization process [129, 130].
- The ions are first produced by photoionizing some hot atoms coming out of an oven, then trapped in a Paul trap. Finally, the ions are transferred from the Paul trap to the electro-optical one.

The first option is not very practical since the strong $6s^2\ {}^1S_0 \leftrightarrow 6s^1 6p^1\ {}^1P_1$ transition used for cooling neutral Barium atoms optically pumps to other internal, long-lived states, so three infrared repumpers are needed for realizing an efficient cooling scheme [131]. Instead, the second option has the advantage of producing a sample of ions in a Paul trap, where they can be cooled with standard techniques below 1 mK. Then, the cold ions can be loaded into the EO potential that, at this temperature level, would be sufficiently deep to keep them confined.

Swapping from the Paul trap to the EO trap can in principle be facilitated if the the ion crystals in the two traps have a similar shape. This request sets a number of constraints on the shape and size of the electrodes, and on the method for creating the deep optical lattice.

Conceiving a Paul trap – EO trap assembly The two main ingredients of the electro-optical trap are the static electric quadrupole potential and the one dimensional optical lattice. On the one hand, the static quadrupole can be easily produced by placing at a negative voltage two collinear metallic tips positioned one in front of the other (see Fig. 3.9.a). On the other hand, the two focused gaussian beams which realize the optical lattice must overlap in between the tips (see Fig. 3.9.b). However, this very simple picture has a drawback: the tip electrodes would make it problematic to perform a high-resolution imaging of a two-dimensional ion crystal trapped on one minimum of the optical lattice, since a tip electrode would lie exactly on the normal axis of the crystal. A possible solution is to change the shape of the tip electrodes, and make them hollow (see Fig. 3.9.c). The constraints for reproducing the proper shape of the quadrupole potential are that these conical electrodes should maintain a cylindrical symmetry around the crystals' axis and that their internal radius should be not much larger than their mutual distance.

Eventually, the EO trap having this simplified design has to be merged with a Paul trap. We decided to use a linear Paul trap, since this ensures the possibility of trapping more than one ion with minimum micromotion in case of problems in running the EO trap. The easiest way to combine the four linear electrodes of the Paul trap with the EO trap is to orient them orthogonally with respect to the EO trap electrodes' axis (see Fig. 3.9.d). The requirement of creating crystals of similar shape and size in the Paul and the EO trap sets a constraint on the position of the endcaps. Therefore, the endcap electrodes can be considered as two tips, placed orthogonally to both the linear electrodes of the Paul trap and the hollow electrodes of the EO trap (see Fig. 3.9.e).

It is important to note that the linear electrodes are rotated with respect to the endcaps' axes by an angle of 45° (see Fig. 3.10). This rotation implies that the operation of the Paul trap is described by a system of two coupled Mathieu equations, which must be solved in order to derive the stability diagram.

Paul trap stability diagram In Sec. 2.2.1, we derived the Mathieu equations in case of a "conventional" linear Paul trap, in which the endcap electrodes are collinear to the trap axis. In this case, however, the expression of the quadrupole potential energy must be transformed by applying the following rotation

$$\begin{pmatrix} x' \\ y' \end{pmatrix} = \begin{pmatrix} \cos(\theta) & \sin(\theta) \\ -\sin(\theta) & \cos(\theta) \end{pmatrix} \begin{pmatrix} x \\ y \end{pmatrix}$$

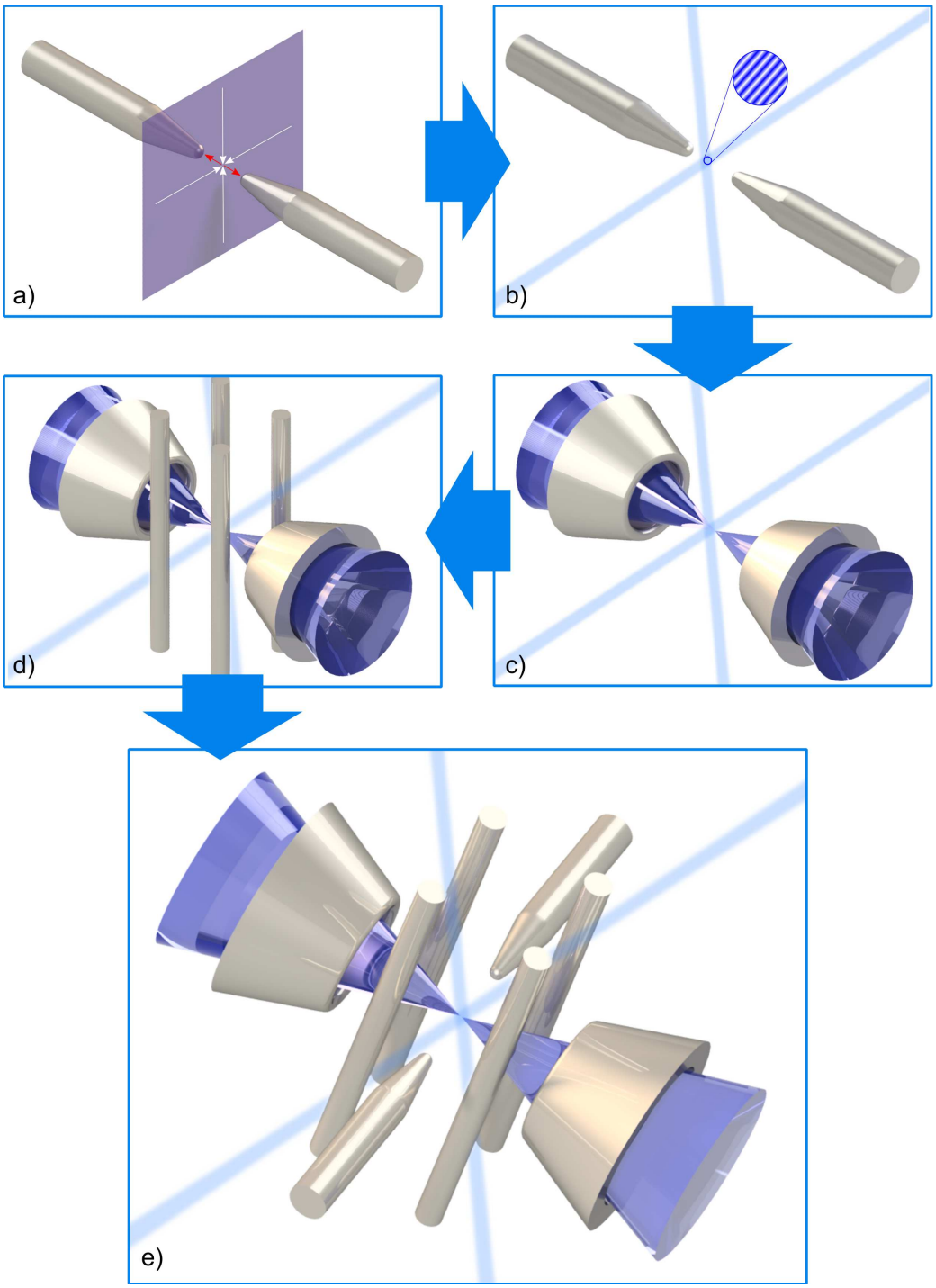

Figure 3.9: The integration of the linear Paul trap in the electro-optical one is described in different steps. The fundamental constraints which lead the toy-model evolution are the possibility to reproduce the same potential with both the traps, and a wide optical access to frontal detect 2D ions' crystals. The blue cones represent the optical access to the ions trapped at the center.

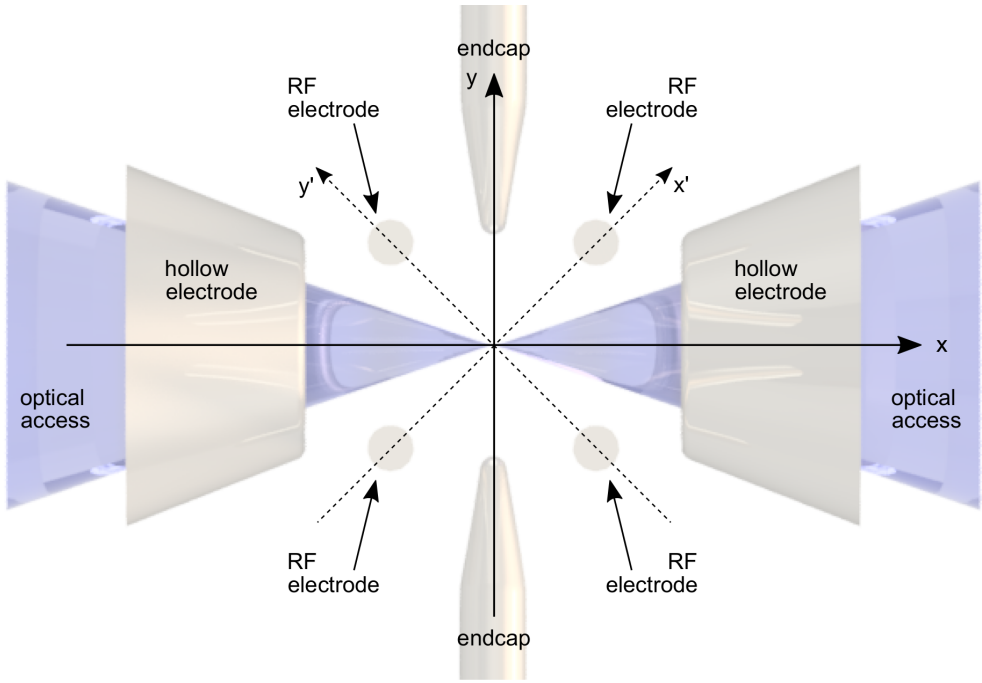

Figure 3.10: Overview of the Paul trap electrodes position in relation with the electro-optical trap hollow electrodes. The RF electrodes are rotated of 45° with respect to the endcaps' frame, and the confinement along the z axis is provided by the negatively charged endcaps.

with θ the coupling angle. The physical meaning of the two coordinates $\{x, y\}$ and $\{x', y'\}$ can be seen in Fig. 3.10. The quadrupole potential in the $\{x, y\}$ frame becomes

$$V_{RF}(x,y) \;=\; -\frac{e_0\phi_{RF}}{2}\frac{\kappa_{RF}}{R_{RF}^2}\left((\cos(\theta)x+\sin(\theta)y)^2-(\cos(\theta)y-\sin(\theta)x)^2\right)\cos(\omega_{RF}\,t)$$

Taking into account the contributions of both the dynamical and static electric potentials, the coupled motion equations for the x and y axes are

$$\begin{cases} \ddot{x} \;=\; 2\,q\left(\cos(\theta)x+\sin(\theta)y\right)\,\cos(2\tau)-a\,x \\ \ddot{y} \;=\; 2\,q\left(\sin(\theta)x-\cos(\theta)y\right)\,\cos(2\tau)-\alpha\,a\,y \end{cases} \tag{3.10}$$

where the parameters q and a are defined in Eq. 2.7, and α is a geometrical factor expressing the ratio between a_x and a_y, i.e. $a_x = a_y/\alpha = a$. The substitution $\omega_{RF}t = 2\tau$ was also performed in order to make Eq. 3.10 time dimensionless.

The stability condition of this system can be evaluated by applying the Floquet theorem. To do so, Eqs. 3.10 must be first expressed as a system of first order differential equations

$$\begin{cases} \dot{x} &= v_x \\ \dot{y} &= v_y \\ \dot{v}_x &= 2\,q\,\Big(\cos(\theta)x + \sin(\theta)y\Big)\,\cos(2\tau) - a\,x \\ \dot{v}_y &= 2\,q\,\Big(\sin(\theta)x - \cos(\theta)y\Big)\,\cos(2\tau) - \alpha a\,y \end{cases}$$

which, in matricial notation, reads

$$\dot{\vec{x}} \;=\; B(\tau)\,\vec{x} \tag{3.11}$$

where $\vec{x} = (x, y, v_x, v_y)^T$ and the periodic matrix $B(\tau) = B(\tau + n\pi)$ (n integer number) is

$$B(\tau) \;=\; \begin{pmatrix} 0 & 0 & 1 & 0 \\ 0 & 0 & 0 & 1 \\ 2q\cos(\theta)\cos(2\tau) - a & 2q\sin(\theta)\cos(2\tau) & 0 & 0 \\ 2q\sin(\theta)\cos(2\tau) & -2q\cos(\theta)\cos(2\tau) - a & 0 & 0 \end{pmatrix}$$

The Floquet theorem states that Eq. 3.11 has at least one solution of the form [132]

$$x^{(j)}(\tau) \;=\; \exp\left(\log(\lambda_j)\,\frac{\tau}{\pi}\right) p_j(\tau) \quad \text{with} \quad p_j(\tau + \pi) = p_j(\tau) \tag{3.12}$$

where λ_j are the eigenvalues of the matrix $Z(\pi)$ defined as

$$\dot{Z}(\tau) = B(\tau)\,Z(\tau) \quad \text{with} \quad Z(0) = \mathbb{I}_4 \tag{3.13}$$

The solution Eq. 3.12 can also be reformulated as

$$x^{(j)}(\tau) \;=\; \exp\left(\log(|\lambda_j|)\,\frac{\tau}{\pi}\right) \exp(i\arg(\lambda_j))\,p_j(\tau)$$

from which is evident that the absolute value of the eigenvalues $|\lambda|$ must be less than unity to obtain a stable solution.

Therefore, in order to ascertain if the trap is stable for a pair of parameters $\{q, a\}$, one has to numerically solve Eq. 3.13 and check the absolute value of the $Z(\pi)$ eigenvalues. The disadvantage of this procedure is that the stability boundaries are not well defined. To overcome this inconvenient and find an approximated expression for the stability boundaries, one can use the multiple-scale perturbation theory [133]. Basically, this approach consists in substituting an independent variable with a pair of fast-scale and slow-scale independent variables. Then, the additional degree of freedom is exploited to remove long-term and non-periodic variations in the approximated solutions, which usually limit their validity only in short time range when standard perturbation techniques are used instead.

For a system of coupled Mathieu equations, the approximated boundaries of the first stability region are

$$\begin{aligned}
a_1 &= -\frac{1}{2}q^2 \\
a_2 &= \frac{1}{2\alpha}q^2 \\
a_3 &= 1-\cos(\theta)q - \left(\frac{\cos(\theta)^2}{8} + \frac{2\sin(\theta)^2(5+\alpha)}{(1+\alpha)(9+\alpha)}\right)q^2 \\
a_4 &= -\frac{1}{\alpha}\left(1-\cos(\theta)q - \left(\frac{\cos(\theta)^2}{8} + \frac{2\sin(\theta)^2(5+1/\alpha)}{(1+1/\alpha)(9+1/\alpha)}\right)q^2\right)
\end{aligned} \tag{3.14}$$

Both these approaches are used to localize the first stability region of our linear Paul trap. The results are presented in Sec. 4.2.1.

3.3 Ultracold atoms physics: Li

The production of the quantum hybrid system constituents, i.e. the trapped ions and the ultracold gas of neutral atoms, follows two processes characterized by different experimental requirements, timescales and instrumentation. However, eventually, these two systems will be merged to form the quantum hybrid system. The experimental setup and the physics related to the production of Lithium quantum gases will be discussed in another ph.d. thesis of another member of the group; nevertheless, we provide here a quick overview of how the quantum degenerate Fermi gas is produced and overlapped with the trapped ions.

In general, the strategy is to produce the quantum gas of Lithium trapped in a MOT in a separate vacuum chamber with the techniques described in Sec. 2.3. After the accumulation in the MOT, the cloud of atoms must be transported into the vacuum chamber hosting the ion trap by physically moving the atoms trapping potential. Moving atoms in ultra-high vacuum systems is a technique that is widely used in the quantum gases community. The methods that are used are mainly two

- Magnetic transport: the atoms trap center is progressively displaced either by a chain of overlapping coils pairs through which a current is applied [134], or by directly moving one coils pair [135].
- Optical transport: this can be realized by slowly shifting the focus of the dipole beam where the atoms have been trapped, or by trapping the atomic gas in a 1D optical lattice, then turned into a moving standing wave by changing the frequency of one of the two beams [136]. However, if the atoms

have to be moved for long distances, the method based on moving optical lattices may be technically more complex since non-gaussian laser beams have to be employed [137]. On the contrary, the strategy of shifting the focus of the dipole trap was proved for distances of 10 s of centimeters [138].

Our choice is to use the optical transport in a dipole trap. In order to simplify the transport process and the merging of the two systems, we decided to physically move the dipole trap focusing lens by mounting it on an air-bearing translation stage, instead of using focus-tunable lenses [139]. The stage we purchased (Aerotech ABL1000-050-E2-PL2) is characterized by a total travel of 50 mm, an accuracy of $\pm 0.2\,\mu$m, and a repeatability of $0.25\,\mu$m.

After the transport, the atoms will be trapped optically by the optical lattice of the EO trap and an additional orthogonal dipolar trap beam. In this trap, the temperature of the atomic cloud will be further lowered by using evaporative cooling, in order to create a quantum degenerate gas inside the EO trap.

Chapter 4

Ion experimental setup

An apparatus for realizing hybrid quantum systems of ions and atoms is in general more articulate and complex than an ordinary atomic physics physics experimental setup. The main reason is the necessity of putting together two basically independent setups, each of which produces one of the sub-systems.

We decided to initially focus on the "ion side" of the experiment because from a technical point of view there is locally a lack of know-how: this experiment represents the first attempt to realize ion trapping in Italy. Therefore, this chapter is entirely dedicated to the ion experimental apparatus.

First, the design of the trap is exposed is Sec. 4.1, while the most significant results of its simulations are reported in Sec. 4.2. Finally, the last section 4.3 is devoted to a quick overview of other fundamental experimental aspects, as the imaging strategy, the RF drive, and the "atomic side" of the setup.

4.1 Ion trap design

The ion trap can be considered as formed by three main parts, the electro-optical trap (Sec. 4.1.1), the Paul trap (Sec. 4.1.2), and the neutral Barium ovens (Sec. 4.1.3), whose components have to be easily integrated in the same structure, thus making its design a very complex and adaptive process. The different parts were designed keeping in mind that their final assembly has to be as much mechanically precise as possible. All the solutions adopted rely on the possibility to machine the pieces with minimal tolerances (Sec. 4.1.4).

At the beginning of the ion trap design process, we focused on the linear Paul trap. One of the main constraint on its design concerns the optical access, which must be adequate for the high numerical aperture objective, the numerous laser beams for manipulating the particles and the optical transport of the neutrals towards the trap center. This necessity naturally lead to a Paul trap characterized

by a wide trapping volume, which must also allow the crossing of the laser beams for creating the optical lattice in the electro-optical trap. Another requirement is to ensure the possibility to realize large 2D ion clouds or crystals to be loaded into the EO trap. Moreover, considering the expected depth of the optical potential, we considered the realization of relatively shallow secular potentials (less than 1 MHz) to ensure a good mode matching with the EO trap.

The first model of the trap electrodes was inspired to the trap dimensions described in Ref. [140], i.e. a segmented trap, the cylindrical rods of which are positioned at the vertices of a square and distant 2.35 mm from its center. Once the dimensions of the trapping volume were fixed, the shapes of the RF electrodes and the endcaps were modeled and projected towards the outside for providing an efficient solution for assembling the electrodes on the ceramic supports and for the electrical connections. Subsequently, the cone electrodes of the EO trap were added and adapted to the Paul trap. A metallic plate was designed to support the trap and host the Barium ovens' system, which is provided with two skimming stages in order not to directly hit the electrodes with the atomic beams.

4.1.1 The electro-optical trap

In the electro-optical trap, ions are trapped along two directions (y and z axes) by a static electric quadrupole potential, whereas along the third direction (x axis) they are confined by a one-dimensional blue-detuned optical lattice. The static quadrupole potential is created by two opposite electrodes (cone electrodes), while the deep optical potential is realized by a bow-tie cavity.

Cone electrodes In principle, the requested electric potential could be created by a pair of needle-shaped electrodes fed by a negative voltage and arranged along the lattice direction. However, the problem with this strategy is that the lattice axis coincides with the imaging direction (refer to Sec. 3.2.3). Therefore a different geometry has to be adopted in order to preserve the possibility of performing the imaging along the x axis. To do so, the same electric potential is produced by a pair of ring-shaped electrodes, ensuring a circular distribution of charges with the x direction as symmetry axis. These rings must be contained in mechanical supports that do not limit the numerical aperture of the imaging. To this end, a conical-shaped design of the electrodes was chosen. In their practical realization, the cone electrodes must also have mechanical features that ensure both their electrical connection and mechanical reference for the alignment with the other electrodes. As additional constraint is that their shape and dimensions must be carefully adapted to the other electrodes since both Paul and electro-optical traps are integrated with each other. The resulting electrode shape is shown in Fig. 4.1.

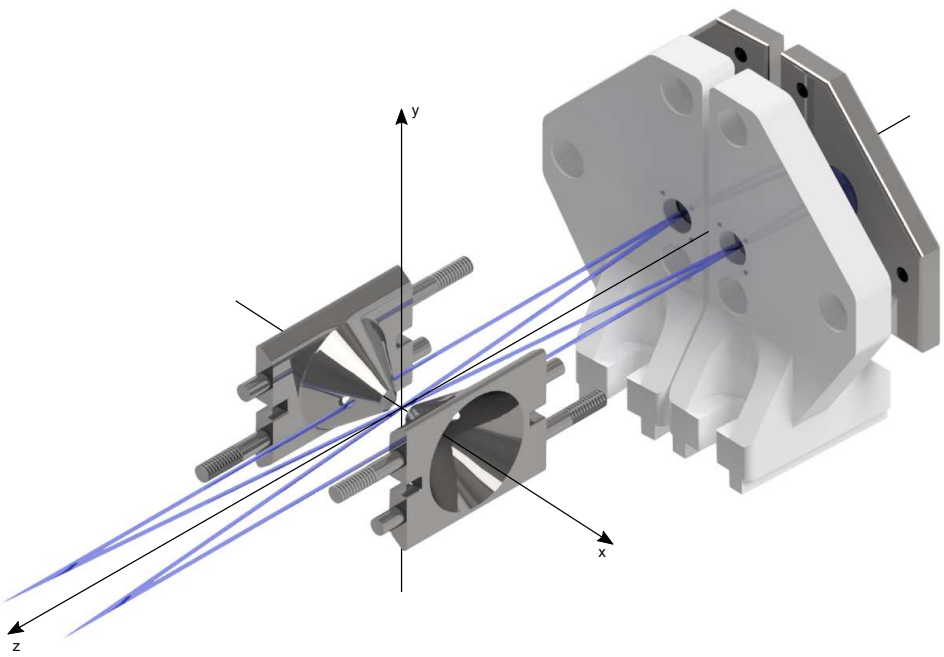

Figure 4.1: CAD assembly of the electro-optical trap, formed by the cone electrodes and the bow-tie cavity mirror mounts. The two mirror mounts on the left side have been removed for a better view.

Optical cavity geometry Our bow-tie cavity is based on a configuration with four curved mirrors, so that the laser beam traveling in the cavity has a focus for each of its arms. In particular, the cavity has been designed in order to have two foci cross at the center of the bow-tie cavity. There, the two running waves create a deep lattice in which the intensity of the two interfering beams is enhanced by a factor proportional to the cavity finesse. Given the cylindrical symmetry of the vacuum chamber, a symmetrical cavity has been preferred: this puts a constraint on the mirrors which must have the same curvature radius.

In order to ensure the possibility of confining atoms and ions in a single minimum of the optical potential, the lattice pitch must be as wide as possible. This implies that the angle formed by the crossed arms must be as small as allowed by the dimensions of the vacuum chamber and the cavity mirrors. In our case, the crossing angle was chosen to be 10°, the waist of the crossed arms 40 μm, and the mirrors curvature radius 100 mm. With these parameters, the bow-tie geometry can be entirely defined in the ABCD matrix formalism by imposing the cavity stability [141]. In our case, the crossed arms are 9.45 cm long, whereas the other two are 9.48 cm long, thus resulting in a cavity[1] strongly elongated over the x axis, as

[1]Such a cavity, having the above mentioned parameters, is described in the stability diagram

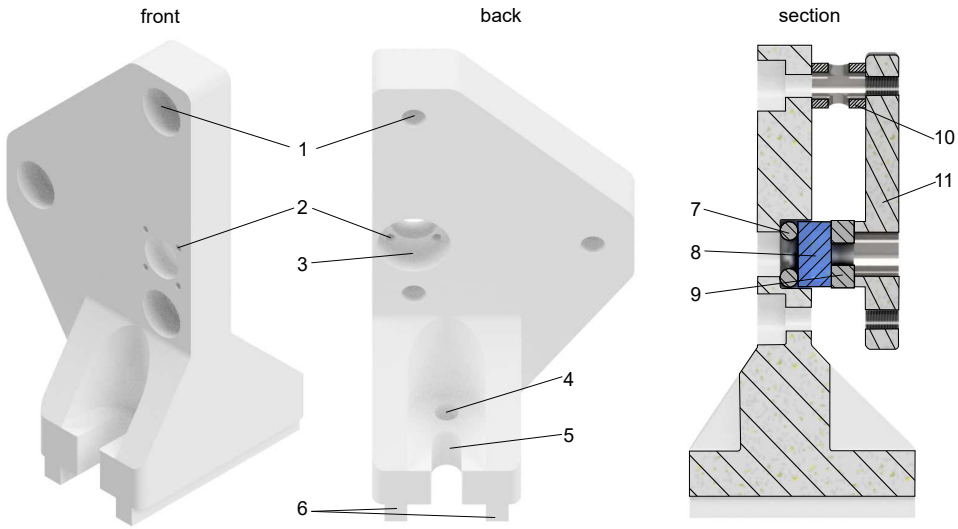

Figure 4.2: Different views of the mirror mount. (1) Screw compartment with the slot for the screw head. (2) Monitoring holes for checking the mirror position. (3) Mirror compartment. (4) Dowel hole. (5) Screw hole for holding the mount on the metallic base. (6) Alignment binaries. (7) Rubber O-ring. (8) Curved mirror. (9) Piezoelectric transducer (optional). (10) Spacer for fixing the cover-to-holder distance (optional). (11) Mirror cover.

can also be seen in Fig. 4.1. To realize a cavity with such a small angle between the crossing beams, a pair of holes has been punched in the cone electrodes in correspondence with the laser beam, thus avoiding any interruption of the cavity path. Although the presence of the holes breaks the axial symmetry of the cone electrodes, numerical simulations show that there is no distortion on the electric potential due to the holes.

Mirror mounts The final goal of the bow-tie cavity is to enhance the power of the resonant running wave and therefore to realize the deepest possible potential for the ions. To this end, the mirrors realizing the cavity must be carefully aligned. To facilitate this operation, we designed mirror mounts composed by two pieces (see Fig. 4.2): a ceramic mirror holder and a metallic cover. In our mounting system, the mirror (referring to Fig. 4.2, element 8), which has a diameter of 6 mm, is attached to a small circular protrusion of the metallic cover (11) with a ultra-high vacuum compatible glue (e.g. Epoxy Technology 353ND). Alternatively, the mirror has to be moved for controlling the cavity length, a circular hollow piezo element (9) (in our case Noliac NAC2121) is inserted between the mirror and the protrusion, and

by the point $\{g_1, g_2\} = \{-0.89, -0.9\}$.

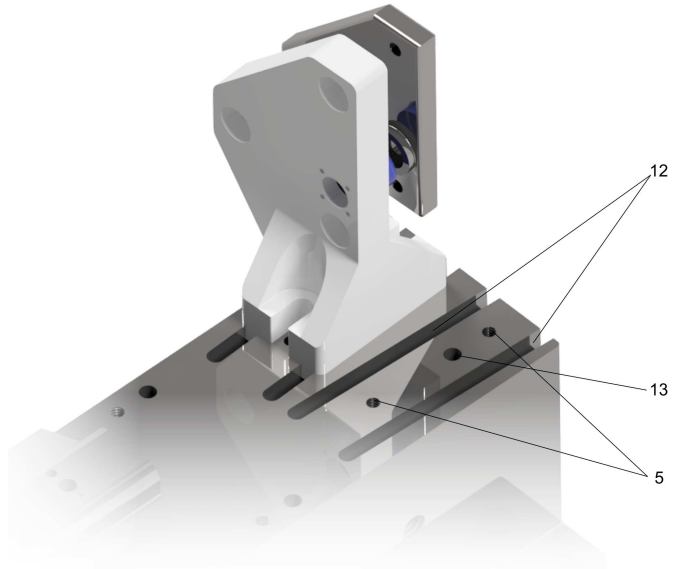

Figure 4.3: CAD assembly of the mirror mount on the metallic base. (5) Threaded holes for the two screws that block the holder on the base. (12) Grooves for aligning the mirror mounts. Their are tilted of 5° towards the center in order to ensure the correct alignment of the mounts. (13) Dowel hole. The numeration follows from Fig. 4.2.

held in position with a thin layer of glue as well. This stack is then connected to the ceramic support by using three small and finely threaded screws (M2x0.25 mm) (1). An elastic element (7) housed in the mirror compartment (3) offers a contrasting force to the mirror (and the piezo, if present) which keeps the cover stable and separated from the holder even if the screws are not completely tightened. In this way, the mirror can be tilted by acting on the screws. In order to facilitate the decoupling between the vertical and the horizontal degrees of freedom, the three screws are placed at the vertices of a triangle with a vertical side. In our system, the elastic element is an O-ring made of DuPont Kalrez 8002, an UHV compatible rubber. In case one wants to rely on the mechanical precision of the assembly, each of the three screws can be inserted in a metallic hollow spacer (10) inserted between the holder and the cover, thus making the whole system "monolithic".

In order to realize the cavity geometry as much accurately as possible, it is crucial to position the four mirror mounts on the base at the exact mutual distance and angle. To ease this task, the mirror mounts are equipped with a pair of parallel rails (6) that can move in the complementary pair of grooves (12) placed on the base (see also Fig. 4.3). In this way, when the mirror mounts are placed onto the base, they automatically assume the right angle. Once the angular orientation is set, to completely fix the position of the mounts along the base grooves, a vented

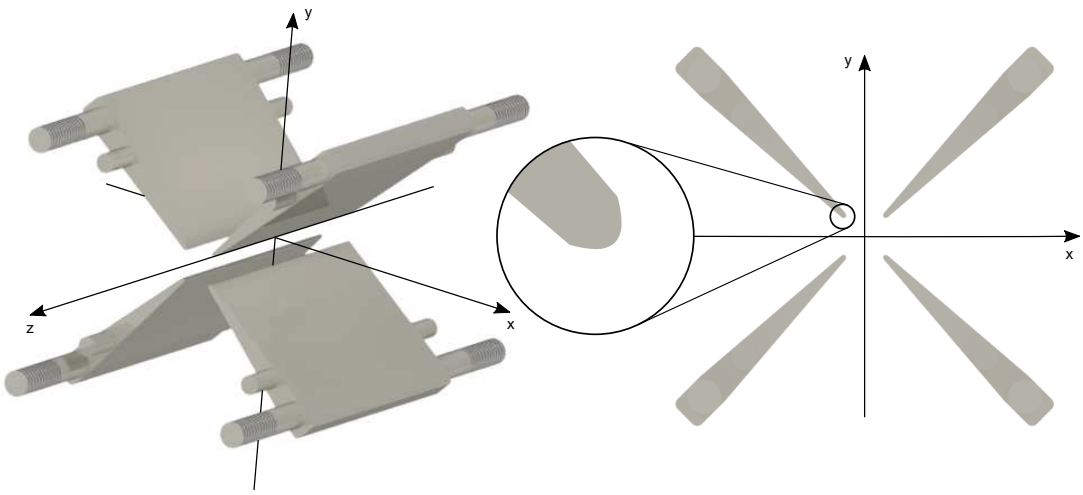

Figure 4.4: CAD representations of the four blade electrodes arrangement, with a zoom on one of their tip, which is characterized by a hyperbolic profile.

dowel is inserted through the ceramic holder (4) into a hole of the base (13), the position of which is calibrated in order to place each mirrors' reflecting surfaces at the right position.

The arrangement of all the elements forming the cavity, from the ones composing the mirror mounts to the elements that ensure their correct positioning on the base, strongly relies on the precision in machining the parts. More details on this aspect will be provided in Sec. 4.1.4.

4.1.2 The Paul trap

In a linear Paul trap, charged particles are confined by two superimposed electrical potentials, one dynamic and the other static. The dynamical one is generated by a set of linear electrodes – with a "blade" shape in our case –, while the static potential is realized by so-called "endcap" electrodes. This paragraph is devoted to the description of the design of both the electrodes and the mechanical parts that hold them in the right position in space.

Blade electrodes Our trap is inspired to conventional linear Paul trap designs (e.g. [142]), and the four electrodes fed with the RF potential are extended along the z axis, as shown in Fig. 4.4. The electrodes are characterized by a blade shape with a very thin tip having a hyperbolic profile to better reproduce an ideal electric quadrupole. Moreover, they are equipped with four pins in order to ensure their spatial positioning – details of the trap assembly will be given in Sec. 4.1.4.

Endcap electrodes The endcap electrodes, which ensure a shallow trapping along the symmetry axis of the RF electrodes, are typically realized by two electrodes places at the edges of the trapping volume. In our case, though, it is fundamental to form crystals resembling as much as possible the ones that are formed in the electro-optical trap, in order to optimize the transition from one trapping potential to the second one. To this end, a negative voltage must be provided by the endcaps at the center of the RF electrodes. In fact, this choice ensures that, depending on the endcaps voltage, the resulting crystal can have a transition from a linear crystal to a two-dimensional laying on the x-z plane.

The easiest way to realize this potential is to place a pair of tips along the y axis fed with a negative voltage (see Sec. 3.2.3). However, similarly to the cone electrodes case, we decided not to occlude completely the optical access along the vertical direction. Therefore each tip was substituted with a pair of endcaps as illustrated in Fig. 4.5. In order to reproduce the same potential created by a hypothetical tip aligned along the positive vertical direction, the distance between the electrodes forming the same pair must be small compared to the distance between the two pairs. In fact, if this condition is not verified the resulting potential takes the shape of a double well, with two distinct minima along the z axis.

The endcap shape is strongly influenced by the presence of the other electrodes, e.g. its lateral sides must follow the blades profile. Differently from the blade electrodes, the endcap tip is characterized by a simple circular profile. In addition, it has a large base in order to ensure a wider contact surface to the lateral support and avoid mechanical instabilities.

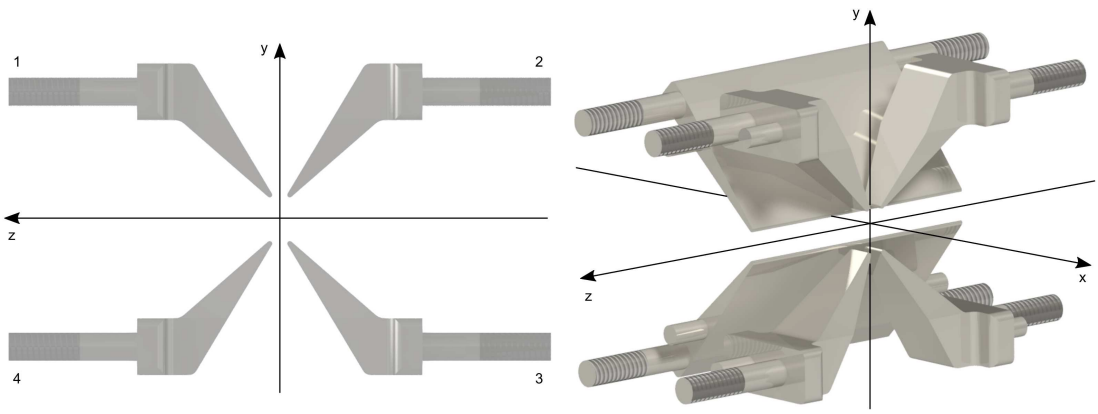

Figure 4.5: CAD assembly of the endcap electrodes and general view of the endcaps with the blade electrodes (two blades have been removed for a better insight).

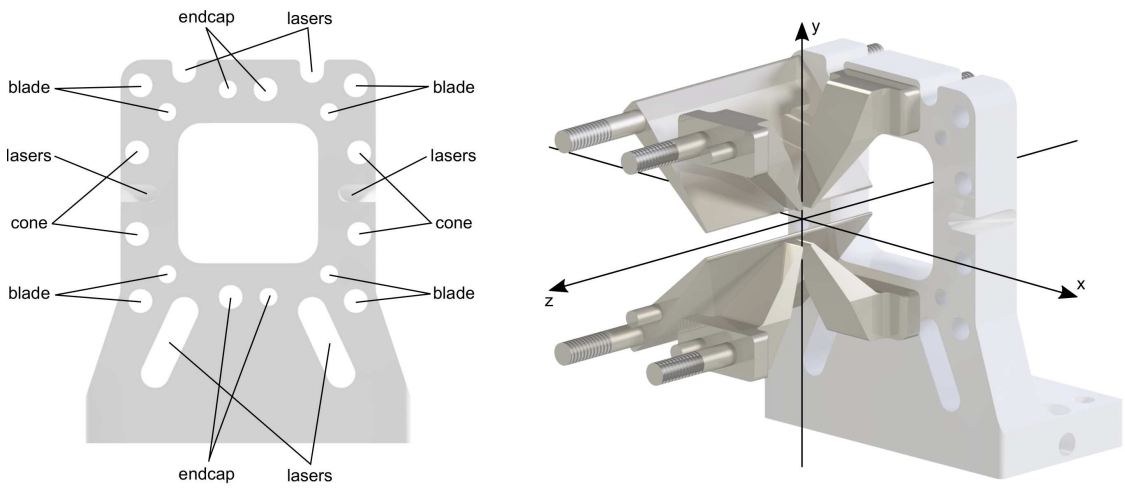

Figure 4.6: On the left, the front view of the ceramic lateral support with the holes scheme for the electrodes. Extra optical accesses are indicated with the label "laser". For example, there is the possibility to shine a laser beam towards the center of the traps by exploiting the cuts made into the lateral side of the supports. On the right, a CAD assembly of some electrodes inserted in a lateral support.

Lateral supports The dielectric supports for the electrodes are designed to host and hold all the electrodes of both the electro-optical and the Paul traps (see Fig. 4.6). In general, each electrode is equipped on the contact interface with a pair of cylindrical extrusions, one of which partially threaded. The thread has the function to make it possible to tight the electrode on the ceramic support with the aid of a nut. Both extrusions are used as dowels that facilitate the alignment and avoid any possible rotation of the electrode around its tip-screw. In addition, the threaded tip which appears on the other side of the ceramic support is exploited to feed the voltage to the electrode by using a tubular crimp lug tighten with a second nut.

The lateral supports are also provided with additional holes and extrusions to ensure extra optical accesses. Specifically, the topmost grooves indicated in Fig. 4.6 can be used to shine a laser beam towards the trap center with an angle of approximately 45° with respect to all the three axes, e.g. useful for cooling processes. Then, other two accesses machined in the lowest part of the support grant an exit to the beams, thus avoiding any laser impingement on the ceramics in the inner part of the trap, the creation of detrimental patch charges on the dielectric material, and reducing the stray light. Finally, other optical access is obtained on the side to shine additional lasers on the x-z plane.

4.1.3 Neutral Barium ovens

We decided to produce the ionic sample through a resonant two-photon photoionization process with continuous radiation at 413 nm, because of the possibility of being isotope-selective and more efficient than the method based on electron-impact ionization [143]. In the photoionization scheme, neutral Barium atoms are first excited with the intercombination line from the ground state $6s^2\ ^1S_0$ to the level $5d6p\ ^3D_1$, then they are ionized by absorbing a second photon at the same wavelength. Hence, this method has the further advantage of requiring only a laser source.

The ion production efficiency has a dependence on the squared laser power (as it is a two-photon process) and an expected rate of about 1 ion/s with a laser power of 4 mW and a beam waist in the center of the trap of about 440 μm [144]. The production rate is affected by the scarce possibility of implementing a laser source that emits a power higher that $\approx$10 mW and by the fact that the first excitation is operated via an intercombination line. In order to improve the efficiency and increase the production rate, a second resonant two-photon scheme can be adopted. This method involves the radiation at 413 nm for ionizing neutral atoms in the state $6s6p\ ^1P_1$, while the transition $6s^2\ ^1S_1 \leftrightarrow 6s6p\ ^1P_1$ is driven by a laser radiation at 553.7 nm. The ionization rate with this second method is expected to increase by a factor 40 with respect to the previous laser waists and the same laser powers, but has the disadvantage of adding a second laser source [144].

Two independent ovens for producing neutral Barium vapors are integrated into the metallic base, below the trap electrodes. The oven's structure is formed by two chimney tubes (refer to Fig. 4.7, element 5), a copper heat-sink (1), a cold ceramic skimmer (11), and the metallic base itself, which actually acts as a second skimmer to trim the atomic vapor distribution.

The chimney tubes are tubular pipes in which solid metallic Barium is crammed. By applying to the thin stripe (6) at their bottom a high current for a short time interval, the heat produced via Joule dissipation warms the ovens up until a stream of atomic vapor is emitted. Therefore, the chimneys design is based on the necessity to facilitate the dissipation, thus the produced heat. In fact, in order to ensure a strong Joule effect, the ovens were produced in stainless steel, a metal characterized by a low thermal conductivity as compared to others. In addition, the electrical resistance is increased by reducing the area passed through by the current (internal and external diameters are respectively 1.20 mm and 1.50 mm).

The tubes are stuck into the heat-sink, which is a copper object with a double aim. First, since the heat-sink can be considered in thermal equilibrium with the cold flange to which it is fixed with the screws (8), it rapidly lowers the temperature of the tubes after the production of the atomic shot, starting from the cold upper side (4). Second, the heat-sink is connected to grounded wires, hence offering to

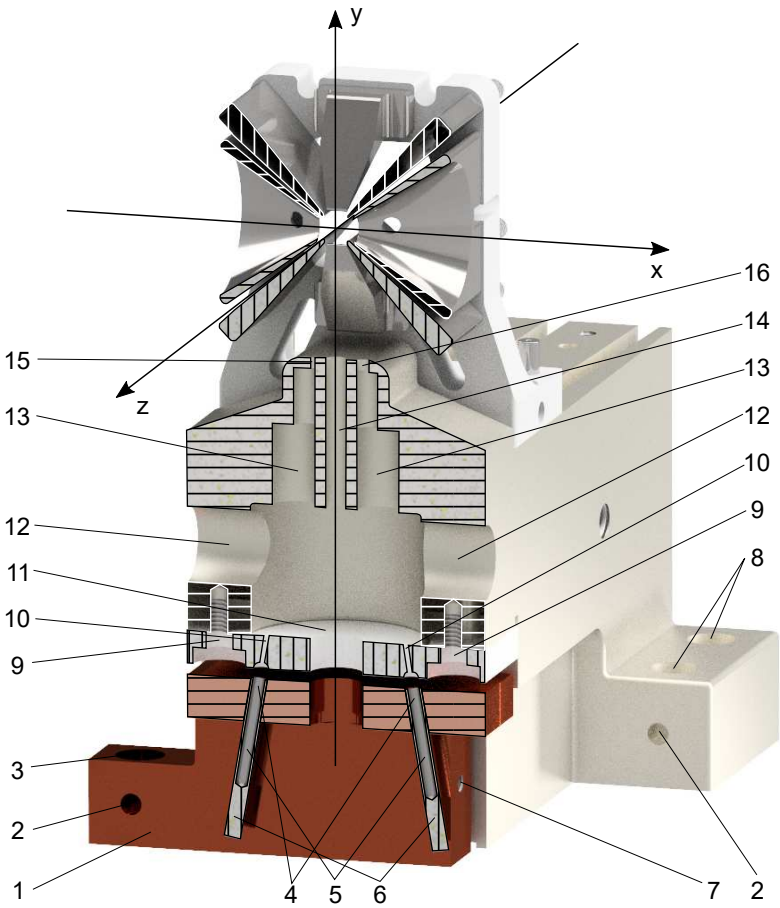

Figure 4.7: CAD section of the ovens system for producing atomic beams of neutral Barium. (1) Copper heat-sink. (2) Venting holes. (3) Screw passing hole for fixing the heat-sink on the flange. (4) Cold upper part of the (5) chimney tubes. (6) Tube stripes for the electric connection. (7) Threaded hole for the ground-connecting the heat-sink. (8) Screw passing holes for fixing the base on the flange. (9) Pipes and (10) screw passing holes of the cold ceramic (11) skimmer. (12) Inspection viewports of the (13) cylindrical oven cavities. (14) Anti-sputter wall for protecting the vertical optical access. (15) and (16) Output holes.

the current a path to flow away.

The atomic beams, which can be independently produced by acting on a specific chimney, are directed towards the trap center. During their flight, the neutral atoms pass through a trimming system composed by the skimmer and the metallic base. The skimmer has a pair of tilted pipes (10) – about 2.5 mm long, with a diameter of 0.5 mm – which reduce the solid angle of the atomic beam. The metallic base, where the skimming element is attached to, is provided with an inner cavity dug via a series of tangent cylindrical removals (13), which culminate with two output holes having

different diameters, 0.4 mm (15) and 1.2 mm (16). In particular, the smaller oven is calibrated to reach the trap center and avoid detrimental electrodes sputtering. Additionally, the optical vertical access is protected by a cylindrical wall (14) in order to avoid that the atomic jets could pass thorough it. The mutual alignment of the ceramic skimmer and the base is a fundamental requirement in order to have a velocity selected atomic beam pointing towards the center of the trap. For accomplish this goal, the correct positioning of the skimmer has been facilitated with two dowels, then removed after having tightened its fixing screws (9). Since the heat-sink alignment, instead, is less decisive, its positioning relies only on two screws (3).

4.1.4 Technical notes on the trap components

In the previous paragraphs, the strategy for what regards the mechanical design of the traps has been discussed. However, other questions must be addressed: what materials are most suited for the realization of the different parts? Are the mechanical parts feasible considering machining tolerances that can be realistically achieved? How can the bottom flange be organized to host the numerous needed feedthroughs?

Materials The materials involved in ion trap building are at least two: a metallic material to produce all the conductive parts like the electrodes, and a dielectric material to support and electrically decouple them. For what regards the electrodes material, there is not a common choice in the ion trapping community, and many different materials – like beryllium copper, molybdenum, gold-plated alumina, etc. – are used [145]. We decided to machine all the electrodes in titanium (alloy Ti6Al4V, also known as "titanium grade 5"), mainly because it has a quite good fabricability and a lower thermal expansion coefficient compared to other materials. Other metallic parts are produced in titanium, as dowels and the trap base.

Regarding the insulating material, we chose to use an aluminum nitride ceramic commercially known as "Shapal Hi-M Soft". This ceramic has the great advantage of combining a high thermal conductivity (92 W/mK) with a low thermal expansion coefficient (about 4.8 μm/m K). We have decided to use this ceramic for machining the trap lateral supports and the cavity mirror holders, since Shapal can be passed through by heat without modifying its shape so much to disturb the optical cavity or stress the electrodes arrangement. Moreover, also the oven skimmer was made in Shapal in order to ensure it as cold as possible.

The only mechanical parts that were not produced neither in titanium nor in Shapal are the oven heat-sink (copper) and the chimney tubes (stainless steel).

Machining tolerances As already anticipated, the successful assembly of a composite ion trap relies on achieving high machining precision. For instance, some

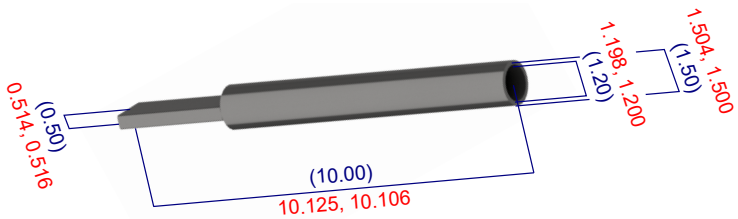

Figure 4.8: Resume of the measurements performed on the two chimney tubes with the CMM. In blue/red, the ideal/real dimensions are reported in millimeters.

delicate points in which a high fabricating precision is strongly required are the system rails-grooves that fixes the angular position of the mirror holders, the blade and cone electrodes length since they must be fastened on both sides on the lateral supports, or the oven tubes diameter because they must be inserted and stuck in the heat-sink. Additionally, dowels are particularly critical, since they represent the means that is used all over the trap mount for the precise positioning of the parts.

In order to reach this level of precision, we closely worked in collaboration with the mechanical workshop that produced the trap components, and the tolerance of $\pm 5\,\mu$m was reached on the most demanding dimensions. After the production, each single trap component was individually measured in a metrological chamber by using an optical microscope and a coordinate measuring machine (CMM). This device is able to measure the size of an object with a μm-level of precision by detecting the coordinates of single points on the part's surface with a physical probe (needle). This measurements procedure ensures that all the produced parts are optimal reproductions of the ideal objects described by the technical drawings within the specified tolerances. In this way, the exact shape of the real trap components is known along with their most crucial feature dimensions as, for instance, the blade's tip width $(0.360 \pm 0.005)\,\mu$m, the electrode dowel-tips, or the external and internal diameters of the chimney tubes (see Fig. 4.8).

Nevertheless, even if all the trap components were machined within the tolerances, other detrimental deviations from the ideal assembly may arise due to the tolerance interplay when different items match. Just to give a clarifying example, an alignment dowel can be produced with a diameter slightly bigger than its ideal value, but still being within the tolerances specified to the constructor, and the corresponding hole into which it should be inserted can be within tolerances as well, but lightly smaller. If this is the case, the dowel may not enter into the hole, making both useless. In order to avoid such unfortunate situations, all the critical points of the whole trap assembly – mainly the dowels inserting, the pairing between the mirror mount rails and the base grooves, the electrodes alignment, and the chimney tubes joint with their heat-sink – were treated with special care during

the construction process, and the part features were adaptively machined. Moreover, more copies of such parts were realized and then characterized by using the CMM. Therefore, only the best combination of matching items was selected in the trap assembly, which was performed in the same metrological chamber. Therefore, after having successfully assembled the trap, this was also tested with the CMM. The most significant measurements performed on the trap assembly are resumed in Fig. 4.9.

Feedthroughs and connections The bottom flange of the vacuum chamber has the central part slightly lowered in order to make the trap's geometrical center at the same height of the lateral viewport centers. As shown in Fig. 4.10, the electric connections are organized in different feedthroughs directly soldered onto peripheral area of the flange. In particular, there are two power feedthroughs (element 3 in Fig. 4.10), each of which having two copper pins, entirely dedicated to the RF for feeding the blades electrodes[2]. The six DC electrodes (four endcaps and two cones) are supplied via the feedthroughs (1), each with four connections. For reasons of space, these feedthroughs are integrated in two CF16 flanges then mounted on the extruded tubes attached of the main flange. The ovens are connected to four single

[2]The capacitance of the power feedthroughs provided by the producer is .

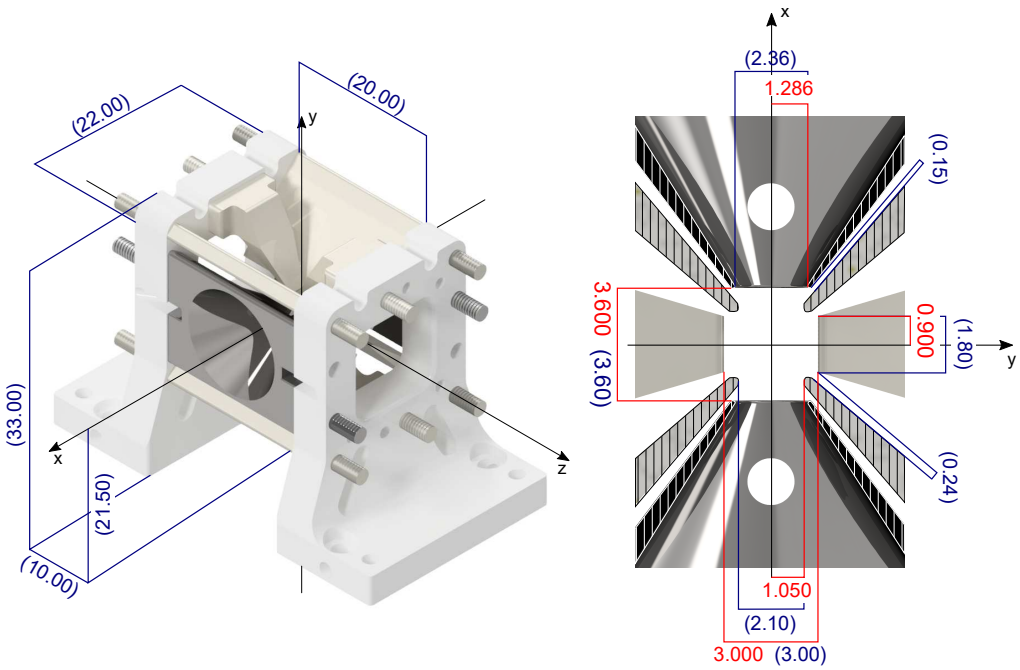

Figure 4.9: Summary of the measurements performed on the electrodes distances. In blue/red, the ideal/real dimensions are reported in millimeters.

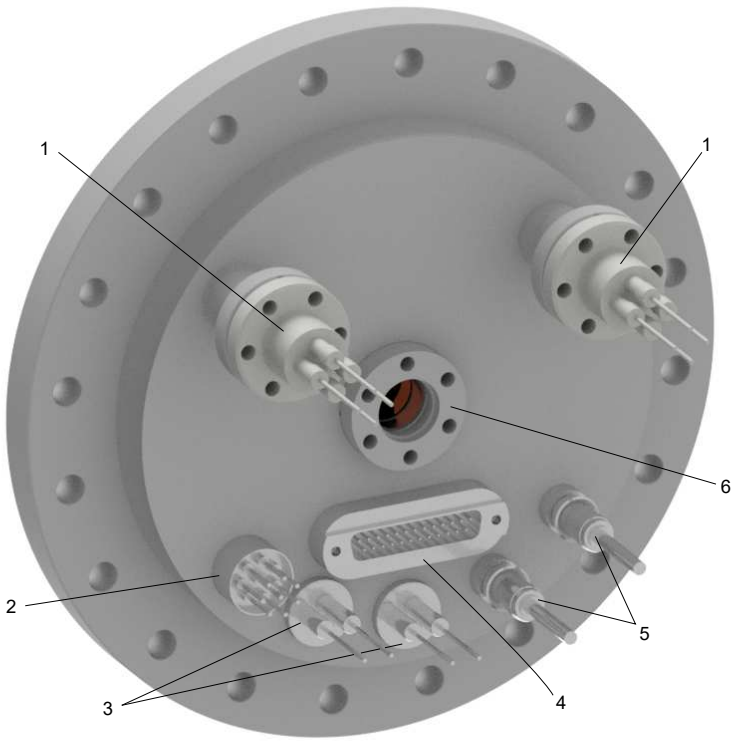

Figure 4.10: CAD representation of the external side of the ions' vacuum chamber lower flange. (1) DC electrodes feedthroughs. (2) Multipole Feedthrough for the optical cavity piezotransducers. (3) RF feedthroughs. (4) D-Sub connection for the objective translator. (5) Oven ground feedthroughs. (6) Viewport for the lower vertical optical access.

feedthroughs, two placed on the bottom flange (5), and two placed in two additional CF16 flanges welded to the main chamber (not visible in Fig. 4.10).

The two piezotransducers of the bow-tie cavity are connected to four of the eight connections of the multipole feedthroughs (2). The same feedthrough is also used to connect to the outstide the thermistor placed on the metallic traps base. Finally, the objective translator is connected to its driver via a 25-poles D-Sub connector (4) directly soldered on the flange. The flange is also equipped with a CF16 viewport (6), which opens a vertical optical access to the traps center.

The wires used for connecting the feedthroughs pins to the different elements in vacuum were obtained from a reel of single-strand copper wire having a diameter of 1 mm. Since the wire is isolated by a layer of UHV-compatible kapton, each wire extremity has been exposed before the connection through consecutive mechanical

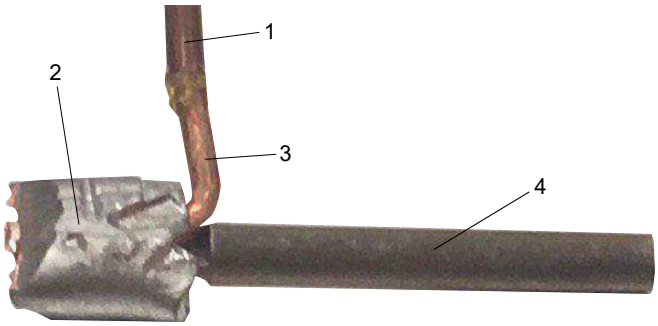

Figure 4.11: Picture of the electrical connection between an oven tube stripe and its supplying wire. (1) Kapton covered wire. (2) Shrink hose. (3) Exposed wire extremity. (4) Oven chimney tube.

removals[3]. In general, all the electrical connections were made by using standard techniques; the only problematic one was the connection to the ovens' chimneys, since the physical space available was particularly small. Initially, we tried to solder the cable to the tube stripes by using the point welding technique[4], but the results were unsatisfying in terms of connection strength and reliability, even using a constantan thin layer to increase the solderability[5]. Therefore, we decided to join the ovens stripes to their respective wires without any soldering technique, but just exploiting the shrink hoses side of thin lugs, as shown in Fig. 4.11. After having tightly pressed the hose around the chimney stripe and the bare copper wire, the circular part of the lug was removed with pincers.

4.2 Simulations on the trapping system

During the design phase, electrical, thermal, and even mechanical simulations were performed on the trap in order to test the geometry and individuate the possible critical points. In the next two sections, the main results of the electric (Sec. 4.2.1) and thermal (Sec. 4.2.2) simulations on the final trapping system are reported.

[3]Actually, the wire is covered by several layers of insulating material which can be scraped away from the extremities with the aid of a sharp scalpel and a microscope. Despite some irregularities and superficial scratches on the copper, the final result is overall more satisfying than the one obtained with chemical etchings.

[4]During the preliminary attempts, we used stainless steel stripes having the same thickness of the real oven tubes stripes.

[5]The junctions with more than one welding point appeared robust and trusty; but they always broke after applying mechanical stresses for testing purposes.

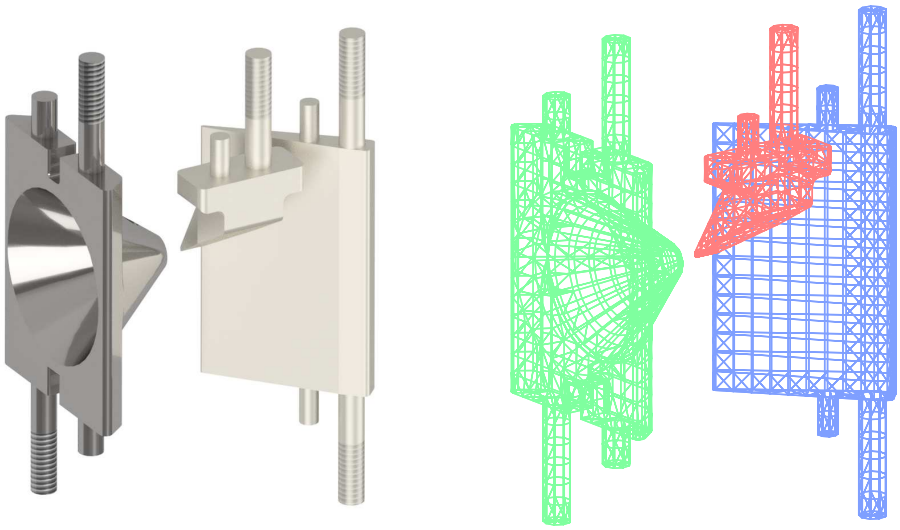

Figure 4.12: On the left, a composition of the three electrode typologies. On the right, their mesh representation.

4.2.1 Electric simulations

The design of the trap electrodes is a result of a series of numerical simulations of the electric potential, which were used to modify the trap components step-by-step. The simulations were based on the static problem approach, which means that the varying electric fields are assumed to slowly change with respect to the electromagnetic wavelength $\lambda = 2\pi c/\omega_{RF}$, where ω_{RF} is the frequency of the dynamical field and c the speed of light. Within this approximation, the interactions between the electric and magnetic fields can be neglected and the whole problem reduces to solve the Laplace equation $\nabla^2\phi = 0$, where $\phi(\vec{r})$ is the electric potential which has two boundary conditions: the voltage on the electrodes surface and the fact that it must tend to zero when $\vec{r}$ goes to infinity. To numerically solve this problem, we used the toolkit ROOT developed by Cern [146] and the package BEMSOLVER [147] in a script written in C language. ROOT is a modular scientific software toolkit mainly written in C++ which contains several classes that are useful to plot data and manage CAD files in drawing exchange format (dxf). BEMSOLVER is a library in which the algorithms required to solve electrostatic problems with complex charges distributions are already implemented and optimized.

The approach of BEMSOLVER is based on the boundary element method (BEM), which converts a volume problem into a surface one. The basic idea underneath this method is to imagine the media as made of vacuum and consider only their surfaces, then to find a continuous electric charge distribution on these surfaces that satisfies the boundary conditions of the original problem. The numerical solution of the superficial charge density can be found by cutting the interfaces between different media in squared or triangular panels (see Fig. 4.12), small enough

to consider uniform the charge density on their surfaces. At this point, the electric potential can be expressed as

$$\phi(\vec{r}) = \frac{1}{4\pi\varepsilon_0} \sum_{i=0}^{N} \left(\int_{S_i} \frac{1}{|\vec{r} - \vec{r}'|} dS' \right) \sigma_i \tag{4.1}$$

where σ_i are the i-th superficial charge densities and N is the panels number. The equation above can be reformulated in a compact way as $A \cdot q = p$, where the $N \times N$ matrix A, which depends only on the mesh geometry, connects the vector q containing the superficial charge distributions σ_i to the vector p representing the applied voltage on the i-th panel.

BEMSOLVER employs two techniques for solving Eq. 4.1. The first is the generalized minimum residual method (GMRES) [148] which aims at computing an approximate solution by running an iterative algorithm until a certain tolerance fixed by the user is reached. This method starts with an initial guess q_0 for the solution, then evaluates the first residual $r_0 = p - Aq_0$, on which the convergence of the algorithm is checked. If another iteration is needed, the new solution vector is computed as

$$q_{i+1} = \sum_{j=0}^{i} \alpha_j q_j + \beta r_i$$

to minimize the new residual r_{i+1} by properly choosing the coefficients α_j and β.

The second employed method is the fast multipole method (FMM) [149], which basically describes the potential in a certain point with the single contribution due to the nearest charge, whereas the effect of the remaining charges is evaluated as a perturbation given by multipole and local expansions.

Paul trap stability diagram From the simulations of the electric potentials generated by feeding different voltages on the electrodes, the geometric coefficients κ_{DC} and κ_{RF}, which describe the electric response in the central trapping region to the applied voltages (see Eq. 2.5), can be extracted. Once the trap geometry has been characterized, the electrical behavior of the traps can be predicted, and the stability diagram of the Paul trap can be evaluated by using both numerical solutions and multiple-scale perturbation theory (see Sec. 3.2.3). There, the coupling angle θ, i.e. the angle describing the rotation of the electrodes with respect to the reference system, was introduced.

The results of the simulations are reported in Fig. 4.13. The green area represents the first stability region for the uncoupled Mathieu equations ($\theta = 0$) and the geometry coefficients of our trap. The first stability region evaluated with the numerical method (black thick dots) is well approximated by the boundaries obtained with the multiple-scale perturbation theory (blue curves) only for small values of q. For $q \gtrsim 0.7$ the boundary curves enclose a region of $\{q, a\}$ pairs (depicted in blue)

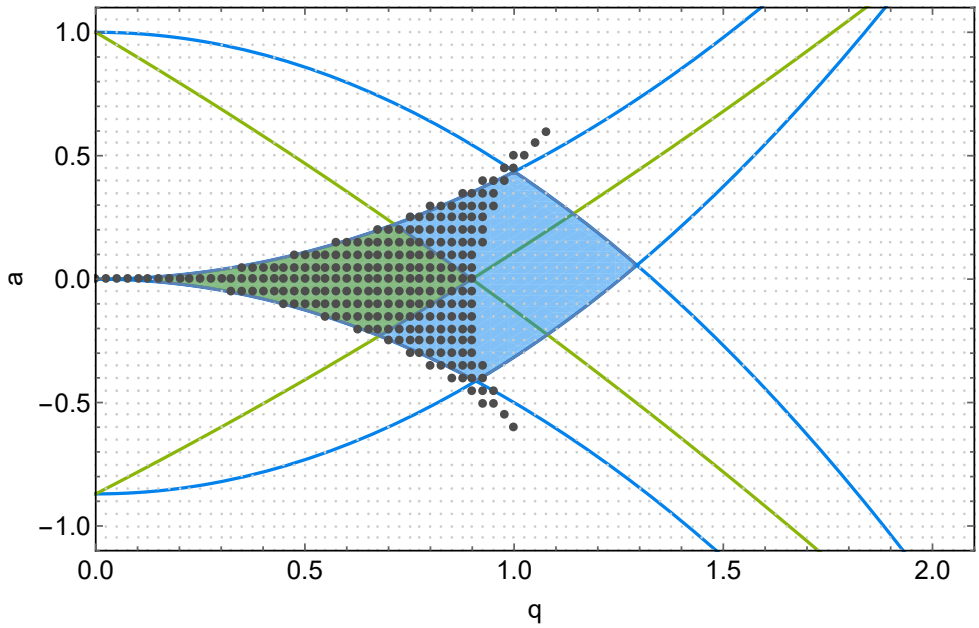

Figure 4.13: Paul trap stability diagram having a coupling angle of 45° (our case). The black thick dots represent $\{q, a\}$ pairs for which the Paul trap (described by a system of coupled Mathieu equations) is stable, whereas the small gray dots indicate instability pairs (see Sec. 3.2.3). The blue curves, calculated with the multiple-scale perturbation theory, enclose a stability region which is wider than the numerically estimated one, yet well describing the stability behavior for small values of q. The green area is the stability region of the corresponding uncoupled system.

for which the numerical method predicts instability. For small q, both coupled and uncoupled systems have stability regions characterized by the same boundaries; nevertheless, the coupled system has in general a wider stability region. However, while the primary stability region does not appreciably vary for small q with nonzero mixing angles θ, the secondary stability regions are highly variable. In Fig. 4.14, both the primary and secondary stability regions of a trap having our geometric coefficients and a coupling angle $\theta = 35°$ are reported for comparison purposes. When $\theta = 45°$, as in our trap arrangement, the maximum coupling is reached: the result is that the secondary stability regions shift towards the primary one and join it forming an exceptional wider triangular-shaped stability region [133], as shown by the black dots in the graph of Fig. 4.13.

The problem of having a discrepancy between the numerical an the analytic calculations is mitigated by the fact that Paul traps are usually operated in the lower part of the stability diagram. For our geometric coefficients, a maximum potential difference on the blade electrodes of 200 V corresponds to $q \approx 0.15$ (see

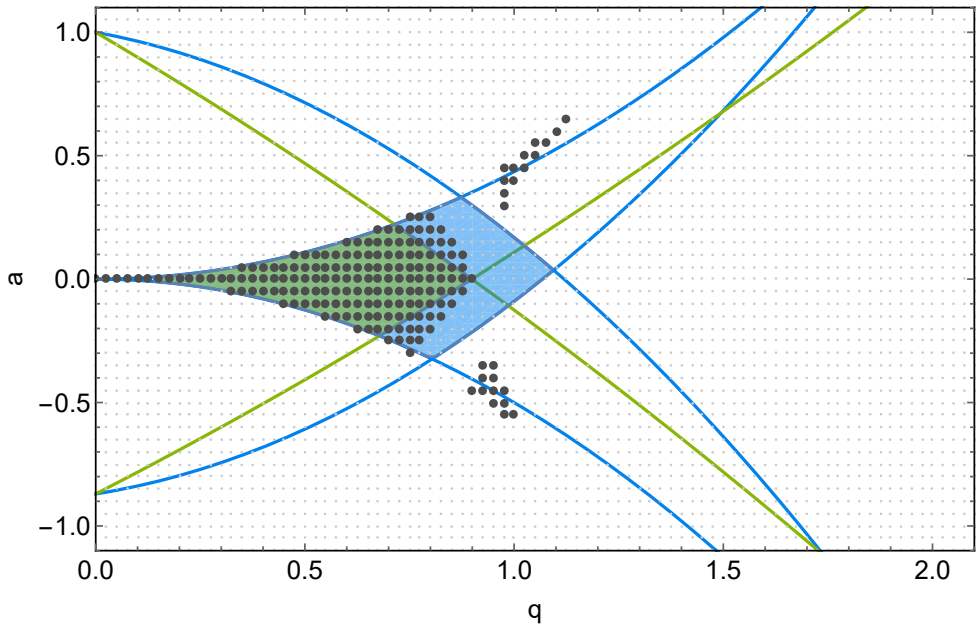

Figure 4.14: Stability diagram of a Paul trap having a coupling angle θ of 35° and the same geometric coefficients of our trap. The three groups of black dots indicate the stability regions: the wider area having small values of q is the primary one, whereas the other two are the secondary stability regions. When the coupling angle grows up to 45° as in our case, these three areas merge together in a single stability region. The symbols' legend is the same of Fig. 4.13.

Eq. 2.7). Fig. 4.15 reports a zoom on the lowest part of the stability diagram of Fig. 4.13 in which the axes are expressed in terms of V_{RF} and V_{DC}. In addition, the trapping condition for the axial direction ($\phi_{DC} < 0$) is indicated, along with the values of V_{RF} and V_{DC} for which the same confinement along y and z directions is realized.

Misalignments and residual axial RF During the simulations, we have considered the trap electrodes as perfectly machined and aligned. This is an ideal case, since misalignments or imperfections may occur during the fabrication or the assembly. Regarding the Paul trap, for instance, any deviation of the blade electrodes from the ideal case causes the presence of a nonzero RF field along the axial direction.

Let us recall the approximate solution 2.10 to the equation of motion for a particle with mass m and charge $+e_0$ in a Paul trap and in presence of an additional DC field [37]

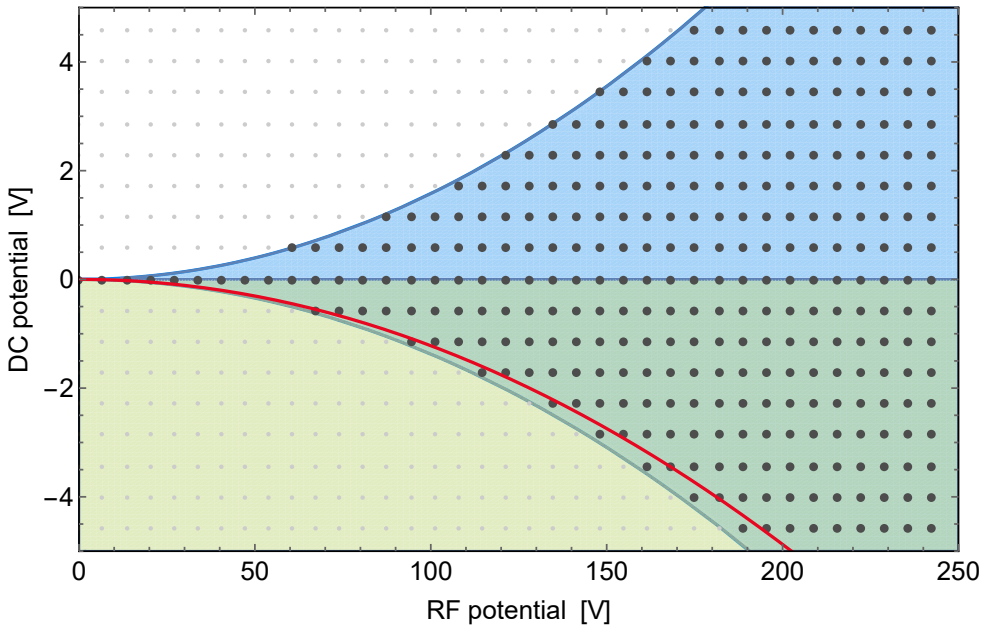

Figure 4.15: Stability diagram of the Paul trap for the low potentials range. In addition to the plot legend of Fig. 4.13, the green shaded area represents the trapping region along the axial direction; whereas the red curve indicates the pairs of RF and DC voltages for which the trapping frequencies along the y and z directions are equal.

$$x_i(t) \approx \left(x_{0,i} + x_{1,i}\cos(\omega_i t + \varphi_i)\right)\left(1 + \frac{q_i}{2}\cos(\omega_{RF} t)\right) \quad \text{with} \quad i = x, y, z$$

where $r_{0,i}$ is the equilibrium position of the ion along the i direction, $r_{s,i}$ is the position shift from $r_{0,i}$ due to stray electric field, ω_{RF} is the RF frequency, and ω_i is the secular motion frequency. The micromotion amplitude along the i-th direction can be estimated as $(r_{0,i}\, q_i)/2$.

Ideally, along the RF electrodes axis, the parameter q_z is null near the trap center; instead it assumes nonzero values by taking into account the finite electrodes length and misalignments effects. In order to evaluate q_z and, consequently, the residual axial micromotion amplitude, a modified version of the trap assembly, having the blade electrodes displaced from their exact position, was simulated. Since the mechanical tolerance on the blades position is 5 μm, the angular deviations were neglected in the simulation, while the linear displacements were considered equal to the tolerance for taking into account the worst possible case. This evaluation shows a residual axial micromotion amplitude of about 0.5 nm, which corresponds to a micromotion energy of about 1 μK.

4.2.2 Thermal simulations

The trap assembly was also tested from the thermal point of view, mainly for what concerns the power dissipated by the RF electrodes and the heating of the neutral Barium ovens. The software used for such simulations is COMSOL Multiphysics.

RF power dissipated Each pair of electrodes can be schematized as a capacitor having a complicated shape and containing a dielectric medium (ceramics of the lateral supports) disposed only around their cylindrical extrusions. As a result, an equivalent series resistance (ESR) can be associated to each electrode, the value of which can be estimated as

$$ESR = \frac{\tan(\delta)}{\omega_{RF}\, C}$$

where C is the lossless electrode capacitance and $\tan(\delta)$ is the loss tangent, which arises from the phasor representation of the equivalent circuit parameters. For Shapal Hi-M Soft, its value is $\tan(\delta) \approx 10^{-3}$. The reactive term of the ESR is responsible for the heating of the parts composing the trap by Joule effect. The electrodes' ESR is calculated by using a COMSOL simulation to estimate the corresponding capacitances C. In the case of the blade electrodes, with $\omega_{RF} = 2\pi \cdot 3.5\,\mathrm{MHz}$ and an RMS amplitude of $200\,\mathrm{V}/\sqrt{2}$, we found an overall dissipated power of 0.69 mW for the upper blades and 0.74 mW for the lower ones.

We used these values to simulate the trap heating due to the RF power losses in stationary conditions, using as the only constraint a fixed temperature for the external side of the flange (293 K). The results showed a small temperature increase on the order of tens of mK, and the hot spots are at the connections between the electrodes and the lateral supports. Regarding the thermal perturbation on the optical cavity, the simulation shows at most a vertical thermal expansion of 0.4 nm for the ceramic lateral supports, while along the other directions there are no appreciable expansions.

Transition from Paul trap to EO trap Studying the temperature variation of the trap is important for estimating possible changes of bow-tie cavity length. In particular, in the transition phase from the Paul trap to the electro-optical trap, a local heating source (dissipated RF power) is turned off, thus possibly causing instabilities and long thermal drifts to the bow-tie cavity and the trapping interference pattern. If the temperature of the system undergoes a decrease of about 2 K, the calculations show that the corresponding variation of the optical cavity length would lead to a shift of the central minimum of the interference pattern equal to the waist of the trapping laser beam. Therefore, the trapped ions would be slowly displaced until reaching the end of the trapping region.

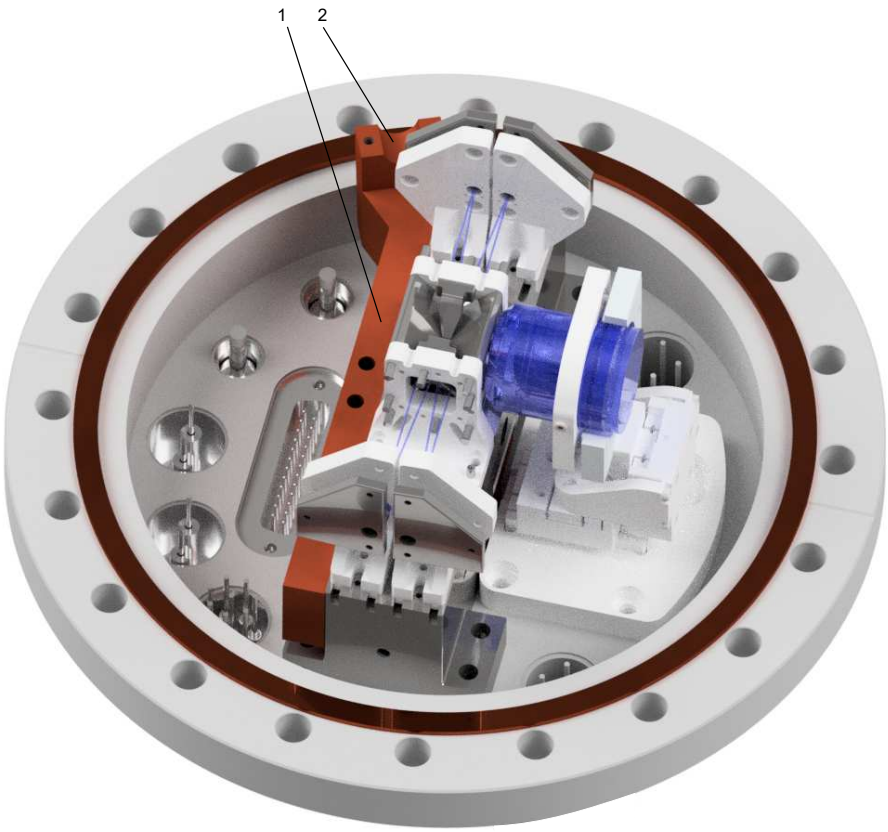

Figure 4.16: CAD assembly of ions' vacuum chamber lower flange. (1) Copper heat-sink. (2) Feedthrough connection housing. The blue transparent object represents the imaging objective (see Sec. 4.3.1).

For better stabilizing the system temperature and avoiding shifts of the confining interference pattern, a plate (element 1 in Fig. 4.16) made in copper is attached to one of the base long sides. This element is thermally connected to outside the vacuum chamber through a thick feedthrough fixed on one of its extremities (2). In this way, the plate works as a "cold finger" that helps dissipating the heat produced in the trap and, possibly, actively control the trap temperature. To this end, a vacuum-compatible thermistor is placed on the plate to monitor the trap assembly temperature.

Oven simulation Several thermal simulations were made with COMSOL on the oven system, mainly for establishing the behavior of the chimney tubes when high current bursts are applied. For instance, the temperature simulated when a current burst of 100 A and duration 200 ms is applied to a single oven tube is plotted in

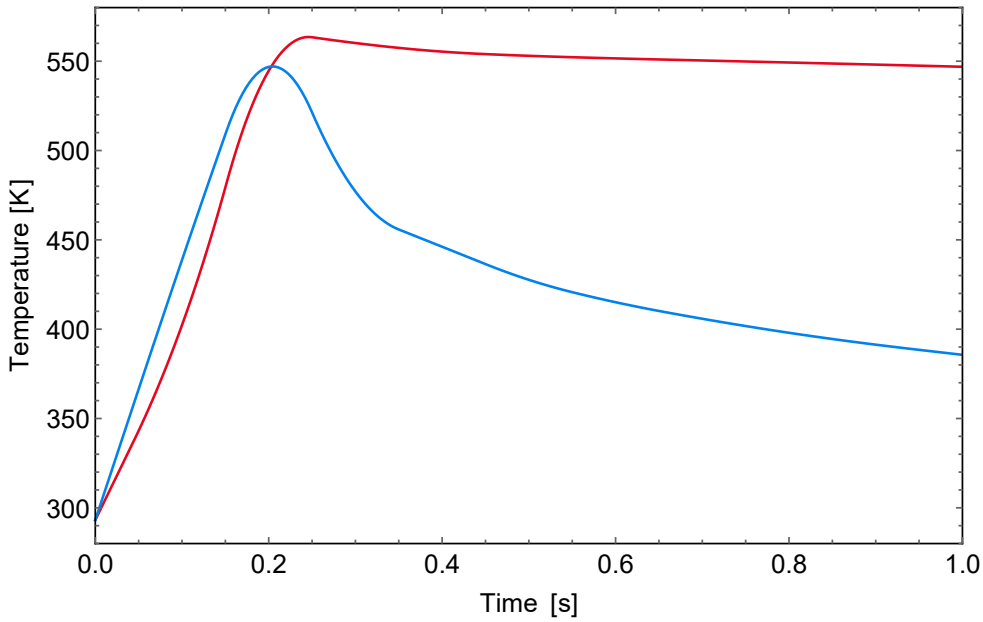

Figure 4.17: Simulation of the temperatures of both the wire connection (red curve) and the connection to the copper heat-sink (blue curve) of a chimney tube as a function of time with an applied current burst of 100 A and duration of 200 ms.

Fig. 4.17 as a function of time[6]. The simulation shows that, during the current feeding, the temperature increases almost uniformly along the tube until reaching about 550 K at the end of the burst. Instead, after the oven is switched off, the temperature starts decreasing from the top of the tube for effect of the copper heat-sink, which maintains the same temperature of the external side of the bottom flange during the whole simulation.

The current pulse duration is a fundamental parameter that has to be experimentally adjusted in order to reach a satisfying trade-off between the number of the atoms in the vapor flux and the minimization of the vacuum pollution. Another aspect that plays a central role in the optimal functioning of the oven is its geometry, and in particular the ratio between the internal and external diameters $\phi_{\text{int}}/\phi_{\text{ext}}$. Increasing this ratio, i.e. reducing the tube section, causes an increment of the dissipated heat via Joule effect. Nevertheless, the diameters' ratio is limited by the feasibility of its mechanical fabrication. In our case, this ratio is 0.8. With lower values, thermal simulations showed a temperature increasing during the current burst much lower than the one we predict for $\phi_{\text{int}}/\phi_{\text{ext}} = 0.8$, thus leading to

[6]During the simulation, the temperature of the copper heat-sink sides in contact with the bottom flange were constrained to the environment one. Both conduction and radiant heat transfers were considered.

longer current pulses in order to obtain proper atomic vapors.

4.3 Other elements of the experimental setup

In this section, a general description of other details of the setup, fundamental for the experimental point of view, but lying outside of this thesis work, is presented. Specifically, these are the imaging strategy (Sec. 4.3.1), the RF drive that supplies the dynamic voltage to the blade electrodes of the Paul trap (Sec. 4.3.2), and the atoms' section of the experimental apparatus (Sec. 4.3.3).

4.3.1 Imaging objective

The ultra-high vacuum chamber is equipped with a high numerical aperture (NA $\simeq 0.5$) objective, UHV compatible and achromatic at both 493 nm and 671 nm, the fluorescence wavelengths of Ba^+ and Li [150]. The choice of placing the objective directly inside the vacuum chamber ensures the possibility of collecting light from a large portion of solid angle and collimating the light rays before they pass through the vacuum view-port, thus solving most of the problems related to aberrations. In fact, the glass window can be schematized as a plate with plane parallel facets which does not disturb or distort a collimated beam. The disadvantage of such a solution is basically the necessity of a sophisticated translator placed inside the vacuum chamber to remotely control the objective, since with numerical aperture of ≈ 0.5 the depth of field is very small ($\approx 10\,\mu$m for both the wavelengths). The objective is held by a compact translator (produced by SmarAct) with 3 spatial and 2 angular axes, entirely made in titanium and other non-magnetic UHV-compatible materials. Moreover, it is equipped with an integrated optical encoder which allows to obtain along the focus direction a resolution of approximately 1 nm upon an overall translation range of about 6 mm.

4.3.2 Radiofrequency drive

For supplying the Paul trap blade electrodes, we designed a compact RF drive built on a PCB and realizing, when connected to the RF electrodes, four interdependent RLC resonant circuits at 3.5 MHz [151]. The four circuits, one per each RF electrode, are equipped with a bias tee to add to each RF signal a DC voltage. A high voltage output is realized by the combination of a low-noise amplifier and the enhancement factor of the RLC circuits, leading to an overall voltage gain of 200. The quality factor of the drive is about $Q \approx 67$, a value that ensures a fast operation of the RF signal, which can be turned off in less than $10\,\mu$s. Finally, the drive is provided with non-invasive pickups in order to monitor the RF signal

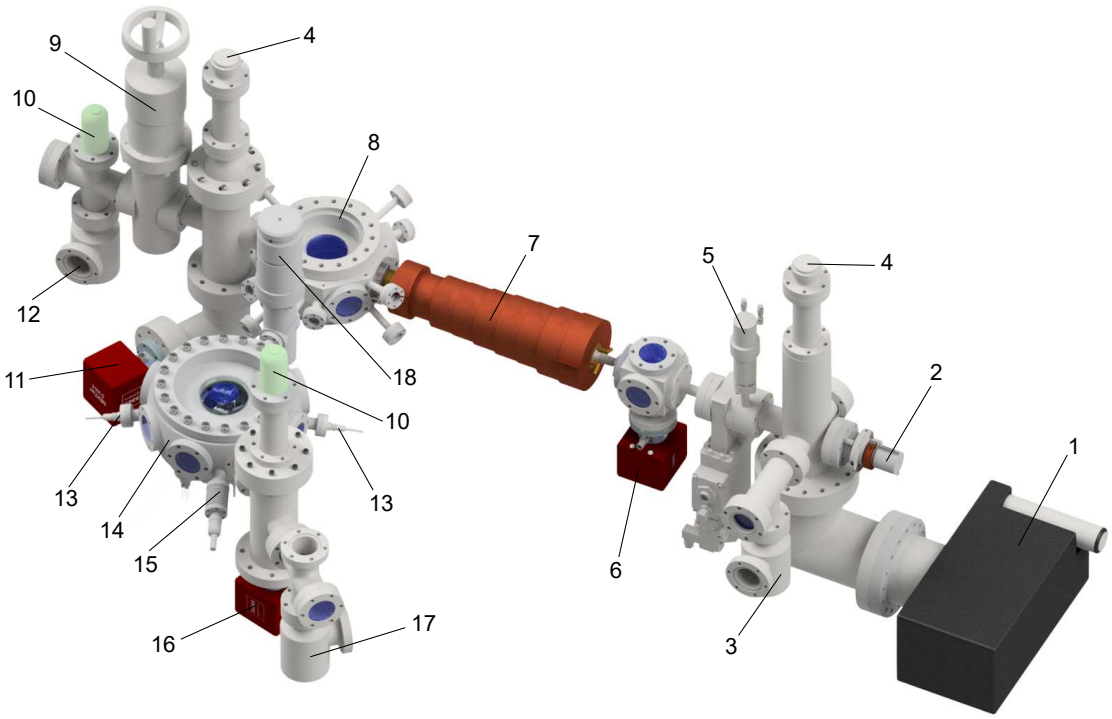

Figure 4.18: CAD assembly of the atom-ion experimental apparatus. (1), (6), (11) and (16) Ionic pumps. (2) Lithium oven. (3), (12) and (17) Shutters for turbo pumps. (4) Titanium sublimation pumps. (5) Oven section isolation shutter. (7) Zeeman slower coils. (8) Lithium MOT chamber. (9) Shutter. (10) Gauges. (13) Power feedthroughs for Barium ovens. (14) Ion chamber. (15) Heat-sink feedthrough. (18) Shutter for separating ions and atoms vacuum chambers.

amplitude and phase, thus allowing to actively stabilize the voltage drop on the blades via feedback loops.

4.3.3 The atom section of the setup

The ion chamber is a part of a wider experimental setup that is currently under construction. The other section is relative to the creation and manipulation of ultracold gases of neutral fermionic Lithium. In the atom oven (element 2 in Fig. 4.18), a solid sample of Lithium is deposited and heated up with a heating strip wrapped around the external side of the oven in order to produce beams of hot atoms directed to the MOT chamber (8). This highly sputtering section of the setup can be isolated by acting on the vacuum valve (5) and is provided with two different kinds of pumps for UHV, a Agilent titanium sublimation pump (4) and two ionic pumps, a Agilent VacIon 75 (1) and a Saes NEXTorr D-100 (6). Anyway, such pumps can not be switched on when the pressure level is not sufficiently low,

therefore a vacuum turbo pump coupled with a simple rotative pump can be attached to the system thanks to a shutter (3) to accomplish the first vacuum stage. Before the hot atoms reach the MOT chamber, they pass through the Zeeman slower (7). On the other side of the chamber with respect to the oven, there are again a Agilent titanium sublimation pump (4) and a Saes NEXTorr D-200 ionic pump (11) whose purpose is to evacuate that section of vacuum apparatus from the uncaught hot atoms; otherwise, they will sputter the viewport through which the Zeeman slower laser beam is shined. For the same reason previously reported, such two pumps can be activated only when the first vacuum stage is realized by a turbo pump attached via the shutter (12). Finally, the reached level of vacuum inside the apparatus can be measured by the Agilent UHV-24p ionization gauge (10) placed near the ion chamber, which can measure pressures until $5 \cdot 10^{-12}$ torr, and the Agilent UHV-24 ionization gauge (10), which has a pressure limit of $2 \cdot 10^{-11}$ torr.

Chapter 5

Ion laser system

In atomic physics experiments, lasers are a fundamental tool for manipulating atomic samples, e.g. by performing spectroscopy measurements, cooling or optical pumping.

Ba^+ ions need a remarkable number of wavelengths in order to be produced and manipulated (see Fig. 5.1). For the photoionization of neutral Barium, a laser at 413 nm is used. Laser cooling can be performed by using either the D1 line ($^2S_{1/2} \leftrightarrow {}^2P_{1/2}$) at 493.5 nm or the D2 line ($^2S_{1/2} \leftrightarrow {}^2P_{3/2}$) at 455 nm. In general, the D1 transition is preferred since there is only one metastable level ($^2D_{3/2}$) to which an atom in the excited ($^2P_{1/2}$) level can decay apart from the absolute ground state, thus only one repumper light source at 650 nm ($^2D_{3/2} \leftrightarrow {}^2P_{1/2}$) is needed. Therefore, for performing the standard Doppler cooling technique on Ba^+

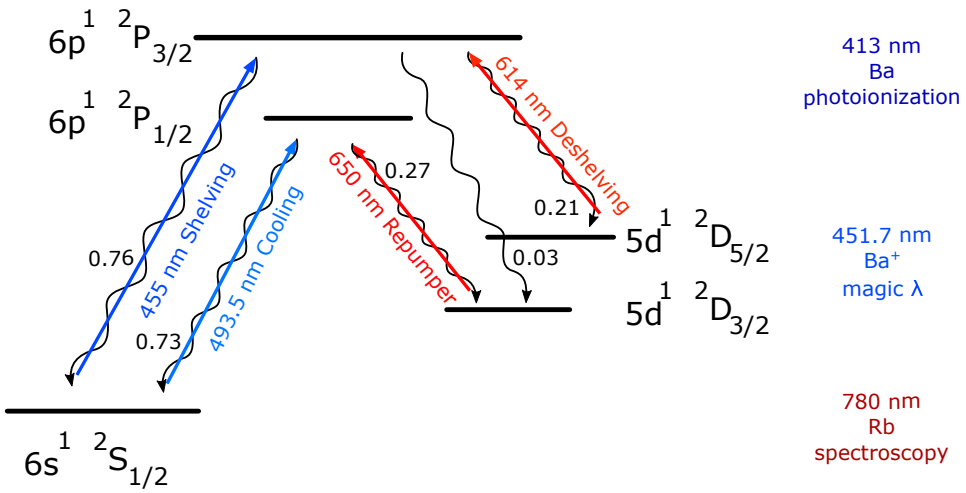

Figure 5.1: The wavelengths needed to produce and manipulate Ba^+ ions. The laser at 780 nm is requested for the locking scheme (see Sec. 5.4). Black numbers represent the branching ratios [152, 153].

transition, lasers at 493.5 nm and 650 nm are requested (the latter acts as a repumper laser by driving the $^2D_{3/2} \leftrightarrow {}^2P_{1/2}$ transition). The D2 transition, instead, can be employed for shelving one of the Zeeman sub-levels of $^2S_{1/2}$ through the $^2S_{1/2} \leftrightarrow {}^2P_{3/2}$ transition (455 nm), leading to an optical pumping of the ion into the $^2D_{5/2}$ level. This level can be pumped out through the $^2D_{5/2} \leftrightarrow {}^2P_{3/2}$ (deshelving) transition (614 nm). Finally, the trapping laser at 451.7 nm is used for the electro-optical trap as discussed in Sec. 3.2.1 and a laser at 780 nm is used as a common reference laser in the locking scheme reported in Sec. 5.4.

Considering the large number of wavelengths needed, we decided for most of the wavelengths to produce in-house laser diodes in external cavities instead of buying commercial ones. To this end, a novel design was developed, the details of which are exposed in Sec. 5.2. The optical circuits are presented in Sec. 5.3, with a particular focus on the trapping and deshelving laser light production. Finally, the last section 5.4 of this chapter is devoted to the lasers locking strategy.

5.1 External cavity diode lasers

Semiconductor laser diodes (LDs) are based on a material with a p-n junction (or a p-i-n structure), in which the gain is generated by the electric current flowing through the junction. In such heterostructure, electrons and holes recombine and release energy by emitting photons in a process that can be spontaneous or stimulated by incident photons. Compared to solid-state lasers (e.g. Ti:Sa lasers), gas lasers (e.g. based on He:Ne), or dye lasers, semiconductor diodes are in general more compact and cheaper, but the drawback is that the emission has a quite large spectral width. The tuning of the output frequency can be realized by changing the injection current or the diode temperature; however, the frequency change is typically either too small or too slow, and the reduction of the emission linewidth cannot be achieved by acting on the laser diode alone. This can instead be done by providing to the diode an external optical feedback, which may be realized by using the diode as a gain medium enclosed in a external cavity composed by an element providing retro-reflection to the gain medium (e.g. a mirror) and frequency-selector elements. This implementation is known as ECDL or External Cavity Diode Laser [154]. With a longer optical cavity, the natural spectral width of the ECDL emitted radiation is reduced (in fact Shawlow–Townes width scales with the inverse of the square of the cavity length [141]).

Usually, LDs have two high-reflective HR facets that create a short Fabry-Perot cavity. Nevertheless, building an ECDL is considerably easier if the front facet is equipped with an AR coating, since otherwise there would be a competition between two overlapped cavities: the short cavity made by the diode's facets and

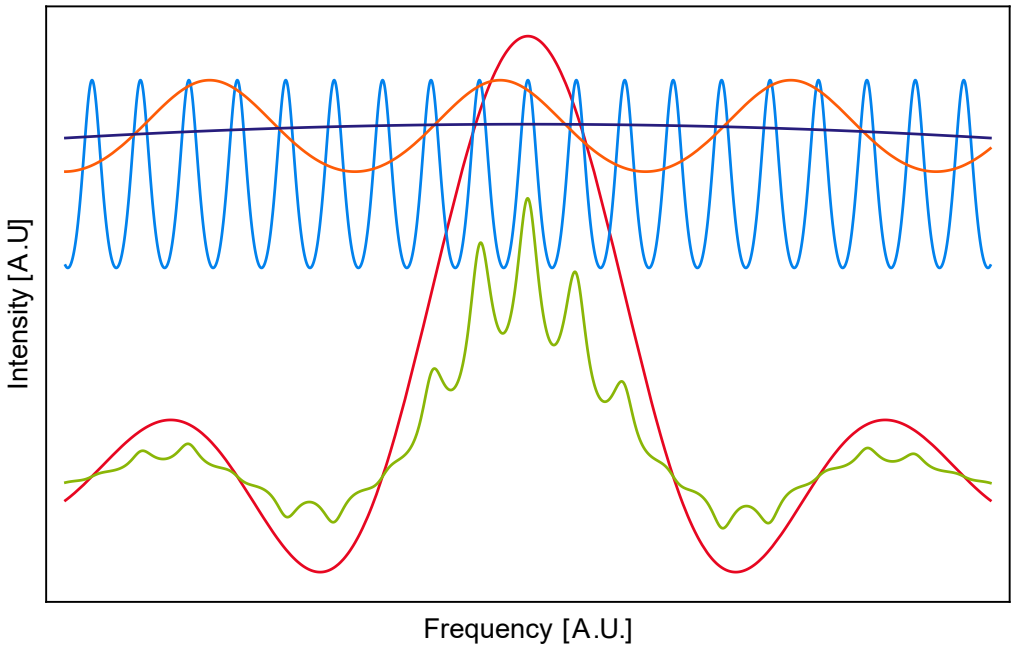

Figure 5.2: Typical spectra involved in the mode competition that determines the ECDL output frequency. The medium gain in dark blue, the internal optical cavity spectrum in orange, the external optical cavity modes in light blue, the frequency-selector spectrum (a diffraction grating in this sketch) in red. The product of these spectra is reported in green. The frequency scales of the spectra are not in scale.

the external cavity.

In general, the output frequency of an ECDL (see Fig. 5.2) is the result of several contributions to the overall gain of the system:

- The gain medium, which has a spectrum centered at a frequency that depends only on the semiconductor junction, is characterized by a very broad line shape. The temperature dependence of the gain medium is quite small (typically 150 GHz/K [141]).

- The internal optical cavity, formed by the rear and the front facets of the laser diode, has the typical spectrum of a Fabry-Pérot cavity. The peak height with respect to the spectrum minima is low since the finesse is very small, and the peak distance (Free Spectral Range) is quite wide since the cavity length is very small. Nevertheless, the presence of this spectrum in the mode competition can be avoided by using a LD with an anti-reflection coated front facet.

- The external optical cavity, which also has a Fabry-Pérot-like spectrum. The modes of this cavity are narrower than the modes of the internal cavity.

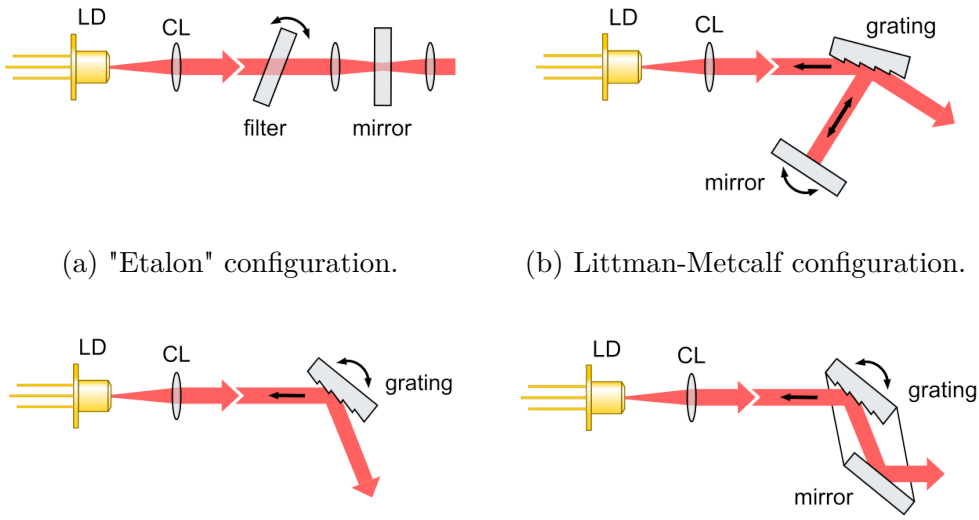

(a) "Etalon" configuration.

(b) Littman-Metcalf configuration.

(c) Littrow configuration.

(d) Improved Littrow configuration.

Figure 5.3: A selection of the most common ECDL configurations. LD stands for laser diode, while CL for collimating lens.

- The frequency-selector element (e.g. an interference filter or a diffraction grating) provides typically a narrow dispersion curve, which has the role of selecting the single mode of the external cavity at which the laser emits, thus achieving coarse selection of the laser output light.

Most common ECDLs configurations

Most of the ECDL implementations are modifications of three main conceptual designs that are reported in the following.

"Etalon" ECDL By exploiting the HR rear facet of the LD, the external cavity can be easily realized by placing a reflective element in front of the diode (see Fig. 5.3a). Here the external cavity is realized by a partially reflective mirror, which is also the output coupler. In order to minimize the dependence of the laser operation from the alignment of the output coupler, a pair of lenses is typically added (one inside and one outside the cavity) in order to focus the spot on the output coupler.

In the "etalon" configuration, the frequency selection is performed by an etalon, i.e. a glass element with HR-coated treated surfaces, that acts as a short Fabry-Pérot resonator, hence transmitting only the resonant frequencies. Alternatively, an interference filter can be employed [155]. In these systems, frequency tuning can

be realized by both tilting the selecting element or changing its temperature. Both these operations cause a variation of the optical path in the selector and, thus, a corresponding changing of the resonant frequency.

Another optical element, which is actually common to all ECDL configurations, is the collimating lens[1]: typically, the light emitted by the LD is divergent and the beam is often astigmatic, so the lens is used to collimate the light in at least one direction (fast divergent direction).

The main drawbacks of this ECDL design are the temperature sensitivity of the interference filter that makes necessary to control the temperature very accurately in order to avoid drifts of the frequency emitted by the laser, and the lower output power due to the transmission losses of the filter (even at the working wavelength).

Littman-Metcalf ECDL In the Littman-Metcalf configuration [156], sketched in Fig. 5.3b, the external cavity is realized by a HR mirror and the frequency selection is operated by a reflective diffraction grating[2], which acts also as output coupler. More in detail, the optical feedback is provided by the first diffracted order, which is reflected back to the grating and then to the laser diode, thus realizing the optical path of the cavity. The laser output beam, instead, is the zero order of diffraction of the grating.

In this configuration, the laser wavelength tuning is realized by moving the mirror: with this operation, both the cavity length change and the feedback frequency selection are achieved. For wide tunability of the ECDL output frequency, the pivot point of the mirror should lie at the intersection of the mirror plane and grating plane, behind the LD rear facet plane [157].

Littrow ECDL In the Littrow configuration [158], reported in Fig. 5.3c, both the output coupler and the frequency-selector are realized by a reflective diffraction grating. In a Littrow ECDL, the grating is oriented in such a way that the first diffracted order is back-reflected to the LD as optical feedback, and the output laser is the zero order refracted light (direct reflection of the grating). Both the coarse and the fine tuning operations are made by rotating the grating, since by this rotation both the central frequency of the frequency selection and the length of the cavity are changed at the same time. The direct advantages of the Littrow

[1] It is very important that the collimating lens is anti-reflection coated for the working wavelength in order to avoid feedback and coupling problems.

[2] In general, diffraction gratings are characterized by different diffraction efficiency as a function of the incoming light polarization. Since the LD is quite sensitive to the optical feedback, it can be damaged by a feedback beam too intense. For this reason, in order to regulate the optical feedback intensity, it is preferable to tune the polarization of the light emitted by the LD that impinges on the grating by rotating the LD itself or, more finely, by placing a half waveplate between the LD and the grating.

approach are the efficiency (it introduces less losses than the Littman-Metcalf design), and the simplicity (the entire system is formed by just a few elements, so the mechanical mounting can in principle be compact, simple and robust). In order to achieve more tunability, the grating tilting has to maintain the tracking between the grating selected frequency and the external cavity resonance. In the Littrow design, the ideal pivotal point for the grating should lie (at the first order of approximation) on the LD emission plane [159, 157]. The main disadvantage of the Littrow configuration is that the laser pointing changes with the laser's frequency. This problem can be circumvented by rigidly attaching to the grating support a mirror parallel to the grating, as shown in Fig. 5.3d. In this way, the output beam angle is preserved, and the beam will be only translated. The maximum displacement is $\approx 2L\Delta\theta$, where L is the distance between the grating and the mirror and $\Delta\theta$ is the angular change of the grating-mirror system [141].

5.2 The design of the external cavity diode laser mountings

For our ECDLs, we decided to adopt the Littrow configuration since it has lower power losses compared with other solutions. Additionally, it can be realized with a quite simple and compact apparatus. We conceived two different designs for the ECDL, which are reported in Sec. 5.2.1 and Sec. 5.2.2.

5.2.1 A "traditional" Littrow design

The first version of the ECDL is based on a Littrow configuration (see Fig. 5.4).

Fig. 5.5 shows the assembly of our Littrow ECDL, the construction of which is explained in the following. The laser diode (1) is blocked by a retaining ring inside a commercial support made by anodized aluminum, named collimating tube (2), which hosts also the collimating lens (3). The lens is pre-mounted in a threaded metallic support, so the collimation of the LD output light can be performed by tightening or loosing the screw-lens inside the tube. The collimation tube is housed in a custom-made tube holder (4), and held in position with a retaining ring. A waveplate support (9) can be added to the diode mounting. It has a groove where the waveplate can be placed which is slightly tilted in order to avoid back-reflections directly into the diode laser. The diffraction grating (4) is attached[3] to its custom-made support (6), which is provided with an extended passing hole for the screw fixing it on the base (12). Such feature ensures the possibility of adjusting the

[3]The grating can be attached to its support with a drop of glue applied on its sides. In this way, the grating can be easily removed and changed without damages.

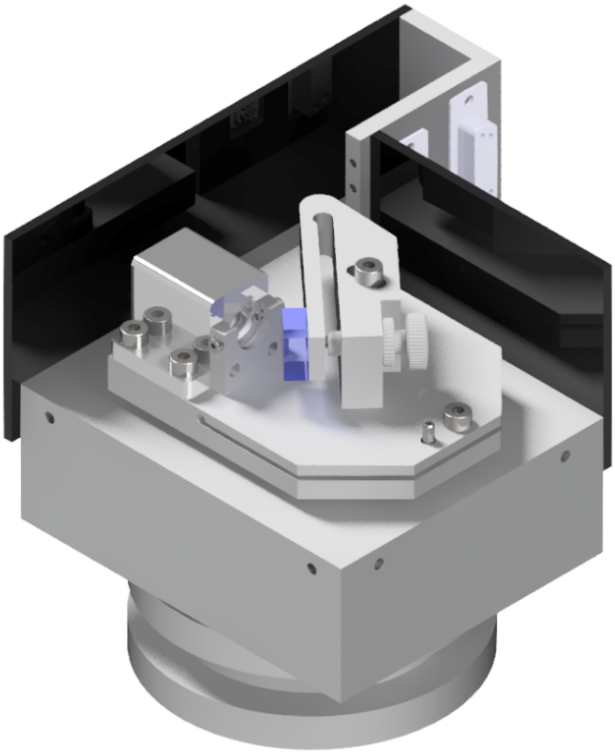

Figure 5.4: CAD assembly of our Littrow ECDL.

position of the pivotal point of the grating support in order to match it with the laser diode emission plane. A micrometer screw (8) is placed behind the grating by a coarse threading nut stuck into the support. A piezoelectric stack (7) is positioned between the grating support and the screw. The tube holder and the grating support are then fixed onto the ECDL base mounting (12), also shown in Fig. 5.6, which has a specific "fork" shape that ensures a vertical tilting of the grating. The inclination angle can be tuned with two adjusting screws: the "push" screw (10), which is a fine threaded bolt held in the ECDL base upper plate with a double-threaded copper nut, and the "pull" screw (11), which is a metric M4 screw inserted in the threaded hole of the lower plate. Additionally, a rubber O-ring is inserted between the screw washer and the base in order to implement an elastic force working against the push screw. The groove that divides the base into the two horizontal plates is 1.5 mm thick. Among the parts tightened to the base, only the grating support is placed over the portion of the base having the "fork" shape. The plates have different thicknesses, so that, during a tuning operation, only the upper plate with the grating support is tilted, whereas the lower one remains basically unchanged. To further enhancing this effect, the groove ends with a cylindrical link unbalanced towards the upper plate in order to facilitate its motion and not

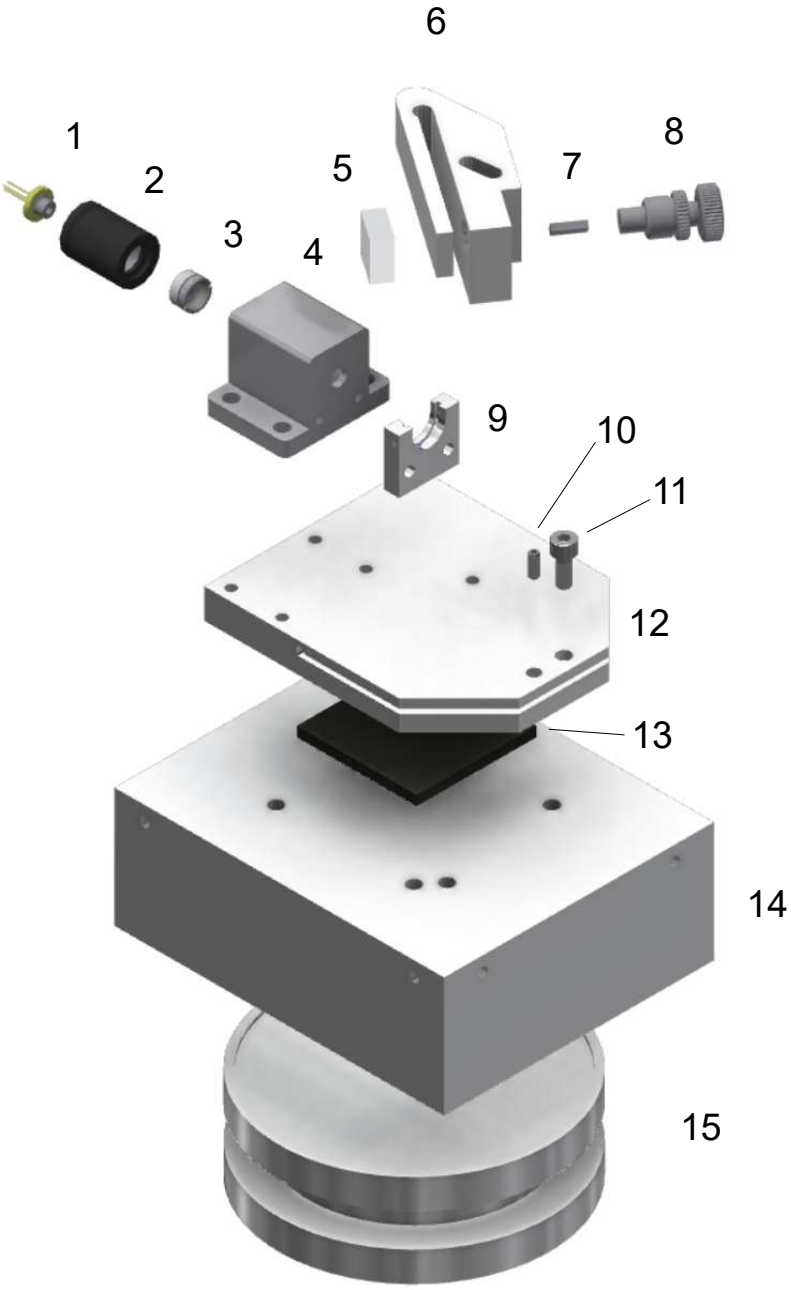

Figure 5.5: Exploded view of our Littrow ECDL. (1) Laser diode. (2) Collimating tube. (3) Collimating lens. (4) Diode tube holder. (5) Diffraction grating. (6) Diffraction grating support. (7) Piezoelectric element. (8) Micrometric screw. (9) Waveplate support (optional). (10) "Pull" screw. (11) "Push" screw. (12) ECDL base mount. (13) Peltier element. (14) Heat-sink. (15) ECDL support. Elements number (4), (6), (9), (12), (14) and (15) are custom made.

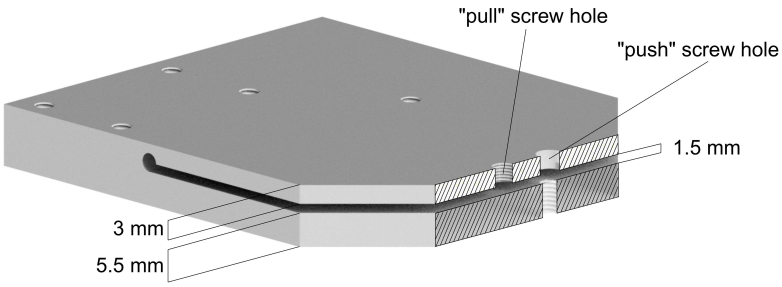

Figure 5.6: Section of the ECDL base mounting.

the inclination of the lower plate. To stabilize the whole system temperature, a Peltier element (13) is positioned between the base and a large aluminum element that plays the role of heat-sink (14). A thermal conductive grease can be spread on both sides of the Peltier to increase the thermal conduction efficiency. The screws connecting the base to the heat-sink must be made in some thermal isolating material, such as teflon or nylon, thus thermally decoupling the two pieces and allowing the Peltier to properly work. Finally, an ECDL support (15) is placed under the heat-sink with some rubber or sorbothane in between, thus reducing the coupling of mechanical vibrations from the table.

5.2.2 A modified Littrow design

The ideal implementation of the Littrow design, i.e. with the pivotal point of the grating on the diode emission plane, is not simple to obtain with generic mounts. Moreover, since the grating is typically placed at approximately 45° with respect to the laser diode output beam, the distance between the optimal pivotal point and the diode is approximately equal to the external cavity length. Therefore, finding the optimal pivotal point is particularly critical when an external cavity longer than a few centimeters is realized. In addition, in the Littrow configuration, the element that is moved (grating) is both the frequency selector and the output coupler of the laser: if the grating is not precisely tilted around the optimal pivotal point, mechanical hysteresis can affect the long-term operation of the laser, causing the need of a continuous maintenance from the user. In a second, modified version of the Littrow design, we aim at solving these problems and simplifying the construction of a stable laser.

The mounting design

The mounting presents a number of solutions common to the “traditional” ECDL mount (see Fig. 5.7).

The ECDL base (13) is the common ground onto which the diode mounting (10)

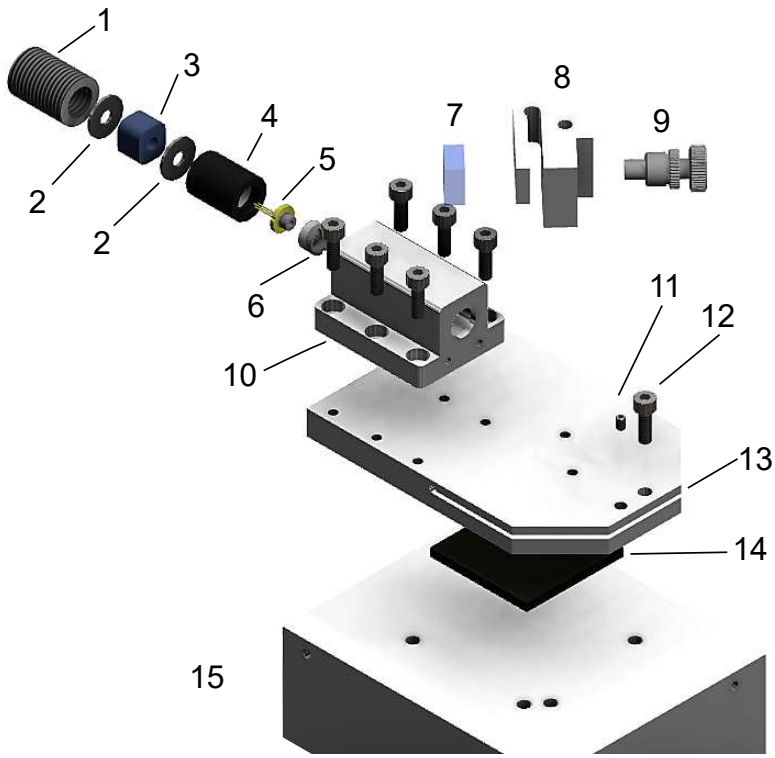

Figure 5.7: Exploded view of the modified Littrow ECDL. (1) Threaded insert. (2) Washer. (3) Piezoelectric element. (4) Collimating tube. (5) Laser diode. (6) Collimating lens. (7) Diffraction grating. (8) Diffraction grating support. (9) Micrometric screw. (10) Tube holder. (11) "Pull" screw. (12) "Push" screw. (13) ECDL base mounting. (14) Peltier element. (15) Heat-sink.

and the diffraction grating support (8) are positioned. Its inclination, thus the grating tilting, can be tuned with the “push” (12) and “pull” (11) screws as in the other version. The system temperature is still stabilized by a Peltier element (14), placed between the base and a heat-sink (15). The diffraction grating (7) is attached to its small support, which has a micrometer screw (9) to adjust the grating frequency selection. The main point of difference is the absence of the piezoelectric element (3) behind the grating: it is instead shifted inside the tube holder (10). As shown in the section view reported in Fig. 5.8, the tube holder now contains the collimating tube (4), with the laser diode (5) and the collimating lens (6), and a circular hollow piezo transducer (3) that works against the restoring force offered by a rubber O-ring (4.1). The piezo is properly positioned and supported by two custom metallic washers (2). Such a stack is finally compressed in the ECDL mounting by a threaded insert (1).

In general, all the custom-made elements of both the Littrow and the modified

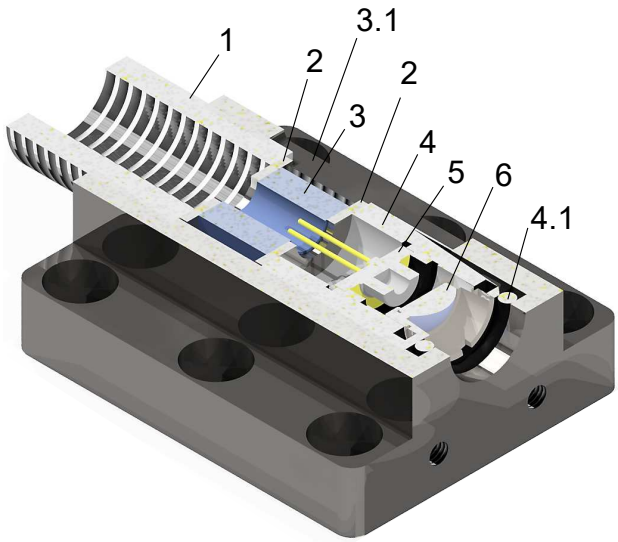

Figure 5.8: A section view of the second ECDL version diode mounting and its contents. (1) Retaining ring. (2) Washer. (3) Piezoelectric element. (3.1) Groove for piezo wires. (4) Collimating tube. (4.1) Rubber O-ring. (5) Laser diode. (6) Collimating lens.

Littrow mounts are made in common aluminum, for example an alloy of the series 6000; with the exceptions of the adjustable elements (grating supports and ECDL bases) that are made in a aluminum alloy of the series 7000, characterized by a higher elasticity. The others are commercial elements, as can be seen in Tab. 5.1 with reference to the element position in Fig. 5.5 and Fig. 5.7.

Item	Fig. 5.5	Fig. 5.7	Note
Collimation lens	3	6	Thorlabs C230TMD-B
Collimation tube	2	4	Thorlabs LT230220P-B
Cylindrical piezo element	/	3	Piezomechanik HPSt 500/10-5/7
Diffraction grating	5	7	Thorlabs GH13-18V
Fine tuning screw	10	11	Thorlabs F3SS15 and N250L3P
Laser diode	1	5	See Tab. 5.2
Micrometer screw	8	9	Eksma Optics 870-0080-D2
Peltier element	13	14	Adaptive ET-161-12-10-E
Stack piezo element	7	/	Piezomechanik PSt 150/2x3/7

Table 5.1: List of the commercial components used in our ECDLs. The lens and grating codes are just indicative, since the coating and the other features of these elements depend on the laser wavelength.

The main difference between the two ECDL designs is that in the modified Littrow ECDL the frequency fine tuning is operated by the piezoelectric element moving the collimating tube, i.e. the laser diode itself. The net advantage of this technique is that the frequency selection performed by the grating and tuning of the external cavity. In this way, the design of the mount does not have to be modified depending on the length of the cavity, and there is no need of opposing to the piezoelectric the elastic force originating from bending metallic parts, which could result in long-term hysteresis. The main drawback of the modified Littrow ECDL is that a better stability is reached at the expense of a reduced tunability, since without moving the grating the tunability range is given by the free spectral range of the external cavity. However, the free spectral range of a 2 cm-long cavity is 7.5 GHz, a value that is much larger than the linewidth of the transitions that we will excite and than the range of tuning that we will use in the experiments; hence, the reduced tunability will not represent a limitation. The design of the modified Littrow ECDL is currently patent pending.

Design characterization

To test the potentiality of the modified Littrow design, we have realized a first laser with an anti-reflection coated 780 nm diode (Eagleyard Photonics, EYP-RWE-0790-04000-0750-SOT01-0000) and a cavity length of 30 mm (FSR 5 GHz). Then, we have moved the grating and placed it on a mirror mount out of the base element, thus extending the cavity length to 120 mm (FSR 1.2 GHz). We will refer to this last ECDL as the "long" one, and the first one as the "short" one. We then compared the behavior of both the two modified Littrow ECDLs. The diode current is supplied by a commercial laser controller (Thorlabs LDC8002) and we used a reflective holographic grating having 1800 grooves/mm (Thorlabs GH13-18V). It must be noted that in the long ECDL the Peltier element stabilizes only the temperature of the laser diode, so the external cavity is free to fluctuate according to the lab temperature changes. The frequency drift for the long ECDL were estimated to be about 150 MHz/min from measurements of laser frequency made by a wavemeter (High Finesse WS-7); while the short ECDL, stabilized in temperature and enclosed in a PVC box, showed frequency drifts of about 20 MHz/min.

By acting on the ECDL temperature, the emission spectrum of the laser diode and the resonant frequencies of the external cavity change, thus causing frequency jumps between different laser emission modes, see Fig. 5.9. The frequency hops, which occur at multiples of the free spectral range, are estimated to be 4.8 GHz (short ECDL) and 1.2 GHz (long ECDL), in good match with the FSRs expected values. Moreover, Fig. 5.9 shows that the long ECDL is more sensitive to temperature changes: this is a direct consequence of the cavity modes that are more finely spaced than short ECDL ones. The frequency output of the ECDLs can be tuned by changing the temperature with a rate of -17.9 GHz/°C in a maximum mode-hop

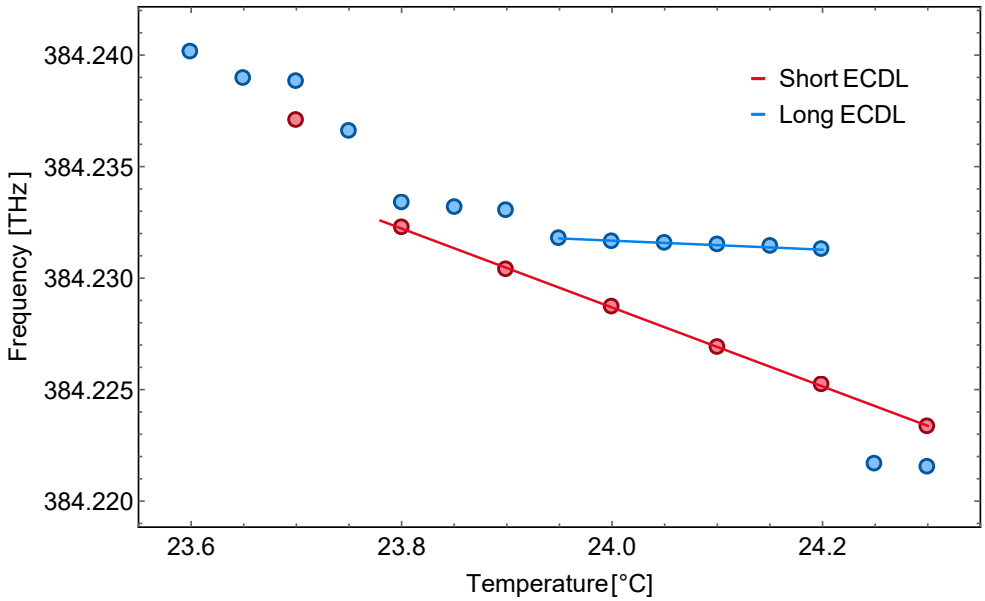

Figure 5.9: Frequency tuning of the short (red) and long (blue) modified Littrow ECDLs as a function of the base temperature. The lines are linear fits of the frequency variations within two mode hops: the frequency of the radiation emitted by the short ECDL (red) has a dependence on the temperature of -17.9 GHz/°C, while in the long ECDL (blue) the frequency varies as the temperature changes with a rate of -2 GHz/°C. The higher instability of the long ECDL is due to the fact that its external cavity is not actively controlled in temperature. Therefore, the cavity length varies after temperature drifts present in the lab, the thermal stability of which is 0.5°C.

free range of about 0.5°C in the short ECDL case, and with a rate of -2 GHz/°C in a smaller range of 0.3°C for the long ECDL.

The difference between the two rates is due to the fact that, in the long ECDL prototype, the cavity length does not homogeneously vary after temperature changes, since its grating support is external to the ECDL mount. Considering a thermal expansion only on half the cavity (the one with the Peltier element), the frequency variation of the long ECDL is $\Delta\nu_{\text{long}} = \alpha c \Delta T / 4L_{\text{long}}$, where α is the linear thermal expansion coefficient and c is the speed of light. Instead, the frequency variation of the short ECDL is $\Delta\nu_{\text{short}} = \alpha c \Delta T / 2L_{\text{short}}$. From the ratio $\Delta\nu_{\text{short}}/\Delta\nu_{\text{long}}$, the tunability range for the short ECDL can be evaluated as a function of $\Delta\nu_{\text{long}}$ and the cavities length ratio. The result is -17.3 GHz/°C, which is in good accordance with the measured value.

The emission frequency can also be manipulated by changing the current fed to the laser diode, as shown in Fig. 5.10. This can be considered a finer method

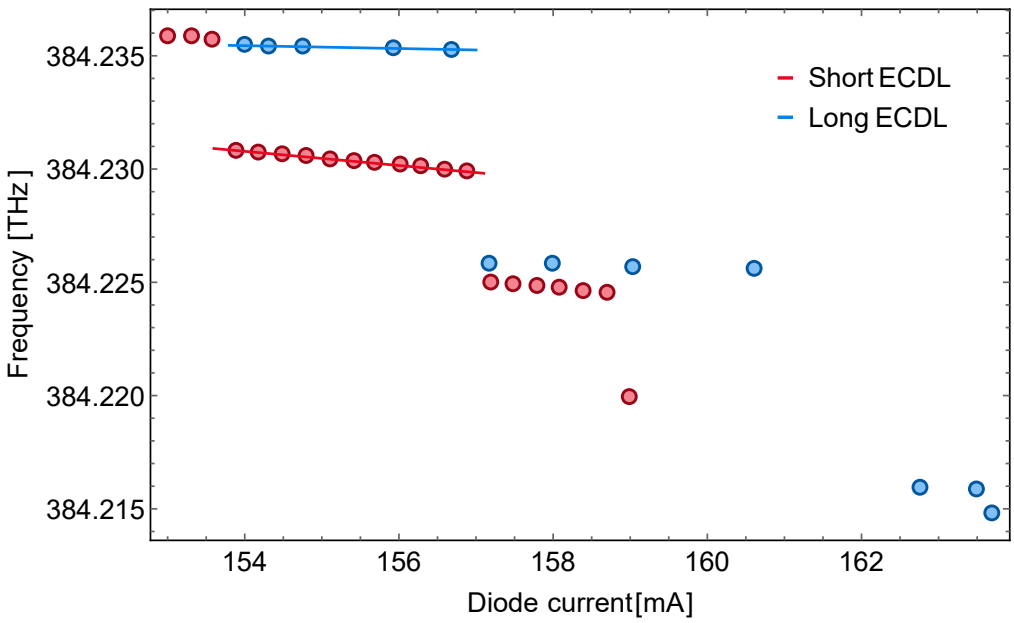

Figure 5.10: Frequency tuning of the short (red) and long (blue) ECDL versions as a function of the laser diode current. The lines are linear fits of the frequency variations within two mode hops. The frequency can be tuned by changing the diode current with a rate of -274 MHz/mA for the short ECDL and -63 MHz/mA for the long ECDL.

to tune the frequency laser than changing the cavity temperature: in fact, in the mode-hop free range, the frequency changes as -274 MHz/mA (short ECDL) and -63 MHz/mA (long ECDL). The ratio between the slopes is proportional to the inverse of the ratio between the cavity lengths: this is a signature that thermal effects are likely to be the main responsible for the frequency dependence on the diode's current.

Another method to change the frequency emission of the ECDL is to modify the external cavity length by using a piezoelectric transducer. In Fig. 5.11 the results are reported. In both cases, a mode-hop free tuning frequency range wide more than twice the FSR was observed: 10.7 GHz (short ECDL) and 3.6 GHz (long ECDL). In the latter case, we were limited by the maximum voltage applicable to the piezo, so we were not able to observe the mode hop.

From the linear fit of the data in Fig. 5.11, the frequency dependence on the voltage applied to the piezo is about 120 MHz for the short ECDL and about 29 MHz for the long ECDL. The different slopes are different even if the piezo displacement is the same in both ECDLs because the external cavity lengths are different and $dL/L \sim d\nu/\nu$. Therefore the ratio of the slopes corresponds to ratio between the FSR and the cavity length, a common factor in both ECDLs.

We also estimated the spectral linewidth of both the short and long modified

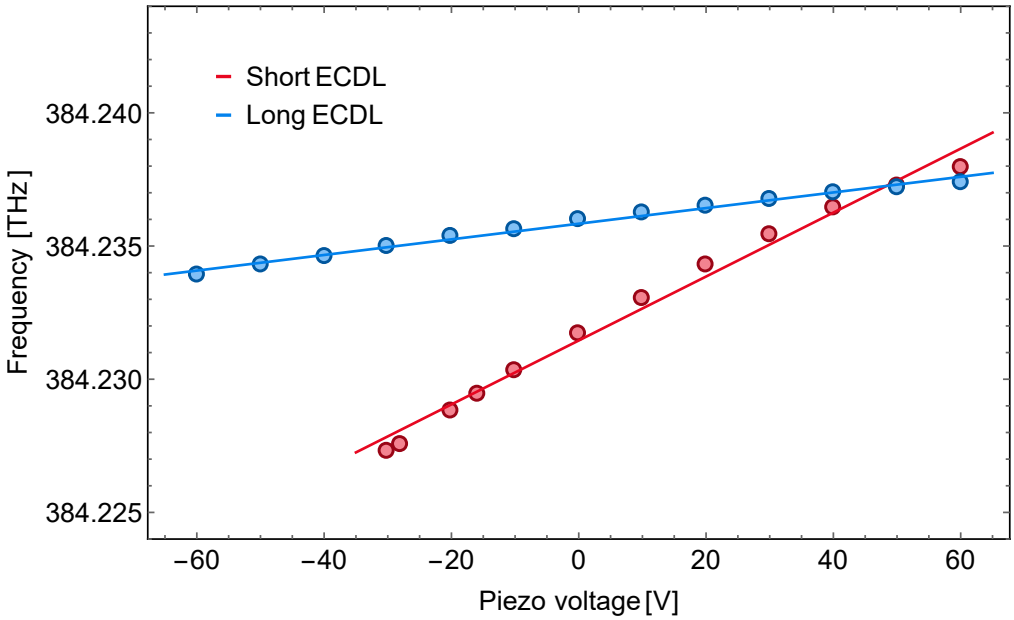

Figure 5.11: Frequency tuning of the short (red) and long (blue) ECDL versions as a function of the piezo voltage. The red and blue solid lines are a linear fit to the data.

Littrow ECDLs via a heterodyne beat measurement between the modified Littrow ECDLs and a standard Littrow ECDL. Each laser is independently locked to the $5^2S_{1/2}\,(F=2) \leftrightarrow 5^2P_{3/2}\,(F'=2{,}3)$ transition in D2 line ^{87}Rb through a saturated absorption spectroscopy scheme. The correction applied to the PZTs in order to lock the lasers is characterized by a maximum frequency of about 15 Hz, therefore only small fluctuations due to slow pressure noise and temperature drifts are corrected. At frequencies higher than 15 Hz, the laser frequency noise is unaltered, so the linewidth remains affected by the intrinsic, thermal and mechanical high frequency noises. The spectral characteristics of the laser emission are shown in Fig. 5.12 for both short and long modified Littrow ECDLs. From the beat signal, information about the relative frequency noise of the two independent lasers can be extrapolated [160]. As anticipated, uncompensated frequency noise affects the beat spectrum and leads to a random distribution well described by a gaussian function peaked in the central beat frequency ν_0. By fitting the peak of the beats with a lorentzian function, the combined linewidths for both the ECDLs are obtained: 540 kHz (short) and 670 kHz (long), which correspond to a single laser linewidth of about 270 kHz (short) and 335 kHz (long). A similar value is obtained if the linewidth is estimated by looking at the full width at -3 dB suppression; with this method we measure 450 kHz (short) and 700 kHz (long), corresponding to an individual frequency linewidth of about 225 kHz and 350 kHz. In principle, the linewidth of the long ECDL should be smaller than the short ECDL one, since the

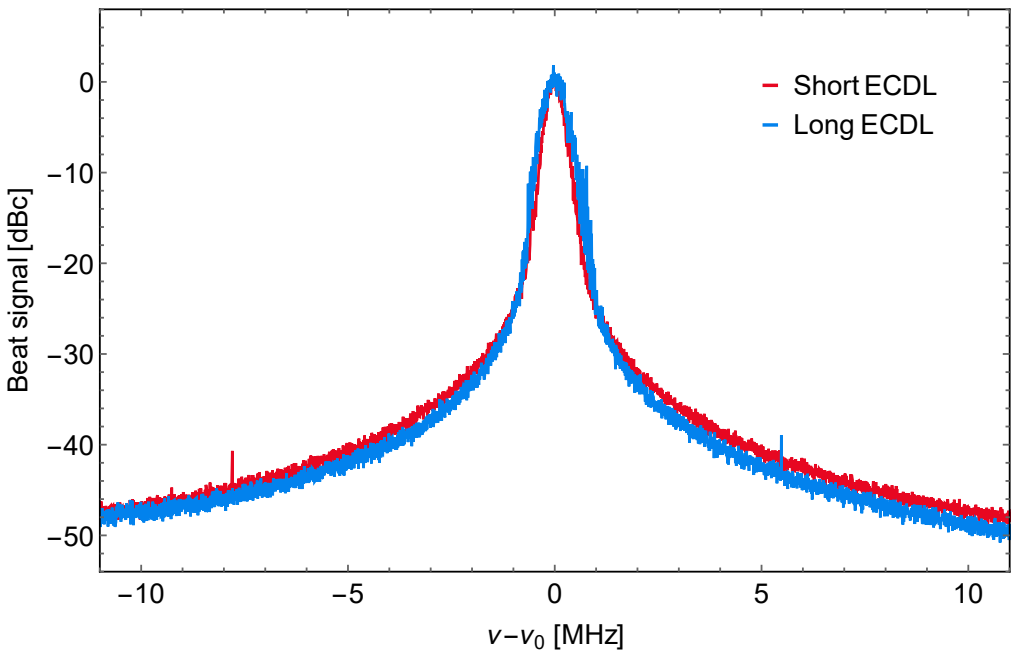

Figure 5.12: In red/blue, the heterodyne beat spectrum between the short/long ECDL mounting and an ECDL configured in a ordinary Littrow scheme. The photodiode beat signals, peaked at frequency ν_0, are recorded with a spectrum analyzer (5 kHz resolution bandwidth, 100 sets average for a total sweep duration of 400 ms.)

longer external cavity ensures narrower resonant modes. However, the linewidth reduction in the long ECDL is not visible: we attribute the slightly larger width of the long ECDL to the mechanical and acoustic noises which affect the long version more than the short one, since in the long ECDL the grating support is not mechanically decoupled from the laser mount.

In conclusion, the results of the characterization of the modified Littrow ECDL prove that it is a valid design for an ECDL, with a relatively simple construction procedure and a good stability, comparable with other optimized Littrow ECDL designs. Moreover, this mounting can be particularly suitable for long external cavities ECDLs, which can be further optimized by compensating for the high frequency noises with a piezo having a wider bandwidth, with an additional feedback loop on the laser diode current modulation or with a infra-cavity electro-optic modulator.

5.3 Laser production and setup

Several lasers are needed to control the Barium ions (see Fig. 5.1). We built an ECDL for generating light of almost all the frequencies that are listed in Tab. 5.2. The table reports also the diodes that were used for each frequency.

LD λ	Model	Aim
413 nm	Nichia NDVA216T	Neutral Barium photoionization
455 nm	Nichia NDBA116T	Shelving laser
650 nm	Exalos EXS0650-006-10-0B00030	Repumper for the D1 transition
780 nm	EYP-RWE-0790-04000-0750-SOT01	Reference laser
903 nm	Innolume GC-920-90-TO-200-B	Seed for the EO trap laser
1228 nm	Innolume GC-1220-110-TO-200-B	Seed for the deshelving laser

Table 5.2: Laser diodes for Ba^+ wavelengths.

In order to make it possible in the future to re-arrange the position of the laser sources and their optical circuits, we decided to build the entire laser system on a number of breadboards disposed on an optical table. These independent breadboards are currently laying on top of the optical table[4], but can in principle be placed on top of pillars in order to make more space on the optical table for other optical circuits. We decided to place on each breadboard the lasers related to the same physical mechanism, e.g. one breadboard hosts the D1 cooling laser and its repumper, one breadboard hosts the D2 cooling laser and its repumper, etc.

A typical structure of an optical circuit for the control of a laser beam generated with an ECDL is sketched in Fig. 5.13. The first operation made on the light is a beam reshaping (if needed), e.g. by using a pair of anamorphic prisms (AP). After that, an optical isolator (IO) is placed in order to protect the laser for possible optical feedback that could affect its operation, thus avoiding optical feedback issues. Then, the beam is divided into three different paths by exploiting the two beams reflected by the front and the rear facets of a sampler. These two reflections are separated by using a D-shaped mirror. The weaker beam (originated from the sampler rear facet) is injected into a fiber and sent to the wavemeter (High Finesse WS-7, absolute accuracy of 60 MHz), which needs only a few μW of light for its operation. The strongest reflection of the sampler is used to lock the laser frequency to an external reference. For this reason, an electro-optical modulator (EOM) is used to create frequency sidebands on the beam before injecting it into a polarization

[4]Small portions of sorbothane sheet are placed in between the metal surfaces in order to ensure an extra-damping of vibrations.

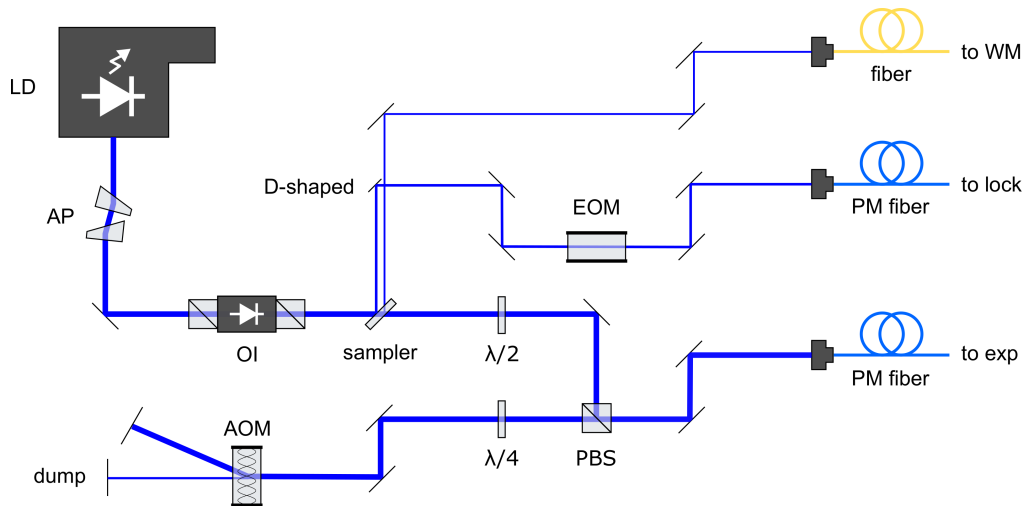

Figure 5.13: General scheme of a laser optical circuit that shows the separation of the laser beam emitted from the ECDL into three different branches: the first directed to the wavemeter, the second used for locking the laser emission and the third sent to the experiment.

maintaining optical fiber (PM fiber) and sending to the locking board. The beam transmitted by the sampler, which has most of the initial power, is frequency shifted by an acoustic-optic modulator (AOM) either in a single-pass or in a double-pass configuration (the latter case is shown in Fig. 5.13), and then sent to the experiment table through a PM fiber. The AOM is used to both finely tune the frequency of the laser to resonance, and to rapidly regulate the laser intensity after the fiber.

This arrangement of optical elements is, with little modifications, used for most of the optical circuits. The only exceptions are the trapping and the deshelving lasers, since these sources are created by frequency doubling infrared lasers (as described in the two following sections).

5.3.1 The trapping laser

The trapping laser will be used in combination with a static electric quadrupole to create the electro-optical (EO) trap for Ba^+ ions. Since our purpose is to continuously cool the ions while they are trapped in the EO potential, the trapping laser should shift the energy levels of the cooling transition ($6s^1\,{}^2S_{1/2} \leftrightarrow 6p^1\,{}^2P_{1/2}$) by the same amount of energy. In order to obtain a strongly confining optical potential and ensure a long lifetime of the ions in the EO trap, the trap depth, which is proportional to the intensity of the trapping radiation, should be as large as possible. Unfortunately, there are no powerful laser sources at 451.7 nm; therefore, a possible solution is performing frequency doubling from an intense laser at 903 nm.

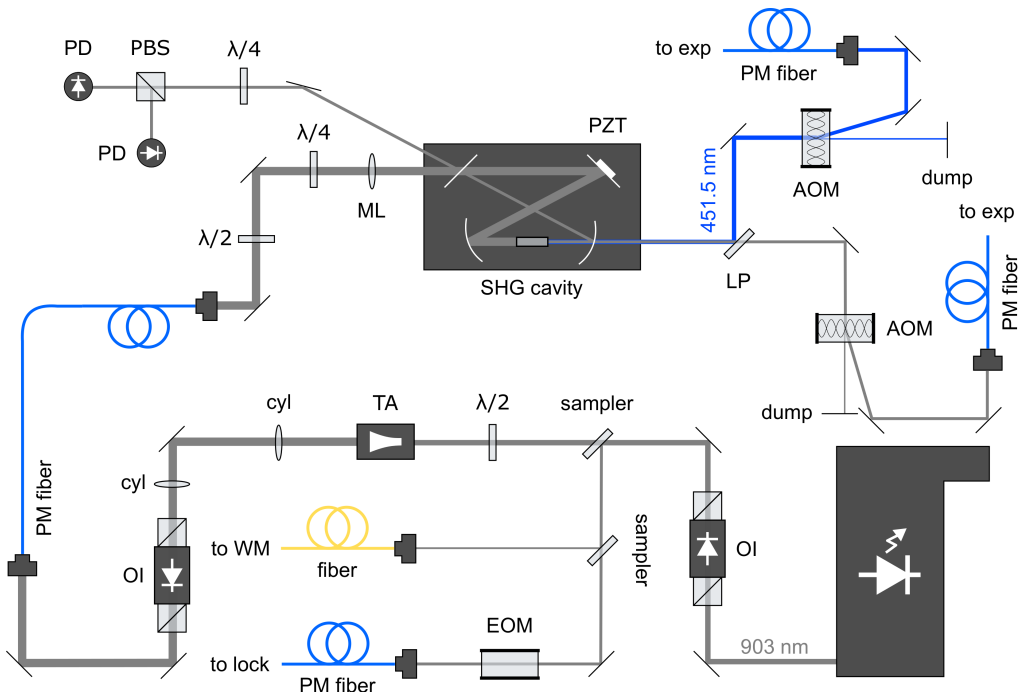

Figure 5.14: Sketch of the optical circuit for producing the 451.7 nm laser light. The scheme is divided into two stages connected by a polarization maintaining fiber (PM fiber): the production and amplification block and the duplication block.

The source laser does not have only to be powerful, it must also be sufficiently narrow in frequency in order to ensure a good coupling to the resonant modes of the bow-tie cavity realizing the optical potential of the EO trap. In order to enhance the laser power, a tapered amplifier (TA) has to be implemented. However, efficient TAs working at the needed wavelength do not exist, so our solution for circumventing this inconvenient is to build an ECDL at 903 nm, amplify it with a tapered amplifier and then duplicate it to 451.7 nm through a second harmonic generation process. In particular, since the ECDL must ensure a narrow linewidth, a relatively long external cavity is used.

The overall optical circuit for producing the 451.7 nm light is depicted in Fig. 5.14. After the long ECDL, an optical isolator (OI) is placed to protect the source from undesired optical feedback. By using two samplers, the laser is divided into three branches: the weaker beam is sent to the wavemeter, the second is used to lock the ECDL, whereas the most intense one is injected in the tapered amplifier (TA). After the amplification, the beam is reshaped by a telescope made of two cylindrical lenses, then a second optical isolator is positioned to avoid back reflections towards the TA. The stage of production and amplification is decoupled from the duplication one by using a polarization maintaining fiber (PM fiber). At this point,

the high power beam at 903 nm is injected in the second harmonic generation cavity (SHG cavity), where a portion of the light is consumed to produce the laser radiation at 451.7 nm. The part of the infrared light back-reflected by the cavity is recovered and exploited to lock the SHG cavity via the Hansch-Couillaud locking method [161]; while the remaining portion of light at 903 nm that passes through the SHG cavity is sent to an acousto-optical modulator (AOM) and then to the experiment via a PF fiber. It will be used to lock the ion bow-tie cavity. The produced light at 451.7 nm is sent to the ion cavity through a PM fiber as well.

The following two paragraphs will describe the special ECDL used for the 903 nm source, along with the design of the tapered amplifier and the second harmonic generation cavity.

Long external cavity diode laser

The mounting adopted for the external cavity diode laser at 903 nm is the modified Littrow design, since this is particularly suited for "long" ECDLs. A few modifications were realized in order to further improve the stability of the emitted radiation.

The laser prototype is shown in Fig. 5.15. First, we changed the design and material (from aluminum to brass) of the tube holder in order to create a bulkier and heavier case that can be better absorb the mechanical vibrations originating from the piezo transducer placed inside. Second, we modified the base design in order to make the whole mounting more stable against temperature fluctuations. The Peltier element was placed under the brass diode mounting to stabilize the LD temperature, while the grating was placed on a new element, the cavity support, made in invar. Invar is an iron alloy characterized by a very low thermal expansion coefficient: 1.2 μm/m K against a typical value of 12 μm/m K for steel. The lengths of the cavity support and of the portion of the ECDL base under the tube holder are in the same ratio as the thermal expansion coefficients of invar and aluminum. This choice ensures a passive thermal stability of the overall cavity, since the expansion of the two materials are opposite in sign and equal in amplitude. The cavity base is placed in a specific groove of the ECDL base, here working also as heat-sink, and held in position by two screws (see Fig. 5.15). An electro-optic modulator can be placed inside the laser cavity by screwing it on the cavity support. This option can be used in case a fast correction of the laser frequency is needed to reduce the linewidth of the emitted light.

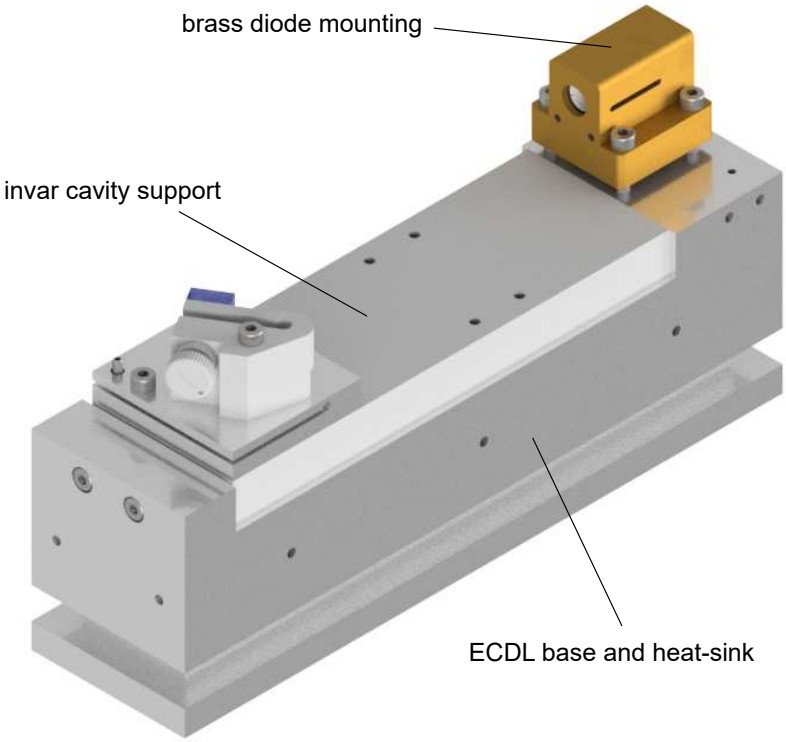

Figure 5.15: CAD assembly of the "long" Littrow ECDL mounting. The tube holder is made in brass, and the ECDL base was modified in order to host an invar support that reduces the effects of thermal expansion.

Tapered amplifier mounting

A tapered amplifier is a semiconductor device used to enhance the power of a seed laser with a process of amplification based on stimulated emission. Therefore, the output light has the characteristics of the seed, e.g. its frequency and linewidth. In a TA a single-mode ridge waveguide is integrated with a tapered gain structure. The seed laser enters the anti-reflection coated front facet of the waveguide, then propagates through it until the tapered region is reached. There, the light diffracts and completely fills the gain region, in which the population inversion is ensured by an electric current signal. Tapered amplifiers are an efficient solution to enhance the power of a laser without altering its features; nevertheless, TAs have also a few drawbacks. For example, they exist only in a small range of wavelengths (red region of the visible light and near infrared), and they are quite delicate elements that can be damaged by even small optical feedback.

Tapered amplifier mountings are in general designed to support the small chip, feed it with high current (typically a few Amps), and stabilize its temperature. Usually they also include high numerical aperture lenses in order to properly inject

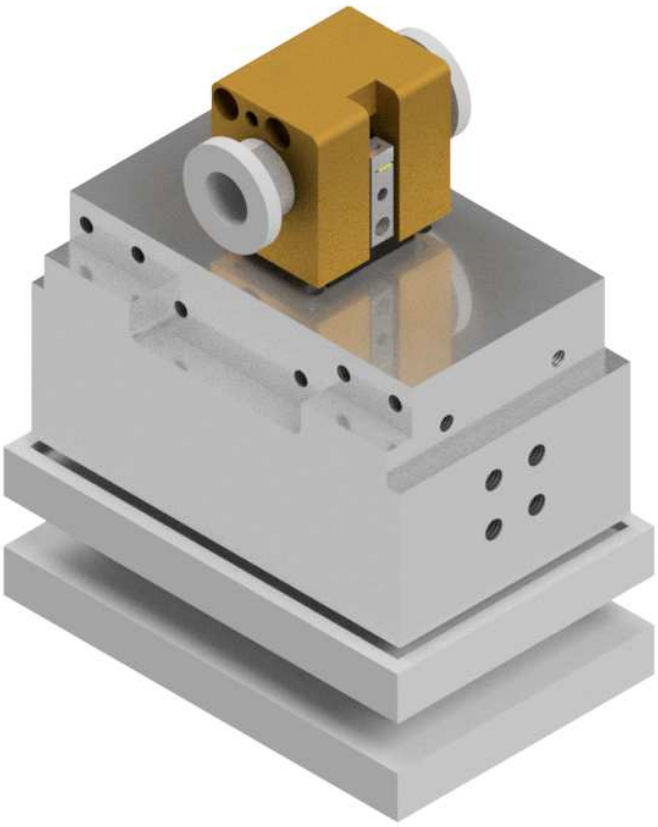

Figure 5.16: CAD assembly of the tapered amplifier mounting.

the seed laser and collimate the output light. We designed a tapered amplifier mount by modifying the design reported in Ref. [162].

Fig. 5.16 shows the view of the complete assembly, while Fig. 5.17 shows its exploded view, to which we now refer for the description of the design. We considered only TA chips characterized by a C-mount package. The chip (element 4 in Fig. 5.17) (Eagleyard Photonics EYP-TPA-0915-01500-3006-CMT03-0000) is enclosed in a case formed by two different parts: the input (5) and output (3) supports. The chip is tightly fixed to the input support by a M2 screw, so that a good thermal and electric contact is granted. The output support is aligned and fixed to the input one by a pair of dowels and three screws. It is extremely important that the two supports are well aligned to each other, since they host the input and output collimating lenses (1), which should be aligned as well as possible to the facets of the TA (width of the input aperture $3\,\mu$m, width of the output aperture $190\,\mu$m). The lenses (both Thorlabs C340TMD-B, f = 4.03 mm, NA = 0.64), which are already provided with a threaded metallic case, are screwed onto the custom lens tubes (2). The tubes are then inserted in the input and output supports. These

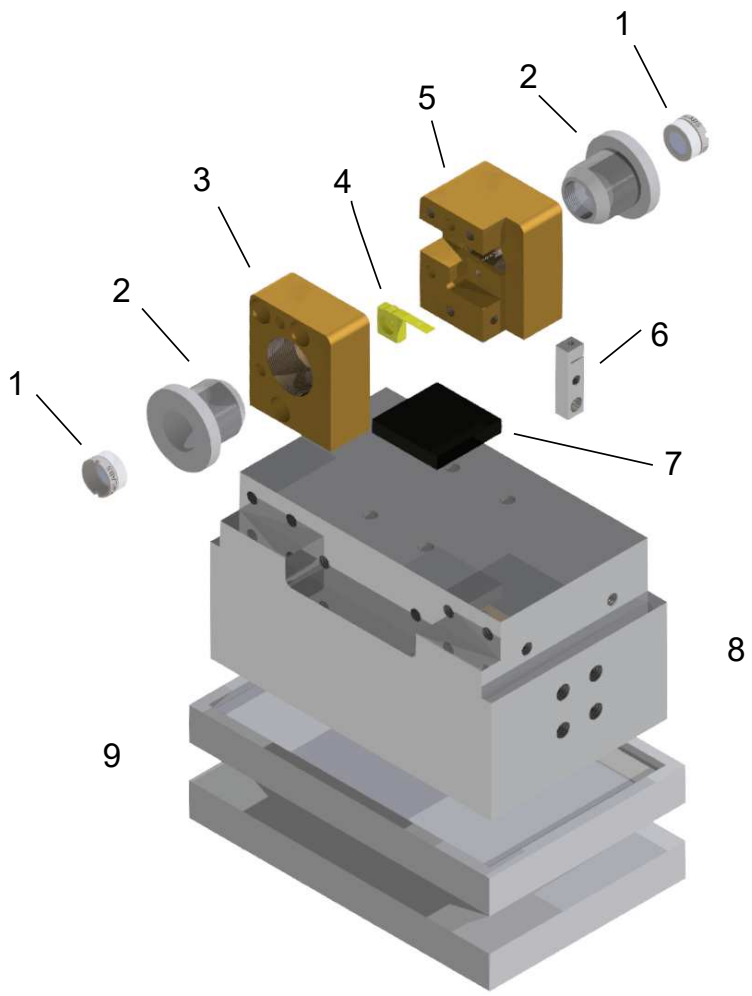

Figure 5.17: Exploded view of the tapered amplifier mounting. (1) Collimation lens. (2) Lens adjusting tube. (3) Output support. (4) Tapered amplifier chip. (5) Input support. (6) Clamper. (7) Peltier element. (8) Heat-sink. (9) Mounting base.

lens tubes are externally threaded with a small pitch (0.25 mm), in order to ensure a fine adjustment of the distance between the lens and the TA facet to be finely adjusted. The lens tubes and the input/output supports are made in different materials (aluminum series 6000 and brass, respectively) in order to avoid problems of friction with the fine thread. All the other custom-made parts of the mount are made in aluminum series 6000. The temperature of the system is measured by an thermistor (NTC 10 kΩ at 25 °C), housed in the input support near the TA chip slot, and regulated by a Peltier element (Adaptive ET-071-10-13-RS), which is driven by a commercial temperature controller (Thorlabs TED8040). The Peltier

is placed between the two brass supports and a heat-sink (8). The heat-sink has four passing holes, which can be connected with rubber tubes to realize a water cooling circuit, in case the heat-sink is not sufficient to dissipate the heat generated by the Peltier element. Finally, the assembly is placed on a simple aluminum base (9) equipped with a sorbothane bearing to damp the mechanical vibrations coming from the table. From the electrical point of view, the TA chip is connected to ground through contact with the input support, while the supplying current is provided by a commercial controller (Thorlabs LDC8040) and fed to the chip via a small clamper (6) attached to the TA cathode. The clamper must be electrically isolated from the rest of the mounting, so it is fixed to the input support with a teflon screw.

Second harmonic generation cavity

Second harmonic generation (SHG) is a nonlinear phenomenon in which a crystal with a non-zero value of the second-order nonlinear susceptibility $\chi^{(2)}$ is used to generate a photon at frequency 2ν after the absorption of two photons of frequency ν from a pumping laser beam. Being a nonlinear phenomenon, the efficiency of the process is proportional to the intensity of the pump laser [141]. For a pulsed laser, the peak intensity is typical sufficient for obtaining an efficient SHG with a single passage of the pump beam in the crystal. For a continuous-wave (CW) pump laser, however, the intensity is typically not sufficient to convert a macroscopic fraction of light in the second harmonic. For this reason, SHG of a CW laser is typically realized in a cavity, which enhances the intensity of light passing by the crystal.

For the generation of blue light, we decided to adopt as SHG medium a periodically poled Lithium Niobate bulk crystal (ppMgO:$LiNbO_3$), doped with magnesium oxide to prevent photorefractive damages and reduce the absorption [163]. This crystal in fact has already been used for producing green and blue light with a good efficiency, even in single-pass configuration [164]. The crystal we used is 25 mm long (width of 2 mm and height of 0.3 mm), therefore the beam waist of the infrared laser must be about 25 μm (or focusing parameter of $\xi = 2.65$) in order to maximize the conversion efficiency (see Appendix B). The front and rear facets of the crystal were treated with an anti-reflection coating which guarantees intensity reflection coefficients lower than 0.5% for both 451.7 nm and 903 nm wavelengths.

Supposing an ideal mismatch condition and with the assumptions that the beam waist is positioned right in the center of the crystal and that the medium absorption at those frequencies can be neglected, we calculate a single-pass conversion efficiency of about 1% (see Appendix B for a detailed calculation).

The enhancement cavity was designed on the basis of these crystal features. The bow-tie cavity is composed by two curved mirrors (curvature radius of 200 mm) placed symmetrically before and after the crystal and other two plane mirrors. The mutual distances between the mirrors are adjusted in order to achieve a beam waist

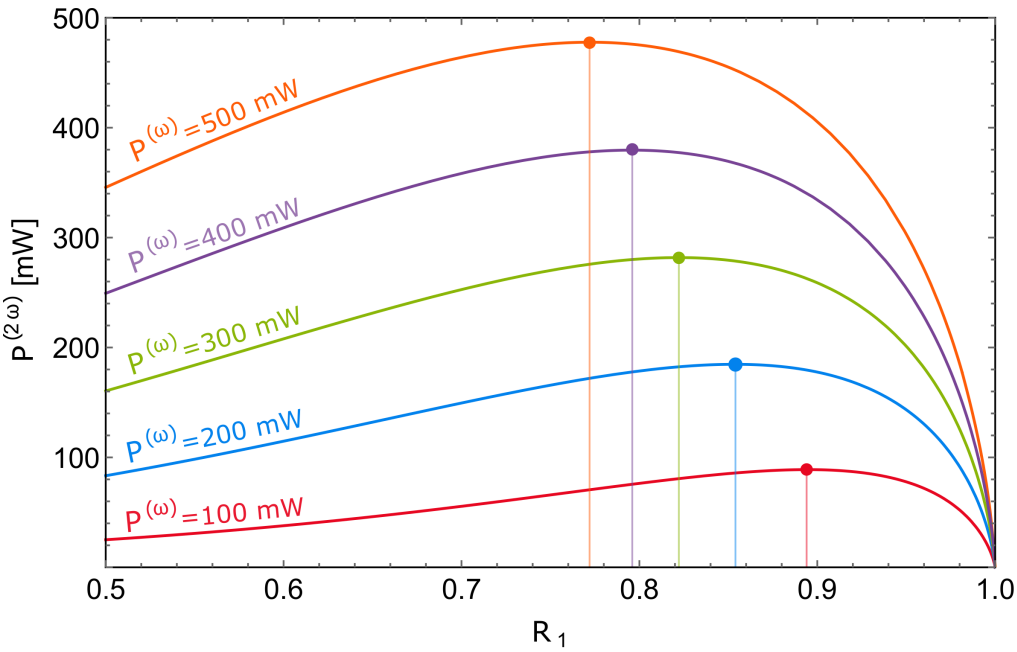

Figure 5.18: A set of second harmonic power evolution plotted for a set of different fundamental powers as a function of the intensity transmission coefficient of the input coupler R_1.

of about 25 μm at the center of the crystal. The ideal intensity reflection coefficient $R_1 = 1 - T_1$ of the input coupler depends on the fundamental power. If we suppose that the intensity reflection coefficients for three mirrors of the cavity are equal to 99.9 % at 903 nm, we can calculate the power of the second harmonic as a function of the reflectivity of the fourth mirror (the input coupler) and of the input power of the pump laser $P^{(\omega)}$ (see Fig. 5.18). For example, by injecting in the cavity 300 mW of pumping light, we expect to obtain about 280 mW of blue light if the input coupler has $R_1 = 0.822$.

The dependence of the second harmonic power on the normalized waist position μ is reported in Fig. 5.19 for the same set of pumping light powers. For the data of both Figs. 5.18 and 5.19, we suppose an ideal value of the mismatch and focusing parameters, and the absence of absorption (see Appendix B). The graphs in Fig. 5.19 are in accordance with the results of Ref. [165], in which the function h – proportional to $P^{(2\omega)}$ (see Appendix B) – is plotted as a function of μ for ideal values of the other parameters.

In Fig. 5.20, the second harmonic power is plotted as a function of ξ in the same ideal conditions.

A CAD assembly of our SHG cavity is shown in Fig. 5.21. The four mounts of the cavity mirrors are fixed to a metallic bulky structure that integrates also a

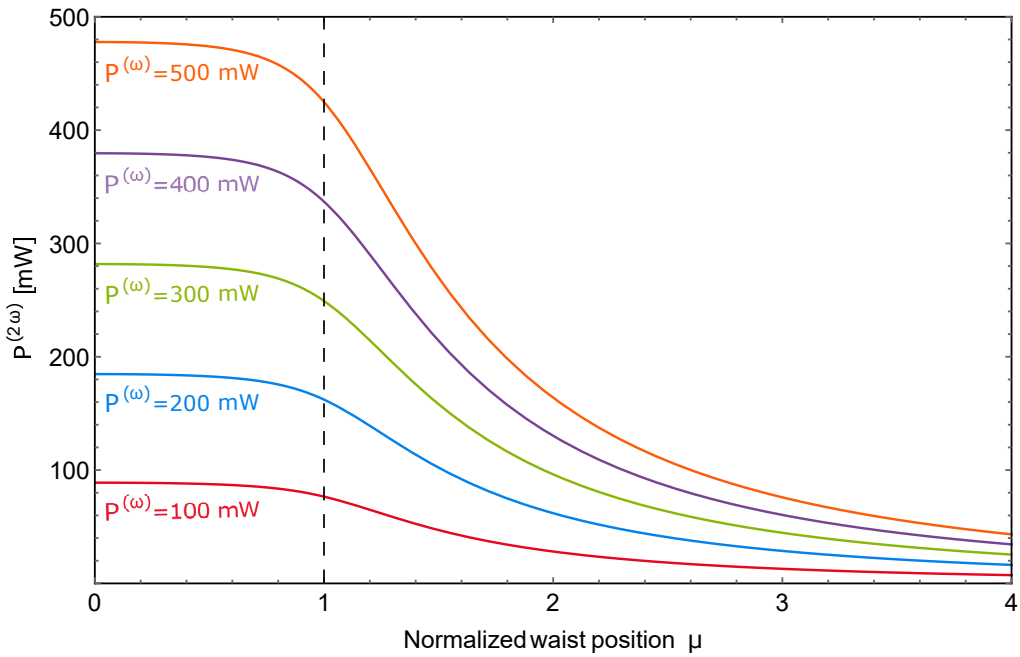

Figure 5.19: SHG power plotted for different fundamental powers as a function of the normalized position of the fundamental waist μ. The graphs are symmetric for $\mu \to -\mu$. If $\mu = 0$, it means that the waist is right in the center of the crystal, instead $\mu = \pm 1$ means that the waist is positioned on a crystal edge.

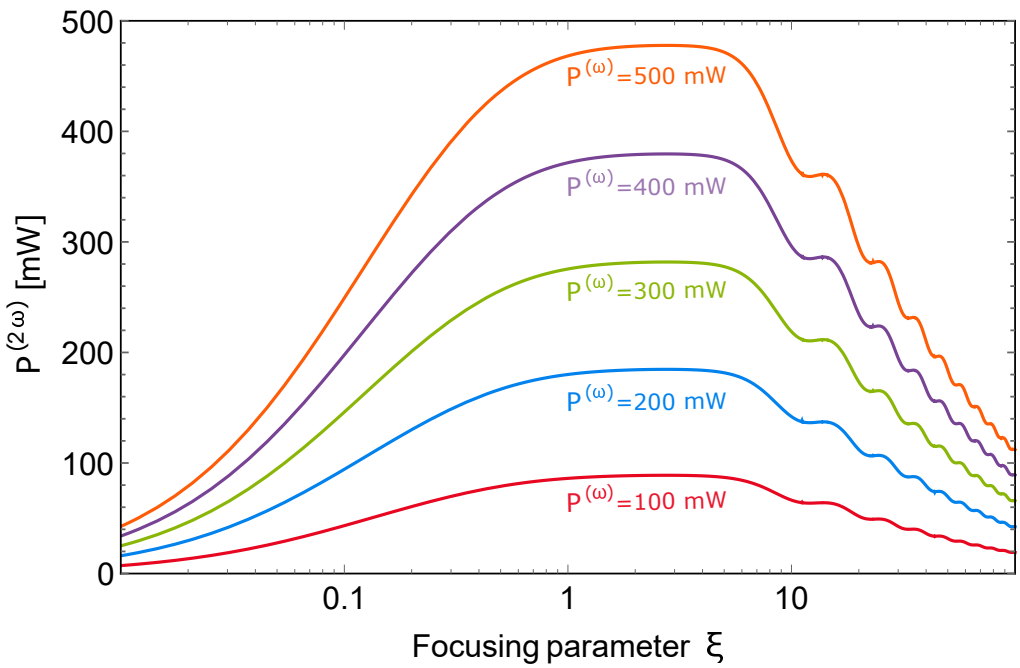

Figure 5.20: SH power plotted for different fundamental powers as a function of the focusing parameter ξ. If $\xi = 1$, it means that the pump beam is considered collimated in the crystal.

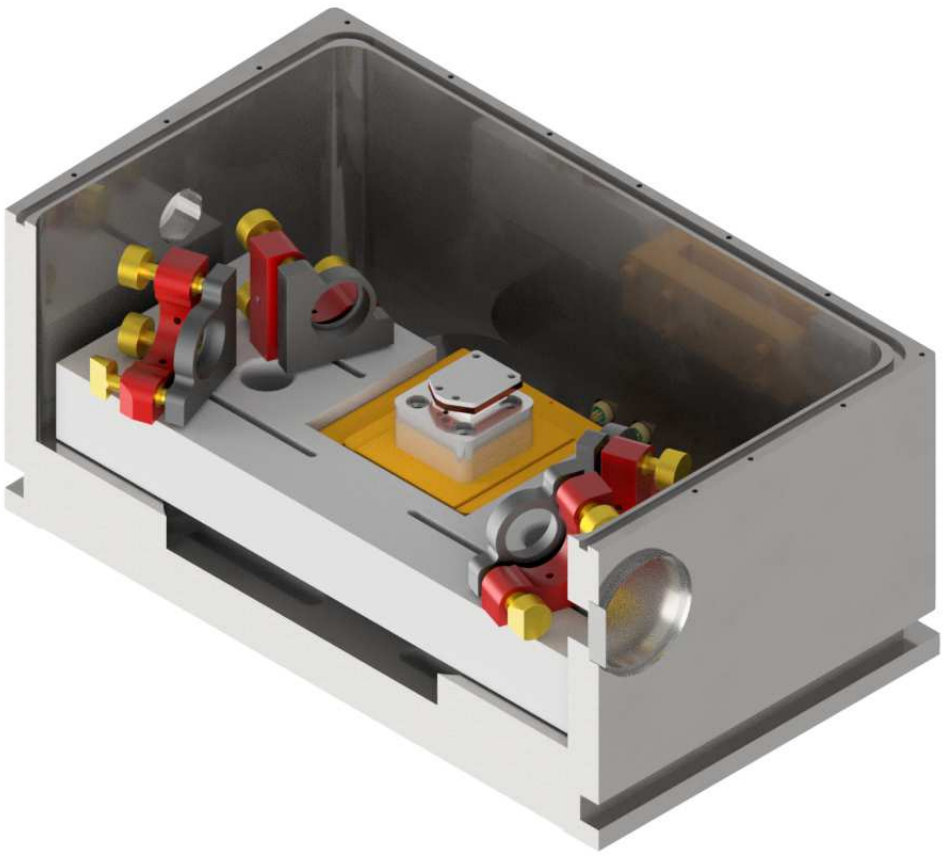

Figure 5.21: A section view of the SHG enhancement cavity CAD assembly.

five-axes stage translator (Newport 9082-V-M, colored in yellow in the sketch), onto which the crystal mounting is positioned. The crystal is supported by a copper plate and protected by a soft teflon cover. Between the copper base and the heat-sink, a Peltier element is placed in order to adjust the crystal temperature. Finally, the cavity is evacuated in order to better stabilize the working condition of the crystal[5].

At the moment of writing this thesis, the efficiency of the SHG is still under optimization. We also became aware of possible issues in the production of blue light in a cavity with a periodically poled crystal due to a local heating of the crystal [166]. If necessary, the crystal can be easily substituted with an LBO crystal, since only the copper plate would have to be modified. With an LBO crystal in a bow-tie cavity, other laboratories at LENS were able to reach a conversion efficiency larger than 50% with comparable conditions (wavelength and input power).

[5]No incidents with the Peltier elements placed in a moderate vacuum realized by a rotative pump were observed in similar setups realized at LENS.

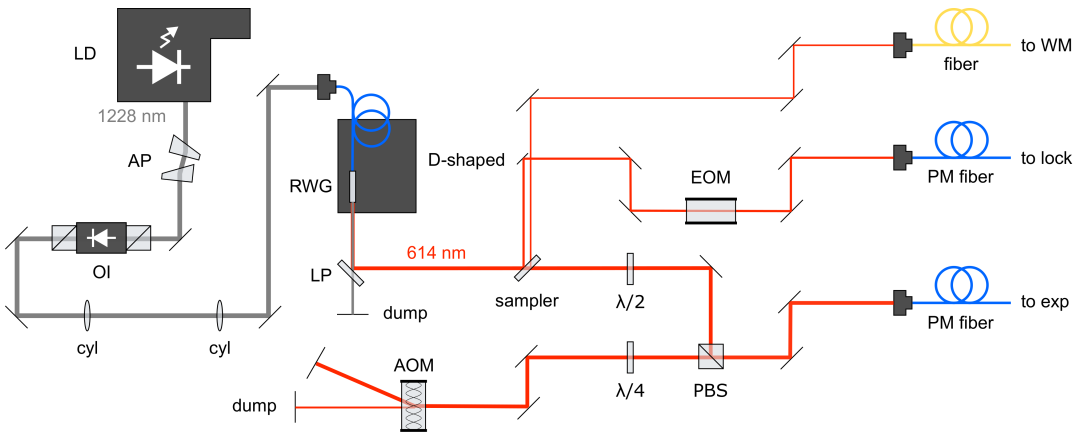

Figure 5.22: Scheme of the deshelving laser production via single-pass second harmonic generation.

5.3.2 The deshelving laser

A laser at 614 nm is necessary for de-populating the long-lived $D_{5/2}$ state through the transition $5d^1\,{}^2D_{5/2} \leftrightarrow 6p^1\,{}^2P_{3/2}$. Unfortunately, a laser diode emitting at such wavelength is not available on the market, therefore the alternative is either to use an incoherent source [167] or to produce the laser light at 614 nm by duplicating a seed laser at 1228 nm. We opted for the laser doubling, since a narrow-frequency, coherent source is more efficient in driving the transition. Considering that the needed laser power is moderate ($\approx$ mW), we decided to duplicate the infrared seed by using a single-pass waveguide mixer (from HC Photonics). This object is an optical frequency conversion platform based on a periodically poled waveguide, made in doped Lithium Niobate (ppMgO:CLN). The expected efficiency at 1228 nm is 5 mW of duplicated light with a pump of 100 mW.

The setup for the production of the deshelving laser is sketched in Fig. 5.22. The laser beam emitted by the ECDL, which is strongly astigmatic, is reshaped by a pair of anamorphic prisms (AP). The source is then protected by an optical isolator (OI) against back-reflections. Then, the beam is injected in the ridge waveguide of the mixer, and the coupling efficiency is increased with the aid of a telescope made of two cylindrical lenses. After the duplication, the light at 614 nm is separated from the remaining infrared light by a long-pass filter. Finally, the beam is divided into three branches and sent to the wavemeter, to the locking circuit and to the experiment (after an acousto-optic modulation in double-pass configuration).

5.3.3 Achieved laser powers

Compared to the corresponding transitions' saturation powers (evaluated for beam waists of 150 μm), we achieved enough laser power for producing and manipulating the ions, as resumed in Tab. 5.3. Concerning the lasers at 451.7 nm and 614 nm at the time of writing this thesis, the duplication setups for generating them are still under optimization since the duplicated light powers that have been so far observed are only a few percent of the expected values. The main issues with both systems are the optimization of the working temperatures of the active media, and the optimization of the pump light couplings, given the fact that the optical modes of the light generated by gain chips and tapered amplifiers is far from having a gaussian shape.

	Transition	λ [nm]	Γ [2π MHz]	I_{sat} [mW/cm^2]	P_{sat} [μW]	P [mW]
Ba	$S_0 \leftrightarrow D_1$	413	0.23	1.28	0.18	9
Ba$^+$	$S_{1/2} \leftrightarrow P_{3/2}$	455	18	79	10.6	7
Ba$^+$	$S_{1/2} \leftrightarrow P_{1/2}$	493.5	15	49	7.1	25
Ba$^+$	$D_{5/2} \leftrightarrow P_{3/2}$	614	6.6	11	1.6	–
Ba$^+$	$D_{3/2} \leftrightarrow P_{1/2}$	650	4.9	7	1	2.6

Table 5.3: List of the wavelengths needed to produce and manipulate Ba$^+$ ions. Linewidths are taken from [108]. Saturation intensities I_{sat} are calculated via Eq. A.8, while saturation powers P_{sat} are evaluated for a beam waist of 150 μm.

5.4 Locking strategy

The frequency of the lasers must be electronically locked to an external reference, which has to remain stable in time. To this end, we use as reference a 780 nm laser locked to the $5^2S_{1/2}\,(F = 2) \leftrightarrow 5^2P_{3/2}\,(F' = 2{,}4)$ transition in D2 line ^{85}Rb with the saturated absorption spectroscopy method. The 780 nm reference laser is then used to lock a cavity (transfer cavity) through a Pound-Drever-Hall technique [168, 169]: one of the mirrors of the cavity (see Fig. 5.24) is equipped with a piezoelectric element to which the electronic feedback signal is sent. In this way, the length of the transfer cavity is actively bound to be a multiple time of the wavelength of the reference laser, and the cavity can be used in turn as a reference for all the other lasers.

Transfer cavity

A section view of the transfer cavity is shown in Fig. 5.23. The two cavity mirrors (4) and (7) are curved mirrors (R = -500 mm), separated by a spacer (6)

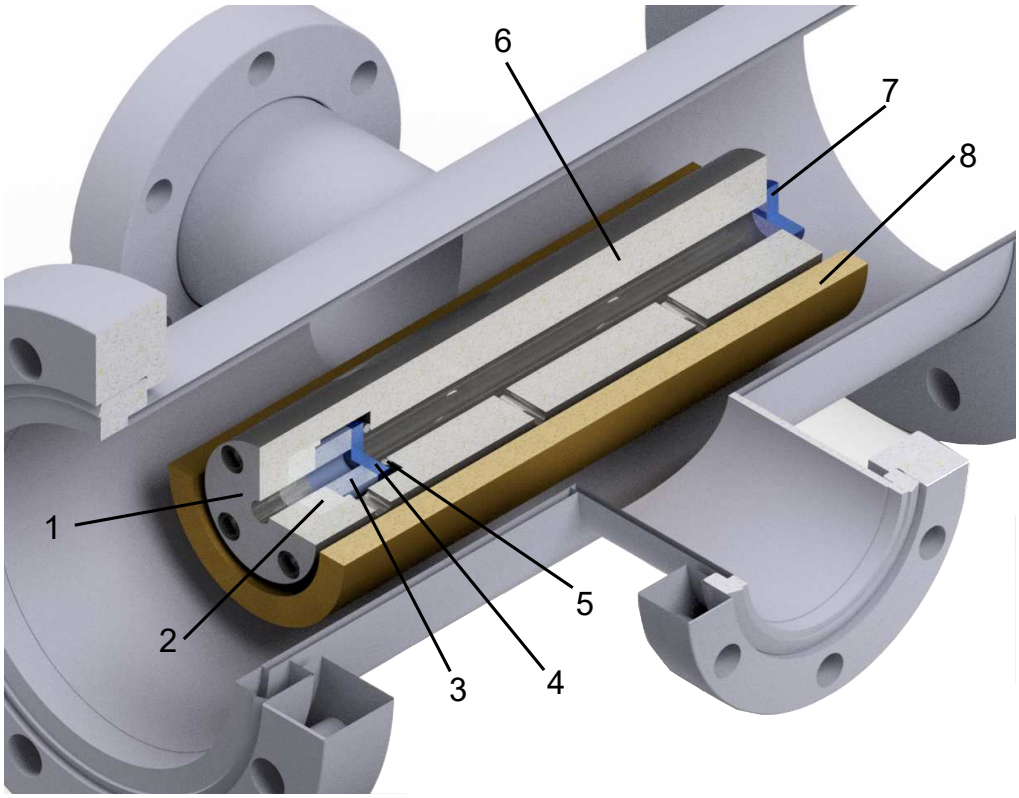

Figure 5.23: A section view of the transfer cavity CAD assembly. (1) Spacer cover. (2) Aluminum compensating element. (3) Cylindrical piezoelectric transducer. (4) Mobile mirror. (5) Rubber O-ring. (6) Invar spacer. (7) Fixed mirror. (8) Cavity support.

that has a length of 10 cm and made out of invar for reducing the cavity length changes due to temperature fluctuations. The mobile mirror rear facet is directly glued on a cylindrical piezo (3), whereas the front facet leans on a rubber O-ring which grants a better frequency response of the piezo by offering a restoring elastic force to the mirror. The other mirror is instead glued (7) on the spacer. In order to increase the stability of the cavity against temperature variations, the piezo (and then the mobile mirror) is held in position by a compensating element in aluminum (2). The ratio between the lengths of the compensating element and the spacer is equal to the ratio between the thermal expansion of the two materials (aluminum and invar, respectively). In this way the thermal expansions of the two materials act in opposite direction and self-compensate, resulting in an increased passive stability of the assembly. Finally, the compensating element-piezo-mirror stack is connected with the spacer cover (1) to the spacer, held by a bulky brass support (8) in a vacuum cross, which can be evacuated via a ball vacuum valve (not shown in the Fig. 5.23).

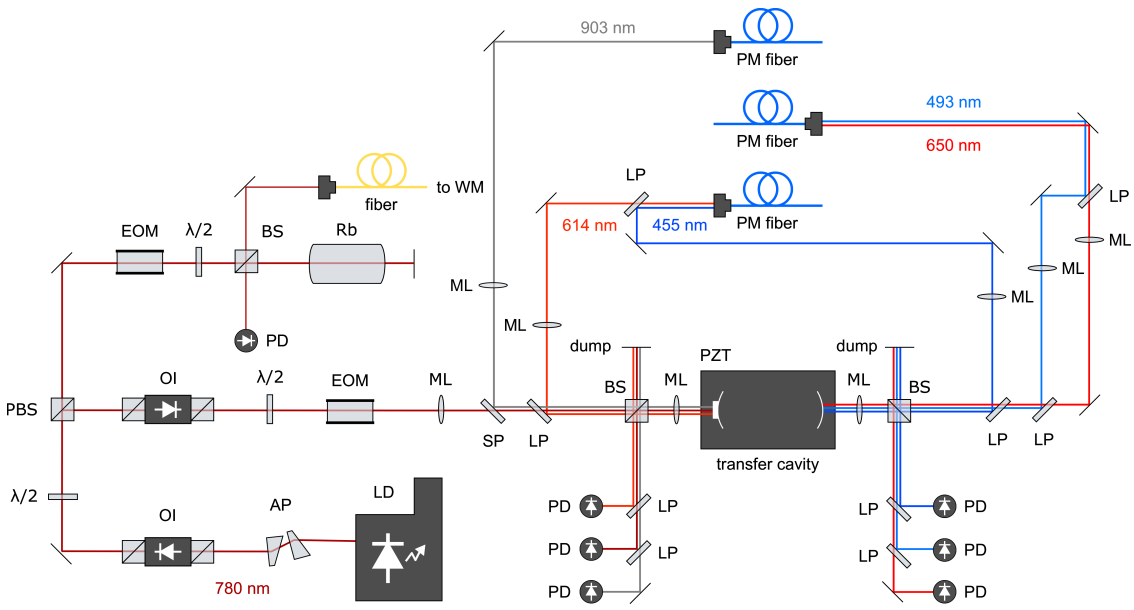

Figure 5.24: Optical scheme of the locking setup.

Estimation of the lasers' linewidths

The locking optical circuit is sketched in Fig. 5.24. The lasers can be injected into the cavity by an arrangement of long-pass and short-pass filters, disposed on both cavity sides.

At the moment of writing this thesis, a stable lock has been realized only for the lasers involved in the first ion trapping attempts in the Paul trap, i.e. the 493.5 nm and the 650 nm lasers. Their linewidths have been estimated from the residual error signal. Defining D as the slope of the carrier in the PDH error signal, then the linewidth (FWHM) of the locked laser $\delta\nu_\lambda$ can be evaluated as [170]

$$\delta\nu_\lambda = 2\sqrt{2\ln(2)}\,\frac{V_{\mathrm{RMS}}}{D} \approx 2.35\,\frac{V_{\mathrm{RMS}}}{D} \tag{5.1}$$

The linewidth (FWHM) evaluated via Eq. 5.1 of the transfer cavity locked on the laser at 780 nm is $\delta\nu_{TC} \approx 450$ kHz (considering also the measured linewidth of the 780 nm laser); whereas the linewidths of the cooling and repumper lasers locked on the cavity are respectively $\delta\nu_{493} \approx 3.2$ MHz and $\delta\nu_{650} \approx 790$ kHz. By taking into account the cavity linewidth, the broadened lasers' linewidths can be calculated as $(\delta\nu_{CT}^2 + \delta\nu_\lambda^2)^{1/2}$. The results are 3.2 MHz for the cooling laser and 900 kHz for the repumper laser. Both linewidths are smaller than the natural linewidths of the corresponding transitions (see Tab. 5.3). The relatively large linewidths and the trend of larger linewidth for lower wavelengths is caused by the poor quality of the mirrors' coatings, which turned out to be considerably worse than the specifics.

This problem hits in particular the lock of the photoionization laser, since we found out that the coating of the transfer cavity mirrors has a reflectivity at 413 nm much lower than we expected. As the detection of a signal sufficient for locking the laser required too much power, we opted for an alternative locking strategy thus reserving as much power as possible for the photoionization process. In particular, we decided to realize a software lock by using a wavemeter (High Finesse WS-7) as detector and the current controller of the laser as actuator (Thorlabs LDC8002). For this purpose, I developed a software able to control both the devices and adjust the laser current in dependence of the laser wavelength drifts. This locking system has shown so far a good stability ($\delta\nu_{413} \approx 1\,\mathrm{MHz}$) for several hours.

Chapter 6

A novel control software

Experiments in atomic, molecular and optical (AMO) physics, are usually managed by a single desktop computer provided with a number of modules mounted directly on the mother-board with PXI style connections or gathered in an external chassis connected to the PC. These modules can have different purposes, typically acquiring data, triggering and synchronizing devices, generating digital, analog and RF signals, performing measurements, and controlling more complex devices such as imaging cameras. The desired temporal sequence of electronic signals is typically pre-loaded into a local buffer memory, and then executed after an external trigger is provided.

In hybrid quantum systems experiments, where two or more quantum systems are combined and made to interact, establishing an efficient control system is particularly challenging. In this case, actually, the equipment used to control the experiment will in general be larger and more diverse than in ordinary AMO physics experiments. Moreover, complications may arise from the typical timescale for the preparation of each quantum system, which may be very different. For instance, the typical duration of an experiment with trapped ions is on the order of tens to hundreds of milliseconds, while the temporal sequence for preparing a quantum gas of neutral atoms can last up to several tens of seconds. As a result, it can be difficult to efficiently manage a hybrid quantum system with the most common control systems based on the execution of pre-loaded sequences. Consequently, the control system can become an unexpected bottleneck and a serious limitation for these kinds of setups.

To face these issues, we decided to design a brand new control system, both hardware and software, that can efficiently manage hybrid quantum system experiments. Part of this project has been recently described in a publication [171].

This chapter is particularly focused on the features (Sec. 6.1) and the design

(Sec. 6.2) of the novel control software, named Yggdrasil[1]. In the last section of the chapter, we provide an overview of the hardware part of the control system (Sec. 6.3), along with a practical case of custom electronic device integration into the control apparatus.

6.1 Control software overview

In our vision, the main characteristics that a software controlling experiments with hybrid quantum system are

Concurrency A control software for experiments with hybrid quantum system should have the capability of independently running different sets of commands at the same time. This would grant the possibility of generating a series of outputs, even if part of the hardware is already occupied by other directives. For example, this feature would be very useful to perform experimental cycles on trapped ions with a portion of the control hardware, whereas the remaining part is used to create an ultracold gas of neutral atoms. Then, when a quantum gas is produced, the two systems can be merged, so that experiments on the hybrid system can be carried out.

Flexibility Complicated experiments as quantum hybrid system ones are managed by equally complex control sequences, which keep being modified and improved following the different experimental needs. For this reason, the flexibility is an important feature for a control software, since commands' sequences have to be easily and quickly adapted to the experiments' changes.

Expandability An ideal software must be able to integrate the control of new or even custom-made devices, without the need of a particularly expert programmer.

Recycling This feature ensures the ability of merging already created and tested sequences into newer or wider ones, especially in "modular" experimental cycles. This possibility is crucial to reduce the development work and the errors caused by the PhD students who run the experiment. For instance, a set of commands that performs a C-NOT gate on a pair of trapped ions can be separately composed, executed, optimized and saved. When that gate is needed in a quantum computation experiment, it will be sufficient to recycle the sub-sequence previously created and import it in the new sequence.

[1]Name of a mythological tree belonging to the Norse cosmology.

Usually, to realize the control application for a AMO physics experiment, a common approach is to use commercial libraries or proprietary data-driven programming environments such as MATLAB or LabVIEW. In particular, the latter is widely used to quickly implement software equipped with a graphic interface for controlling commercial boards, e.g. by National Instruments or other companies [172, 173, 174].

In the LabVIEW case, the programs are coded in a visual language, where variables and functions are depicted as graphical objects in a canvas, arranged and connected by wires on the basis of the software aims. The programming paradigm is based on data availability, so the sections of the program can be executed as soon as their input data are available. This inherently hinders the creation of programs where the execution of sequential operations is requested, as in AMO physics control experiments [175].

Developing scripts in MATLAB for managing instruments is also possible, even if MATLAB is more frequently exploited to code programs which read data directly from the interfaced devices and elaborate them.

The remaining alternative approach is to write the control software in a general-purpose programming language, e.g. C#/C++ [176, 177], Python [178, 179] or Perl [180]. Some of these options are characterized by a text-based sequence programming approach [178, 180, 179], which sacrifices the graphical aspect and a user-friendly management. Moreover, some of these already existing projects are explicitly designed to control commercial devices instead of custom instrumentation [176]; whereas others do not offer enough flexible solutions, making them incapable of quickly adapting the software to hardware modifications or expansions [177].

The main idea behind Yggdrasil is to collect in a new control application some of the useful features that are already present in similar software developed in the AMO physics community, e.g. the presence of an intuitive graphical user interface, the features previously listed, and the possibility to implement automatized processes like self-optimization [179], in the perspective of managing a quantum hybrid system experiment.

6.2 The application architecture

One of the main Yggdrasil characteristics is its Graphical User Interface (GUI) that makes it user-friendly and intuitive. Text-based interfaces [178, 180, 179] require that the user types code lines on a keyboard to interact with the application, therefore a high knowledge of its commands is needed to use it. Instead, graphic-based interfaces are much more simple to work with, since they allow to control a software through easily readable icons and graphic indicators. In particular, Yggdrasil has a GUI based on a Multiple Document Interface (MDI), in which

multiple windows refer to a single parent window. This kind of interface design is in contrast with the single document interface one, in which all windows are independent to each other. The great advantage of MDI is that the child windows can share their data and even the same menu bars, thus increasing the efficiency in space usage and eliminating the repetition of identical icons sets.

Yggdrasil design follows the rules of the Model-View-Controller (MVC) architectural pattern, which is usually applied to develop interfaces where the software is decoupled into three different, yet interconnected, modules [181], for an efficient, reusable and parallel code development. This approach is mainly adopted to separate the internal information from the way it is represented by the GUI and accepted or modified by the user. The three modules at the base of the design are

Model The model is the main element. It represents the data structure of the software that remains independent from the user interface or the way the data are presented. In addition, it is responsible for managing the data and the rules of the application. The model receives the user inputs from the controller.

View The view is a visual representation of the information provided by the model. Multiple ways to display the same data are possible, such as lists or tables.

Controller The controller is the interactive part of the pattern. The controller processes, validates and sends the user inputs to the model or the view.

Yggdrasil has been developed in C++, a widely known, well-documented and free programming language. Its code has been written, debugged and compiled in the integrated development environment of Microsoft Visual Studio 2015. For the GUI construction, the cross-platform application framework Qt (version 5.9) has been adopted. Basically, Qt provides several useful modules containing optimized classes for managing threads, operating on data clusters and, most of all, creating intuitive interfaces by combining graphic elements called “widgets” (windows gadgets). Widgets as buttons, scroll-bars or check-boxes, are the fundamental constituents of a GUI since they facilitate user-application interactions in different manners, such as displaying (e.g. labels, text boxes, canvas), editing (edit-lines) or organizing information (tabbing panels or windows).

The experimental sequence structure in Yggdrasil is presented in Sec. 6.2.1. Then, the composition of the model behind the user interface is illustrated in Sec. 6.2.2. Finally, the views and controllers available in Yggdrasil are reported in Sec. 6.2.3, along with some screenshots of the application during the creation of a sequence example.

6.2.1 The structure of the experimental sequences

The files produced by Yggdrasil in the custom extension `.fbl` are called "sequences". They are like a big container in which all the possible data that contribute to properly define an experimental cycle are organized in a hierarchical structure.

In order to more efficiently construct the sequences, two different kinds of object can be used. The first is the "parameter", which represents a number (or a list of numbers) provided with an identification name and, in case, a unit of measure. The second is the "waveform", a finite collection of data resulting from the evaluation of an analytical formula which can even contain the previously defined parameters.

The fundamental constituents of an experimental sequence in Yggdrasil are called "elements", which can be implemented by using waveforms. In fact, elements basically contain the vector of values that will be physically generated. Each element can be employed by placing it in a structure named "channel". A channel is just a virtual container that gathers elements and empty intervals in a time-organized queue. A real physical channel can be associated to the virtual channel in a second time: this operation establishes the analog or digital nature of all the data contained, and relates them to the same physical actuator. Then, a collection of channels can be enclosed in wider structures called "instructions", which are then arranged in "tasks". The duty of an instruction is to merge each data vector of the elements in a number of bigger vectors corresponding to the different physical channels. This merging operation is performed by respecting the "time position" of the elements in the channels, the time schedule of the instructions in the task and the associations between physical and virtual channels. This means that data vectors belonging to different instructions but related to the same physical channel will be merged in the same final data vector. In general, instructions can be overlapped in time, but it is obviously forbidden for a channel to execute more commands at the same time. Finally, the tasks can be organized in a certain temporal order and in a given logic relation between each other by conditional statements. In fact, a task can represent just a section of a longer routine, for instance the loading of the atoms in a magneto-optical trap or the operations which realize a quantum logic gate on a crystal of trapped ions. The temporal disposition of the tasks forms the sequence, the "widest" construct which describes the whole operations collection needed to carry out an experimental routine.

An artificial sequence composed by five digital and two analog channels is sketched in Fig. 6.1. The simple-framed small rectangles in each channel stand for the elements arranged in a time order. The gaps between them are automatically filled with the last value of the previous element in the channel, taking into account that the starting default value of each channel is always zero. Therefore, the possible gap at the beginning of a channel (e.g. the first gap in "Dig2" before the "ON" element) is interpreted as a collection of zeros until the first element appears.

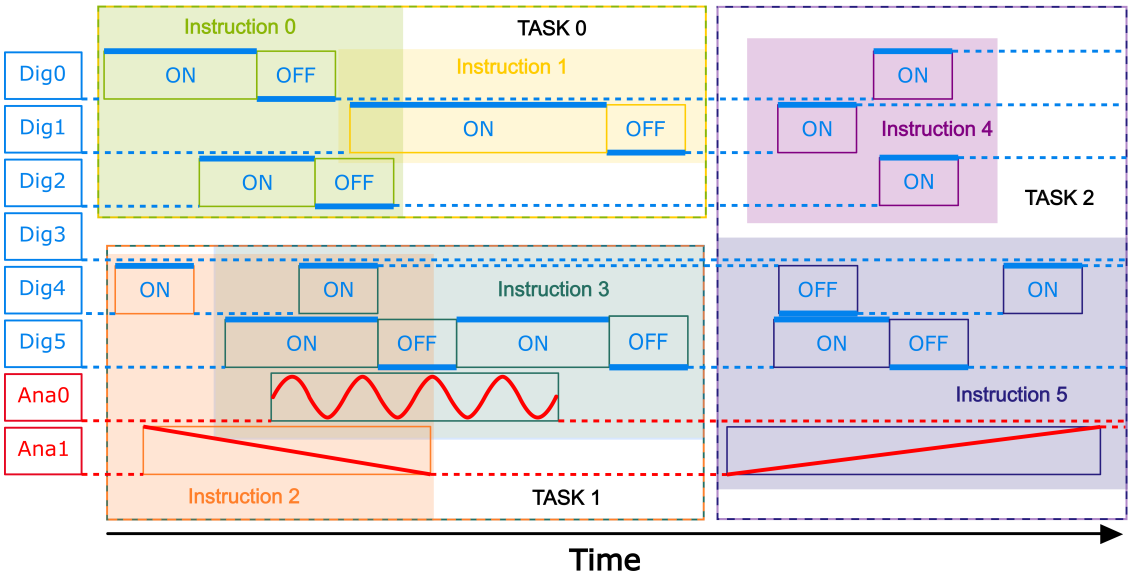

Figure 6.1: Sketch of the experimental sequence composition in Yggdrasil. This artificial example is composed by three tasks involving both digital and analog commands organized in a succession of hierarchical containers.

After that, the next gap is filled with the last element value. As described above, by associating a physical actuator to the virtual channel, the elements (e.g. both the yellow elements and the violet one for the channel "Dig1") are categorized by the software as either digital or analog commands, and executed by the same physical channel linked to the virtual one. Elements' collections of different channels, characterized in the sketch by shaded colored rectangles, can be encapsulated in the same instruction. The latter is a useful structure for representing more complicated commands acting on multiple channels. An example can be the production of the ions starting from neutral atoms: this operation can be performed by an instruction which contains analog signals to drive the oven current and digital ones to switch on/off the photoionization laser beam. Finally, the instructions related to the same logic duty are gathered in a common task, represented in the sketch by the dashed-frame rectangles. For example, a task can describe all the required commands and timings to create a magneto-optical trap of cold atoms or perform a quantum logic gate on trapped ions.

6.2.2 Model structure

The model is the element of the MVC pattern devoted to the management of the application data. Its design has been influenced by two main requests: the ability to be easily expanded for hosting new generic data, and the necessity of generating as less code as possible (a condition that leads to a better efficiency and less work needed for developing and optimizing the application). The solution to this problem lies in the way the data are stored, provided and, most of all, related with each other. Specifically, Yggdrasil model has been conceived as a tree-like structure, i.e. a data structure composed by "nodes" (or "vertices") linked together by "connections" (or "edges") without forming any cycle. A tree is characterized by an ancestral node, called "root", which has a number of nodes related at different levels originating a hierarchy.

In Yggdrasil, each `.fbl` file has its own model managed by an instance of the `FileModel` class[2], whose part of the header is reported in Code 6.1.

```
class FileModel : public QAbstractItemModel
{
    public:       // Read-only model methods
    QVariant data(const QModelIndex & index, int role) const;
    QModelIndex index(int row, int column, const QModelIndex) const;
    QModelIndex parent(const QModelIndex & index) const;

    public:       // Editing methods
    bool setData(const QModelIndex & index, const QVariant & val);
    bool insertRows(int pos, int rows, const QModelIndex & parent);
    bool insertColumns(int pos, int cols, const QModelIndex & parent);
    bool removeRows(int pos, int rows, const QModelIndex & parent);
    bool removeColumns(int pos, int cols, const QModelIndex & parent);
    bool moveRows(const QModelIndex & sourceParent, int sourceRow, int
        count, const QModelIndex & destinationParent, int destinationRow);

    public:       // Drag and drop methods
    QMimeData mimeData(const QModelIndexList & indexes) const;
    bool dropMimeData(const QMimeData* data, int row, int column, const
        QModelIndex & parent) const;

    public:       // Getters
    FileModelAbstractItem* root() const;
    FileModelAbstractItem* sequence (const int & seq) const;
```

[2]A C++ class is a structure containing data ("attributes") and functions ("methods") whose access can be regulated.

```
    FileModelAbstractItem* itemFromIndex(const QModelIndex & index)
        const;

    public:       // Serialization methods
    void serialize(QDataStream & stream) const;
    void deserialize(QDataStream & stream);

    private:      // Attributes
    FileModelAbstractItem* abstractRoot;
}
```

Code 6.1: Partial header of the `FileModel` class reporting its most significative methods and attributes.

The tasks of this class are providing data from the model, modifying the tree composition and serializing the information (which means saving the information in a `.fbl` file). To achieve these duties, it has methods as `parent` and `index` [3], useful to navigate through the tree, and functions as `insert/remove/moveRows` and `insert/removeColumns` in order to change and expand the model structure, in addition to the `serialize` and `deserialize` methods which are devoted to store and retrieve the model data.

The most important `FileModel` attribute is "abstractRoot", a pointer to the tree root, which does not have any visual representation (that is the reason why its pointer is called "abstract"). The root is an instance of `FileModelAbstractItem`, the mother class of each single node hosted by the model.

```
class FileModelAbstractItem
{
    public:       // Editing methods
    virtual bool setData(const int & col, const QVariant & val);
    virtual bool insertChild(const int pos) {return false;}
    virtual bool removeChild(const int pos);
    virtual bool insertColumn(const int pos) {return false;}
    virtual bool removeColumn(const int pos) {return false;}

    public:       // Getters
    FileModelAbstractItem* parent() const;
    FileModelAbstractItem* child (const int & i) const;
```

[3]The model indexes are instances of the Qt class `QIndexModel`. They contain all the information required to localize within the model structure the position of the node which they refer to.

```
    public:       // Serialization methods
    void serialize(QDataStream & stream) const;
    void deserialize(QDataStream & stream);

    protected:    // Attributes
    FileModelAbstractItem* parent;
    QList<FileModelAbstractItem*> children;

    protected:    // Attributes
    VariantList values;
}
```

Code 6.2: Partial header of the `FileModelAbstractItem` class.

As can be seen from the section of its header resumed in Code 6.2, the class `FileAbstractItemModel` has two fundamental attributes: `parent` and `children`. The former is a pointer to the parent node, so the instance of the model root is mainly characterized by the fact that its `parent` points to `NULL`. The former is a dynamic list of pointers which connect the node with all its child nodes. For example, let's suppose that a tree node A has a child B. The connection between A and B is represented by a pair of opposite links: in fact, in the `children` list of A there will a pointer to B, that in turn has its `parent` pointing back to A. In both `parent` and `children` methods, the pointer type is `FileModelAbstractItem`, therefore every instance of the class `FileModelAbstractItem` or its descending classes can be included in the model. This mechanism is very relevant for the code efficiency and working, since allows to specialize the child nodes of the tree, which inherit the set of basic properties common to each node (e.g. the editing methods or the `parent` and `children` attributes). In this view, `FileModelAbstractItem` constitutes the backbone class from which all the classes useful to store the model data are derived.

The Yggdrasil model structure is sketched along with the `FileModelAbstractItem` inheritance chain in Fig. 6.2. The classes `FileModelParamItem`, `FileModelWaveformItem` and `FileModelSerialItem` share the same sub-structure inside the tree and are directly derived from `FileModelAbstractItem`: each instance of the first two classes contains all the useful data for describing a parameter or a waveform (value, analytic expression, name, description, ...), while the third class is used to store the information about a serial device and its configuration (see Sec. 6.3.2 for more details on serial objects). Since these classes inherit from `FileModelAbstractItem`, their instances can be part of the model. Moreover, for the same principle, an empty instance can be used as a "branch" (a node with children), in other words, as a container for "leaves" (nodes without children). This is the case of the "Parameters", "Waveforms" and "Serials" instances shown in the figure.

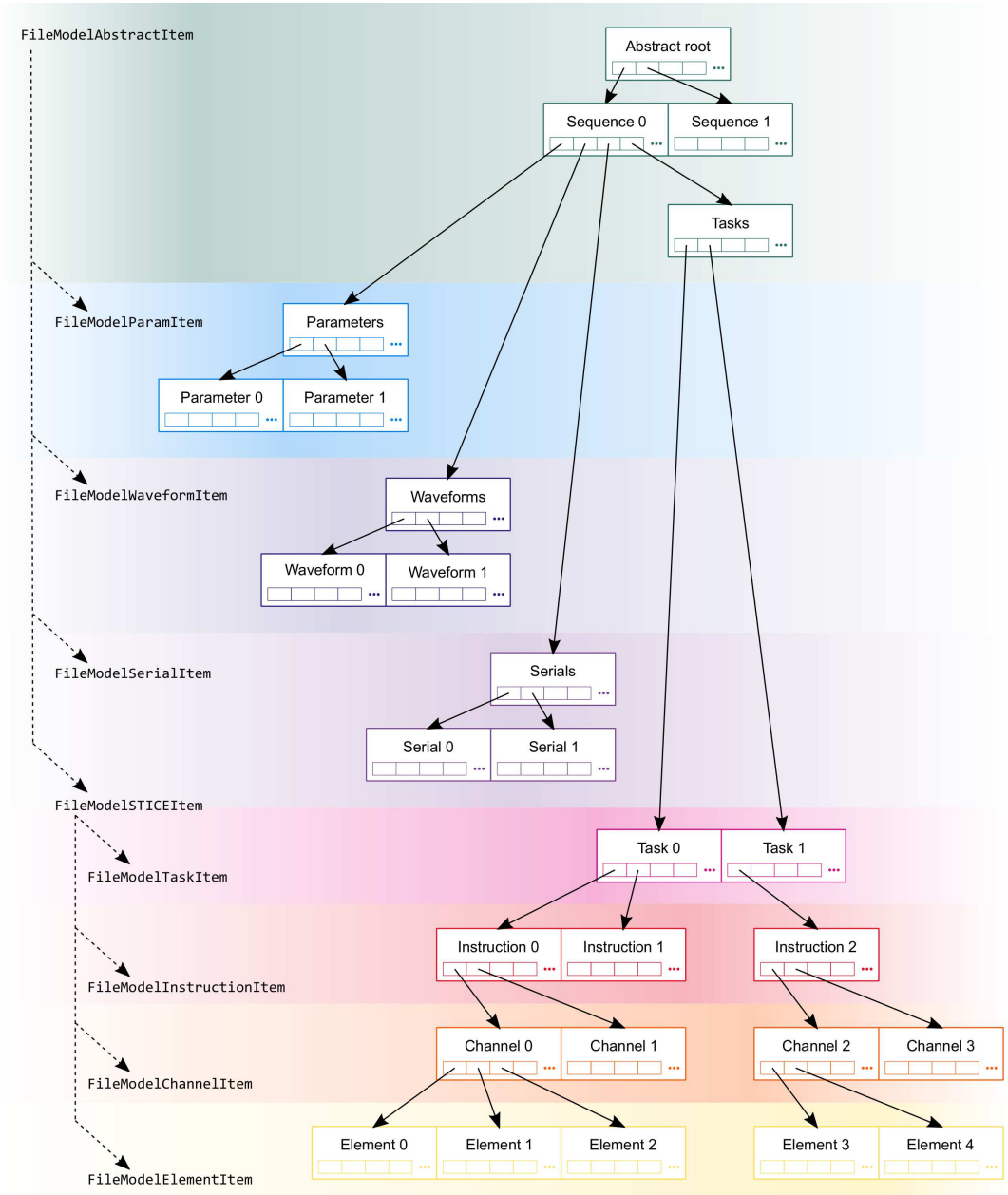

Figure 6.2: Software model structure and its classes inheritance diagram. Each white rectangle stands for an `item` class instance, whose type is specified by a color. The small rectangles inside the instances represent instead the first four elements of the `children` list, whereas the full arrows indicate the pointers that link a node to its children. On the left side, the `FileModelAbstractItem` inheritance chain is showed with dashed arrows.

The result is a more organized model structure without the necessity of creating new classes or writing unnecessary code lines.

As can be seen in Fig. 6.2, an experimental cycle is developed starting from an instance of `FileModelAbstractItem`. Usually, there is only a sequence in the model, therefore the model root has only a child and all the remaining nodes has "Sequence 0" as their ancestor. In particular, a sequence node has automatically provided with a child, which is equally an instance of `FileModelAbstractItem`: it is the "Tasks" node, the container for all the tasks. As explained in the previous section, the tasks are constructed by elements arranged in channels and instructions. All these objects are individually described by instances of the specialized classes `FileModelTaskItem`, `FileModelInstructionItem`, `FileModelChannelItem` and `FileModelElementItem`, which become part of the model tree following the connections rule illustrated in the figure (the elements are leaves of a channel, the channels are branches of an instruction, and so on). The above mentioned four classes are more closed with each other in comparison to other classes because they have similar duties: for this reason, they descend indirectly from `FileModelAbstractItem` through `FileModelSTICEItem`[4], their real mother class.

Fig. 6.2 shows also that other sequences can be grafted in the tree root. This possibility is very useful in order to exploit instructions or tasks from other sequences during the composition of a brand new experimental cycle. Therefore, the recycling of previously tested and optimized sequences is always possible, thus facilitating the composition process and reducing the errors propagation. This feature is granted by Yggdrasil capability of storing and retrieving sequences data through the functions `serialize` and `deserialize`, present in every class involved in the model definition.

When the user decides to save a sequence, its model is traduced in raw data and saved in a `.fbl` file. The process starts with the call to the `FileModel::serialize` method which saves the tree root, as showed in Code 6.3.

```
/* Text of the FileModel "serialize" method */
void FileModel::serialize(QDataStream & stream) const {
    if(abstractRoot) stream << *abstractRoot;
}

/* Text of the non-member function which defines the behavior of the
operator << with FileModelAbstractItems */
```

[4]The acronym S.T.I.C.E. stands for sequence, task, instruction, channel and element.

```
QDataStream & operator<<::serialize(QDataStream & out, const
    FileAbstractItemModel & node) {
    node.serialize(out);
    return out;
}

/* Text of the FileModelAbstractItem "serialize" method */
void FileModelAbstractItem::serialize(QDataStream & stream) const {
    stream << attribute1;
    ...
    stream << attributeN;
    stream << children.size();
    foreach(child in children) {
        stream << child->metaObject()->className();
        stream << child;
    }
}

/* "Serialize" method of a generic ChildClass derived from
   a ParentClass (e.g. FileAbstractItemModel) */
void ChildClass::serialize(QDataStream & stream) const {
    ParentClass::serialize(stream);
    stream << attributeN+1;
    ...
    stream << attributeN+M;
}
```

Code 6.3: Pseudocode highlights from some of the different methods involved in the serialization process.

The « operator, as reported in the second pseudocode text, is defined in such a way that the `serialize` method of the interested node is called and then the "stream" object[5] itself is returned. At this point, when the `ChildClass::serialize` method of a generic class is invoked, the `ParentClass::serialize` is called and then its own attributes are saved via the properly defined « operator. The call to its parent `serialize` method ensures that all the node attributes inherited from its ancestors are automatically saved. The calls chain keeps going back from daughter to mother serialization until the last call to `FileModelAbstractItem::serialize` is made. For example, let's suppose to save a toy model with only a parameter "param0" directly connected to "Sequence0". The invocation to `FileModel::serialize` originates a hierarchy of calls to the different `serialize`

[5]Instance of the Qt class `QStreamData`. It is helpful to manage the data streaming toward and backward an external file.

methods which is reported here in the following.

```
abstractRoot - FileModelAbstractItem::serialize starts
abstractRoot - attribute1 saved
abstractRoot - attributeN saved
abstractRoot - children number "1" saved
abstractRoot - first child className "FileModelAbstractItem" saved
       Sequence0 - FileModelAbstractItem::serialize starts
       Sequence0 - attribute1 saved
       Sequence0 - attributeN saved
       Sequence0 - children number "1" saved
       Sequence0 - first child className "FileModelParamItem" saved
              Param1 - FileModelParamItem::serialize starts
              Param1 - FileModelAbstractItem::serialize starts
              Param1 - attribute1 saved
              Param1 - attributeN saved
              Param1 - children number "0" saved
              Param1 - FileModelAbstractItem::serialize stops
              Param1 - attributeN+1 saved
              Param1 - attributeN+M saved
              Param1 - FileModelParamItem::serialize stops
       Sequence0 - FileModelAbstractItem::serialize stops
abstractRoot - FileModelAbstractItem::serialize stops
}
```

The deserialization process follows a pattern similar to the serialization one. The main difference lies in the fact that during a deserialization a correct tree reconstruction requests to know exactly the class type of a given node (for allocating the proper memory) and the number of its children. For this reason, in the serialization process, each node is stored along with its class name and the number of its child nodes.

6.2.3 Views and controllers in sequences construction

When a blank sequence file is created in Yggdrasil, it has the aspect shown in Fig. 6.4. The window/sequence is completely occupied by a custom view widget called “ChannelViewer”, which is initially empty. Other views that help the user in the sequence construction are enclosed in docking panels, like the “browser”, the most important view in a sequence. The browser is an interacting tree-like representation of the model nodes. Other useful panels are the parameters and waveforms lists, which are displayed by table views, and the Log file, which is an editable text space where messages and errors are reported. All these panels can be displaced around and outside the main window, closed, re-opened, and docked

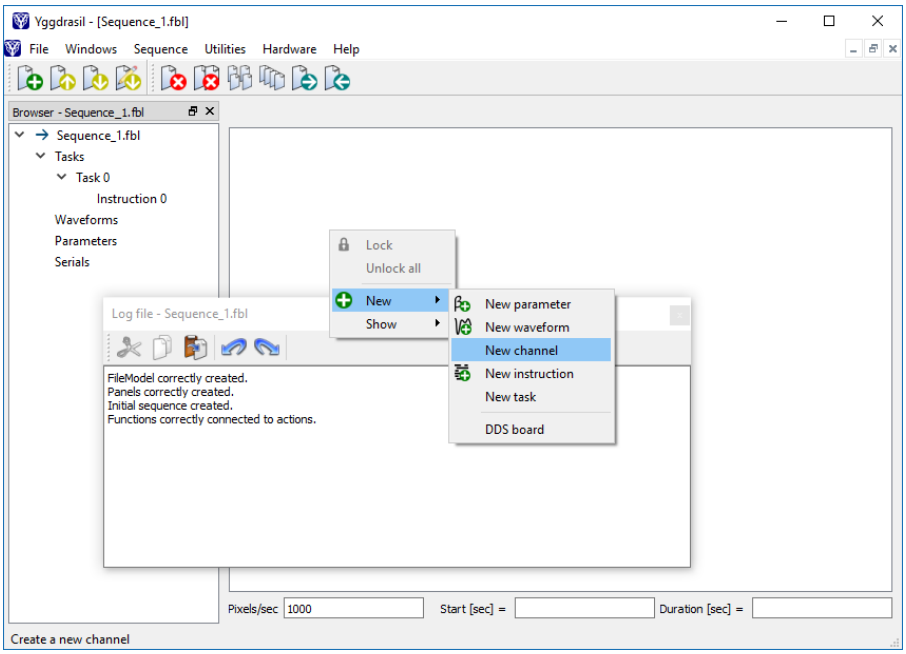

Figure 6.3: Screenshot of a new born file "Sequence_1.fbl". The docked browser along the floating Log file are shown. The white space behind the log file is the empty ChannelViewer, an Yggdrasil custom view.

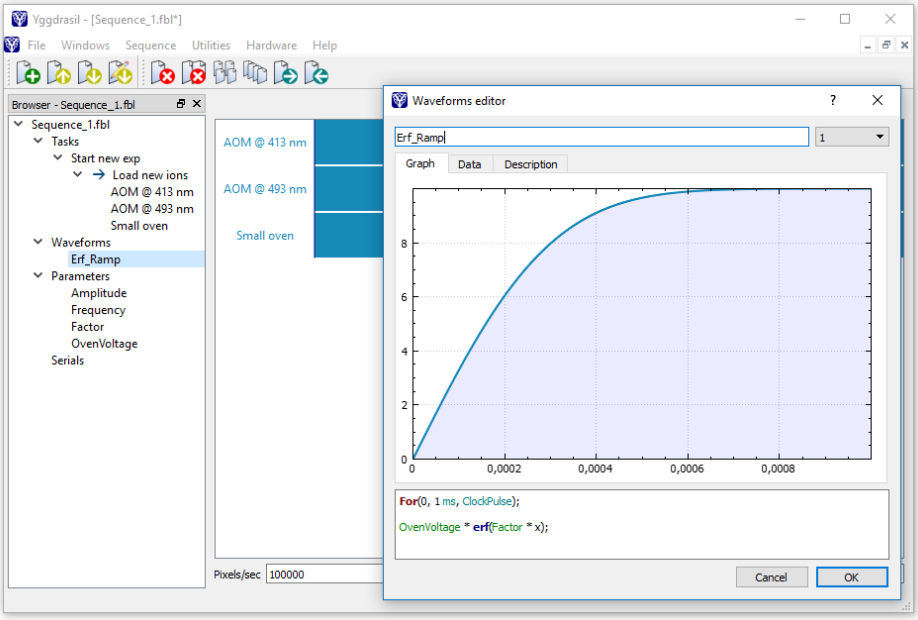

Figure 6.4: Yggdrasil screenshot during the definition of a waveform. The dialog window in the foreground is the controller to create a waveform.

in custom configurations as tabbed panels in order to save space on the screen.

During the construction of a sequence, the user can define parameters, waveforms and channels, or modify/delete previously created objects. All these changes can be operated in an easy way on the view with the aid of the controllers[6], and have consequences on the model structure underneath. In Fig. 6.4, a sequence with four parameters and three channels is presented. The screenshot has been taken during the definition of a waveform, which is described by a native analytic function and two parameters. The dialog window in the foreground called "waveform editor" is actually the controller used to create the waveform. It is equipped with a text editor for the formula, an interactive and zoomable canvas[7] to plot the function, dedicated spaces for adding a description and retrieving the function data.

In general, in Yggdrasil the controllers are always dialog panels which can be activated through a menu or a double-click on the views (e.g. the browser). From a coding point of view, since the controllers share several features and the graphic aspect, all the classes that stand behind them inherit from the same virtual parent class `FileModelDelegate`.

In Yggdrasil, the definition of parameters is useful but not necessary as the creation of the waveforms: in fact, the channels are populated by elements which arise exactly from the waveforms. Elements are simply created by dragging a waveform from the browser and dropping it onto the ChannelViewer. The position in which the waveform is dropped determines both the belonging channel and the time position of the element (anyway it can be adjusted in any moment with a dedicated controller). With this simple and intuitive method, the elements can be arranged in time-ordered queues on the channels of an instruction ("Load new ions" in the screenshots). With the same procedure, the instructions can be joined to form tasks, as explained in Sec. 6.2.1. While the sequence composition evolves, in the background Yggdrasil takes care of the data vectors contained in each object. For example, the data vector of a channel is a collection of values whose total number depends on the duration of the instruction and on the hardware clock frequency (since a new value is generated at each clock pulse). When a waveform with a duration equal to Δt is dropped on a channel in the time position t_n, then the data of that channel vector, from t_n to $t_n + \Delta t$, have to be updated. Obviously two elements can not be executed in concurrency by the same channel, so if by chance an element pops up in a time portion of the channel occupied by another element, the second element (in terms of their starting times) automatically shifts to the end of the first one, thus granting that no overlapping occurs. The "cut-and-sew" process

[6]In Qt language, the controllers are also known as "delegates".

[7]The interactive plot is based on the widget "QtCustomPlot".

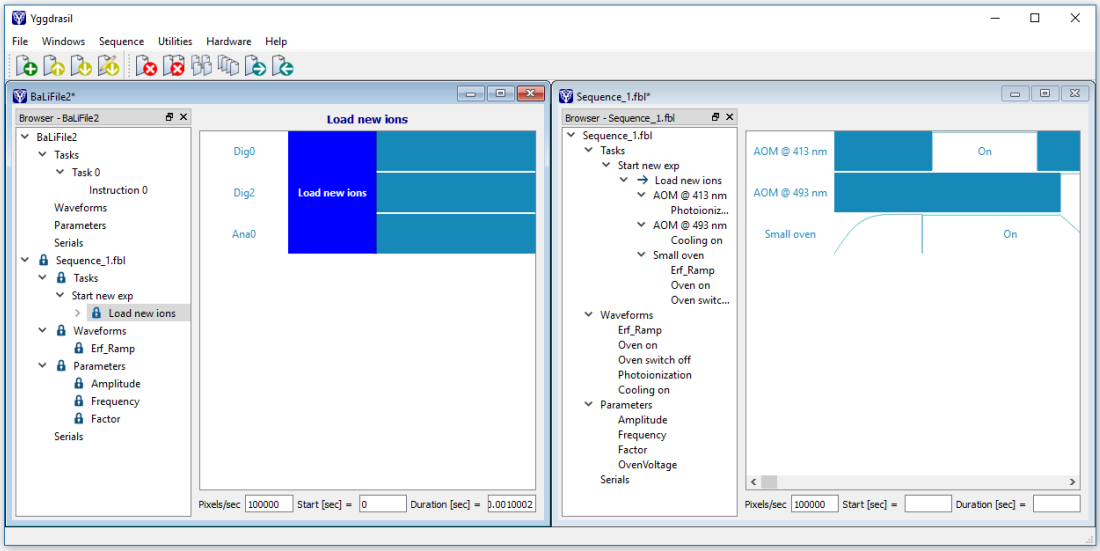

Figure 6.5: Screenshot of Yggdrasil during the creation of a sequence starting from a previously defined one.

of the data vectors is even more complicated when two instructions are merged together to realize a task, because Yggdrasil has to pay attention to the possible overlaps between the elements of the channels defined in both the instructions. In that case, one element shifts in time with respect to the other, but even all the other elements of the shifted instruction have to be moved, with the risk of causing further time-shifting.

A second way to create a sequence is starting from a previously defined (and possible optimized) one, as shown in Fig. 6.5. Actually, a saved sequence can be deserialized and be inserted in the model of a second one, thus making possible the recycling of its parameters, waveforms, instructions and tasks. This capability is fundamental to increase the efficiency and speed up the creation of new experimental cycles.

6.3 Control instrumentation

Yggdrasil constitutes the software part of a complete control system. The hardware counter-part of this project has been developed in collaboration with Claudio Calosso and co-workers from the Italian National Institute of Metrological Research (INRiM), and it will be further discussed in Sec. 6.3.1.

Yggdrasil has been designed to be easily adapted to different hardware devices, both commercial and custom-made. In fact, Yggdrasil was first tested by using two

commercial electronic cards, one producing digital signals (National Instruments, PXIe-6535) and one producing analog ones (National Instruments, PXIe-6738). These boards come with a `.dll` functions library which can be exploited to integrate their control into any custom software. The basic idea behind this integration is that dialogue between the software and the hardware is written only by using the provided functions of the library, and is enclosed in a "wrap" class which translates the Yggdrasil native data formats into the ones requested by the library prototypes.

The control of custom-made instrumentation is also possible with Yggdrasil. An example of a custom board integration is reported in Sec. 6.3.2.

6.3.1 The hardware part of the complete control system

Field-Programmable Gates Arrays (FPGAs) are the best means to reliably produce and detect fast and precise electronic signals, since they are programmable and ensure synchrony and a high power of parallel calculus. However, driving a complex experiment, such as a ion-atom hybrid system one, with a single FPGA chip is impossible, because of the limited internal memory and the finite number of I/O pins in the FPGA that would limit the number of signals that can be processed. Therefore, our solution consists in realizing a network of FPGAs linked between each other with a fast connection protocol, which controls Analog-to-Digital Converters (ADCs), Digital-to-Analog Converters (DACs), and Direct Digital Synthesizers (DDSs).

The strategy is to design only two different kinds of electronic board in order to reduce the complexity of the electronic hardware. A board (slave) is equipped – in a limited number – with different types of I/O signals that are needed to run an experiment, and to implement it into a scalable structure so that the number of channels can be increased by adding more slots to the general hardware. The action of the slave boards is controlled and reconfigured by one or more masters (the second type of design boards), which can independently manage the electronic signals generated by the slaves.

More in details, the two types of modules are

Master it handles the communication with the computers by using the Local-Area Network (LAN) standard, collects the data, and coordinates the slave boards. This module is based on a System on Chip (Cyclone V SOC) that integrates an FPGA and a processor. The latter increases the versatility of the hardware, since, with respect to an FPGA, it provides a larger memory and it allows to exectute more complex operations.

Slave it includes an FPGA and all the front-ends. Each module has two DDSs, four ADCs, four DACs, six digital outputs, and two digital inputs.

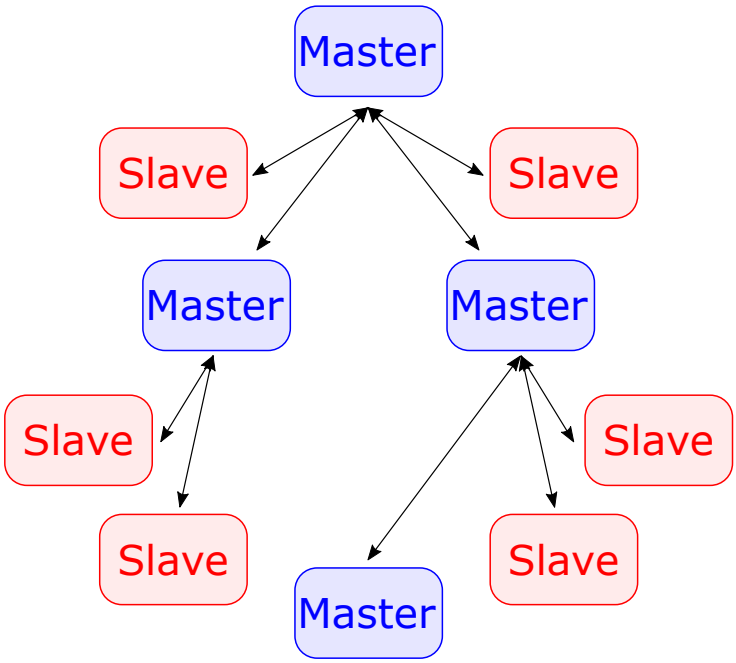

Figure 6.6: Example of the tree structure of the electronic hardware. The main master board communicates to the computer and coordinates the action of up to 6 slave boards. In case more slaves are needed, additional masters can be connected to a master present at any level of the tree.

In addition, a common advantage of both the two kinds of boards is that they need a single power supply of +12 V, whereas the other required voltages are generated by the voltage regulators present on board. Therefore, the whole system can be in principle powered by external batteries, a useful feature that allows to detach the control system from the noisy line and to manage portable experiments.

In order to make the system scalable and the distributed computation possible, the modular architecture of the electronics is based on a tree-like structure (see Fig. 6.6), as in the Yggdrasil design. The main master board is connected to the computers through a LAN and manages the entire system. Due to the limitations of the FPGA, no more than 6 devices (slave boards or secondary masters) can be connected to the main master. The simplest configuration is formed by 6 slaves connected to a master, and is characterized by 24 ADCs, 24 DACs, and 12 DDSs used as RF generators. However, if 6 slave boards were not sufficient, a second master can be substituted to a slave and connected to the main master; then, up to 6 other slaves can be linked to the second master, expanding the system to 11 slaves and 2 masters. Interestingly, this architecture makes the system scalable without any fundamental limitation, since an arbitrary number of master nodes can be added to the tree.

Within this architecture, it is fundamentals that the communication between the different modules of the tree structure is as fast as possible, in order to avoid delays and synchronization losses. That is the reason why the boards are interconnected with a fast serial link (up to about 3 Gbps) based on the transceivers embedded in the FPGAs. The efficiency of the communication between two modules of the system depends on their proximity in space and their hierarchy. For example, the most efficient communication between two slaves is realized if they are connected to the same master and they are physically close in space. Differently, slaves on different tree levels, i.e. connected to different masters, will suffer from a reduced data bandwidth. For instance, in the case of a certain amount of data sent from an ADC to a DAC for configuring a custom digital transfer function (e.g., a PID transfer function), the full data rate (100 MSa/s) and the lowest latency (few clock cycles) can be reached if the ADC and the DAC are on the same slave module. Instead, if they are on different slave modules connected to the same master, the sample rate is about one order of magnitude lower, causing more latency between input and output. Finally, the bandwidth would be further lowered by an additional order of magnitude if the slave modules are interconnected through different masters, but it can still reach the value of hundreds of kHz. A more detailed description of the hardware can be find in Refs. [171, 182].

6.3.2 Communication with a custom serial device

The lasers circuits described in Sec. 5.3 include optical devices as EOMs and AOMs whose functioning depends on their driving RF. The same RF is often used to generate an error signal by demodulating in a lock-in amplifier the photodiode signal of a modulated light. We have realized with Claudio Calosso at INRiM a double-purpose board that can be configured to work either as a lock-in amplifier or as an RF synthesizer (Fig. 6.7).

The board is based on a Direct Digital Synthesis (DDS) chip (Analog Devices AD9959, 4 channels at 500 MSPS with independent frequency/amplitude/phase control, 10 bits of amplitude resolution), controlled by an on-board microcontroller (Arduino Nano). If the board is configured to work as a lock-in, the output frequencies (R_0 and R_1) of two output channels (C_0 and C_1, respectively) are set to be equal, then RF_1 is sent to an EOM, while RF_0 is sent to an on-board mixer (Mini-Circuits, JMS-2W). The same can be done with the other two channels of the DDS, thus obtaining two independent lock-in amplifiers with the same board. Instead, if the board is configured as an AOM driver, then the four radiofrequencies independently generated by the DDS chip can be directly sent to the devices.

The control of the slot has been integrated with Yggdrasil thanks to the presence of a microcontroller on-board, which is fundamental for allowing the application to

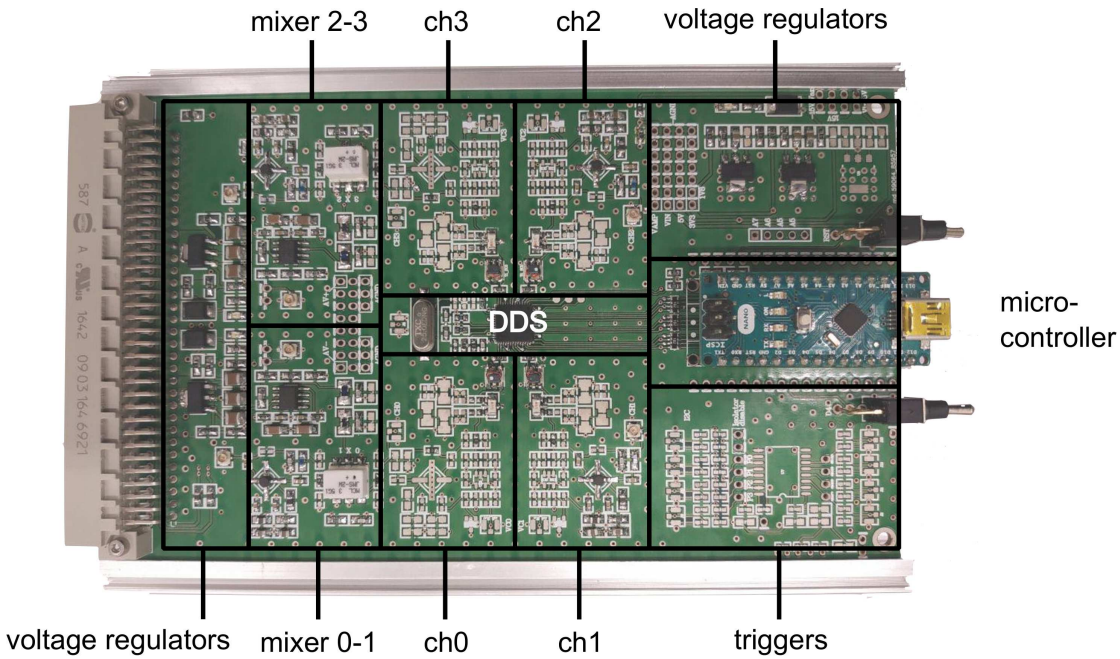

Figure 6.7: Picture of the double-purpose electronic board: by changing the configuration, it can work as a lock-in amplifier or an AOM driver.

communicate with the DDS, and for managing its memory registers. Consequently, the communication between Yggdrasil and the DDS, intermediated by the arduino, is divided into two segments: the communication between Yggdrasil and arduino, and the one between arduino and the DDS. The first is based on the serial protocol, so the data bits are transmitted in series down a micro-USB connection. The second, instead, follows the Serial Peripheral Interface (SPI), a synchronous serial data protocol used for quickly exchanging data.

The steps of the communication pattern are

- Yggdrasil sends to microcontroller commands and data codified in a simple meta-language developed *ad hoc*, which is formed by just the four commands reported in Code 6.4.
- the arduino script receives and translates the commands, then send them to the DDS in the accepted format.
- an answer is given to Yggdrasil at the end of the communication, which is equal to the command itself if there were no error during the data transmission. The Read function is an exception, since in that case arduino sends back to Yggdrasil the original command with the requested data.

```
/* Reset */
<s>

/* Update */
<u>

/* Write */
<w, registerNr, byteNr, newByte0, newByte1, newByte2, newByte3>

/* Read */
<r, registerNr, byteNr, readByte0, readByte1, readByte2, readByte3>
```

Code 6.4: Functions of the meta-language developed for the communication between Yggdrasil and the board microcontroller.

Yggdrasil to arduino communication Yggdrasil provides an intuitive graphic interface for modifying the DDS register contents. A change in the configuration is translated in a combination of meta-language commands and then sent to the arduino. The transmission operations are hosted in a different thread with respect to the application one, in order to parallelize the process and avoid freezing time. For example, let's suppose to vary the frequency of the first channel to the value 532.4 kHz. The user just change a number in a line-edit widget, but Yggdrasil produces and sends the following commands

```
<w, 0, 1, 32>
/* The channel 1 is activated and the other three channels are switched
   off, so in the register 0 (1 byte) the number 0010 0000 (= 32) is
   written. */

<w, 4, 4, 0, 139, 144, 192>
/* In the register 4 (4 bytes) the tuning word corresponding to 532.4
   kHz is written in 4 separated bytes. */

<u>
/* The DDS chip and the output frequency are updated. */
```

The commands production in terms of meta-language (which in turn is modeled on the data format accepted by the DDS) is not trivial, due to the fact that several DDS register bytes are dedicated to a collection of data, and not only to a single value. For instance, logic configurations, as a channel switched on or off, need just a bit to be stored, and consequently a register with only a byte can host a bundle of 8 states. This aspect of the registers reflects on the command construction,

since a user input can permute only a bit of memory, whereas the others must stay unaltered. This issue is circumvented in Yggdrasil by preserving a copy of the registers in a dedicated tree node, instance of the class `FileModelSerialItem`.

Arduino to DDS chip communication An arduino script is commonly divided into two functions: the first is `setup`, which is executed when the device is switched on or when a reset is called; the second is `loop` which keeps running after `setup` in an infinite loop. In this case, the script has been written in such a way that the setup function is responsible for the initialization of the SPI communication with the DDS, and the loop function has been instructed to recognize the meta-language commands and translate them into the DDS accepted data format. The `setup` function is reported in Code 6.5.

```
#include <SPI.h>

// ARDUINO NANO PINS FOR DDS
const int resetPin = 5;
const int ioUpdatePin = 7;
const int slaveSelectPin = 10;

void setup()
{
    Serial.begin(115200);

    // PIN SETTINGS
    pinMode(slaveSelectPin, OUTPUT);
    pinMode(ioUpdatePin, OUTPUT);
    pinMode(resetPin, OUTPUT);

    // RESET
    digitalWrite(slaveSelectPin, HIGH);
    digitalWrite(ioUpdatePin, LOW);
    digitalWrite(resetPin, HIGH);
    delay(100); // ms
    digitalWrite(resetPin, LOW);
    delay(100); // ms

    // SPI SETUP
    SPI.begin();
    SPI.setDataMode(SPI_MODE0);
}
```

Code 6.5: Text of the `setup` function of the arduino script.

Chapter 7

Conclusions and outlooks

This thesis is the first doctoral work on a new experimental activity at INRiM and at LENS that aims at realizing a hybrid system of trapped ions and ultracold atoms that can enter the quantum regime, i.e. that can undergo a coherent evolution. This represents an ambitious goal that no experimental group has so far been able to achieve. For creating this composite physical system, it is necessary to design and implement a complex apparatus in which the setups for creating and manipulating the two individual sub-systems must be seamlessly merged together.

A common thread in all the design phases of this novel experiment has been the vision of creating a strong technical backbone that can sustain the operation of a complex machine both in its first period and in future improvements. An example is undoubtedly the ion trap, the central element upon which all future experiments hinge. The trap assembly, which comprises both a linear Paul trap and the electro-optical trap, is the result of a long design process during which we made a strong use of numerical simulations of several aspects of the trap operation: the generation of the electrical potential, the heat distribution on the electrodes, the mechanical and thermal stress on the mirror mounts of the bow-tie cavity. Also the production of the technical drawing of each trap component was a stimulating challenge for an experimental physicist without any engineer background, especially considering that the local workshop at LENS did not have neither the know-how nor the capability of producing these small and precise parts.

The design of the ECDL mount and the development of a novel control program are two important parts of the technical backbone. On the one hand, the new ECDL designs, and in particular the modified Littrow one, represent an important asset for the group, especially considering the large number of laser sources that are needed to cool and manipulate the atom-ion mixture. On the other hand, the control program has been explicitly designed for our experiment, but in general is optimized for running any hybrid quantum system for which one may need to control separately different parts of the apparatus, e.g. for performing more than one experiment at the same time.

At the time of writing this thesis, we are dealing with the last steps for generating ultra-high vacuum in the ion trapping chamber. The experimental setup of the ions has been assembled, as well as all the laser sources and optical circuits for cooling and manipulating Barium ions. We can not wait to start the search for fluorescence light emitted by the first "Italian" trapped ions.

First, when the experiment will be in operation, we will start with the characterization of the linear Paul trap. This will include thermometry measurements on the ion samples and excess micromotion detection. Then, we will try to optically trap the ions in the EO trap. This phase will include the identification of the best procedure for transferring the ions from the Paul trap to the EO trap. At the same time, we will complete the experimental apparatus for producing quantum gases of Lithium. At the moment of writing, other members of the group are implementing the optical circuits for cooling and trapping the Lithium atoms, while most of the parts composing the vacuum setup are ready to be assembled. Therefore, we expect to proceed with the construction of the last part of the complete vacuum setup in parallel with the first measurements with the trapped ions. Finally, when also the "atomic" part of the experiment will be completed, we will merge the two vacuum systems. Then, we will first learn how to translate the ultracold atomic gas via optical transport before overlapping the quantum gases and the trapped ions, in order to realize a controllable quantum atom-ion mixture, the components of which will be simultaneously confined, cooled and detected.

In the longer term, this apparatus will be able to perform experiments that aim at shading light over open problems in atom-ion physics. The presence of the so-far elusive atom-ion Feshbach resonances will be investigated [183], and the coherence of the atom-ion coupling will be studied. Ideally, if the coherence can be maintained for a sufficiently long time, we could explore the entanglement between the ions and the atoms: the evolution of a small quantum gas can be entangled to a single ion internal state [184], thus realizing Schrödinger's cat-like states. Moreover, we plan at performing also metrological measurements by detecting possible collisional frequency shifts in high-precision spectroscopy of the $^2S_{1/2} \leftrightarrow {}^2D_{5/2}$ transition in Ba^+ in the presence of a dense Li buffer gas [185]. This first experiments will pave the way to use atom-ion quantum mixtures for tackling existing challenges in experimental quantum physics from a novel standpoint.

Appendix A

Atom-field interaction: the radiative force

The interaction between a classic monochromatic field and an atom is here derived in dipole approximation, i.e. the field wavelength is assumed to be longer than the atom size, so the field variations over the atom dimensions are neglected. The field with frequency ω has the form

$$\vec{E}(\vec{r},t) = \frac{1}{2}\,\vec{\varepsilon}\,E_0(\vec{r})\,e^{-i\omega t} \,+\, \text{c.c.},$$

where $\vec{\varepsilon}$ is the unitary polarization vector. The atom is instead modeled as a two-level system whose ground $|g\rangle$ and excited $|e\rangle$ states have an energy difference of $\hbar\,\omega_0$.

The hamiltonian describing the atom-field interaction is

$$\mathcal{H}_{AF} \,=\, -\,\vec{d}\cdot\vec{E} \tag{A.1}$$

where $\vec{d} = -|e|\vec{r}$ is the dipole operator, which can be developed as

$$\vec{d} \,=\, -e\,\langle g|\vec{r}\,|e\rangle\,\Big(|g\rangle\langle e| \,+\, |e\rangle\langle g|\Big)$$

Therefore Eq. A.1 can be rewritten as

$$\mathcal{H}_{AF} \,=\, \frac{\hbar}{2}\Big(\Omega(\vec{r})\;|e\rangle\langle g| \,+\, \Omega^*(\vec{r})\;|g\rangle\langle e|\Big) \tag{A.2}$$

where $\Omega(\vec{r})$ is the Rabi frequency defined as

$$\Omega(\vec{r}) \,=\, \frac{2\,e\,\langle g|\vec{\varepsilon}\cdot\vec{r}\,|e\rangle\,E_0(\vec{r})}{\hbar} \,=\, |\Omega(\vec{r})|\,e^{\phi(\vec{r})}$$

In order to evaluate the force experimented by the atom due to its interaction with the field, we can express the force operator in the Heisenberg picture as

$$\begin{aligned}\vec{F} &= \frac{\partial \vec{p}}{\partial t} = \frac{i}{\hbar}[\mathcal{H}, \vec{p}] = -\nabla \mathcal{H}_{AF} \\ &= -\frac{\hbar}{2}\nabla\Omega(\vec{r})\ |e\rangle\langle g| + \text{c.c.} \\ &= -\frac{\hbar\,\Omega(\vec{r})}{2}\left(\frac{\nabla|\Omega(\vec{r})|}{|\Omega(\vec{r})|} + \nabla\phi(\vec{r})\right)|e\rangle\langle g| + \text{c.c.}\end{aligned} \tag{A.3}$$

Since we are interested in the mean force $\langle\vec{F}\rangle$ acting on the atom, the mean value of operator $|e\rangle\langle g|$ has to be taken. This mean value finds a direct correspondence with the element ρ_{ge} of the density matrix [186]. In fact, given the generic atomic state ψ as the superposition of the two free atomic hamiltonian eigenstates

$$\psi = a_g|g\rangle + a_e|e\rangle$$

where a_g and a_e are two complex coefficients such that $|a_g|^2 + |a_e|^2 = 1$, the density matrix operator can be defined as

$$\hat{\rho} = |\psi\rangle\langle\psi| = \begin{pmatrix} |a_g|^2 & a_e^* a_g \\ a_g^* a_e & |a_e|^2 \end{pmatrix} = \begin{pmatrix} \rho_{gg} & \rho_{eg} \\ \rho_{ge} & \rho_{ee} \end{pmatrix} \tag{A.4}$$

where the diagonal elements represent the probability to find an atom in a level (ground ρ_{gg} or excited ρ_{ee}), while the off-diagonal elements the coupling strength between the levels. The explicit expressions of the density matrix elements can be found by solving the optical Bloch equations [187]. These equations describe the dynamics of a two-state quantum system interacting with an monochromatic electromagnetic radiation providing the temporal variations of the two coherences (ρ_{eg} and ρ_{ge}) and the population difference (i.e. $\rho_{gg} - \rho_{ee}$) between the two states $|g\rangle$ and $|e\rangle$.

In rotating wave approximation [188], ρ_{ge} can be written as

$$\begin{aligned}\rho_{ge} = \rho_{eg}^* &= \frac{\Omega^*}{2}\frac{\delta + i\Gamma/2}{\delta^2 + \Gamma^2/4 + \Omega^2/2} \\ &= \frac{i\Omega^*}{2\,(s+1)(\Gamma/2 + i\delta)}\end{aligned} \tag{A.5}$$

where $\delta = \omega - \omega_0$ represents the detuning between the laser frequency and the atomic resonance,

$$\Gamma = \frac{\omega_0^3 e^2}{3\pi\epsilon_0\hbar c^3}\langle e|\vec{r}|g\rangle^2$$

is the radiative decay rate, and

$$s(\vec{r}) = \frac{\Omega^2/2}{\Gamma^2/4 + \delta^2}$$

is the saturation parameter.

Hence, the mean radiative force of Eq. A.3 can be expressed by taking into account Eq. A.5 as

$$\begin{aligned}\langle\vec{F}\rangle &= \frac{\hbar s(\vec{r})}{1+s(\vec{r})}\left(-\delta\frac{\nabla\Omega(\vec{r})}{\Omega(\vec{r})} + \frac{\Gamma}{2}\nabla\phi(\vec{r})\right) \\ &= \langle\vec{F}_{dip}\rangle + \langle\vec{F}_{rad}\rangle\end{aligned} \tag{A.6}$$

Equation A.6 suggests that the mean force is composed by two different contributions $\langle\vec{F}_{dip}\rangle$ and $\langle\vec{F}_{rad}\rangle$, analyzed in the following.

A.1 Dipolar force

The first term of Eq. A.6 can be rewritten in terms of $\nabla s(\vec{r})$ as

$$\nabla s(\vec{r}) = 2\,s\frac{\nabla\Omega(\vec{r})}{\Omega(\vec{r})}$$

$$\vec{F}_{dip} = -\frac{\hbar\,s\,\delta}{1+s}\frac{\nabla\Omega(\vec{r})}{\Omega(\vec{r})} = -\frac{\hbar\,\delta}{2}\nabla\log(1+s) = -\nabla U_{dip}(\vec{r})$$

where the mean value sign $\langle\cdot\rangle$ has been dropped for simplicity. The last passage of the Eq. A.1 reveals the conservative nature of the radiative force contribution: in fact, it can be expressed as the gradient of a scalar function U_{dip}, which can be further developed as

$$U_{dip}(\vec{r}) = \frac{\hbar\,\delta}{2}\log(1+s) = \frac{\hbar\,\delta}{2}\log\left(1+\frac{I(\vec{r})/I_{sat}}{1+4\delta^2/\Gamma^2}\right) \tag{A.7}$$

where

$$I_{sat} = \frac{c\varepsilon_0\Gamma^2\hbar^2}{4e^2|\langle g|\vec{\varepsilon}\cdot\vec{r}|e\rangle|^2} \tag{A.8}$$

is the saturation intensity, and ε_0 is the vacuum dielectric constant.

Eq. A.7 gives the dipolar potential on a stationary atom for any field intensity. It can be noticed that U_{dip} keeps increasing with the field intensity I, even if logarithmically, and the detuning δ determines if the force on the atom is attractive or repulsive.

$$\begin{aligned}&\delta < 0 \Rightarrow \omega < \omega_0 \text{ (red detuning)} \quad \Rightarrow F_{dip} > 0 \text{ (attractive)} \\ &\delta > 0 \Rightarrow \omega > \omega_0 \text{ (blue detuning)} \quad \Rightarrow F_{dip} < 0 \text{ (repulsive)}\end{aligned}$$

When the angular frequency of the field is far from the atom resonance in comparison with the Rabi frequency and the decay rate, i.e. $|\delta| \gg \{|\Omega|, \Gamma\}$, then the dipole force assumes the form [120]

$$U_{dip} \approx \frac{\hbar\,|\Omega(\vec{r})|^2}{4\,\delta} = \frac{\hbar\Gamma^2}{8\delta}\frac{I(\vec{r})}{I_{sat}} = \frac{3\pi c^2}{2\omega_0^3}\frac{\Gamma}{\delta}\,I(\vec{r}) \tag{A.9}$$

Atomic polarizability

The dipole potential can be also expressed in terms of the atomic polarizability $\alpha(\omega)$. Relaxing the two-level approximation and reintroducing the counter-rotating term in the dipole potential, Eq. A.9 for the state $|\alpha\rangle$ in large detuning conditions becomes

$$\begin{aligned} U_{dip,\,\alpha}(\omega) &= \sum_\beta \left(e^2 \frac{|\langle\alpha|\vec{\varepsilon}\cdot\vec{r}\,|\beta\rangle|^2\,|E_0(\vec{r})|^2}{\hbar\,(\omega_{\beta\alpha}-\omega)} - e^2 \frac{|\langle\alpha|\vec{\varepsilon}\cdot\vec{r}\,|\beta\rangle|^2\,|E_0(\vec{r})|^2}{\hbar\,(\omega_{\beta\alpha}+\omega)} \right) \\ &= -e^2 \sum_\beta \frac{2\,\omega_{\beta\alpha}\,|\langle\alpha|\vec{\varepsilon}\cdot\vec{r}\,|\beta\rangle|^2}{\hbar\,({\omega_{\beta\alpha}}^2+\omega^2)}\,|E_0(\vec{r})|^2 \\ &= -\alpha(\omega)\,|E(\vec{r})|^2 \end{aligned}$$

Including the angular-momentum degeneracy, the two generic state $|\alpha\rangle$ and $|\beta\rangle$ can be written as $|J, m_J\rangle$ and $|J', m_{J'}\rangle$. The polarizability now yields

$$\alpha_{J,m_J}(\omega) = \sum_{J',m_{J'}} 2\,\omega_{J',J}\,\frac{\langle J, m_J|\vec{\varepsilon}\cdot\vec{r}\,|J', m_{J'}\rangle\,\langle J', m_{J'}|\vec{\varepsilon}\cdot\vec{r}\,|J, m_J\rangle}{\hbar\,({\omega_{J',J}}^2+\omega^2)}$$

This tensor can be decomposed into its irreducible parts, and the general atomic polarizability can be expanded as [189]

$$\begin{aligned} U_{dip,\,J,\,m_J}(\omega) = &-\frac{1}{2}\,\alpha_J^{(0)}(\omega)\,|E(\vec{r})|^2 \\ &+\frac{m_J}{2\,J}\,\alpha_J^{(1)}(\omega)\,|\vec{E}(\vec{r})^*\times\vec{E}(\vec{r})| \\ &-\frac{1}{2}\,\alpha_J^{(2)}(\omega)\left(\frac{3m_J^2-J(J+1)}{J(2J-1)}\right)\frac{3E_z-|E(\vec{r})|^2}{2} \end{aligned} \tag{A.10}$$

where the scalar, vector and tensor polarizability are respectively

$$
\begin{aligned}
\alpha_J^{(0)}(\omega) &= \frac{2}{3\,(2J+1)\hbar}\sum_{J'}\frac{e^2\,\omega_{J',J}}{\omega_{J',J}^2-\omega^2}|\langle J'||\vec{r}||J\rangle|^2 \\
\alpha_J^{(1)}(\omega) &= -\frac{1}{(2J+1)\hbar}\sum_{J'}\frac{e^2\,\omega}{\omega_{J',J}^2-\omega^2}|\langle J'||\vec{r}||J\rangle|^2 \\
&\left(-\frac{\delta_{J-1,J'}}{J}-\frac{\delta_{J,J'}}{J(J+1)}+\frac{\delta_{J+1,J'}}{J+1}\right) \\
\alpha_J^{(2)}(\omega) &= \alpha_J^{(0)}(\omega)\left(-\delta_{J-1,J'}+\frac{2J-1}{J+1}\delta_{J,J'}-\frac{J(2J+1)}{(J+1)(2J+3)}\delta_{J+1,J'}\right)
\end{aligned}
$$

where $\delta_{x,y}$ is the Kronecker delta and $\langle J'||\vec{r}||J\rangle$ is the reduced matrix element.

In general, if the $J = 1/2$ as in alkali-like atoms ground state and the electric field polarization is linear, only the scalar part $\alpha^{(0)}$ of the atomic polarizability contributes to the dipolar potential energy, which reduces to

$$
\begin{aligned}
U_{dip,\,J}(\omega) &= -\frac{1}{6\hbar}\sum_{J'}\frac{e^2\,\omega_{J',J}}{\omega_{J',J}^2-\omega^2}\,|\langle J'||\vec{r}||J\rangle|^2\,|E(\vec{r})|^2 \\
&= -\frac{1}{3\varepsilon_0 c\hbar}\sum_{J'}\frac{e^2\,\omega_{J',J}}{\omega_{J',J}^2-\omega^2}\,|\langle J'||\vec{r}||J\rangle|^2\,I(\vec{r})
\end{aligned}
\tag{A.11}
$$

In the two-level atom and RWA approximations, Eqs. A.9 and A.11 are equivalent.

A.2 Radiation pressure

The second term of Eq. A.6 can be expressed in terms of ρ_{ee} as follows

$$
\begin{aligned}
\rho_{ee} &= \frac{1}{2}\frac{\Omega^2/2}{\delta^2+\Gamma^2/4+\Omega^2/2} = \frac{1}{2}\frac{s}{(s+1)} \\
\vec{F}_{rad} &= \left(\Gamma\,\rho_{ee}\right)\left(\hbar\,\nabla\phi(\vec{r})\right)
\end{aligned}
\tag{A.12}
$$

In case the field is described by a plane wave, $\phi(\vec{r}) = \vec{k}\cdot\vec{r}$ and $\nabla\phi(\vec{r}) = \vec{k}$. Since ρ_{ee} represents the probability for an atom to be in the $|e\rangle$ state and Γ the decay rate from $|e\rangle$ to $|g\rangle$, then the force $\vec{F}_{rad}$ can be interpreted as the the total photon scattering rate multiplied for the momentum recoil $\hbar\vec{k}$ (that is the reason why this radiative force contribution is called radiation pressure). Instead, in case the field is a standing wave (for example produced by the interference of two counter-propagating plane waves), $\phi(\vec{r})$ is constant and consequently the radiation pressure is null.

The radiation pressure does not vanish near the resonance ($\delta \approx 0$) as instead the dipole force which tends to zero linearly with the detuning. For this reason, the radiation pressure is much more sensitive to the velocity of the atom, since it affects the laser frequency in the atom's frame due to the Doppler effect. If $\vec{v}$ is the atom velocity, then the detuning becomes

$$\delta_{\text{eff}} = \omega - \omega_0 - \vec{k} \cdot \vec{v}$$

and the radiation pressure can be reformulated to include the velocity dependence as

$$\vec{F}_{rad} = \frac{\hbar\Gamma}{4} \frac{\Omega^2/2}{\delta^2 - (\vec{k} \cdot \vec{v})^2 + \Gamma^2/4 + \Omega^2/2} \nabla\phi(\vec{r}) \tag{A.13}$$

Appendix B

Second harmonic generation theory

Second harmonic generation (SHG), a specific case of sum-frequency generation, is an non-linear optical process in which two photons with the same frequency interact with a non-linear material, annihilate and generate a new single photon with twice the energy of the initial photons.

In general, the response of a material to an optical stimulation can be expressed in terms of the induced polarization $\vec{P}$, which can be written as [141]

$$P_k = \varepsilon_0 \left(\chi_k^{i\,(1)} E_i \, + \, \chi_k^{i,j\,(2)} E_i E_j \, + \, \chi_k^{i,j,l\,(3)} E_i E_j E_l \, + \, \ldots \right) \tag{B.1}$$

where ε_0 is the vacuum dielectric constant and the coefficients $\chi^{(n)}$ are the n-order tensors describing the material electric susceptibility.

If the optical response of the material is linear and isotropic, then the electric susceptibility is a number and Eq. B.1 reduce to

$$\vec{P} = \varepsilon_0 \, \chi^{(1)} \, \vec{E} \quad \text{with} \quad n^2 = \varepsilon/\varepsilon_0 = (1 + \chi^{(1)}) \tag{B.2}$$

where n is the refractive index of the material.

The SHG process arises from the interaction of the electric field with a non-linear material at the second order of the electric susceptibility. Including the first and the second orders of the polarization $\vec{P}$ and taking into account Eq. B.2, the Ampere's law can be written in differential form as

$$\frac{1}{\mu_0} \nabla \times \vec{B} = \frac{\partial \vec{D}}{\partial t} = \varepsilon \, \frac{\partial \vec{E}}{\partial t} \, + \, \frac{\partial \vec{P}^{(2)}}{\partial t}$$

By substituting the curl of Faraday's law, the above equation yields

$$\nabla^2 \vec{E} - \mu_0 \, \varepsilon \, \frac{\partial^2 \vec{E}}{\partial t^2} = \mu_0 \, \frac{\partial^2 \vec{P}^{(2)}}{\partial t^2} \tag{B.3}$$

To solve Eq. B.3, the following assumptions are made

- the plane wave $\vec{E}$ rotates at $2\,\omega$ and the source of the non-linear polarization $\vec{P}^{(2)}$ is the input electric field with a frequency of ω, then the two electric fields can be expressed by

$$E_i^{(\omega)} = \epsilon_i^{(\omega)}\, E_0^{(\omega)} \exp(-i\omega t - k^{(\omega)} z) \;+\; c.c.$$

$$E_i^{(2\omega)} = \epsilon_i^{(2\omega)}\, E_0^{(2\omega)} \exp(-i2\omega t - k^{(2\omega)} z) \;+\; c.c.$$

  where $\epsilon_i^{(\omega)}$ and $\epsilon_i^{(2\omega)}$ with $i = x, y$ are the components of the electric polarization vectors. $E_0^{(\omega)}$ and $E_0^{(2\omega)}$ are the field amplitudes.

- the electrical polarization vectors slowly vary as a function of z.
- the second derivatives in x and y vanish.
- this relation is valid

$$\frac{dE_i^{(2\omega)}}{dz}\, k^{(2\omega)} \gg \frac{d^2 E_i^{(2\omega)}}{dz^2}$$

Applying the listed approximations, Eq. B.3 becomes

$$\frac{dE_k^{(2\omega)}}{dz} \;=\; -\,i\,\frac{\omega}{2}\sqrt{\frac{\mu_o}{\varepsilon^{(2\omega)}}}\sum_{i,j}\chi_k^{i,j\,(2)}\, E_i^{(\omega)}\, E_j^{(\omega)}\, e^{-2ik^{(\omega)}z} \tag{B.4}$$

where $\varepsilon^{(2\omega)}$ is the electric permittivity of the medium at $2\,\omega$. Equation B.4 can be integrated with $E^{(2\omega)}(z = 0) = 0$ as boundary condition and with the supposition that there is no depletion of $E^{(\omega)}$ along the crystal. The result is

$$E_k^{(2\omega)}(L) \;=\; -\,\frac{\omega}{2}\sqrt{\frac{\mu_0}{\varepsilon^{(2\omega)}}}\sum_{i,j}\chi_k^{i,j\,(2)}\, E_i^{(\omega)}\, E_j^{(\omega)}\,\frac{e^{i\Delta k L}}{\Delta k} \tag{B.5}$$

where L is the length of the material and $\Delta k = k^{(2\omega)} - 2k^{(\omega)}$.

From Eq. B.5, the efficiency of the doubling process can be evaluated as the ratio between generated $(2\,\omega)$ and incoming (ω) light intensities

$$\frac{I^{(2\omega)}}{I^{(\omega)}} \;\sim\; \frac{\omega^2 L^2}{(n^{(\omega)})^3}\, I^{(\omega)}\,\frac{\sin^2(\Delta k L/2)}{(\Delta k L/2)^2} \tag{B.6}$$

This equation shows the characteristic dependence of the efficiency on the medium length and the incoming light power, i.e. the power of the second harmonic depends on the second power of the fundamental power.

The last factor of Eq. B.6 vanishes when $\Delta K \cdot L = 2\pi$, whereas reaches its maximum value when $\Delta k = 0$, which is known as phase matching condition. In order to obtain the most efficient SHG process, the fundamental and the second harmonic must be in a perfect phase matching, meaning that their phase velocities in the medium and their refraction indexes must be equal

$$v^{(2\omega)} = v^{(\omega)} \quad \text{and} \quad n^{(2\omega)} = n^{(2\omega)} \tag{B.7}$$

In order to realize these conditions, two methods are usually employed: exploiting the birefringence of the medium (birefringent crystals) or obtaining the condition of "quasi-phase matching". The first option is based on the fact that the index of refraction increases with frequency in normal dispersion conditions. If the fundamental polarization is aligned with the optical axis of a positive uniaxial, i.e. it propagates with a refraction index (called extraordinary, n_e) larger than the second harmonic one (ordinary refraction index, n_o), then there is a wavelength for which the two refraction indexes have the same value. The drawback is that this condition is valid only for a single wavelength. However, n_e can be tuned by changing the angle between the propagation of the fundamental and the crystal optical axis: this makes the phase matching possible for a wider range of wavelengths. Another drawback is that the energy propagation of the fundamental and the second harmonic diverges. The displacement of the two beams, the so-called "walk-off", limits the effective crystal length and the conversion efficiency. Moreover, also the output beam quality will get worse.

The second solution for achieving the conditions resumed in Eqs. B.7 is the so-called quasi-phase matching, a method based on the possibility of modulated the wave vector k by injecting the fundamental into a gain medium whose refractive index periodically varies with a period of Λ. In such case, the phase matching condition yields

$$\frac{2\pi}{\Lambda} + \Delta k = 0$$

which can be reformulated as

$$\Lambda = \lambda \left(\frac{1}{r}\right)$$

where $r = \Delta\lambda/\lambda$ is the phase mismatch ($\Delta\lambda$ represents the difference between the optimal and the desired wavelengths). Therefore, the spatial period of the crystal needed for the quasi-phase matching should be equal to the desired wavelength times the reciprocal of the phase mismatch. For instance, with a mismatch of 5%, the proper crystal should be built with a spatial periodicity of five times the wavelength.

In quasi-phase matching condition, thermal stabilization becomes extremely important since temperature fluctuations cause variations of the refractive index and the periodicity length Λ of the crystal [190], accordingly to

$$\Delta T = \frac{0.443\,\lambda}{L}\left|\frac{\partial \Delta n}{\partial T} + \alpha\,\Delta n\right|^{-1}$$

where ΔT is the temperature acceptance, α is the thermal expansion coefficient of the crystal and $\Delta n = n^{(2\omega)} - n^{(\omega)}$.

The treatment above described of the second harmonic generation process has been derived by assuming the laser beams as plane waves. A more realistic model is to consider them as gaussian beams focused into the center of the crystal in order to enhance the local intensity and thus the conversion efficiency [191]. This means that there is an optimal value of the fundamental beam waist ω_0 (and Rayleigh range z_R as well) which arises from a trade-off between a strong focusing and a weaker one. In the first case, high intensity in the center of the crystal can be obtained, but also a rapid beam expansion that will not exploit the entire length of the medium. In the second case, instead, the crystal would be adequately exploited, but the second harmonic intensity will suffer due to scarce conversion efficiency. In order to obtain an even more realist picture of this process, the double refraction and the medium absorption should be considered too: in fact, the presence of these two mechanisms can reduce the SHG efficiency.

By defining the following significant parameters[1]

$z_R = \pi\omega_0^2/\lambda$	Rayleigh range
$\sigma = z_R \Delta k$	phase mismatch
$\delta_0 = \omega_0/z_R = (2/z_R k^{(\omega)})^{1/2}$	diffraction semi-angle
ρ	walk-off angle
$\beta = \rho/\delta_0$	normalized walk-off angle
$\xi = L/2z_R$	crystal length in Rayleigh range units
$\alpha^{(\omega)}, \alpha^{(2\omega)}$	absorption coefficients
$\kappa = (\alpha^{(\omega)} - \alpha^{(2\omega)}/2)\, z_R/2$	normalized absorption coefficient
z_0	beam waist position
$\mu = (L - 2z_0)/L$	normalized beam waist position

[1]These parameters describe the laser beam in the crystal. If the crystal was removed, the beam would have Rayleigh range $z_R/n^{(\omega)}$, diffraction semi-angle $\delta_0 n^{(\omega)}$, wave-vector $k_1/n^{(\omega)}$, and waist position $z_0/n^{(\omega)}$.

and rewriting the fundamental gaussian beam as a function of the z-coordinate in Rayleigh range units as

$$E^{(\omega)} = \frac{1}{1+i\tau}\exp\Big(ik^{(\omega)}z - \frac{r^2}{\omega_0(1+i\tau)}\Big) \quad \text{with} \quad \tau = z/z_R$$

the second harmonic power can be described as [165]

$$P^{(2\omega)} \simeq {P^{(\omega)}}^2\, L\, k^{(\omega)}\, h(\sigma,\beta,\kappa,\xi,\mu)\exp\Big(-(\alpha^{(\omega)}+\alpha^{(2\omega)}/2)\, L\Big) \tag{B.8}$$

where $h(\sigma,\beta,\kappa,\xi,\mu) =$

$$\frac{1}{4\xi}\exp\Big(2\,\mu\,\xi\,\kappa\,L\Big)\int\int_{-\xi(1-\mu)}^{\xi(1+\mu)} d\tau\, d\tau'\, \frac{\exp\Big(-\kappa(\tau+\tau')+i\sigma(\tau-\tau')-\beta^2(\tau-\tau')^2\Big)}{(1+i\tau)(1-i\tau)}$$

Interestingly, the above equation shows that the second harmonic power scales with the crystal length rather than its square power, as in the case of plane waves (see Eq. B.6). The function $h(\sigma,\beta,\kappa,\xi,\mu)$ contains all the optimizable parameters that describe the second harmonic generation in a crystal with a focused gaussian beam as fundamental source, but it can be simplified if the beam waist is supposed to be right in the center of the crystal ($\mu = 0$) and if the medium absorption can be neglected ($\kappa = 0$). At this point, the double refraction coefficient B and the aperture length L_a can be defined as

$$B = \beta\xi^{1/2} = \rho\,(L\,k_1)^{1/2}/2$$

$$L_a = \sqrt{\pi}\omega_0/\rho$$

The aperture length can be interpreted as the distance over which the fundamental and the second harmonic separate. Instead, the double refraction coefficient can be thought as the inverse of the fraction of the crystal length over which the two beams overlap [192]. Therefore, if e.g. $B = 5$, the beams overlap for a distance equal to the 5% of the crystal length. If a periodically poled crystal is chosen as non-linear medium, then the double refraction coefficient is null ($B = 0$) since in quasi-phase matching condition both the fundamental and the second harmonic are ordinary waves and have the same polarization [193]. With these assumptions, Eq. B.8 yields

$$H(\sigma,\xi) \equiv h(\sigma,\,0,\,0,\,\xi,\,0) = \frac{1}{4\xi}\Big(\int_{-\xi}^{\xi}\frac{\cos(\sigma\tau)+\tau\sin(\sigma\tau)}{1+\tau^2}\,d\tau\Big)^2$$

which depends only on the phase mismatch and the focusing parameter. The phase mismatch can be manipulated by adjusting and tilting the position of the

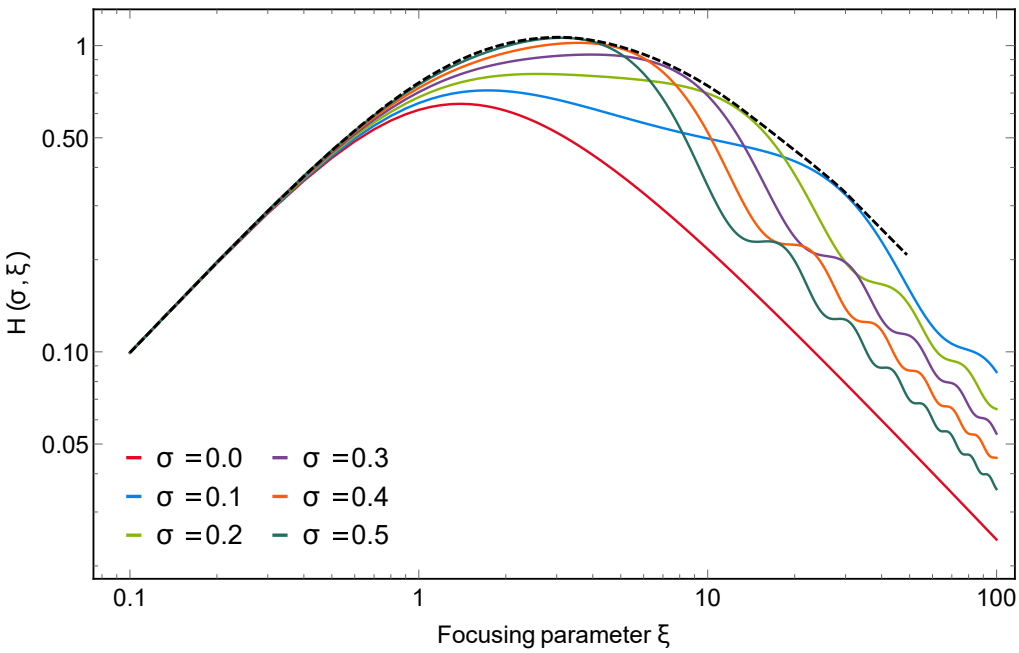

Figure B.1: A set of $H(\sigma, \xi)$ functions plotted for different mismatch parameters σ. The black dashed line is the upper envelope of these curves, and its highest value is reached at $\xi = 2.84$.

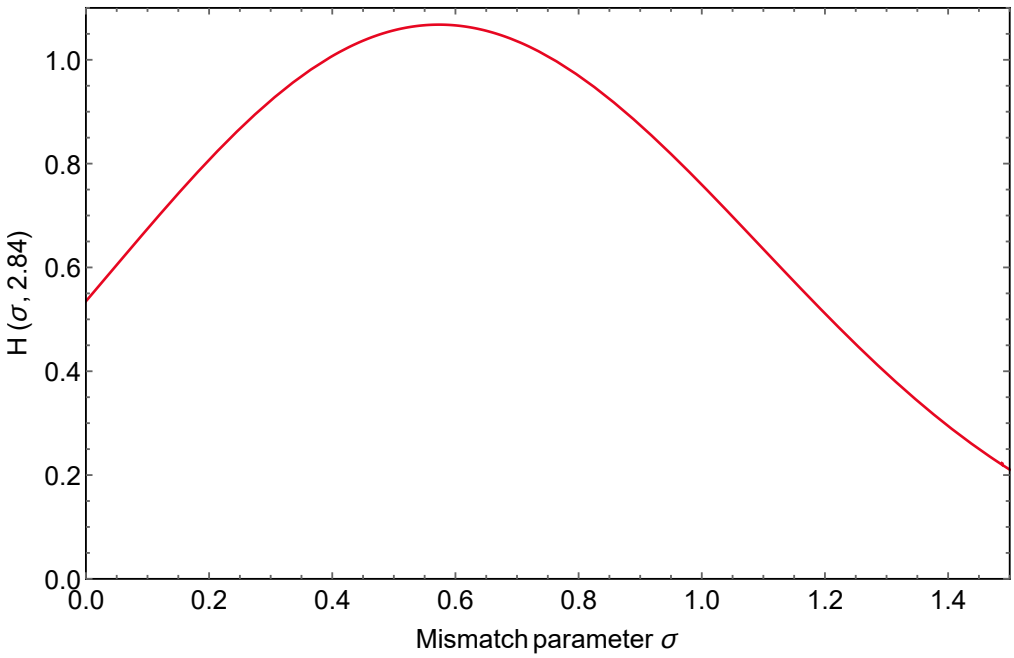

Figure B.2: Plot of the function $H(\sigma, \xi)$ with the optimized focusing parameter $\xi = 2.84$. Its maximum value assumed is 1.068.

crystal with respect to the fundamental beam direction, or by properly tuning the crystal temperature.

The evolution of $H(\sigma, \xi)$ as a function of the beam focusing is reported in Fig. B.1 for a set of σ values. The black dashed line is the upper envelope of the curves $H(\sigma, \xi)$ evaluated at different σ, and represents the collection of the best mismatching conditions for each focusing parameter. The ξ value that maximizes the envelope is 2.84 [165]. In the end, $H(\sigma, 2.84)$ is plotted in Fig. B.1 as a function of σ. Under ideal focusing conditions, the maximum value assumed by $H(\sigma, \xi)$ is 1.068.

SHG with optical resonators Typically, single-pass SHG has a low conversion efficiency, therefore a common technique for enhancing the second harmonic power is to use a resonant cavity that increases the incident fundamental beam power by a factor depending on the cavity finesse $\mathcal{F}$, and the second harmonic by $\mathcal{F}^2$ [194]. Usually, a bow-tie cavity is used for this scope, since it does not provide any back-reflection to the laser source and, in addition, its traveling wave passes through the crystal only in a single direction, thus producing only a SHG beam instead of two opposite beams as in a standing wave resonator.

The cavity must be designed on the basis of the features of the non-linear crystal: in particular, the crystal length and the optimal mismatch parameter impose a constraint on the beam waist inside the medium. The insertion of an optical element in the cavity can cause power losses due to the reflections on its facets. The solutions to this inconvenience can be using an anti-reflection coated crystal or cutting the crystal in such a way that the beam impinges on it at Brewster's angle. Once the crystal has been selected, the geometry of the cavity can be built to produce the desired waist in the right position. The mirrors coating has to be defined by taking into account that the impedance matching strategy must include the fundamental power depletion due to the second harmonic generation.

If the intensity of the second harmonic in Eq. B.8 is reformulated as

$$I^{(2\omega)} = \eta \, {I^{(\omega)}}^2 \tag{B.9}$$

the intensity transmission coefficient of the first mirror T_1 (input coupler) for the fundamental beam in impedance matching condition must be [141]

$$T_1 = \frac{L}{2} + \sqrt{\frac{L^2}{4} + \eta I^{(\omega)}} \tag{B.10}$$

where L are the total amount of losses during a cavity round trip (assumed to be $L \ll 1$ in this formula derivation). The impedance-matched second harmonic intensity is then

$$I^{(2\omega)} = \frac{4\,\eta\,{I^{(\omega)}}^2}{\left(L + \sqrt{L^2 + 4\,\eta\,I^{(\omega)}}\right)^2}$$

Bibliography

[1] M. Drewsen. "Ion Coulomb crystals". In: *Physica B Condensed Matter* 460 (Mar. 2015), pp. 105–113. DOI: 10.1016/j.physb.2014.11.050.

[2] D. J. Wineland et al. "Experimental issues in coherent quantum-state manipulation of trapped atomic ions". In: *eprint arXiv:quant-ph/9710025* (Oct. 1997). eprint: quant-ph/9710025.

[3] D. Leibfried et al. "Quantum dynamics of single trapped ions". In: *Rev. Mod. Phys.* 75 (1 Mar. 2003), pp. 281–324. DOI: 10.1103/RevModPhys.75.281. URL: https://link.aps.org/doi/10.1103/RevModPhys.75.281.

[4] H. Häffner, C. F. Roos, and R. Blatt. "Quantum computing with trapped ions". In: 469 (Dec. 2008), pp. 155–203. DOI: 10.1016/j.physrep.2008.09.003. arXiv: 0809.4368 [quant-ph].

[5] Andrew D. Ludlow et al. "Optical atomic clocks". In: *Rev. Mod. Phys.* 87 (2 June 2015), pp. 637–701. DOI: 10.1103/RevModPhys.87.637. URL: https://link.aps.org/doi/10.1103/RevModPhys.87.637.

[6] S. Willitsch. "Coulomb-crystallised molecular ions in traps: methods, applications, prospects". In: *International Reviews in Physical Chemistry* 31.2 (2012), pp. 175–199. DOI: 10.1080/0144235X.2012.667221. URL: https://doi.org/10.1080/0144235X.2012.667221.

[7] John Weiner et al. "Experiments and theory in cold and ultracold collisions". In: *Rev. Mod. Phys.* 71 (1 Jan. 1999), pp. 1–85. DOI: 10.1103/RevModPhys.71.1. URL: https://link.aps.org/doi/10.1103/RevModPhys.71.1.

[8] F. Nogrette et al. "Single-Atom Trapping in Holographic 2D Arrays of Microtraps with Arbitrary Geometries". In: *Physical Review X* 4.2, 021034 (Apr. 2014), p. 021034. DOI: 10.1103/PhysRevX.4.021034. arXiv: 1402.5329 [physics.atom-ph].

[9] Immanuel Bloch, Jean Dalibard, and Wilhelm Zwerger. "Many-body physics with ultracold gases". In: *Rev. Mod. Phys.* 80 (3 July 2008), pp. 885–964. DOI: 10.1103/RevModPhys.80.885. URL: https://link.aps.org/doi/10.1103/RevModPhys.80.885.

[10] C. Chin et al. "Feshbach Resonances in Ultracold Gases". In: *arXiv e-prints*, arXiv:0812.1496 (Dec. 2008), arXiv:0812.1496. arXiv: 0812.1496 [cond-mat.other].

[11] M. Lewenstein et al. "Ultracold atomic gases in optical lattices: mimicking condensed matter physics and beyond". In: *Advances in Physics* 56.2 (2007), pp. 243–379. DOI: 10.1080/00018730701223200. URL: https://doi.org/10.1080/00018730701223200.

[12] H. Bernien et al. "Probing many-body dynamics on a 51-atom quantum simulator". In: 551 (Nov. 2017), pp. 579–584. DOI: 10.1038/nature24622. arXiv: 1707.04344 [quant-ph].

[13] C. Monroe. "Quantum information processing with atoms and photons". In: 416 (Mar. 2002), pp. 238–246. DOI: 10.1038/416238a.

[14] T. Udem, R. Holzwarth, and T. W. Hänsch. "Optical frequency metrology". In: 416 (Mar. 2002), pp. 233–237. DOI: 10.1038/416233a.

[15] S. M. Dickerson et al. "Multiaxis Inertial Sensing with Long-Time Point Source Atom Interferometry". In: *Physical Review Letters* 111.8, 083001 (Aug. 2013), p. 083001. DOI: 10.1103/PhysRevLett.111.083001. arXiv: 1305.1700 [physics.atom-ph].

[16] Michał Tomza et al. "Cold hybrid ion-atom systems". In: *arXiv e-prints*, arXiv:1708.07832 (Aug. 2017), arXiv:1708.07832. arXiv: 1708.07832 [physics.atom-ph].

[17] Z. Idziaszek et al. "Multichannel quantum-defect theory for ultracold atom-ion collisions". In: *New Journal of Physics* 13.8, 083005 (Aug. 2011), p. 083005. DOI: 10.1088/1367-2630/13/8/083005. arXiv: 1104.5600 [physics.atom-ph].

[18] Carlo Sias and Michael Köhl. "Hybrid quantum systems of ions and atoms". In: *arXiv e-prints*, arXiv:1401.3188 (Jan. 2014), arXiv:1401.3188. arXiv: 1401.3188 [cond-mat.quant-gas].

[19] C. Kollath, M. Köhl, and T. Giamarchi. "Scanning tunneling microscopy for ultracold atoms". In: *Phys. Rev. A* 76 (6 Dec. 2007), p. 063602. DOI: 10.1103/PhysRevA.76.063602. URL: https://link.aps.org/doi/10.1103/PhysRevA.76.063602.

[20] C. Zipkes et al. "A trapped single ion inside a Bose-Einstein condensate". In: 464 (Mar. 2010), pp. 388–391. DOI: 10.1038/nature08865. arXiv: 1002.3304 [cond-mat.quant-gas].

[21] L. Ratschbacher et al. "Controlling chemical reactions of a single particle". In: *Nature Physics* 8 (Sept. 2012), pp. 649–652. DOI: 10.1038/nphys2373. arXiv: 1206.4507 [physics.atom-ph].

[22] F. H. J. Hall et al. "Light-Assisted Ion-Neutral Reactive Processes in the Cold Regime: Radiative Molecule Formation versus Charge Exchange". In: 107, 243202 (Dec. 2011), p. 243202. DOI: 10.1103/PhysRevLett.107.243202. arXiv: 1108.3739 [physics.atom-ph].

[23] A. Härter and J. Hecker Denschlag. "Cold atom-ion experiments in hybrid traps". In: *Contemporary Physics* 55 (Jan. 2014), pp. 33–45. DOI: 10.1080/00107514.2013.854618. arXiv: 1309.5799 [physics.atom-ph].

[24] H. Massey. "Atom-atom and atom-ion collisions: I. Collisions between neutral atoms in which no excitation occurs". In: *Contemporary Physics* 12.6 (1971), pp. 537–558. DOI: 10.1080/00107517108205659. URL: https://doi.org/10.1080/00107517108205659.

[25] M. P. Langevin. "Une formule fondamentale de théorie cinétique". In: *Ann. Chim. Phys.* 5 (1905).

[26] Zong-Chao Yan et al. "Variational calculations of dispersion coefficients for interactions among H, He, and Li atoms". In: *Phys. Rev. A* 54 (4 Oct. 1996), pp. 2824–2833. DOI: 10.1103/PhysRevA.54.2824. URL: https://link.aps.org/doi/10.1103/PhysRevA.54.2824.

[27] A. Derevianko et al. "High-Precision Calculations of Dispersion Coefficients, Static Dipole Polarizabilities, and Atom-Wall Interaction Constants for Alkali-Metal Atoms". In: *Phys. Rev. Lett.* 82 (18 May 1999), pp. 3589–3592. DOI: 10.1103/PhysRevLett.82.3589. URL: https://link.aps.org/doi/10.1103/PhysRevLett.82.3589.

[28] R. Côté and A. Dalgarno. "Ultracold atom-ion collisions". In: *Phys. Rev. A* 62 (1 June 2000), p. 012709. DOI: 10.1103/PhysRevA.62.012709. URL: https://link.aps.org/doi/10.1103/PhysRevA.62.012709.

[29] H. G. Dehmelt. "Radiofrequency Spectroscopy of Stored Ions I: Storage". In: *Advances in Atomic and Molecular Physics* 3 (1968), pp. 53–72. DOI: 10.1016/S0065-2199(08)60170-0.

[30] W. Paul. "Electromagnetic traps for charged and neutral particles". In: *Reviews of Modern Physics* 62 (July 1990), pp. 531–540. DOI: 10.1103/RevModPhys.62.531.

[31] W. M. Itano et al. "Cooling methods in ion traps". In: *Physica Scripta Volume T* 59 (Jan. 1995), pp. 106–120. DOI: 10.1088/0031-8949/1995/T59/013.

[32] Milton Abramowitz and Irene A. Stegun. *Handbook of Mathematical Functions with Formulas, Graphs, and Mathematical Tables*. New York: Dover, 1964.

[33] J. Hansen. "Stability diagrams for coupled Mathieu-equations". In: *Ingenieur-Archiv* 55.6 (Nov. 1985), pp. 463–473. ISSN: 1432-0681. DOI: 10.1007/BF00537654. URL: https://doi.org/10.1007/BF00537654.

[34] M. Drewsen and A. Brøner. "Harmonic linear Paul trap: Stability diagram and effective potentials". In: 62.4, 045401 (Oct. 2000), p. 045401. DOI: 10.1103/PhysRevA.62.045401.

[35] G. Werth, V.N. Gheorghe, and F.G. Major. *Charged Particle Traps II*. Springer, 2009.

[36] R. Alheit et al. "Observation of instabilities in a Paul trap with higher-order anharmonicities". In: *Applied Physics B: Lasers and Optics* 61 (Sept. 1995), pp. 277–283. DOI: 10.1007/BF01082047.

[37] D. J. Berkeland et al. "Minimization of ion micromotion in a Paul trap". In: *Journal of Applied Physics* 83 (May 1998), pp. 5025–5033. DOI: 10.1063/1.367318.

[38] T. F. Gloger et al. "Ion-trajectory analysis for micromotion minimization and the measurement of small forces". In: 92.4, 043421 (Oct. 2015), p. 043421. DOI: 10.1103/PhysRevA.92.043421. arXiv: 1503.07031 [physics.atom-ph].

[39] Y. Ibaraki, U. Tanaka, and S. Urabe. "Detection of parametric resonance of trapped ions for micromotion compensation". In: *Applied Physics B: Lasers and Optics* 105 (Nov. 2011), pp. 219–223. DOI: 10.1007/s00340-011-4463-x.

[40] C. Zipkes et al. "Cold Heteronuclear Atom-Ion Collisions". In: *Phys. Rev. Lett.* 105 (13 Sept. 2010), p. 133201. DOI: 10.1103/PhysRevLett.105.133201. URL: https://link.aps.org/doi/10.1103/PhysRevLett.105.133201.

[41] Steven Chu et al. "Three-dimensional viscous confinement and cooling of atoms by resonance radiation pressure". In: *Phys. Rev. Lett.* 55 (1 July 1985), pp. 48–51. DOI: 10.1103/PhysRevLett.55.48. URL: https://link.aps.org/doi/10.1103/PhysRevLett.55.48.

[42] William D. Phillips and Harold Metcalf. "Laser Deceleration of an Atomic Beam". In: *Phys. Rev. Lett.* 48 (9 Mar. 1982), pp. 596–599. DOI: 10.1103/PhysRevLett.48.596. URL: https://link.aps.org/doi/10.1103/PhysRevLett.48.596.

[43] William D. Phillips and Harold Metcalf. "Laser Deceleration of an Atomic Beam". In: *Phys. Rev. Lett.* 48 (9 Mar. 1982), pp. 596–599. DOI: 10.1103/PhysRevLett.48.596. URL: https://link.aps.org/doi/10.1103/PhysRevLett.48.596.

[44] E. L. Raab et al. "Trapping of neutral sodium atoms with radiation pressure". In: *Physical Review Letters* 59 (Dec. 1987), pp. 2631–2634. DOI: 10.1103/PhysRevLett.59.2631.

[45] C.J. Foot. *Atomic physics*. Oxford master series in physics. Oxford University Press, 2005. ISBN: 9780198506966. URL: https://books.google.it/books?id=kXYpAQAAMAAJ.

[46] W. Ketterle, D. S. Durfee, and D. M. Stamper-Kurn. "Making, probing and understanding Bose-Einstein condensates". In: *arXiv e-prints*, cond-mat/9904034 (Apr. 1999), cond–mat/9904034. arXiv: cond-mat/9904034 [cond-mat].

[47] R. Blatt and C. F. Roos. "Quantum simulations with trapped ions". In: *Nature Physics* 8 (Apr. 2012), pp. 277–284. DOI: 10.1038/nphys2252.

[48] C. Zipkes et al. "Kinetics of a single trapped ion in an ultracold buffer gas". In: *New Journal of Physics* 13.5, 053020 (May 2011), p. 053020. DOI: 10.1088/1367-2630/13/5/053020. arXiv: 1012.0304 [physics.atom-ph].

[49] A. Mohammadi et al. "Minimizing rf-induced excess micromotion of a trapped ion with the help of ultracold atoms". In: *arXiv e-prints*, arXiv:1811.12267 (Nov. 2018), arXiv:1811.12267. arXiv: 1811.12267 [cond-mat.quant-gas].

[50] M. Cetina, A. T. Grier, and V. Vuletic. "Micromotion-Induced Limit to Atom-Ion Sympathetic Cooling in Paul Traps". In: *Phys. Rev. Lett.* 109 (25 Dec. 2012), p. 253201. DOI: 10.1103/PhysRevLett.109.253201. URL: https://link.aps.org/doi/10.1103/PhysRevLett.109.253201.

[51] Michał Krych and Zbigniew Idziaszek. "Description of ion motion in a Paul trap immersed in a cold atomic gas". In: *arXiv e-prints*, arXiv:1312.0279 (Dec. 2013), arXiv:1312.0279. arXiv: 1312.0279 [cond-mat.quant-gas].

[52] Ziv Meir et al. "Dynamics of a Ground-State Cooled Ion Colliding with Ultracold Atoms". In: 117.24, 243401 (Dec. 2016), p. 243401. DOI: 10.1103/PhysRevLett.117.243401. arXiv: 1603.01810 [physics.atom-ph].

[53] M. Krych. Private communication.

[54] H. Kanamori and E. E. Brodsky. "The physics of earthquakes". In: *Reports on progress in physics* 67 (2004).

[55] N. Johnson et al. "Pattern in Escalations in Insurgent and Terrorist Activity". In: *Science* 333 (July 2011), p. 81. DOI: 10.1126/science.1205068. arXiv: 1101.0987 [physics.soc-ph].

[56] Ralph G. Devoe. "Power-Law Distributions for a Trapped Ion Interacting with a Classical Buffer Gas". In: 102, 063001 (Feb. 2009), p. 063001. DOI: 10.1103/PhysRevLett.102.063001. arXiv: 0903.0637 [physics.atom-ph].

[57] C. Zipkes et al. "Kinetics of a single trapped ion in an ultracold buffer gas". In: *New Journal of Physics* 13.5, 053020 (May 2011), p. 053020. DOI: 10.1088/1367-2630/13/5/053020. arXiv: 1012.0304 [physics.atom-ph].

[58] S. Schmid, A. Härter, and J. H. Denschlag. "Dynamics of a Cold Trapped Ion in a Bose-Einstein Condensate". In: 105, 133202 (Sept. 2010), p. 133202. DOI: 10.1103/PhysRevLett.105.133202. arXiv: 1007.4717 [cond-mat.quant-gas].

[59] A. Härter et al. "Single Ion as a Three-Body Reaction Center in an Ultracold Atomic Gas". In: *Physical Review Letters* 109.12, 123201 (Sept. 2012), p. 123201. DOI: 10.1103/PhysRevLett.109.123201. arXiv: 1206.0242 [physics.atom-ph].

[60] K. Ravi et al. "Sympathetic and swap cooling of trapped ions by cold atoms in a MOT". In: *arXiv e-prints*, arXiv:1112.5825 (Dec. 2011), arXiv:1112.5825. arXiv: 1112.5825 [physics.atom-ph].

[61] M. Knoop, M. Vedel, and F. Vedel. "Lifetime, collisional-quenching, and j-mixing measurements of the metastable 3D levels of Ca^+". In: *Phys. Rev. A* 52 (5 Nov. 1995), pp. 3763–3769. DOI: 10.1103/PhysRevA.52.3763. URL: https://link.aps.org/doi/10.1103/PhysRevA.52.3763.

[62] Martina Knoop, Michel Vedel, and Fernande Vedel. "Collisional quenching and j-mixing rate constants for the $3D$ levels of Ca^+". In: *Phys. Rev. A* 58 (1 July 1998), pp. 264–269. DOI: 10.1103/PhysRevA.58.264. URL: https://link.aps.org/doi/10.1103/PhysRevA.58.264.

[63] W. G. Rellergert et al. "Evidence for sympathetic vibrational cooling of translationally cold molecules". In: 495 (Mar. 2013), pp. 490–494. DOI: 10.1038/nature11937.

[64] L. Ratschbacher et al. "Decoherence of a Single-Ion Qubit Immersed in a Spin-Polarized Atomic Bath". In: 110, 160402 (Apr. 2013), p. 160402. DOI: 10.1103/PhysRevLett.110.160402. arXiv: 1301.5452 [quant-ph].

[65] Hauke Doerk, Zbigniew Idziaszek, and Tommaso Calarco. "Atom-ion quantum gate". In: *Phys. Rev. A* 81 (1 Jan. 2010), p. 012708. DOI: 10.1103/PhysRevA.81.012708. URL: https://link.aps.org/doi/10.1103/PhysRevA.81.012708.

[66] T. Secker et al. "Controlled long-range interactions between Rydberg atoms and ions". In: *Phys. Rev. A* 94 (1 July 2016), p. 013420. DOI: 10.1103/PhysRevA.94.013420. URL: https://link.aps.org/doi/10.1103/PhysRevA.94.013420.

[67] Ch. Schneider et al. "Optical trapping of an ion". In: *Nature Photonics* 4 (Nov. 2010), pp. 772–775. DOI: 10.1038/nphoton.2010.236. arXiv: 1001.2953 [quant-ph].

[68] I. Buluta and F. Nori. "Quantum Simulators". In: *Science* 326 (Oct. 2009), p. 108. DOI: 10.1126/science.1177838.

[69] I. Bloch, J. Dalibard, and S. Nascimbène. "Quantum simulations with ultracold quantum gases". In: *Nature Physics* 8 (Apr. 2012), pp. 267–276. DOI: 10.1038/nphys2259.

[70] J. Zhang et al. "Observation of a many-body dynamical phase transition with a 53-qubit quantum simulator". In: 551 (Nov. 2017), pp. 601–604. DOI: 10.1038/nature24654. arXiv: 1708.01044 [quant-ph].

[71] U. Bissbort et al. "Emulating Solid-State Physics with a Hybrid System of Ultracold Ions and Atoms". In: *Physical Review Letters* 111.8, 080501 (Aug. 2013), p. 080501. DOI: 10.1103/PhysRevLett.111.080501. arXiv: 1304.4972 [cond-mat.quant-gas].

[72] R. Gerritsma et al. "Bosonic Josephson Junction Controlled by a Single Trapped Ion". In: *Phys. Rev. Lett.* 109 (8 Aug. 2012), p. 080402. DOI: 10.1103/PhysRevLett.109.080402. URL: https://link.aps.org/doi/10.1103/PhysRevLett.109.080402.

[73] A. Negretti et al. "Generalized Kronig-Penney model for ultracold atomic quantum systems". In: *Phys. Rev. B* 90 (15 Oct. 2014), p. 155426. DOI: 10.1103/PhysRevB.90.155426. URL: https://link.aps.org/doi/10.1103/PhysRevB.90.155426.

[74] T. Sikorsky et al. "Spin-controlled atom-ion chemistry". In: *Nature Communications* 9, 920 (Mar. 2018), p. 920. DOI: 10.1038/s41467-018-03373-y.

[75] Joop J. Gilijamse et al. "Near-Threshold Inelastic Collisions Using Molecular Beams with a Tunable Velocity". In: *Science* 313.5793 (2006), pp. 1617–1620. ISSN: 0036-8075. DOI: 10.1126/science.1131867. eprint: http://science.sciencemag.org/content/313/5793/1617.full.pdf. URL: http://science.sciencemag.org/content/313/5793/1617.

[76] S. E. Maxwell et al. "High-Flux Beam Source for Cold, Slow Atoms or Molecules". In: *Physical Review Letters* 95.17, 173201 (Oct. 2005), p. 173201. DOI: 10.1103/PhysRevLett.95.173201. eprint: physics/0508100.

[77] Dieter Gerlich and Stevan Horning. "Experimental investigation of radiative association processes as related to interstellar chemistry". In: *Chemical Reviews* 92.7 (1992), pp. 1509–1539. DOI: 10.1021/cr00015a003. eprint: https://doi.org/10.1021/cr00015a003. URL: https://doi.org/10.1021/cr00015a003.

[78] Ralf Schützhold et al. "Analogue of Cosmological Particle Creation in an Ion Trap". In: 99, 201301 (Nov. 2007), p. 201301. DOI: 10.1103/PhysRevLett.99.201301. arXiv: 0705.3755 [quant-ph].

[79] David Smith. "The ion chemistry of interstellar clouds". In: *Chemical Reviews* 92.7 (1992), pp. 1473–1485. DOI: 10.1021/cr00015a001. eprint: https://doi.org/10.1021/cr00015a001. URL: https://doi.org/10.1021/cr00015a001.

[80] C. Champenois et al. "Ion ring in a linear multipole trap for optical frequency metrology". In: *Phys. Rev. A* 81 (4 Apr. 2010), p. 043410. DOI: 10.1103/PhysRevA.81.043410. URL: https://link.aps.org/doi/10.1103/PhysRevA.81.043410.

[81] N. Huntemann et al. "Single-Ion Atomic Clock with 3 $\times 10^{-18}$ Systematic Uncertainty". In: *Physical Review Letters* 116.6, 063001 (Feb. 2016), p. 063001. DOI: 10.1103/PhysRevLett.116.063001. arXiv: 1602.03908 [physics.atm-clus].

[82] G. K. Campbell et al. "The absolute frequency of the ^{87}Sr optical clock transition". In: *Metrologia* 45 (Oct. 2008), pp. 539–548. DOI: 10.1088/0026-1394/45/5/008. arXiv: 0804.4509 [physics.atom-ph].

[83] A. C. Vutha, T. Kirchner, and P. Dubé. "Collisional frequency shift of a trapped-ion optical clock". In: 96.2, 022704 (Aug. 2017), p. 022704. DOI: 10.1103/PhysRevA.96.022704. arXiv: 1705.10019 [physics.atom-ph].

[84] A. M. Hankin et al. "Systematic uncertainty due to background-gas collisions in trapped-ion optical clocks". In: *arXiv e-prints*, arXiv:1902.08701 (Feb. 2019), arXiv:1902.08701. arXiv: 1902.08701 [physics.atom-ph].

[85] A. Härter et al. "Minimization of ion micromotion using ultracold atomic probes". In: *Applied Physics Letters* 102.22, 221115 (June 2013), p. 221115. DOI: 10.1063/1.4809578. arXiv: 1302.6157 [physics.atom-ph].

[86] Robin Côté. "From Classical Mobility to Hopping Conductivity: Charge Hopping in an Ultracold Gas". In: *Phys. Rev. Lett.* 85 (25 Dec. 2000), pp. 5316–5319. DOI: 10.1103/PhysRevLett.85.5316. URL: https://link.aps.org/doi/10.1103/PhysRevLett.85.5316.

[87] R. Côté, V. Kharchenko, and M. D. Lukin. "Mesoscopic Molecular Ions in Bose-Einstein Condensates". In: *Phys. Rev. Lett.* 89 (9 Aug. 2002), p. 093001. DOI: 10.1103/PhysRevLett.89.093001. URL: https://link.aps.org/doi/10.1103/PhysRevLett.89.093001.

[88] Andrew T. Grier et al. "Observation of Cold Collisions between Trapped Ions and Trapped Atoms". In: *Phys. Rev. Lett.* 102 (22 June 2009), p. 223201. DOI: 10.1103/PhysRevLett.102.223201. URL: https://link.aps.org/doi/10.1103/PhysRevLett.102.223201.

[89] Prateek Puri et al. "Synthesis of mixed hypermetallic oxide $BaOCa^+$ from laser-cooled reagents in an atom-ion hybrid trap". In: *Science* 357.6358 (Sept. 2017), pp. 1370–1375. DOI: 10.1126/science.aan4701. arXiv: 1709.02399 [physics.atom-ph].

[90] D. S. Goodman et al. "Measurement of the low-energy $Na^+ - Na$ total collision rate in an ion-neutral hybrid trap". In: *Phys. Rev. A* 91 (1 Jan. 2015), p. 012709. DOI: 10.1103/PhysRevA.91.012709. URL: https://link.aps.org/doi/10.1103/PhysRevA.91.012709.

[91] K. Ravi et al. "Cooling and stabilization by collisions in a mixed ion-atom system". In: *Nature Communications* 3, 1126 (Oct. 2012), p. 1126. DOI: 10.1038/ncomms2131.

[92] J. M. Kwolek et al. "Measurement of charge exchange between Na and Ca^+ in a hybrid trap". In: *Phys. Rev. A* 99 (5 May 2019), p. 052703. DOI: 10.1103/PhysRevA.99.052703. URL: https://link.aps.org/doi/10.1103/PhysRevA.99.052703.

[93] Artjom Krükow et al. "Reactive two-body and three-body collisions of Ba^+ in an ultracold Rb gas". In: *Phys. Rev. A* 94 (3 Sept. 2016), p. 030701. DOI: 10.1103/PhysRevA.94.030701. URL: https://link.aps.org/doi/10.1103/PhysRevA.94.030701.

[94] A. Härter et al. "Population distribution of product states following three-body recombination in an ultracold atomic gas". In: *Nature Physics* 9.8 (Aug. 2013), pp. 512–517. DOI: 10.1038/nphys2661.

[95] S. Jyothi et al. "Photodissociation of Trapped $Rb_2{}^+$: Implications for Simultaneous Trapping of Atoms and Molecular Ions". In: 117.21, 213002 (Nov. 2016), p. 213002. DOI: 10.1103/PhysRevLett.117.213002. arXiv: 1601.01119 [physics.atom-ph].

[96] Bastian Höltkemeier et al. "Buffer-Gas Cooling of a Single Ion in a Multipole Radio Frequency Trap Beyond the Critical Mass Ratio". In: 116.23, 233003 (June 2016), p. 233003. DOI: 10.1103/PhysRevLett.116.233003. arXiv: 1505.06909 [physics.atom-ph].

[97] H. Fürst et al. "Dynamics of a single ion-spin impurity in a spin-polarized atomic bath". In: *Phys. Rev. A* 98 (1 July 2018), p. 012713. DOI: 10.1103/PhysRevA.98.012713. URL: https://link.aps.org/doi/10.1103/PhysRevA.98.012713.

[98] Thai M. Hoang, Peter D. D. Schwindt, and Yuan-Yu Jau. "Thermal Atom-Ion Collisions in K-Yb$^+$ Hybrid System". In: *arXiv e-prints*, arXiv:1901.00905 (Jan. 2019), arXiv:1901.00905. arXiv: 1901.00905 [physics.atom-ph].

[99] Tomas Sikorsky et al. "Phase Locking between Different Partial Waves in Atom-Ion Spin-Exchange Collisions". In: *Phys. Rev. Lett.* 121 (17 Oct. 2018), p. 173402. DOI: 10.1103/PhysRevLett.121.173402. URL: https://link.aps.org/doi/10.1103/PhysRevLett.121.173402.

[100] James R. Anglin and Wolfgang Ketterle. "Bose-Einstein condensation of atomic gases". In: 416.6877 (Mar. 2002), pp. 211–218. DOI: 10.1038/416211a.

[101] H. A. Fürst et al. "Prospects of reaching the quantum regime in Li?Yb$^+$ mixtures". In: *Journal of Physics B Atomic Molecular Physics* 51.19, 195001 (Oct. 2018), p. 195001. DOI: 10.1088/1361-6455/aadd7d. arXiv: 1804.04486 [physics.atom-ph].

[102] Thomas Huber et al. "A far-off-resonance optical trap for a Ba$^+$ ion". In: *Nature Communications* 5, 5587 (Nov. 2014), p. 5587. DOI: 10.1038/ncomms6587. arXiv: 1408.3269 [physics.atom-ph].

[103] Alexander Lambrecht et al. "Long lifetimes in optical ion traps". In: *arXiv e-prints*, arXiv:1609.06429 (Sept. 2016), arXiv:1609.06429. arXiv: 1609.06429 [quant-ph].

[104] M. Enderlein et al. "Single Ions Trapped in a One-Dimensional Optical Lattice". In: *Physical Review Letters* 109.23, 233004 (Dec. 2012), p. 233004. DOI: 10.1103/PhysRevLett.109.233004. arXiv: 1208.3329 [physics.atom-ph].

[105] Julian Schmidt et al. "Optical Trapping of Ion Coulomb Crystals". In: *Phys. Rev. X* 8 (2 May 2018), p. 021028. DOI: 10.1103/PhysRevX.8.021028. URL: https://link.aps.org/doi/10.1103/PhysRevX.8.021028.

[106] A. Lambrecht et al. "Long lifetimes and effective isolation of ions in optical and electrostatic traps". In: *Nature Photonics* 11 (Nov. 2017), pp. 704–707. DOI: 10.1038/s41566-017-0030-2.

[107] T. Schmid et al. "Rydberg Molecules for Ion-Atom Scattering in the Ultracold Regime". In: *Phys. Rev. Lett.* 120 (15 Apr. 2018), p. 153401. DOI: 10.1103/PhysRevLett.120.153401. URL: https://link.aps.org/doi/10.1103/PhysRevLett.120.153401.

[108] Energy levels of singly ionized Barium available at https://physics.nist.gov/PhysRefData/Handbook/Tables/bariumtable6.htm.

[109] NIST, Basic atomic and spectroscopic data, http://physics.nist.gov/PhysRefData/ADS/index.html.

[110] W. Neuhauser et al. "Visual observation and optical cooling of electrodynamically contained ions". In: *Applied Physics* 17 (Oct. 1978), pp. 123–129. DOI: 10.1007/BF00885243.

[111] M. E. Gehm. Properties of ^{6}Li, Feb. 2003. Available at https://www.physics.ncsu.edu/jet/techdocs/pdf/PropertiesOfLi.pdf.

[112] Olaf Mandel et al. "Coherent Transport of Neutral Atoms in Spin-Dependent Optical Lattice Potentials". In: *Phys. Rev. Lett.* 91 (1 July 2003), p. 010407. DOI: 10.1103/PhysRevLett.91.010407. URL: https://link.aps.org/doi/10.1103/PhysRevLett.91.010407.

[113] Anton Mazurenko et al. "Experimental realization of a long-range antiferromagnet in the Hubbard model with ultracold atoms". In: *arXiv e-prints*, arXiv:1612.08436 (Dec. 2016), arXiv:1612.08436. arXiv: 1612.08436 [cond-mat.quant-gas].

[114] V. Bužek et al. "Cavity QED with cold trapped ions". In: 56 (Sept. 1997), pp. 2352–2360. DOI: 10.1103/PhysRevA.56.2352.

[115] M Keller et al. "Deterministic cavity quantum electrodynamics with trapped ions". In: *Journal of Physics B: Atomic, Molecular and Optical Physics* 36.3 (Jan. 2003), pp. 613–622. DOI: 10.1088/0953-4075/36/3/318. URL: https://doi.org/10.1088%2F0953-4075%2F36%2F3%2F318.

[116] Rasmus B. Linnet et al. "Pinning an Ion with an Intracavity Optical Lattice". In: *Phys. Rev. Lett.* 109 (23 Dec. 2012), p. 233005. DOI: 10.1103/PhysRevLett.109.233005. URL: https://link.aps.org/doi/10.1103/PhysRevLett.109.233005.

[117] Leon Karpa et al. "Suppression of ion transport due to long-lived subwavelength localization by an optical lattice." In: *Physical review letters* 111 16 (2013).

[118] Ian Counts et al. "Multislip Friction with a Single Ion". In: *Phys. Rev. Lett.* 119 (4 July 2017), p. 043601. DOI: 10.1103/PhysRevLett.119.043601. URL: https://link.aps.org/doi/10.1103/PhysRevLett.119.043601.

[119] C. Schneider et al. "Influence of static electric fields on an optical ion trap". In: 85.1, 013422 (Jan. 2012), p. 013422. DOI: 10.1103/PhysRevA.85.013422. arXiv: 1112.3858 [physics.atom-ph].

[120] R. Grimm, M. Weidemüller, and Y. B. Ovchinnikov. "Optical Dipole Traps for Neutral Atoms". In: *Advances in Atomic Molecular and Optical Physics* 42 (2000), pp. 95–170. DOI: 10.1016/S1049-250X(08)60186-X. eprint: physics/9902072.

[121] H. Kogelnik and T. Li. "Laser beams and resonators". In: 5 (Oct. 1966), p. 1550. DOI: 10.1364/AO.5.001550.

[122] T. Huber et al. "A far-off-resonance optical trap for a Ba^+ ion". In: *Nature Communications* 5, 5587 (Nov. 2014), p. 5587. DOI: 10.1038/ncomms6587. arXiv: 1408.3269 [physics.atom-ph].

[123] J. Kaur et al. "Magic wavelengths in the alkaline-earth-metal ions". In: 92.3, 031402 (Sept. 2015), p. 031402. DOI: 10.1103/PhysRevA.92.031402. arXiv: 1508.00653 [physics.atom-ph].

[124] Richard C. Thompson. "Ion Coulomb crystals". In: *Contemporary Physics* 56.1 (Jan. 2015), pp. 63–79. DOI: 10.1080/00107514.2014.989715. arXiv: 1411.4945 [quant-ph].

[125] H. M. Van Horn. "Dense Astrophysical Plasmas". In: *Science* 252.5004 (1991), pp. 384–389. ISSN: 0036-8075. DOI: 10.1126/science.252.5004.384. eprint: http://science.sciencemag.org/content/252/5004/384.full.pdf. URL: http://science.sciencemag.org/content/252/5004/384.

[126] E. Urban et al. "Coherent Control of the Rotational Degree of Freedom of a Two-Ion Coulomb Crystal". In: *arXiv e-prints*, arXiv:1903.05763 (Mar. 2019), arXiv:1903.05763. arXiv: 1903.05763 [quant-ph].

[127] C. Raman et al. "Evidence for a Critical Velocity in a Bose-Einstein Condensed Gas". In: *Phys. Rev. Lett.* 83 (13 Sept. 1999), pp. 2502–2505. DOI: 10.1103/PhysRevLett.83.2502. URL: https://link.aps.org/doi/10.1103/PhysRevLett.83.2502.

[128] Kristian Fenech. "Kinematics and thermodynamics of a two-dimensional Fermi gas". PhD thesis. Swinburne University of Technology, 2016.

[129] Marko Cetina et al. "Bright source of cold ions for surface-electrode traps". In: *Physical Review A* 76.4, 041401 (Oct. 2007), p. 041401. DOI: 10.1103/PhysRevA.76.041401. arXiv: physics/0702025 [physics.atom-ph].

[130] Jeremy M. Sage, Andrew J. Kerman, and John Chiaverini. "Loading of a surface-electrode ion trap from a remote, precooled source". In: *Physical Review A* 86.1, 013417 (July 2012), p. 013417. DOI: 10.1103/PhysRevA.86.013417. arXiv: 1205.6379 [physics.atom-ph].

[131] S. De et al. "Magneto-optical trapping of barium". In: *Physical Review A* 79, 041402 (Apr. 2009), p. 041402. DOI: 10.1103/PhysRevA.79.041402. arXiv: 0807.4100 [physics.atom-ph].

[132] P. W. Likins and K. G. Lindh. "Infinite determinant methods for stability analysis of periodic-coefficient differential equations". In: *AIAA Journal* 8 (Apr. 1970), pp. 680–686. DOI: 10.2514/3.5741.

[133] A. Ozakin and F. Shaikh. "Stability analysis of surface ion traps". In: *arXiv e-prints* (Sept. 2011). arXiv: 1109.2160 [quant-ph].

[134] M. Greiner et al. "Magnetic transport of trapped cold atoms over a large distance". In: *Phys. Rev. A* 63 (3 Feb. 2001), p. 031401. DOI: 10.1103/PhysRevA.63.031401. URL: https://link.aps.org/doi/10.1103/PhysRevA.63.031401.

[135] J. Goldwin et al. "Measurement of the interaction strength in a Bose-Fermi mixture with ^{87}Rb and ^{40}K". In: *Phys. Rev. A* 70 (2 Aug. 2004), p. 021601. DOI: 10.1103/PhysRevA.70.021601. URL: https://link.aps.org/doi/10.1103/PhysRevA.70.021601.

[136] J. A. Sauer et al. "Cavity QED with optically transported atoms". In: *Phys. Rev. A* 69 (5 May 2004), p. 051804. DOI: 10.1103/PhysRevA.69.051804. URL: https://link.aps.org/doi/10.1103/PhysRevA.69.051804.

[137] S. Schmid et al. "Long distance transport of ultracold atoms using a 1D optical lattice". In: *New Journal of Physics* 8 (Aug. 2006), p. 159. DOI: 10.1088/1367-2630/8/8/159. eprint: cond-mat/0605736.

[138] T. L. Gustavson et al. "Transport of Bose-Einstein Condensates with Optical Tweezers". In: *Phys. Rev. Lett.* 88 (2 Dec. 2001), p. 020401. DOI: 10.1103/PhysRevLett.88.020401. URL: https://link.aps.org/doi/10.1103/PhysRevLett.88.020401.

[139] J. Léonard et al. "Optical transport and manipulation of an ultracold atomic cloud using focus-tunable lenses". In: *New Journal of Physics* 16, 093028 (Sept. 2014), p. 093028. DOI: 10.1088/1367-2630/16/9/093028. arXiv: 1406.2336 [cond-mat.quant-gas].

[140] P. Herskind et al. "Loading of large ion Coulomb crystals into a linear Paul trap incorporating an optical cavity". In: *Applied Physics B: Lasers and Optics* 93.2-3 (Nov. 2008), pp. 373–379. DOI: 10.1007/s00340-008-3199-8. arXiv: 0804.4589 [quant-ph].

[141] W. Nagourney. *Quantum electronics for atomic physics*. Ed. by Oxford University Press. 2010.

[142] P. F. Herskind et al. "Positioning of the rf potential minimum line of a linear Paul trap with micrometer precision". In: *Journal of Physics B Atomic Molecular Physics* 42.15, 154008 (Aug. 2009), p. 154008. DOI: 10.1088/0953-4075/42/15/154008. arXiv: 0905.3147 [quant-ph].

[143] S. Gulde. "Implementing quantum gates with ion traps". PhD thesis. Universit at Innsbruck, 2003.

[144] G. Leschhorn, T. Hasegawa, and T. Schaetz. "Efficient photo-ionization for barium ion trapping using a dipole-allowed resonant two-photon transition". In: *Applied Physics B: Lasers and Optics* 108 (July 2012), pp. 159–165. DOI: 10.1007/s00340-012-5101-y. arXiv: 1110.4040 [physics.atom-ph].

[145] M. Doležal et al. "Analysis of thermal radiation in ion traps for optical frequency standards". In: *Metrologia* 52, 842 (Dec. 2015), p. 842. DOI: 10.1088/0026-1394/52/6/842. arXiv: 1510.05556 [physics.atom-ph].

[146] ROOT, the modular scientific software toolkit developed by Cern, available at http://root.cern.ch/.

[147] Kilian Singer et al. "Colloquium: Trapped ions as quantum bits: Essential numerical tools". In: *Reviews of Modern Physics* 82 (July 2010), pp. 2609–2632. DOI: 10.1103/RevModPhys.82.2609. arXiv: 0912.0196 [quant-ph].

[148] Y. Saad and M. Schultz. "GMRES: A Generalized Minimal Residual Algorithm for Solving Nonsymmetric Linear Systems". In: *SIAM Journal on Scientific and Statistical Computing* 7.3 (1986), pp. 856–869. DOI: 10.1137/0907058.

[149] L. Greengard and V. Rokhlin. "A fast algorithm for particle simulations". In: *Journal of Computational Physics* 73 (Dec. 1987), pp. 325–348. DOI: 10.1016/0021-9991(87)90140-9.

[150] A. Detti. "Design and simulation of an optical objective for the imaging of Lithium atoms and Barium ions". MA thesis. University of Florence, astrophysics and physics department, 2016.

[151] A. Detti et al. "A compact radiofrequency drive based on interdependent resonant circuits for precise control of ion traps". In: *Review of Scientific Instruments* 90, 023201 (Feb. 2019), p. 023201. DOI: 10.1063/1.5063305.

[152] D. De Munshi et al. "Precision measurement of branching fractions of $^{138}Ba^{+}$: Testing many-body theories below the 1% level". In: *Phys. Rev. A* 91 (4 Apr. 2015), p. 040501. DOI: 10.1103/PhysRevA.91.040501. URL: https://link.aps.org/doi/10.1103/PhysRevA.91.040501.

[153] N. Yu, W. Nagourney, and H. Dehmelt. "Radiative Lifetime Measurement of the Ba^{+} Metastable $D_{3/2}$ State". In: *Phys. Rev. Lett.* 78 (26 June 1997), pp. 4898–4901. DOI: 10.1103/PhysRevLett.78.4898. URL: https://link.aps.org/doi/10.1103/PhysRevLett.78.4898.

[154] C. E. Wieman and L. Hollberg. "Using diode lasers for atomic physics". In: *Review of Scientific Instruments* 62 (Jan. 1991), pp. 1–20. DOI: 10.1063/1.1142305.

[155] X. Baillard et al. "Interference-filter-stabilized external-cavity diode lasers". In: *Optics Communications* 266 (Oct. 2006), pp. 609–613. DOI: 10.1016/j.optcom.2006.05.011. eprint: physics/0605046.

[156] K. Liu and M. G. Littman. "Novel geometry for single-mode scanning of tunable lasers". In: *Optics Letters* 6 (Mar. 1981), p. 117. DOI: 10.1364/OL.6.000117.

[157] P. McNicholl and H. J. Metcalf. "Synchronous cavity mode and feedback wavelength scanning in dye laser oscillators with gratings". In: 24 (Sept. 1985), pp. 2757–2761. DOI: 10.1364/AO.24.002757.

[158] L. Ricci et al. "A compact grating-stabilized diode laser system for atomic physics". In: *Optics Communications* 117 (Feb. 1995), pp. 541–549. DOI: 10.1016/0030-4018(95)00146-Y.

[159] M. de Labachelerie and G. Passedat. "Mode-hop suppression of Littrow grating-tuned lasers". In: 32 (Jan. 1993), pp. 269–274. DOI: 10.1364/AO.32.000269.

[160] M. Nazarathy et al. "Spectral analysis of optical mixing measurements". In: *Journal of Lightwave Technology* 7 (July 1989), pp. 1083–1096. DOI: 10.1109/50.29635.

[161] T.W. Hansch and B. Couillaud. "Laser frequency stabilization by polarization spectroscopy of a reflecting reference cavity". In: *Optics Communications* 35.3 (1980), pp. 441–444. ISSN: 0030-4018. DOI: https://doi.org/10.1016/0030-4018(80)90069-3. URL: http://www.sciencedirect.com/science/article/pii/0030401880900693.

[162] J. C. B. Kangara et al. "Design and construction of cost-effective tapered amplifier systems for laser cooling and trapping experiments". In: *American Journal of Physics* 82 (Aug. 2014), pp. 805–817. DOI: 10.1119/1.4867376.

[163] Z. Jiangou et al. "Optical absorption properties of doped lithium niobate crystals". In: *Journal of Physics Condensed Matter* 4 (Mar. 1992), pp. 2977–2983. DOI: 10.1088/0953-8984/4/11/022.

[164] M. Maiwald et al. "600 mW optical output power at 488 nm by use of a high-power hybrid laser diode system and a periodically poled MgO:LiNbO3 bulk crystal". In: *Opt. Lett.* 31.6 (Mar. 2006), pp. 802–804. DOI: 10.1364/OL.31.000802.

[165] G. D. Boyd and D. A. Kleinman. "Parametric Interaction of Focused Gaussian Light Beams". In: *Journal of Applied Physics* 39 (July 1968), pp. 3597–3639. DOI: 10.1063/1.1656831.

[166] M. De Rosa. Private communication.

[167] J. A. Sherman. "Single barium ion spectroscopy: light shifts, hyperfi ne structure, and progress on an optical frequency standard and atomic parity violation". PhD thesis. University of Washington, 2007.

[168] R. W. P. Drever et al. "A Gravity-Wave Detector Using Optical Cavity Sensing". In: *General Relativity and Gravitation 1980*. Ed. by E. Schmutzer. 1983, p. 265.

[169] R. W. P. Drever et al. "Laser frequency stabilization by polarization spectroscopy of a reflecting reference cavity". In: *Applied Physics B* 31.2 (1980), pp. 97–105.

[170] D. S. Elliott, R. Roy, and S. J. Smith. "Extracavity laser band-shape and bandwidth modification". In: 26.1 (July 1982), pp. 12–18. DOI: 10.1103/PhysRevA.26.12.

[171] E. Perego et al. "A scalable hardware and software control apparatus for experiments with hybrid quantum systems". In: *Review of Scientific Instruments* 89.11, 113116 (Nov. 2018), p. 113116. DOI: 10.1063/1.5049120.

[172] National Instruments, http://www.ni.com/.

[173] MKS Automation and Control, http://www.mksinst.com/product/catalog.aspx?CatalogID=6.

[174] CAS DataLogger data acquisition systems, http://www.dataloggerinc.com/data-acquisition-systems.

[175] Scott F. Owen and David S. Hall. "Fast line-based experiment timing system for LabVIEW". In: *Review of Scientific Instruments* 75.1 (2004), pp. 259–265. DOI: 10.1063/1.1630833. URL: https://doi.org/10.1063/1.1630833.

[176] Aviv Keshet and Wolfgang Ketterle. "A distributed, graphical user interface based, computer control system for atomic physics experiments". In: *Review of Scientific Instruments* 84.1 (2013), p. 015105. DOI: 10.1063/1.4773536. URL: https://doi.org/10.1063/1.4773536.

[177] CONTROL, available at http://www.strontiumbec.com.

[178] P. T. Starkey et al. "A scripted control system for autonomous hardware-timed experiments". In: *Review of Scientific Instruments* 84.8 (2013), p. 085111. DOI: 10.1063/1.4817213. URL: https://doi.org/10.1063/1.4817213.

[179] Bourdeauducq, Sébastien et al. (2016). ARTIQ 1.0. Zenodo. 10.5281/zenodo.51303.

[180] Peter E. Gaskell et al. "An open-source, extensible system for laboratory timing and control". In: *Review of Scientific Instruments* 80.11 (2009), p. 115103. DOI: 10.1063/1.3250825. URL: https://doi.org/10.1063/1.3250825.

[181] T. Reenskaug and J. O. Coplien. The DCI Architecture: A New Vision of Object-Oriented Programming, Mar. 2009. Available at http://www.artima.com/articles/dci_vision.html.

[182] M. Pomponio. "Design and realization of generalized electronic instrumentation for experiments with ultracold ions and atoms". MA thesis. Politecnico di Torino, 2017.

[183] Z. Idziaszek et al. "Quantum theory of ultracold atom-ion collisions". In: 79.1, 010702 (Jan. 2009), p. 010702. DOI: 10.1103/PhysRevA.79.010702. arXiv: 0806.4002 [physics.atom-ph].

[184] Michael Knap et al. "Time-Dependent Impurity in Ultracold Fermions: Orthogonality Catastrophe and Beyond". In: *Phys. Rev. X* 2 (4 Dec. 2012), p. 041020. DOI: 10.1103/PhysRevX.2.041020. URL: https://link.aps.org/doi/10.1103/PhysRevX.2.041020.

[185] W. F. McGrew et al. "Atomic clock performance enabling geodesy below the centimetre level". In: 564 (Dec. 2018), pp. 87–90. DOI: 10.1038/s41586-018-0738-2.

[186] Daniel A. Steck, Quantum and Atom Optics, available online at http://steck.us/teaching (revision 0.12.4, 10 January 2019).

[187] C. Cohen-Tannoudji and D. Guéry-Odelin. *Advances in Atomic Physics: An Overview*. World Scientific, 2011. ISBN: 9789812774972.

[188] J. P. Gordon and A. Ashkin. "Motion of atoms in a radiation trap". In: 21 (May 1980), pp. 1606–1617. DOI: 10.1103/PhysRevA.21.1606.

[189] B. K. Sahoo, R. G. E. Timmermans, and K. Jungmann. "Accurate determination of the electric dipole matrix elements, lifetimes, polarizabilities and light-shift ratios in Ba+ and Ra+". In: *arXiv e-prints* (Sept. 2008). arXiv: 0809.5167 [physics.atom-ph].

[190] M. M. Fejer et al. "Quasi-phase-matched second harmonic generation - Tuning and tolerances". In: *IEEE Journal of Quantum Electronics* 28 (Nov. 1992), pp. 2631–2654. DOI: 10.1109/3.161322.

[191] D. A. Kleinman, A. Ashkin, and G. D. Boyd. "Second-Harmonic Generation of Light by Focused Laser Beams". In: *Physical Review* 145 (May 1966), pp. 338–379. DOI: 10.1103/PhysRev.145.338.

[192] G. D. Boyd et al. "Second-Harmonic Generation of Light with Double Refraction". In: *Physical Review* 137 (Feb. 1965), pp. 1305–1320. DOI: 10.1103/PhysRev.137.A1305.

[193] G. Masada. "Evaluation of Second Order Nonlinearity in Periodically Poled KTiOPO 4 Crystal Using Boyd and Kleinman Theory". In: 2014.

[194] A. Ashkin, G. Boyd, and J. Dziedzic. "Resonant optical second harmonic generation and mixing". In: *IEEE Journal of Quantum Electronics* 2 (June 1966), pp. 109–124. DOI: 10.1109/JQE.1966.1074007.

This Ph.D. thesis has been typeset by means of the TEX-system facilities. The typesetting engine was pdfLATEX. The document class was `toptesi`, by Claudio Beccari, with option `tipotesi=scudo`. This class is available in every up-to-date and complete TEX-system installation.